SPIM

Thèse de Doctorat

école doctorale sciences pour l'ingénieur et microtechniques
UNIVERSITÉ DE BOURGOGNE

Moisture absorption characteristics and effects on mechanical behaviour of carbon/epoxy composite:

Application to bonded patch repairs of composite structures

King Jye WONG

SPIM

Thèse de Doctorat

école doctorale sciences pour l'ingénieur et microtechniques
UNIVERSITÉ DE BOURGOGNE

THESIS
Submitted for the degree of Doctor of Philosophy of
Université de Bourgogne
Specialisation: Mechanics

Presented by
King Jye WONG

18 June 2013

MOISTURE ABSORPTION CHARACTERISTICS AND EFFECTS ON MECHANICAL BEHAVIOUR OF CARBON/EPOXY COMPOSITE: APPLICATION TO BONDED PATCH REPAIRS OF COMPOSITE STRUCTURES

Members of Jury

Françis COLLOMBET	Professor, Université de Toulouse	Chairman
Peter DAVIES	Research Engineer (HDR), IFREMER	Reviewer
Fréderic JACQUEMIN	Professor, Université de Nantes	Reviewer
Mohd Nasir TAMIN	Professor, Universiti Teknologi Malaysia	Examiner
Shahram AIVAZZADEH	Professor, Université de Bourgogne	Supervisor
Xiao-Jing GONG	Assoc.Prof.(HDR), Université de Bourgogne	Supervisor

DEDICATION

To my wife, Ru Yin (茹茵) and my daughter, Ï-nîng (语甯).

ACKNOWLEDGEMENTS

First of all, I would like to express my sincere and heartfelt thanks to Professor Dr. Shahram Aivazzadeh, Professor Dr. Gong Xiao-Jing and Professor Dr. Mohd Nasir Tamin for their patience and guidance through my studies at DRIVE, ISAT, Université de Bourgogne.

Sincere appreciation is extended to Professor Dr. Françis Collombet, Dr. Peter Davies and Professor Dr. Fréderic Jacquemin for their willingness to be the members of jury of my thesis. Their valuable comments and suggestions are highly acknowledged.

I am indebted to many of the academic, administrative and technical staffs at ISAT. Thanks to Professor Dr. Stéphane Fontaine and Professor Dr. Philippe Leclaire for their support to make my studies possible. I would like to extend my gratitude Dr. Jérome Rousseau, Dr. Olivier Sicot and Dr. Papa-Birame Gning for their generosity in sharing their knowledge. Special thanks to Dr. Benoît Piezel, for his help in MATLAB programming and comments on the French abstract. Not to forget Madam Carolyn Assencio, Madam Corrine Gralhien and Miss Aurélie Battut, who are always there whenever I need their help. I gratefully appreciate Mr. Bernard Adam, Mr. Pascal Rouault, Mr. Jean-Noël, Mr. Sylvain Erard, Mr. Anthony Perriot, Mr. Matthieu Gatellet and Mr. Arnold for all their technical supports. I would also like to express my gratitude to Madam Françoise Hervet for her teaching in French language, although I do not progress well.

To my family members, colleagues and friends, thank you very much.

Two-year financial support is provided by the Ministry of Higher Education Malaysia and Universiti Teknologi Malaysia.

My deepest appreciation is delivered to my wife, Ru Yin for all her sacrifices, love and care throughout all these years. Thank you Ï-nîng, my little lovely angel, you are always my joy in all circumstances.

Thank you God, for making all these happened!

Table of Contents

List of Figures

List of Tables

CHAPTER 1. INTRODUCTION

1.1. Motivation

Carbon fibre reinforced polymer (CFRP) composites are widely employed in advanced structural applications such as aircraft wing skin and fuselage, automobile body panels and marine deck structures. Composites have advantages of high specific strength and stiffness over metals. This could greatly reduce the weight of the structure which in turn benefits the industry in cost saving. For example, it was reported that 1 kg of weight reduction in an aircraft can save over 2900 litres of fuel per year [1-2]. However, the mechanical properties of fibre reinforced composites can be very sensitive to environmental parameters, such as temperature, humidity, light or other corrosive environments, especially those controlled by the properties of matrix and fibre/matrix interface. To be used as structural materials, durability is always important. Hence, thorough understanding on the response of the composites under different loading conditions is inevitable. Development of accurate materials models for prediction of deformation and failure of the composite with ageing degradation is necessary to facilitate optimum design and fabrication of composite structures.

It is well known that some high performance structures are always subjected to varying temperature and moisture exposures throughout their entire service lifetime. The temperature and moisture levels could vary throughout the day (see Figure 1.1), from take off to landing or vice-versa, during seasonal change or geographical difference. Continuous exposure at high temperature and moisture levels may lead to the change in mechanical behaviour of the aircraft structural components. Furthermore, cyclic thermal, moisture and mechanical loadings could even further deteriorate the performance of the structures and then lead to premature failure of the structure. The rudder failure of the Concorde G-BOAF happened on 12 April 1989 was identified as an example, where the ageing effects played an essential role [3]. It was reported that moisture ingression through unsealed rivet heads caused corrosion, which led to skin debonding from the honeycomb structure core and eventually brought to ultimate failure of the rudder structure. The rotor failure of a Robinson R22 Mariner helicopter VH-OHA on 20 June 2003 was another accident [4]. The main cause of this accident was believed to be the localised pitting corrosion that was provoked by the penetration of salt water into the inboard bolthole along the adhesive crack.

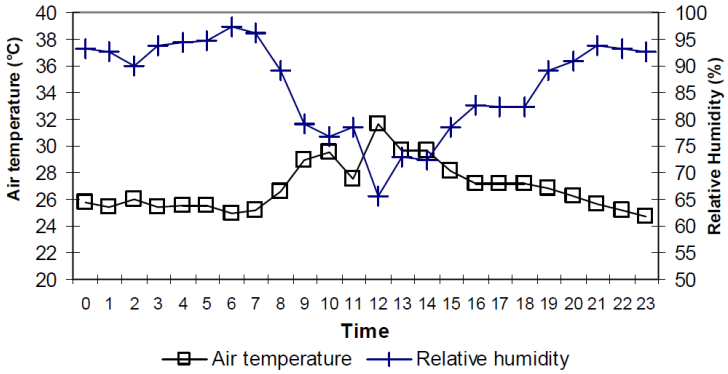

Figure 1.1: Daily air temperature and relative humidity variation in Johor Bahru, Malaysia [5].

In addition, quite often the structures in service are inevitably subjected to low velocity impact damages due to hail impact, ice strike, bird strike, ground vehicles and ground service equipment impacts. Damages weaken the materials, which cause early failure of the structures. To restore the load carrying ability of the materials, repair methods are employed.

As a temporary repair method, patch repair has the advantages of simple and less preparation time compared to other adhesive bonding repairs such as scarf and step sanded repairs. It can be implemented by removing the damaged region, followed by patches attachment using an adhesive. However, this method requires good surface preparation. Besides, external patches lead to aerodynamics disturbance and load path eccentricity, where high shear and peel stresses at patch edges are introduced [6]. Moreover, adhesives are also sensitive to environmental parameters, where the problem of stress corrosion cracking has to be considered.

1.2.Objectives and scopes

The aim of this study is to contribute to the methodology of predicting the mechanical behaviour of a composite structure under ageing. The moisture absorption and the corresponding changes in the mechanical behaviour are studied not only on the carbon/epoxy composite, but also on its bonded joints. The objectives include:

i. To quantify the water ingression behaviour in carbon/epoxy laminates as function of thicknesses;

ii. To determine the tensile and interface properties of the carbon/epoxy composite at different moisture content levels;

iii. To characterise the delamination behaviour of adhesive bonded composite joints under water penetration.

The scopes of the research cover:

i. Materials:

   a. Carbon/epoxy composites: T600S/R367-2, TR50S/R368-1, TR50S/R367-2 and T600S/R368-1;

   b. Adhesives: Araldite2015 and ESP110;

ii. Specimens and stacking sequences:

   a. Elementary tensile tests: $[0]_8$, $[90]_8$ and $[\pm 45]_{2S}$;

   b. Delamination tests: $[0_8//0_8]$ and [0/45/90/-45/90/-45/45/-45/0/90/0/45/0/45/-45/45/90/0/90/-45/90/-45/0/45//0/45/90/-45/90/-45/45/-45/0/90/0/45/0/45/-45/45/90/0/90/-45/90/-45/0/45];

   c. Unnotched and notched quasi-isotropic laminates: $[45/-45/0/90]_S$, $[-45/45/90/0]_S$, $[45/90/-45/0]_S$ and $[-45/0/45/90]_S$;

   d. Double-sided repairs with circular patches: $[\pm 45]_S$ and $[\mp 45]_S$;

iii. Testing parameters and variables:

   a. Ageing conditions: demineralised water at 70^oC;

   b. Testing conditions: ambient, quasi-static tests;

iv. Finite element modelling of delamination specimens and patch bonded repairs.

1.3.Organisation of thesis

This thesis is organised as follows:

Chapter 1 mainly provides the motivation, objectives and scopes of this study.

Chapter 2 gives a review of moisture absorption mechanisms and phenomena in polymers and composite materials, followed by the description of the mathematical models for Fickian and non-Fickian diffusion. The chapter then summarises the moisture and temperature effects on polymers, polymeric composites and adhesive bonded joints. In particular, the finite element modelling approaches on the durability of adhesive joints is reviewed. It is ended with the summary of circular patches bonded composite joints.

Chapter 3 discusses the water absorption behaviour in the carbon/epoxy composites used in this study. Specifically, the water uptake behaviour at various thicknesses/number of plies is investigated experimentally. An original model of water uptake process is proposed based on the experimental data. Herein, Fickian absorption is used for single-ply composites and a two-phase diffusion model for multi-ply composites. The water concentration profiles across the laminate thickness are also discussed.

Chapter 4 focuses on how elementary tensile and interface properties vary with moisture content. Elementary tensile properties are characterised through longitudinal, transverse and shear specimens tested under tensile loading, whereas interface properties are determined through mode I DCB, mode II ENF and mixed-mode I+II MMF tests. In addition, effects of fabrication techniques (hot-press and vacuum bagging) and adjacent plies orientation (0//0 and 0//45) at dry condition are analysed. Furthermore, mode I fibre bridging behaviour is characterised using a newly proposed linear-exponential bridging law. The delamination behaviour is then simulated through finite element method. Interface cohesive parameters are identified through simulations.

Chapter 5 reports the moisture effects on the delamination behaviour of adhesive bonded composite joints. Similarly, DCB, ENF and MMF tests are conducted. Apart from that, effects of adhesive type (ductile Araldite2015 and brittle ESP110) and surface treatment method

(sandpaper polished and plasma treated) are also studied. Mode II R-curve behaviour is characterised after that. It is followed by finite element modelling of the adhesive bonded joints using continuum damage modelling (CDM) approach. CDM parameters at each case are calibrated through the simulations.

Chapter 6 studies the quasi-isotropic laminates and their bonded repairs. Firstly, the width effect on the tensile strength of unnotched specimens is investigated. Next, effects of stacking sequence on the unnotched and notched specimens are characterised. Then, studies are carried out on the repairs by different methods: two adhesives (ductile Araldite 2015 and brittle ESP110), two methods of surface treatment (sandpaper polished and plasma treated) and two patch stacking sequences ($[\pm 45]_S$ and $[\mp 45]_S$). Finite element simulations are performed on the repaired composites using the calibrated CZM and CDM parameters. The damage mechanisms are further discussed by the correlation with acoustic emission (AE) data.

Chapter 7 continues the composite repairs study under ageing condition. Unnotched and notched wet specimens are also prepared and tested as reference. The aged repaired specimens are simulated using finite element method and associated with AE data after that.

This thesis is ended with general conclusions of the study and some recommended future works, which are listed in Chapter 8.

CHAPTER 2. LITERATURE REVIEW

2.1.Introduction

In order to expose to the background of this work, a general literature review is given in this chapter. Firstly, the water absorption in polymers and composites is discussed from the mechanisms and physical phenomena during moisture ingression; the factors that affect the absorption of moisture to the mathematical models to describe the Fickian and non-Fickian diffusion. Then, effects of moisture and temperature on the mechanical properties of the engineering materials including resins/adhesives, composites and adhesive joints are reviewed. This chapter is continued with the finite element modelling approaches on the durability of adhesive joints and ended with some of the published research works on external patches repaired composites.

2.2.Moisture absorption mechanisms and phenomena

According to Hopfenberg and Frish [7], when the solvent penetrates into the solute, several transport mechanisms could occur, which is shown in Figure 2.1 below:

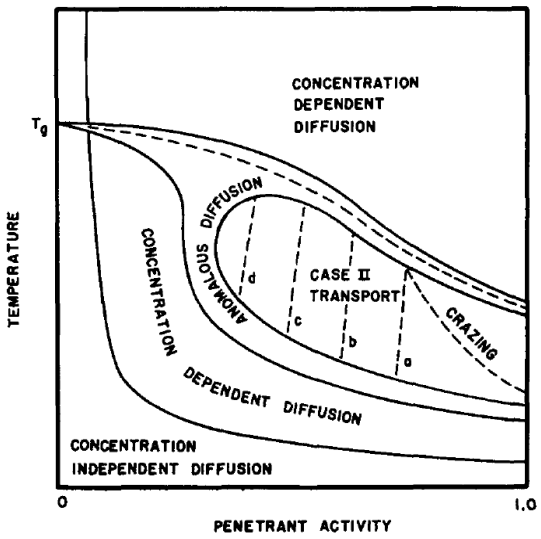

Figure 2.1: Relationship between environment temperature and penetration activity on the likelihood sorption transport in a solvent-solute system [7].

Besides, Bond describes the moisture sorption locations and mechanisms in polymeric composites [8], which is shown in Figure 2.2 below.

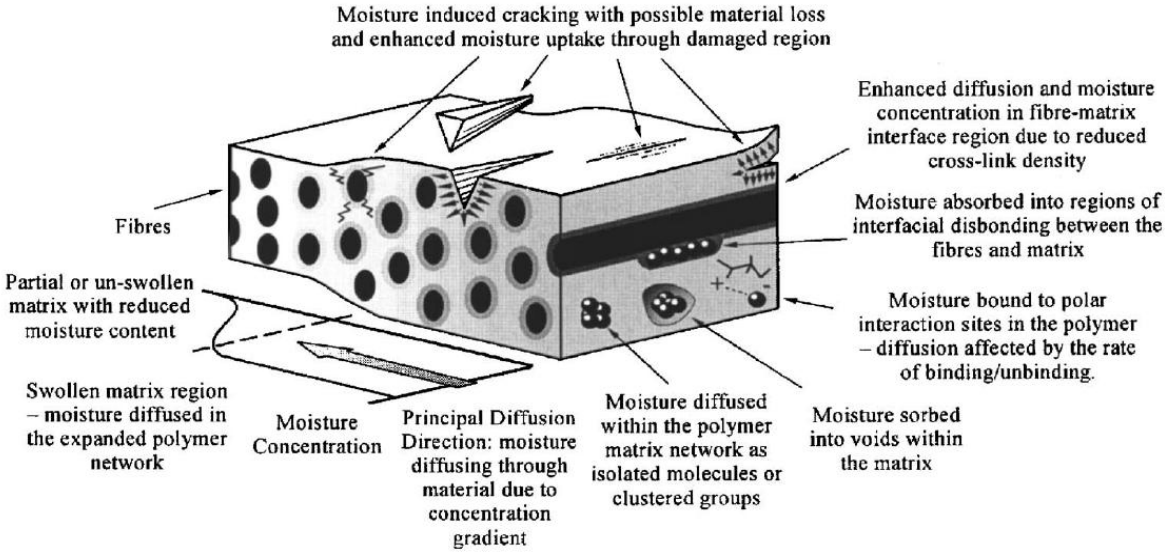

Figure 2.2: Moisture sorption locations and mechanisms in polymeric composites [8].

In the following, detail discussion on the moisture absorption mechanisms and phenomena described in Figure 2.1 and Figure 2.2 will be presented.

a. Concentration independent Fickian diffusion

In Fickian diffusion, moisture could diffuse into the materials through atomic motion. Spherical water molecules of approximately 0.096nm radius can move randomly (Brownian motion) and site in the voids (sub-microscopic network and free volume) of the material network by concentration gradient.

In polymers, the moisture free volume which acts as additive increases the total free volume in the material [9]. The material void diameter must be larger than 3Å to accommodate a water molecule [10]. It was also reported elsewhere that the pore size must be 3-5Å for "true" diffusion [11]. This mechanism is called vacancy diffusion, and comparatively low activation energy (thermal energy of the atomic vibrations) and surrounding temperature (but still high enough to overcome the energy barriers to atomic motion) are sufficient for water penetration. During diffusion, the water molecules are free and thus the movement of the molecules is independent of each other. There is no interaction between the water molecules and those of the polymer. The mobility of penetration is much lesser than the stress relaxation rate of the polymer structure [12]. As diffusion progresses, moisture concentration gradient is weakened. When equilibrium is attained, the net diffusion is equal to zero.

Free water molecules diffusion could induce plasticisation in the polymer material. From the micro-structure point of view, plasticisation refers to the interruption of Van Der Waals bonds between polymer chains by the moisture [13]. Consequently, the spaces among polymer molecules are enlarged for further water absorption, which lowers the interfacial strength of the polymer chains and causes the polymer molecules to move more freely [14]. Plasticisation is diffusion controlled and depends on the dilution process and the intermolecular bond formation

[13]. It was also reported that the increment of 1% of the absorbed moisture could lead to an average of 20^{o}C reduction in T_g [15-16]. For a typical glassy polymer such as epoxy, reduction in T_g is not favourable. This is because beyond T_g, the epoxy structure changes from glassy (hard) to rubbery (soft) state which could lead to a rapid change in the physical properties of the epoxy [9]. It was also reported that as a direct consequence of plasticisation of the matrix in glass/epoxy composites, their glass transition temperature, T_g can be reduced linearly with the increase in moisture content [17]. Anyhow, one beneficial aspect of matrix plasticisation in fibre-reinforced composites is that residual stresses introduced during material fabrication could be relaxed [13, 15-16]. In addition, the viscoelasticity of the material could also be enhanced [13].

It is generally recognised that the plasticisation of fibre-reinforced polymer composites causes property changes and primary properties which are sensitive to moisture include inter-laminar shear strength (ILSS), ultimate tensile and compressive strength, fracture strain and stiffness [13].

b. Concentration dependent Fickian diffusion

Concentration dependent diffusion occurs when the environment temperature is higher than T_g of polymers. When T_g is approached, the holes size and segmental mobility are augmented [18] and the internal stress relaxation is no more instantaneous [19]. Consequently, the diffusivity is history-dependent and boundary concentrations are time-dependent [20-21]. It was also revealed that the diffusion coefficient is concentration dependent when swelling is significant [22], because swelling could cause variation in the boundary condition of moisture concentration. This will affect the moisture gain in the material. Besides, it was reported that oxidation could occur in composite materials at high temperature, so as to lead to a permanent change in the nature of the matrix and causes corrosion on the fibre surface [15, 23-25].

c. Non-Fickian or anomalous

Anomalies are recognised when the moisture mobility and the stress relaxation rate in the polymer are comparable [12]. It happens usually at temperature below T_g. In fact, these anomalies in water diffusion can be explained by a coupling of Fickian diffusion and polymer relaxation phenomena. It was argued that non-Fickian behaviour occurred due to slow responses in the polymer crystalline regions [26], where the retardation in the stress relaxation was due to unequal swelling of the upper and lower surfaces of the solute [27]. Stress relaxation rate was identified to be the dominant factor that determines the time for steady-state permeation [28]. Another mechanism of water uptake is called adsorption. The phenomenon of the adsorption are identified such that the polar water molecules interact with the polymer network and form hydrogen bonds with hydroxyl groups in the polymer chain by altering the inter-chain hydrogen bonding. This subsequently interrupts the cross-linking in the polymer network, the inter-segmental hydrogen bond length is therefore augmented [29].

It was reported that polymers with fewer polar groups reduce the moisture sensitivity and hence the maximum moisture content, M_m and T_g decrease with increased cross-linking [13]. According to Long and Thompson, anomalous diffusion is accentuated in the polymer that exhibits large chain-chain interactions due to small size, regular spacing and polar nature of the hydroxyl side groups [30]. Liquid molecules that combine with the polymer molecules in the glassy state could become part of the glassy structure when equilibrium is achieved [31]. This

binding effect is also known as dual-mode sorption, where some solvent molecules could diffuse freely within the polymer while others are restrained by the interaction with polymer molecules. The interaction level of the penetrant-polymer pair and the interaction effect on the polymer network will affect the amount of moisture absorbed in a solvent-solute system [8]. Diamant et al. suggested that higher levels of cross-linking may remove possible interaction sites, and additional linking may retard the equilibration of the polymer due to the increased difficulty for the water molecules to access to the polymer sites [32].

Hydrolysis is the corresponding chemical reaction to describe the binding of the water molecules to the polymer chains. In a polymer, the level of the hydrolysis depends on the number of the groups available in the polymer macromolecular chains that could react chemically with water molecules. Hydrolysis could reduce the cohesive mechanics of the molecular network and increase the mobility of the molecules. Hydrolysis leads to the degradation of the molecular structure which in turn causes progressive loss in the mechanical properties of the polymer. This reaction is slow at ambient temperature (from several months up to several years), but could be very fast at elevated temperature or by the chemical agents such as acids [15, 23-25]. Hydrogen bonding was generally found to degrade the material properties [29, 33].

In composite materials, the non-Fickian response is also attributed to the low cross-link density region surrounding the fibres that generates a preferential diffusion path for the water molecules [34]. In this case, the effects of both interaction and relaxation mechanisms could be further enhanced and the diffusion coefficient could be as high as ten times compared to the neat resin. The preferential paths may not alter the diffusion mechanisms but affect the uptake curve.

d. Case II transport

Case II transport denotes the water transport where the penetration mobility is much greater than the stress relaxation rate [12]. This kind of transport also occurs at exposure temperature below T_g of the material. In other words, the polymer relaxation due to swelling is much slower than the boundary diffusion rate, which in turn induces large internal stress. The water molecules cause a sharp advancing boundary that separates the inner glassy region from the outer swollen shell [12]. It is believed that the solvent boundary advances at a constant velocity [12, 19] and the solvent concentration is uniform behind the advancing front [12]. This leads to linear increment of weight gain with time [12] and the initial and equilibrium extent of swelling are the same behind the advancing front [19]. Graphically, the sorption curve of Case II transport is distinguished by comparatively abrupt cut-off effects [12]. According to Bond [8], Case II transport has not been found in the moisture sorption into glassy epoxies.

e. Solvent crazing-stress cracking

Being classified as an inherent aspect of Case II transport in glassy polymers at high penetration activity and below T_g of the material [7], opacity or crazing (cavitation in the material) is treated as a consequence of anomalous transport elsewhere [8]. Hence, in a broader point of view, damage and subsequent degradation occur only (although not necessary) after the departure from Fickian diffusion. This hypothesis seems to be reasonable as Case II transport has been equalised to anomalous transport as well (although not common) [35].

In composite materials, residual stresses are introduced during fabrication and moisture exposure, and external loading when the material is in service, because of the different

coefficient of thermal expansion between fibres and matrix [8]. Microcrack damage could occur within or on the surface of the composite if the level of residual stresses is sufficient high. However, cracking due to initial thermal residual stresses generated during fabrication by the shrinkage of the matrix on the fibre is rarely observed by researchers [8]. This could be attributed to comparatively high moisture-induced swelling stresses or degradation of the fibre/matrix interface due to capillary action. Capillarity happens when water ingresses along the fibre/matrix interface and leads to cavities or micro-cracking through capillary action. Consequently, fibre/matrix interface debonds and crack propagates along fibre surfaces, and additional moisture transport takes place through these cracks.

Swelling by hygrothermal stresses is an effect of volumetric changes due to moisture content as a consequence of rearrangement of marcomolecules of the polymer to relieve the stresses and is independent of the thermal expansion [8, 29]. As the water molecules diffuse into a glassy polymer, the surfaces (swollen region) tend to expand and increase the area and thus create a tensile stress on the unswollen or less swollen region. Consequently, the underlying layer is under a compressive stress. Hence, swelling is mainly in the diffusion direction. Also, as swelling stresses lead to a more opened network structure for additional water ingression, it leads to reduction in T_g [36-37]. Besides, since the unswollen/less swollen region decreases as diffusion progresses, the tensile and compressive stresses vary with time as well. Therefore, it is reasonable to assume that diffusivity is dependent on the internal stress [29]. In composite materials, hygrothermal stresses induced by the differential dilatation between the matrix and the fibre are mainly located at the fibre/matrix interfaces. Swelling is a reversible effect, however, the damage caused by significant swelling is irreversible. Swelling effect due to osmosis stresses could cause the dissolution of the primary bond under high activation energy and thus induce local fracture (crazing and cracking) at or near the advancing diffusion front [13, 31, 35-36, 38-40]. Stress cracking was observed by Asmussen and Ueberreiter [41]. In addition, small transverse cracks at the boundary between the core and the swollen phase were found by Alfrey and his co-workers [12]. Damage is likely to increase the relaxation rate at the boundary between swollen and unswollen regions. Even if the osmosis stresses are too small to cause local fracture, polymer relaxations at the boundary may still be biased by these stresses.

Solvent crazing-stress cracking leads to local weakening effect and clustering of solvent molecules [10, 42]. Water in the crazes is in equilibrium with its surroundings and the water flows in and out due to hydrostatic pressure difference. The holes generated by the clusters will remain as long as the polymer is in the glassy state. Mechanically crazed samples “heal” when heated above T_g, where the polymer segments mobility is restored and the holes close permanently when the absorbed water is removed [43]. Under cyclic ageing (immersion in hot water followed by cooling), some permanent damage occurred, new holes are created and hence water uptake is increased [10].

Damage is worsened by external loading under severe environments. External loading could lead to departure from Fickian behaviour, increased diffusivity, solubility and M_m, which are accompanied by significant interface and matrix dominated properties degradation [44-46]. It was reported that interlaminar cracks were observed in pre-stressed aged specimens, where cracks were initiated and propagated along the resin-rich areas at the interfaces [44].

Table 2.1 summarises the levels, mechanisms and phenomena which are related to the moisture absorption in composite materials.

Table 2.1: Levels, mechanisms and phenomena related to moisture absorption in composite materials [47].

Levels	Mechanisms	Phenomena
Organic matrix	diffusion, adsorption	swelling, plasticisation, dissolution, reduction in T_g, hydrolysis, cracking
Micro-cavity	capillarity	swelling, cracking
Interface	diffusion, adsorption, capillarity	swelling, cracking, interface debonding
Fibre	diffusion, adsorption	hydro-oxidation, surface corrosion, cracking

2.3.Factors affecting moisture transport in polymers and polymer composites

According to the classification by George and Thomas [48], the factors that affect the degree of the transport process in a polymer include:

a. Nature of polymers

The nature of the polymer is the predominant factor for the moisture transport. According to George and Thomas [48], the free volume within polymer and segmental mobility of the polymer chains affect the diffusion directly whereas the saturation level, cross-linking, degree of crystallininty and nature of substituent influence the moisture ingress indirectly. Glassy polymers such as epoxy, polypropylene, polyethylene, polyacrylamide, polystyrene, polyimides are hard and brittle. The chain mobility is restricted where the motion is largely vibratory within a frozen quasi-lattice. In addition, the density of the polymer is high with little void space (0.2-10%), hence the diffusion is more complex. It has been reported as well that below T_g, there is 1/40 free volume in the material [49]. George and Thomas [48] described that T_g is altered when the free volume is changed at a given temperature. Polymer mixed with a miscible liquid that contains more free volume than the pure polymer will lower the T_g. For polymers with lower T_g, the diffusivity is higher due to greater segmental mobility. As for rubbery polymers such as polyurethane and poly(dimethyl siloxane), they are unsaturated, with comparatively large segmental mobility and large amount of free volume between molecules. These enable smooth and easy diffusion for small molecules. Not only that, larger molecular size decreases the chain segmental mobility and hence decreases the sorption rate and magnitude. In addition, diffusion is faster in polycrystalline materials compared to single crystals due to accelerated diffusion along grain boundaries. At high temperature, crystallinity is induced which reduces the free energy of mixing and hence the solvent uptake. The volume fraction of the crystalline phase could be decreased by increasing the rubber content in the material and hence accelerates the swelling.

b. Nature of cross-links

It is known that the inhomogeneous network structure of cross-linked epoxy resins is a mixture of highly cross-linked micelles (microgel particles) integrated in a less highly cross-linked matrix and high density micelles which are more water resistance [31]. This complicates the moisture diffusion process. Besides, higher chain network flexibilities could enhance the

maximum solvent uptake of the polymer and increasing the crosslink density could decrease the permeation rate [48].

c. Effect of plasticisers

Addition of plasticisers in the polymer increases the segmental mobility and the penetration transport, which increases the diffusion coefficient and lowers the solubility coefficient [48].

d. Size and shape of solvents

It was reported that increasing penetrant size decreases the diffusivity [50-51]. Besides, increasing the chain length of the penetrant was found to decrease the equilibrium penetrant uptake [50]. In addition, some research works found that higher diffusion coefficients were attained in flattened or elongated molecules compared to spherical molecules or equal molecular volume [52-53].

e. Reinforcements

The moisture transport in a reinforced system is dependent on the nature, bonding ability and compatibility of the reinforcements with the polymers. Generally, neat polymers are less restrained [48]. Reinforced polymers would exhibit glasslike properties, and the effect is probably unlimited to the region near the particle surface only [54]. In general, at least below T_g, filler raises the activation energy [18]. With the presence of the filler (even low surface area), the mobility of the mechanical chain is greatly reduced due to the competitive adsorption of solvent molecules on the filler surface and hence the reinforced resin system is relatively impermeable to liquid water [18, 54]. This could weaken the polymer-filler interaction. In addition, the filled polymer could also be plasticised by the solvent vapour. Both effects could increase the number of possible configurations of polymer molecules near the filler surfaces [54].

In composite materials such as carbon/epoxy composites, due to the difference in the coefficient of thermal (CTE) and moisture (CME) expansion, matrix (higher CTE and CME) swelling is restricted by the fibre (lower CTE and CME), and hence the swelling in composites is anisotropic. In good fibre/matrix interfacial adhesion systems, swelling effect is not significant [55-56]. Swelling is decreased with an increase of fibre content and addition of bonding agents [55]. Restricted swelling leads to lower solvent uptake. In addition, incompatible fillers tend to generate voids at the interface, which increase the free volume and an increase in permeability. As for inert fillers which are compatible with the polymer matrix, they are able to site in the free volume within the polymer matrix and create a tortuous path for the penetrant molecules [27]. The tortuous level depends on the volume fraction, shape and orientation of the reinforcements. For example, it was reported that increasing carbon black particle size decreased the penetration rate at higher degrees of equilibrium, due to wrinkles formed at the rubber surface [57]. It was also reported that upon moisture exposure, the reduction in ILSS and impact strength was more significant in glass/epoxy composites with higher glass fibre volume fraction [58].

f. Temperature

Generally, increasing temperature decreases the solubility, increases diffusivity and increases moisture content because the increment in the driving force is greater than the

decrement in the solubility [10]. Variation of diffusivity, sorptivity and permeability coefficients with temperature could be described by Arrhenius relationship.

Gillat and Broutman studied cross-ply ($[0/90]_{2S}$ and $[90]_8$) T300 graphite/epoxy composites immersed in water at 25 and 80°C for unstressed cross-ply specimens, 60°C for stressed specimens at 0, 25, 45 and 65% of the ultimate tensile strength and 80°C for $[90]_8$ specimens [44]. Results showed that the maximum moisture content, diffusivity and initial slope of the sorption curve increase with the immersion temperature. Fickian behaviour was observed for 25 and 60°C aged specimens, but non-Fickian behaviour was found for high temperature (80°C) exposed specimens. Lv et al. revealed that high temperature increased the molecular chain relaxation, decreased T_g and weakened the molecules banding strength [14]. This caused space formation between molecules and enhanced water ingression. Water absorption and maximum moisture content were thus increased and the samples were attacked in a more aggressive manner.

2.4.Mathematical models to describe moisture diffusion

This part summarises the different models proposed in the literature to describe moisture diffusion. According to Frish [59], the anomalous transport can be modelled using:

i. Molecular, statistical-dynamical theory
ii. Complete macroscopic field theory
iii. Partial continuum theory
iv. Empirical model

The empirical approach is significantly less complicated compared to other three methods. Empirical models emphasise on the description of the transport process observed experimentally by using some fitting parameters with or without physical sense. In the following, the discussion will be focusing on the empirical approach. In addition, since Case II transport is not likely to occur in epoxy resins [8], the discussed models will be confined within Fickian and non-Fickian diffusion.

Firstly, the general mathematical expression for different types of transport in a slab geometry is described using the equation below [60]:

$$\frac{M}{M_m} = kt^n \tag{2.1}$$

where M is the instantaneous moisture content, M_m is the maximum moisture content that could be achieved in the system, k is the kinetic constant, and n is the diffusion exponent, which is classified in Table 2.2 as follows:

Table 2.2: Type of transport and its corresponding diffusion exponent [59].

Type of transport	n
Fickian	0.5
Anomalous	0.5-1
Case II transport	1

By finding the best fit diffusion exponent value with the experimental results, the type of transport and thus the corresponding physical mechanisms governing the moisture ingression could be predicted.

2.4.1.Fickian diffusion

Fickian diffusion of water or humid air in engineering materials (both absorption and desorption) could be described by Fickian second law (nonsteady-state diffusion) firstly proposed in 1855 [61]. Fickian second law describes that the concentration profile and the concentration gradient are changing with time. Concentration gradient is the driving force of the diffusion (although it is not a force in the mechanistic sense). Fickian single free phase model illustrates that the water molecules absorbed are linked to the matrix by unbound hydrogen bonds. In the following discussion, one-dimensional diffusion (in the *z*-direction) in a homogeneous material is assumed, which is shown in Figure 2.3 below:

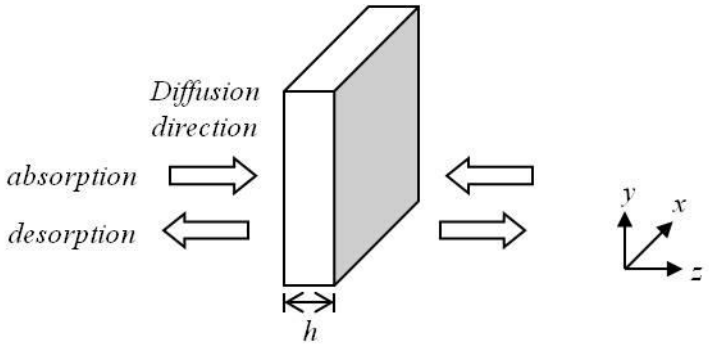

Figure 2.3: Schematic diagram of one-dimensional diffusion.

At constant diffusivity level, the diffusion is described by the following equation:

$$\frac{\partial c}{\partial t} = \frac{\partial}{\partial z}\left(D_z(T)\frac{\partial c}{\partial z}\right) = D_z(T)\frac{\partial^2 c}{\partial z^2} \tag{2.2}$$

where:
c = moisture concentration
D_z = moisture diffusivity (independent of distance, time and concentration)

Upon the dispersal of the water molecules, the exposed surfaces reach concentration equilibrium instantaneously and do not vary with time. Hence, the boundary conditions are:

$$\begin{aligned} c &= c_i \qquad 0 < z < h \qquad t \le 0 \\ c &= c_m H(t) \quad z = 0, z = h \quad t > 0 \end{aligned} \tag{2.3}$$

where c_i is the initial moisture concentration, c_m is the constant boundary moisture concentration and $H(t)$ is the Heaviside step function.

The solution of Equations (2.2) and (2.3) given by Jost [62] is:

$$\frac{c - c_i}{c_m - c_i} = 1 - \frac{4}{\pi}\sum_{j=0}^{\infty}\frac{1}{(2j+1)}\sin\frac{(2j+1)\pi z}{h}\exp\left[-\frac{(2j+1)^2\pi^2 D_z(T)t}{h^2}\right] \tag{2.4}$$

where h is thickness of the test coupon and t is the exposure time.

Integrating the above equation over the thickness of the material, the following equation is obtained:

$$G(T,t)=\frac{m-m_i}{m_m-m_i}=1-\frac{8}{\pi^2}\sum_{j=0}^{\infty}\frac{\exp\left[-(2j+1)^2\pi^2\left(\frac{D_z(T)t}{h^2}\right)\right]}{(2j+1)^2} \tag{2.5}$$

where:
m_i = initial moisture weight
m_m = maximum moisture weight
$G(t)$ = moisture absorption function and can be approximated as:

$$G(T,t)=1-\exp\left[-7.3\left(\frac{D_z(T)t}{h^2}\right)^{0.75}\right] \tag{2.6}$$

Generally, it is interested to represent the moisture absorption level in percentage. The instantaneous moisture content, $M(t)$ can be expressed as:

$$M(T,t)=\frac{w-w_i}{w_m}\times 100 \tag{2.7}$$

where:
w = instantaneous weight of the material
w_i = initial weight of the material
w_m = maximum weight of the material

As $w = w_i + m$,

$$M(T,t)=\frac{w_i+m-w_i}{w_m}\times 100=\frac{m}{w_m}\times 100 \tag{2.8}$$

Rearranging Equation (2.5),

$$m=G(T,t)(m_m-m_i)+m_i \tag{2.9}$$

which leads to the following equation:

$$M(T,t)=G(T,t)(M_m-M_i)+M_i \tag{2.10}$$

where:
M_m = maximum moisture content
M_i = initial moisture content

The moisture content can thus be expressed as:

$$M(T,t)=(M_m-M_i)\left\{1-\frac{8}{\pi^2}\sum_{j=0}^{\infty}\frac{\exp\left[-(2j+1)^2\pi^2\left(\frac{D_z(T)t}{h^2}\right)\right]}{(2j+1)^2}\right\}+M_i \tag{2.11}$$

or

$$M(T,t)=(M_m-M_i)\left\{1-\exp\left[-7.3\left(\frac{D_z(T)t}{h^2}\right)^{0.75}\right]\right\}+M_i \tag{2.12}$$

From Equation (2.12), at constant temperature and moisture exposure level, the time required to reach particular moisture content can be expressed by:

$$t = \frac{h^2}{D_z}\left[\frac{-1}{7.3}\ln\left(1-\frac{M(t)-M_i}{M_m-M_i}\right)\right]^{4/3} \tag{2.13}$$

At the absence of initial moisture content (M_i = 0), the time required to reach 99.9% of the moisture equilibrium of a material is approximated as:

$$t_{99.9} = \frac{0.93h^2}{D_z} \tag{2.14}$$

A typical moisture absorption plot that follows Fickian diffusion is shown in Figure 2.4 below:

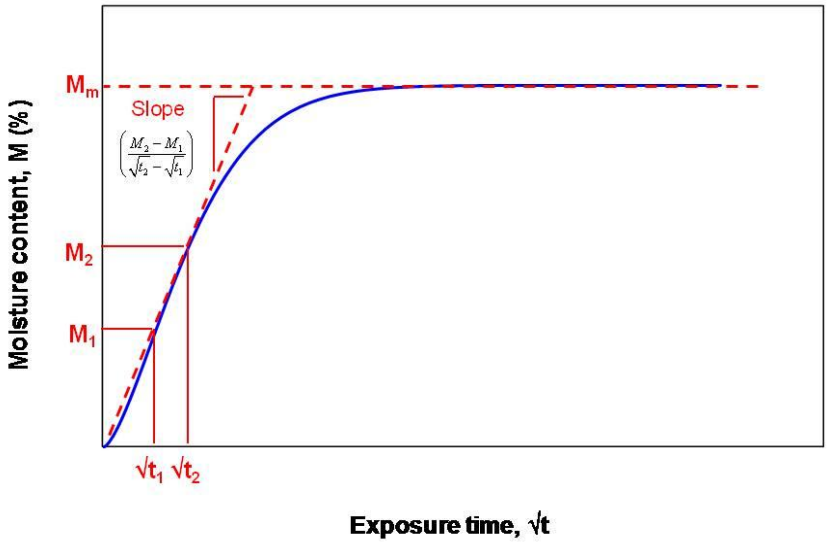

Figure 2.4: Illustration of Fickian diffusion.

With the slope of the initial linear portion of the moisture absorption curve determined from the experiment data, the moisture diffusivity is described by the equation below:

$$D_z = \pi\left(\frac{h}{4M_m}\right)^2\left(\frac{M_2-M_1}{\sqrt{t_2}-\sqrt{t_1}}\right)^2 \tag{2.15}$$

During moisture diffusion, the exposed surfaces may be in rubber state (due to the instantaneous concentration equilibrium) while the inner portion is still in the glassy state. Fickian diffusion assumes that when the solvent disperses into the polymer from the outer rubbery region to the inner glassy region, the polymer segments reach new equilibrium configuration instantaneously. Consequently, the internal stress at the rubbery state is relaxed immediately and hence a new mechanical equilibrium is attained [19]. It is important to note that Fickian diffusion is valid with the absence of swelling.

2.4.2.Non-Fickian diffusion

Moisture uptake behaviour in polymeric materials may not be always described well using Fickian single phase model. Figure 2.5 illustrates non-Fickian diffusion behaviour in a polymeric material, where Fickian diffusion law (upper Fickian) is found to overestimate water concentration at the shoulder region. If the initial slope is followed, lower M_m is predicted using Fickian diffusion law (lower Fickian). Non-Fickian features are recognised when the following conditions from *M(t)* versus $t^{1/2}$ curve are not fulfilled [63]:

i. The initial slope of the sorption curve is linear up to 60% of M_m
ii. Beyond the linear portion, the sorption curve slows down until M_m is attained
iii. Reduced sorption curves (the abscissa axis as $t^{1/2}$/*thickness*) at different thickness are super-imposable

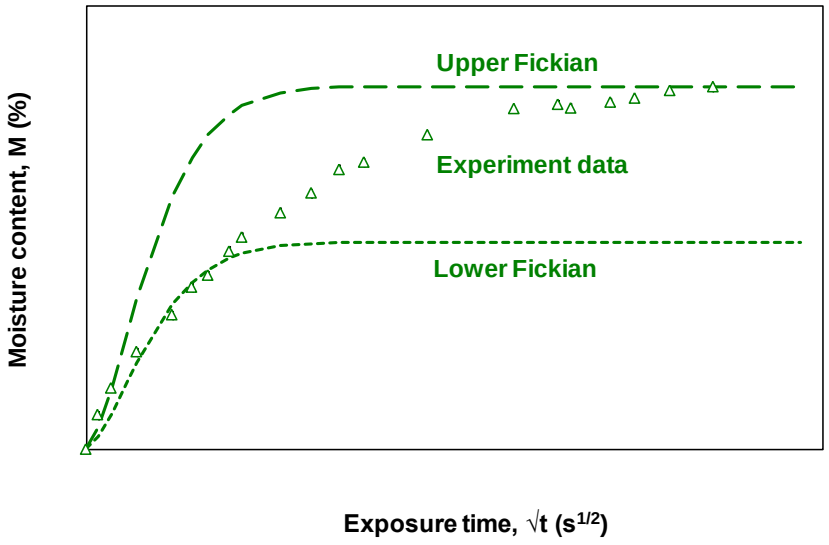

Figure 2.5: Illustration of non-Fickian diffusion.

A number of researches have proposed different models to describe non-Fickian diffusion behaviour. One of the approaches is to modify Fickian diffusion law by introducing time-varying diffusion coefficient or time-varying boundary conditions. Whitney and Browning [64] studied the moisture uptake in Hercules 3501-5 epoxy resin and AS/3501-5 graphite/epoxy composites. The testing conditions are as described in Table 2.3 below.

Table 2.3: Testing conditions of 3501-5 epoxy and AS/3501-5 graphite/epoxy composites by Whitney and Browning [64].

Material	Stacking sequence	Total thickness (mm)	Relative humidity (%)	Temperature (^{o}C)
Neat resin	-	3.18	75	23, 71, 82
Composite	$[0]_4$ $[0/90]_s$	0.64	75	71
			95	38, 49, 60, 71
			Water	38

Their results showed that Fickian diffusion was followed in neat resin and unidirectional laminates but not in bi-directional laminates. They suggested that non-Fickian behaviour could be caused by concentration-dependent diffusion process. The diffusion coefficient could vary with the stress state in the material. In bi-directional laminate, owing to the restriction of matrix shrinkage in both directions, there were large tensile residual stresses in the out-of-plane direction in between the plies. This led to the formation of voids and cracks, which increased the initial through-the-thickness diffusion coefficient and reduced after that by swelling. As swelling continued, the diffusivity could further decrease due to residual stresses in compression. Due to the difficulty in obtaining concentration dependent diffusivity solution, the stress dependent diffusion was described using time-dependent diffusion coefficient approach, where the entire water exposure period was divided into two regions and described by two different diffusivities respectively. In their model, the diffusivity varied linearly with respect to the exposure time. It was found in their studies that M = 0.4% was the division point, where it was deduced that the swelling was started to be effective beyond that moisture content. This approach was shown to improve the experimental and theoretical curves, however, considerable discrepancy was still observed.

The similar approach was examined by Bao and Yee [65] on the short term uptake behaviour of woven carbon fibre reinforced bismaleimide composites. The authors employed two different time dependent diffusivity, $D(t)$ equations:

$$D(t) = D_o(-k\sqrt{t}) \tag{2.16}$$

$$D(t) = D_o \exp(-k\sqrt{t}) \tag{2.17}$$

Both D_o and k are fitting parameters. However, both equations did not seem to fit the experimental results well.

Time dependence diffusivity was also analysed by Roy et al. [66], where the diffusivity is expressed in Prony series form as:

$$D(t) = D_o + \sum_{r=1}^{R} D_r[1-\exp(-t/\tau_r)] \tag{2.18}$$

where D_o, D_r are the unknown temperature-dependent Prony coefficients and τ_r is the corresponding retardation time. The concentration profile is thus expressed as:

$$\frac{c-c_i}{c_m-c_i} = 1-\frac{4}{\pi}\sum_{j=0}^{\infty}\frac{(-1)^j}{2j+1}\exp\left[\frac{-(2j+1)^2\pi^2}{h^2}\times\left\{D_o t+\sum_{r=1}^{R}D_r[t+\tau_r(\exp(-t/\tau_r)-1)]\right\}\right]\cos\frac{(2j+1)\pi x}{h} \tag{2.19}$$

which leads to moisture weight gain as

$$\frac{M-M_i}{M_m-M_i} = 1-\frac{8}{\pi}\sum_{j=0}^{\infty}\frac{1}{(2j+1)^2}\exp\left[\frac{-(2j+1)^2\pi^2}{h^2}\times\left\{D_o t+\sum_{r=1}^{R}D_r[t+\tau_r(\exp(-t/\tau_r)-1)]\right\}\right] \tag{2.20}$$

Through finite element approach, it was found that good agreement was achieved for the moisture uptake behaviour of an epoxy adhesive aged in salt water at 23, 50, 60 and 70^{o}C. The approach was also applied by LaPlante et al. [67] to describe the non-Fickian diffusion behaviour of FM300 adhesive in deuterated water (D_2O) at 70^{o}C. However, since Prony series is involved in the equation, the solution is very complex and time-consuming due of multiple coefficients.

Another model proposed by Chen et al. [68] to describe the concentration dependent diffusivity as following:

$$D(c) = D_o + a\frac{c}{c_m} \tag{2.21}$$

where D_o is the diffusivity at zero concentration, c and c_m is the instantaneous and saturated moisture concentration respectively, and a is a fitting parameter. The equation was solved using finite element analysis and good correlation was found in fitting the experimental moisture uptake curves of moulding compounds of MP8000 and CEL9220M aged at 85°C/60%RH and 85°C/85%RH.

Celik et al. [69] proposed that the non-Fickian moisture diffusion could be described using moisture dependent diffusivity according to a power-law fit:

$$D\left(\frac{M}{M_m}\right) = a\left(\frac{M}{M_m}\right)^b \tag{2.22}$$

where a and b are fitted through experimental results. Through numerical simulation, the moisture uptake behaviour of three different inhomogeneous organic substrates used in electronics packaging was found to be fitted well using this approach.

The previous approach deals with non-Fickian data by modifying and fitting the diffusion coefficient. In the following discussion, the models considering diffusion-relaxation coupling effect will be described. It is assumed that the initial period of the penetration uptake is diffusion dominated and the second stage is dominated by relaxation. Therefore, different functions for penetrant diffusion and polymer-penetrant interaction or polymer relaxation have to be super-imposable. In other words, the transport is a combined effect of physical diffusion and chemical interactions. To simplify the analyses, the initial moisture concentration, c_i and thus initial moisture content, M_i are assumed to be negligible. Experimentally, this condition can be easily achieved by heating the specimens in the oven over a period until the weight is stabilised. Generally, these two-phase models are based on the hypothesis that both physical (water molecules diffuse and reside in the free volume) and chemical (water molecules bond strongly with certain hydrophilic functional groups such as hydroxyls in the resin) mechanisms occur simultaneously [67, 70-71]. The total moisture concentration at any instant of time c, is taken as the sum of the moisture concentration by Fickian diffusion c_I, and by non-Fickian concentration c_{II}, which can be described as:

$$M = M_I + M_{II} \tag{2.23}$$

In terms of moisture content, it is written as:

$$c = c_I + c_{II} \tag{2.24}$$

Cai and Weitsman [72] considered the non-Fickian behaviour is due to the viscoelastic behaviour of polymers. As the response of the materials is time-dependent, even under constant ambient condition, the boundary condition, c is not constant and is a function of time:

$$c = f(t) \quad z = 0, z = h \quad t > 0 \tag{2.25}$$

Using the suggestion by Long and Richman [73], the respective boundary condition is written as:

$$c = [c_o + c_1(1 - e^{-\psi t})]H(t) \quad z = 0, z = h \quad t > 0 \tag{2.26}$$

where c_o is the initial boundary condition, c_1 is the coefficient of the viscoelastic boundary condition, ψ is the relaxation rate constant and $H(t)$ is the Heavyside step function. With the Prony series expression, the boundary condition is thus considered as

$$c = \left[c_o + \sum_{n=1}^{N} c_n (1 - e^{-\psi_n t}) \right] H(t) \quad z = 0, z = h \quad t > 0 \tag{2.27}$$

This boundary condition illustrates that an extended time is required for the equilibrium of the surface moisture content and the chemical potential of the external vapour.

Crank [74] solved the concentration profile of this approach with the boundary conditions of

$$c = (1 - e^{-\psi_n t}) H(t) \quad z = 0, z = h \quad t > 0 \tag{2.28}$$

The solutions by incorporating viscoelastic boundary condition are proposed as following:

$$c = c_o c_I + \sum_{n=1}^{N} c_n c_{II} \qquad z = 0, z = h \qquad t > 0 \tag{2.29}$$

and

$$M = c_o M_I + \sum_{n=1}^{N} c_n M_{II} \tag{2.30}$$

This time dependent boundary concentration approach was used successfully to characterise the moisture uptake behaviour of a particle-filled epoxy-based structural adhesive in distilled water at 30, 35, 40, 45, 50, 70^{o}C [71, 75].

In the works of Berens and Hopfenberg [76-77], the relaxation mechanism was assumed to be a first-order expression as:

$$\frac{dM_{II}}{dt} = \psi [M_{mII} - M_{II}] \tag{2.31}$$

where M_{mII} is the maximum moisture content by anomalous transport and ψ is again referring to the relaxation rate constant which has to be determined empirically. In order to take into account multiple viscoelastic processes within the polymer structure which are having different relaxation time, the second moisture content term can be expressed as a series:

$$M_{II} = \sum_{n}^{N} M_{mII,n} (1 - e^{-\psi_n t}) \tag{2.32}$$

The total moisture uptake for one-dimensional case in a rectangular laminated plate is thus:

$$M = M_{mI} \left\{ 1 - \frac{8}{\pi^2} \sum_{j=0}^{\infty} \frac{\exp\left[-(2j+1)^2 \pi^2 \left(\frac{D_z(T) t}{h^2} \right) \right]}{(2j+1)^2} \right\} + \sum_{n=1}^{N} M_{mII,n} (1 - \mathrm{e}^{-\psi_n t}) \tag{2.33}$$

Experimental results by Berens and Hopfenberg [76-77] showed that maximum of two relaxation processes were enough to fit the experimental data. Experimental data that could be well-fitted using single relaxation term suggested that the polymer-penetrant interaction and relaxation mechanisms were similar or there was only one dominant mechanism. As for data fitted using two relaxation terms, the contributions of both mechanisms could be considered separately. The

model was applied on PEEK and epoxy polymer systems and illustrated good fit of the experimental data as well [23]. This model with single relaxation term was also implemented by Pritchard and Speake [78] to describe non-Fickian behaviour in unsaturated polyester resin and glass/polyester composites.

Dual mode sorption (DMS) model developed by Barrer et al. [79] considered that Langmuir adsorption isotherm was expected to contribute to part of the sorption isotherm, where diffused water molecules could form bonds with reactive groups in the polymer. This model was later referred by Vieth and Sladek [80] to correlate the kinetics of the penetrant to the equilibrium of the sorption. Herein, a first-order reversible reaction, that describes the bound molecule concentration interchange with respect to time, is introduced through two probability terms:

i. Probability of free molecules to become bound molecules (P_B)
ii. Probability of bound molecules to become free molecules (P_F)

In this manner, the kinetical equation can be expressed by:

$$\begin{aligned} \frac{\partial(c_I + c_{II})}{\partial t} &= D_z \frac{\partial^2 c_I}{\partial z^2} \\ \frac{\partial c_{II}}{\partial t} &= D_z \frac{\partial^2 c_I}{\partial z^2} - \frac{\partial c_I}{\partial t} \\ &= P_B c_I - P_F c_{II} \end{aligned} \tag{2.34}$$

The moisture uptake was then solved by Carter and Kilber [81] and Gurtin and Yatomi [82] as:

$$M = M_m \left[1 - \left(\frac{P_F}{P_B + P_F} \right) \left\{ 1 - \frac{8}{\pi^2} \sum_{j=0}^{\infty} \frac{\exp\left[-(2j+1)^2 \pi^2 \left(\frac{D_z(T)t}{h^2} \right) \right]}{(2j+1)^2} \right\} \right] + M_m \left(\frac{P_F}{P_B + P_F} - 1 \right) e^{-P_F t} \tag{2.35}$$

The equation above is valid under the condition of:

$$P_B \text{ and } P_F \gg \frac{\pi^2 D_z}{h^2} \tag{2.36}$$

Carter and Kilber [81] suggested that the binding probability during the initial stage of absorption is small and the dominant transport process is Fickian diffusion. Besides, the free water molecules are uniformly distributed before saturated with bound water molecules. When more moisture amount is absorbed, water molecules have higher tendency to interact with the polymer network which brings to hydrogen bonding and the transport process slows down. This change in the network structure is permanent and cannot be recovered through desiccation process.

Equation (2.35) has been applied by Bonniau and Bunsell [83] to illustrate the moisture ingression in woven composites (E-type glass fibre reinforced Bisphenol A epoxy) at various temperatures (25, 40, 60, 80 and 90^{o}C) and various relative humidity (from 10 to100%). The composites were fabricated using three different types of hardener: diamine, dicyandiamide and anhydride. Results indicated that at all laminate thicknesses (h=0.2, 0.5, 1 and 2mm) of diamine

hardened composites, the moisture uptake followed Fickian diffusion. However, for composites with dicyandiamide hardener, non-Fickian behaviour was observed and could be described well using Langmuir two-phase model. It was also reported that $P_F/(P_B+P_F)$=0.7 at all temperatures. As for anhydride hardened composites, considerable material loss was observed due to resin erosion, and hence was difficult to describe the uptake behaviour using any model.

In addition, this Langmuir model has been also applied to describe the non-Fickian behaviour with successful correlation in different materials, such as bismaleimide resin [38], FM300 epoxy adhesive [67], DGEBA-based epoxy adhesives [70], Fiberite ANC3K/948A1 graphite/epoxy composites [84], EC 2216 epoxy adhesive [85], Hysol EA9360 adhesive and T-300 plain weave reinforced epoxy composites [86]. Ameli et al. [70] showed that P_B and P_F were strongly dependent on the relative humidity particularly at elevated temperature.

Comparing diffusion-relaxation and dual mode sorption (DMS) models, some clear similarities can be found. Firstly, there is a diffusion term and secondly, the non-Fickian term is expressed by an exponential term that decreases and tends to zero with time. In order to obtain a trivial solution of the diffusion-relaxation model, Bond [87] rewrote the single-relaxation diffusion-relaxation model as:

$$M = \phi M_m \left\{ 1 - \frac{8}{\pi^2} \sum_{j=0}^{\infty} \frac{\exp\left[-(2j+1)^2 \pi^2 \left(\frac{D_z(T)t}{h^2} \right) \right]}{(2j+1)^2} \right\} + (1-\phi) M_m \left\{ 1 - e^{\psi t} \right\} \qquad (2.37)$$

where ϕ is the fraction of moisture content corresponding to each phase, which has to be determined empirically. As for application in Langmuir model, the probability terms could be estimated by solving both models at large exposure time, where:

$$\frac{\pi^2 D_z}{h^2} t \gg 1 \qquad (2.38)$$

such that

$$\frac{M}{M_m} \approx \phi + (1-\phi)(1-e^{\psi t}) \approx \left(1 - \frac{P_B e^{-P_F t}}{P_B + P_F} \right) \qquad (2.39)$$

The probability terms can thus be estimated as:

$$P_B = \frac{(1-\phi)P_F}{\phi} \text{ and } P_F = -\psi \qquad (2.40)$$

Parallel dual Fickian (PDF) model is another non-Fickian diffusion model that considers parallel diffusion (homogeneous and non-polar) and relaxation terms (due to hydrogen bonding between water molecules and polymer hydroxyl groups). The model was based on the modification of Jacobs-Jones model [88-89], which considers only two Fickian diffusion in parallel. PDF model is written as:

$$M = M_{mI} \left\{ 1 - \frac{8}{\pi^2} \sum_{j=0}^{\infty} \frac{\exp\left[-(2j+1)^2 \pi^2 \left(\frac{D_{zI} t}{h^2} \right) \right]}{(2j+1)^2} \right\} + M_{mII} \left\{ 1 - \frac{8}{\pi^2} \sum_{j=0}^{\infty} \frac{\exp\left[-(2j+1)^2 \pi^2 \left(\frac{D_{zII} t}{h^2} \right) \right]}{(2j+1)^2} \right\} \qquad (2.41)$$

or simplified as:

$$M = M_{mI} \left\{ 1 - \exp\left[-7.3 \left(\frac{D_{zI} t}{h^2} \right)^{0.75} \right] \right\} + M_{mII} \left\{ 1 - \exp\left[-7.3 \left(\frac{D_{zII} t}{h^2} \right)^{0.75} \right] \right\} \qquad (2.42)$$

From Equations (2.41) and (2.42), it is apparent that the effective diffusion is a superposition of two single Fickian models in parallel with different diffusion parameters (M and D). This model was employed successfully in describing the anomalous diffusion in DGEBA epoxy resin with different percentage of plasticiser aged at 15, 40 and 70^{o}C in distilled water [90]. The exceptional cases were exposure at high temperature (70^{o}C) for plasticiser other than 0%, where Fickian diffusion was followed.

PDF model was also successfully applied to describe the short term moisture absorption behaviour in woven and hybrid W-U-W carbon/BMI composites [65]. Here, W refers to woven fabric and U indicates uni-weave fabric. Contrary to uni-weave and hybrid U-W-U carbon/BMI composites which followed Fickian diffusion law [37, 91], the authors highlighted the significance of the outer plies influence in the diffusion process as the diffusion was largely influenced by the initial water uptake rate which was concentrated at the near surface regions [92-93]. It is worth to mention that D_{zI} was found to be greater than D_{zII}, which implied rapid initial water uptake and retarded ingression during the relaxation stage. Besides, both diffusivities increased with the temperature, whereas the maximum moisture contents at both stages were in a decreasing manner.

Besides, Bao and Yee [65] refitted as well the results by Whitney and Browning [64] on bi-directional laminates using PDF model. With constant values of M_{mI}=0.15% and D_{zI}=8×10^{-5} mm^2/s, close agreement was obtained.

Loh and his co-workers [94] used the PDF model to describe the anomalous moisture uptake behaviour in a rubber toughened epoxy adhesive (Araldite 2007) at 50^{o}C. The adhesive was tested at 81.2%RH, 95.8%RH and deionised water with 0.4, 0.8 and 2mm thicknesses. In their studies, the parameters were fitted using a least mean-squares approach together with a uni-variant search method. From their results, it was found that D_{zI} could be treated as constant whereas M_{mI}, M_{mII} and D_{zII} varied with the relative humidity and the thickness of the adhesive. M_{mII} increased with the relative humidity and the thickness but M_{mI} did not exhibit a general trend. D_{zII} was always lower than D_{zI} (which is similar to the results reported in reference [65]) and increased with thickness. However, no specific trend was observed with respect to the relative humidity. In addition, their experimental results revealed that when the specimens were thicker, the diffusion behaviour was more towards Fickian diffusion.

PDF model was also employed with great success to fit the moisture uptake behaviour in electronics packaging used commercial epoxy mould compounds (EMCs) at 60^{o}C/85%RH and 85^{o}C/85%RH [95]. M_{mI} was found to be independent on the exposure temperature, and the first stage diffusivity was in one or two orders higher than the second stage diffusion coefficient. Besides, the diffusivity at both stages and the total saturated concentration were found to increase with the temperature. Successful application of PDF model in non-Fickian diffusion of two different EMC was also reported in reference [96].

For long-term water uptake behaviour in bismaleimide (BMI) resin immersed in distilled water at 70^{o}C, Bao et al. [37] proposed the following equation:

$$M = M_m\left\{1-\exp\left[-7.3\left(\frac{D_z t}{h^2}\right)^{0.75}\right]\right\} + k\sqrt{t}\cdot M_m\left\{1-\exp\left[-7.3\left(\frac{D_z t}{h^2}\right)^{0.75}\right]\right\} \qquad (2.43)$$

In this equation, the first term refers to the diffusion-controlled stage while the second term describes the relaxation process. The term *k* is a constant obtained through fitting of measured data. This model fits well for linear weight gain in the second phase.

The same model was applied later on the long-term immersion behaviour of 3- and 12-ply uni-weave carbon/BMI composites [91]. For 3-ply composite, diffusion was in the transverse direction, whereas for 12-ply composite, water uptake was examined in both parallel and perpendicular directions to the fibre. Excellent description of the model implied that the water uptake was resin dominated. One major difference was that the Fickian diffusivities in all directions of the composite were lower than the resin. Secondly, in long term, the slope in the relaxation stage and thus the total weight gain of the composite were lower compared to the resin. This was due to the existence of fibres and the fibre/matrix interfaces, which constrained the long-ranged mobility of the polymer molecules [91]. The authors suggested that interfaces could induce strong contact between the polymer chains and the reinforcement, which in turn influenced the glass transition temperature, T_g as well. However, the local segmental motions during the Fickian stage were not affected by interfaces. This model was later on applied to the long term water uptake behaviour of 3-ply woven and hybrid carbon/BMI composites [65] with great success. For hybrid composites, the lay-ups were U-W-U and W-U-W, where U and W refer to uni-weave and woven fabrics, respectively. Combining all the long-term moisture absorption results discussed above by Bao and his co-workers [37, 65, 91], it could be deduced that the slope of the relaxation stage and the maximum moisture content were decreased with the increment in the fibre volume fraction. This suggests that the matrix was the dominant constituent in moisture absorption.

The same model was recently applied by Karbhari and Xian [97] to describe the water uptake behaviour in high fibre volume fraction pultruded unidirectional carbon/epoxy composites. Utilisation of the model to characterise the water uptake behaviour of E-glass (E-8204)/epoxy (DER383) reinforced with Cloisite 30B and Cloisite 10A montmorillonites composites at 80^{o}C was reported as well in reference [98].

To describe the secondary uptake behaviour in FM73 rubber toughened epoxy adhesive, a delayed dual Fickian (DDF) model was proposed by adding a power function into the PDF model, which is described as follows [99]:

$$M = M_{mI}\left\{1-\frac{8}{\pi^2}\sum_{j=0}^{\infty}\frac{\exp\left[-(2j+1)^2\pi^2\left(\frac{D_{zI}t}{h^2}\right)\right]}{(2j+1)^2}\right\} + M_{mII}\left\{1-\frac{8}{\pi^2}\sum_{j=0}^{\infty}\frac{\exp\left[-(2j+1)^2\pi^2\left(\frac{D_{zII}t}{h^2}\right)\right]}{(2j+1)^2}\right\} + H(t-t_1)(at^b+c) \tag{2.44}$$

where $H(t-t_1)$ is the Heaviside step function, t_1 is the starting time of the secondary uptake, and *a*, *b* and *c* are parameters to be determined from curve-fitting. However, adding three parameters increases the difficulty in solving the equation. Furthermore, it is difficult to describe the parameters physically.

In order to take into account the pseudo-equilibrium state during the moisture absorption, Ameli et al. [70] proposed a sequential dual Fickian (SDF) model, where the second stage uptake (non-Fickian) starts only after the completion of the first stage diffusion (Fickian). Mathematically, the model is expressed as:

$$M = M_{mI}\left\{1-\frac{8}{\pi^2}\sum_{j=0}^{\infty}\frac{\exp\left[-(2j+1)^2\pi^2\left(\frac{D_{zI}t}{h^2}\right)\right]}{(2j+1)^2}\right\} + H(t-t_I)M_{mII}\left\{1-\frac{8}{\pi^2}\sum_{j=0}^{\infty}\frac{\exp\left[-(2j+1)^2\pi^2\left(\frac{D_{zII}(t-t_I)}{h^2}\right)\right]}{(2j+1)^2}\right\} \quad (2.45)$$

where t_I is the time when second stage diffusion starts. The model was found to fit well the non-Fickian moisture uptake data of two different types of commercial DGEBA-based heat-cured rubber-toughened structural epoxy adhesives with environment conditions listed in Table 2.4 below.

Table 2.4: Exposure conditions of commercial DGEBA-based heat-cured rubber-toughened structural epoxy adhesives 1 and 2 [70].

T(^{o}C) / RH(%)	20	40	50	60
31	-	1	-	-
43	1	1	-	1
75	-	1	-	-
82	1	1, 2	1	1, 2
95	1, 2	1, 2	1	1, 2

It was found that for adhesive 1, at low temperature and relative humidity (20^{o}C/43%RH, 40^{o}C/31%RH and 40^{o}C/43%RH), the moisture uptake behaviour followed Fickian diffusion. At other conditions, both adhesives exhibited non-Fickian behaviour. The first stage diffusivity, D_{zI} was independent of the relative humidity at all temperatures and the second stage diffusivity, D_{zII}, was independent of both relative humidity and temperature. In addition, D_{zI} was always greater than D_{zII}. The first and second stages transition period, t_I, was found to decrease with the relative humidity. In adhesive 1, t_I was independent of temperature, whereas in adhesive 2, slight variation was found with temperature. The first stage saturated moisture content, M_{mI} increased with relative humidity and independent with temperature. As for the second stage saturated moisture content, M_{ImII}, increment with both relative humidity and temperature was observed.

Besides, adhesive 2 was more resistant to water penetration compared to adhesive 1, with lower D_{zI}, D_{zII}, M_I, M_{II} and t_I. Comparison with Langmuir model revealed that SDF model exhibited higher physical significance than PDF model. However, in their studies, the thickness effects were not investigated.

The authors further proposed that t_I could be expressed in the similar form as Arrhenius equation:

$$t_I = t_{Io}\exp\left(\frac{Q}{RT}\right) \quad (2.46)$$

where t_{Io} is the transition time constant, Q is the activation energy, R is the universal gas constant (8.314×10^{-3} kJ $mol^{-1}K^{-1}$), T is the temperature. Plotting the experimental obtained t_I with $1/T$ and fitting the curve with an exponential equation $y=a.exp(b)$, the transition time constant and activation energy could be estimated.

2.5.Environmental effects on the performance of engineering materials

This section will describe the effects of moisture and temperature on the mechanical properties of the materials used in a composite system including polymers, fibre reinforced polymer composites and adhesive joints. A particular attention is given to those of composites. Firstly, elementary properties of unidirectional laminates are discussed, such as the longitudinal, transverse and in-plane shear properties under tensile and compressive loadings. Secondly, the environmental effects on the mechanical behaviour of multidirectional laminates, woven and short fibre composites are discussed. It is followed by the comparison of flexural and inter-laminar shear strength under ageing. Next, interface properties under environmental exposure are presented. Finally, the moisture influence on the adhesive joints is discussed. The values presented are normalised values which refer to the residual properties fraction. For example, 1.0 means that the property is invariant after ageing, 0.8 indicates the respective property has reduced by 20% as compared to the dry specimen, and 1.2 implies that the environment exposure has beneficial influence on the property such that 20% increment was observed.

2.5.1.Environmental effects on neat resins and adhesives

Neat resins or adhesives are generally recognised to be very sensitive to the environment conditions. Moisture effects could be reversible (such as swelling) and irreversible (such as microcracking). The details of these effects are described in Section 2.2. Subsequently, the constitutive response of the bulk resin/adhesive such as modulus, strength and/or failure strain varies with the moisture absorption. In general, moisture increases the flexibility and ductility of resin/adhesive [100], and decreases elastic modulus and strength [101-102]. However, in certain polymers, positive moisture effect could be observed. In fact, if the loss of low molecular weight substances in the polymer upon water absorption is more significant than water plasticisation effect, the elastic modulus upon moisture ageing can be increased [103]. Hence, it is essential to understand how the environmental conditions affect the structural behaviour to avoid unexpected failure.

Moisture effects on the neat resins/adhesives are summarised in Table 2.5 below. Unless otherwise stated, all tests were carried out under tensile loading.

Table 2.5: Moisture effects on adhesives/resins properties.

Type of adhesives/resins	*T*(^{o}C)	*RH*(%)	*M*(%)	*E*	*S*	ε	Reference
120^{o}C cured epoxy	70	95	4.8	0.6	0.7	0.9	[104]
180^{o}C cured epoxy	70	95	2.4	1.0	0.9	0.9	[104]
3501-5 epoxy	RT	95	5.6	0.8	0.9	1.0	[9]
Araldite2015	60	DW	8.4	0.2	0.3	-	[105]
AV119 (Araldite 2007)	50	DW	7.6	0.6	0.5	1.0	[94]
Bisphenol A	90	DW	0.8	2.0	0.7	0.5	[103]
Bisphenol B	90	DW	0.9	9.4	5.8	0.3	[103]
DGEBA epoxy (compressive)	50	≈85	1.9	0.6	1.0	1.0	[106]
DGEBA epoxy	70	DW	4.0	0.8	0.9	-	[107]
DGEBA epoxy (bending)	80	DW	2.7	0.8	0.8	-	[29]
E04	67	DW	5.9	0.5	0.4	1.0	[108]
E32	RT	DW	9.7	0.2	0.4	3.7	[109]
EA9321	50	95.8	3.9	0.9	0.9	1.0	[110]
EA 9346	67	DW	5.3	0.9	0.7	0.9	[108]
EC 216 epoxy	60	DW	9.6	0.1	-	-	[85]
Epoxy	50	DW	NA	0.4	-	-	[111]
Epoxy + alumina particles	50	DW	NA	0.5	-	-	[111]
Epoxy + aluminium particles	50	DW	NA	-	0.2	-	[111]
Epoxy + barium sulphate particles	50	DW	NA	0.3	-	-	[111]
Epoxy + calcium carbonate particles	50	DW	NA	-	0.1	-	[111]
Epoxy + silane treated silica	50	DW	NA	0.8	0.7	-	[111]
Epoxy + untreated silica	50	DW	NA	0.7	0.5	-	[111]
FM73	50	96	2.2	0.7	0.7	1.0	[112]
FM1000	50	DW	10.0	≈0	0.3	52.0	[113]
Hysol 9321 • Tensile • Shear	 40 40	 90 90	 NA NA	 0.6 0.6	 0.8 0.7	 1.2 1.4	[114]
Isophthalic	90	DW	2.0	0.3	0.3	0.3	[103]
Low styrene content DCPD orthophthalic polyester	40	SW	1.3	1.1	-	0.4	[115]

Low styrene emission orthophthalic polyester	40	SW	1.4	1.0	-	0.6	[115]
Modified epoxy	90	97	1.5	0.1	0.5	1.2	[101]
Polyurethane							[116]
• Unfilled	20	DW	2.5	1.0	0.8	-	
• Barytes-filled	20	DW	4.5	0.3	0.6	-	
Redux 410							[114]
• Tensile	40	90	NA	0.8	0.9	0.7	
• Shear	40	90	NA	0.8	0.7	2.1	
Sikadur 31PBA	30	100	NA	0.6	0.6	1.9	[117]
Standard orthophthalic polyester	40	SW	1.2	1.1	-	0.4	[115]
Unsaturated polyester	30-100	DW	5.5	0.4	-	-	[78]
Vinyl ester	90	DW	1.2	1.0	1.6	0.4	[103]
Vinyl ester	40	SW	0.6	1.3	-	0.5	[115]

* Values are normalised with respect to the properties at unaged condition.
T=ageing temperature, *RH*=relative humidity, *M*=corresponding moisture content, RT=room temperature, DW=demineralised water, SW=sea water, *E*=modulus, *S*=strength, ε=failure strain, NA=not available.

2.5.2.Environmental effects on elementary mechanical properties of unidirectional polymer composites

Generally, the properties of polymeric composites vary under "hot-wet" environment as well. In advanced materials such as glass and carbon fibre reinforced polymer composites, the properties controlled by the matrix are more sensitive to moisture. Hence, the change due to moisture in longitudinal tensile stiffness and strength is usually much smaller than that in transverse tensile, shear and flexural properties [13]. Browning et al. [9] also reported that moisture and temperature had very minimal effects on longitudinal properties. Besides, shear modulus and strength were not reduced by the moisture absorption, but non-linearity is increased. In addition, the reduction of the strength in $[90]_8$ composite (transverse tensile strength) was higher than the neat resin. Both phenomena could be due to interface degradation and residual stress induced by swelling. These two effects were believed to be more prevalent when specimens were tested at room temperature or below, where the matrix was more brittle. Also, the flaw in brittle materials was found to have more significant effect in tensile than shear properties. Hence, it is important to investigate the variation in the mechanical properties under humid and elevated temperature conditions.

Table 2.6 to Table 2.8 summarise moisture and temperature effects on elastic moduli and strengths of different types of composites under tensile, shear and compressive loadings.

Table 2.6: Moisture effects on modulus and strength of unidirectional composites under tensile loading.

Composite	*T*(^{o}*C*)	*RH*(%)	*M*(%)	Elementary properties						Reference
				Longitudinal		Shear		Transverse		
				E	*S*	*E*	*S*	*E*	*S*	
6376C/T400 carbon/epoxy	40	90	NA	0.8	0.8	-	-	0.8	1.0	[114]
Boron/AVCO 5505	177	NA	0.5	1.0	0.8	-	-	0.4	0.9	[118]
Courtaulds HMS/Hercules 3002M	177	NA	0.5	1.0	1.0	-	-	1.0	0.3	[118]
E-glass/Epoxy	RT	DW	1.7	0.9	0.6	-	-	-	-	[119]
Glass/Polyester	30-100	DW	4.5	-	0.7	-	-	-	-	[78]
Hercules AS-5/3501	RT	95	1.6	1.0	1.0	1.0	1.1	0.9	0.4	[9]
Hercules AS-5/3501	130	NA	1.9	1.0	1.0	-	-	0.3	0.6	[120]
HT-S/(8183/137-NDA-BF_3;MEA)	120	NA	0.5	-	-	-	-	1.0	0.6	[121]
IM7/DGEBA carbon/epoxy										[122]
• Untreated fibre	25	95	2.0	0.5	0.5	-	-	-	-	
• Silane treated fibre	25	95	2.0	0.6	0.7	-	-	-	-	
Modmor II/Narmco 5206	177	NA	0.5	1.0	1.0	-	-	0.4	0.3	[118]
T300 Carbon/Polyetherimide	70	85	NA	1.0	0.9	0.9	0.9	-	-	[123]
Thornel 300/Fiberite 1034	27-150	100	≈1.5	-	0.7	-	-	-	0.5	[124]
Thornel 300/Narmco 5208	177	NA	1.1	1.0	0.9	-	-	1.0	0.3	[125]
Thornel 300/Narmco 5208	27-150	NA	0.9	-	-	-	-	0.7	0.5	[126]
Vicotex M10/1130 glass/epoxy	72	DW	≈1.3	1.0	0.4	0.7	0.5	0.6	0.5	[47]

* Values are normalised with respect to the properties at unaged condition.

T=ageing temperature, *RH*=relative humidity, *M*=corresponding moisture content, RT=room temperature, DW=demineralised water, *E*=modulus, *S*=strength, NA=not available.

Table 2.7: Temperature effects on modulus and strength of unidirectional composites under tensile loading.

Composite	*T*(^{o}*C*)	*RH*(%)	*M*(%)	Elementary properties						Reference
				Longitudinal		Shear		Transverse		
				E	*S*	*E*	*S*	*E*	*S*	
Boron/AVCO 5505	177	NA	0.3	1.0	1.0	-	-	0.1	0.5	[118]
Boron/Narmco 5505	147	DRY	-	-	0.7	-	-	-	0.5	[127]
Courtaulds HMS/Hercules 3002M	177	NA	0.1	1.0	1.0	-	-	0.3	0.2	[118]
E-glass/Epoxy	65	DW	7.8	0.8	0.8	-	-	-	-	[119]
Hercules AS-5/3501	149	95	1.6	1.0	1.0	0.2	0.5	0.2	0.3	[9]
Hercules AS-5/3501	129	NA	1.9	1.0	1.0	-	-	0.3	0.3	[120]
Hercules AS-5/3501	177	DRY	-	1.0	1.0	-	-	-	0.6	[128]
HT-S/710 Polyimide	227	DRY	-	1.0	1.0	-	-	-	1.0	[128]
HT-S/(8183/137-NDA-BF_3;MEA)	177	NA	0.5	-	-	-	-	0.1	0.2	[121]
Modmor II/Narmco 5206	177	NA	0.4	1.0	0.9	-	-	0.3	0.3	[118]
PRD49/ERLB-4617	127	DRY	-	0.7	0.7	-	-	-	-	[129]
T300 Carbon/Polyetherimide	80	DRY	-	1.0	0.9	0.9	0.9	-	-	[123]
Thornel 300/Fiberite 1034	149	NA	1.5	-	1.0	-	-	-	0.2	[124]
Thornel 300/Narmco 5208	177	NA	1.1	1.0	0.7	-	-	1.0	0.4	[125]
Thornel 300/Narmco 5208	149	NA	0.9	-	-	-	-	0.6	0.7	[126]
Vicotex M10/1130	72	DW	1.3	1.0	1.0	1.0	1.0	-	-	[47]

* Values are compared to the properties measured at room temperature at the same relative humidity and moisture content indicated.
T=temperature, *RH*=relative humidity, *M*=corresponding moisture content, DW=demineralised water, *E*=modulus, *S*=strength, NA=not available.

Table 2.8: Moisture and temperature effects on modulus of unidirectional composites under compressive loading.

Composite	*T*(^oC)	*RH*(%)	*M*(%)	Compressive modulus				Reference
				Longitudinal		Shear		
				Mois	Temp	Mois	Temp	
Boron/AVCO 5505	177	NA	0.5	1.0	1.0	0.2	0.2	[118]
Courtaulds HMS/Hercules 3002M	177	NA	0.6	1.0	1.0	0.4	0.3	[118]
Hercules AS-5/3501	129	NA	1.9	1.0	1.0	0.3	0.2	[120]
Modmor II/Narmco 5206	177	NA	0.4	1.0	1.0	0.5	0.4	[118]
T300 Carbon/Polyetherimide[a]	70	85	NA	1.0 (0.8)	1.0 (0.9)	-	-	[123]
Thornel 300/Fiberite 1034[b]	149	NA	1.5	1.0	1.0	0.2	0.1	[130]
Thornel 300/Narmco 5208	177	NA	1.1	1.0	1.0	1.0	0.8	[125]

**T*=ageing temperature, *RH*=relative humidity, *M*=corresponding moisture content, NA=not available, Mois=moisture effects as compared to the unaged condition, Temp=temperature effects with respect to the properties measured at room temperature which are aged at the same *RH* and *M*.

[a] Values in bracket refer to the normalised longitudinal compressive strength.

[b] Buckling test. Others refer to compressive test.

2.5.3.Environmental effects on mechanical properties of multidirectional, woven and random fibre polymer composites

In real life applications, the multidirectional composites are usually designed to optimise the load carrying capability in structural components. The performance of a multidirectional laminate under ageing is strongly depending on its lay-up. For example, moisture could reduce the thermal residual stresses in the composites by matrix swelling and increase the static strength if the lay-up configuration was optimised [129]. Besides, it was reported that moisture and temperature have very minimal effects on quasi-isotropic (QI) laminate properties, including strength, stiffness and failure strain, because they were fibre-dominated [9]. However, beyond the longitudinal failure stain, the stress-strain curves of QI composites were dominated by $\pm 45^{o}$ plies and hence the influence by the environments became more noticed. Actually, degradation due to moisture in the matrix properties changed the failure mode from fibre-dominated to matrix-dominated. Gillat and Broutman [44] reported that the strength degradation in 90^{o}-plies led to damage initiation in the cross-ply laminates at a lower stress level compared to the dry specimens. Consequently, diffusion was accelerated and the strength was further degraded. In addition, irreversible damage in the composite was enhanced as well. Also, the delamination cracks were found to be independent on the transverse cracks, which indicated that the environmental damage enhanced the moisture penetration and accelerated the weakening of the interface resin-rich areas.

Sometimes, in certain mechanical structures, woven and short fibre composites are employed. Their mechanical response can be quite different to that of multidirectional laminate.

Table 2.9 to Table 2.11 describe the effects of moisture and temperature on tensile and compressive properties of those composites. Unless otherwise stated, unnotched specimens are referred.

Table 2.9: Moisture effects on modulus and strength of multidirectional, woven and short fibre composites under tensile loading.

Composite	Fibre orientation	*T*(°C)	*RH*(%)	*M*(%)	*E*	*S*	Reference
Glass/Polyphenylene sulphide	Short						[131]
• R-4		NA	95, 100	0.5	-	0.7	
• R-7		NA	95, 100	0.6	-	0.7	
• A-100		NA	95, 100	0.4	-	0.7	
• A-200		NA	95, 100	0.5	-	0.7	
Glass/Polyphenylene sulphide	Chopped mat						[131]
• AG11-20 (moulded)		NA	95, 100	5.4	0.7	0.6	
• AG20-40 (moulded)		NA	95, 100	4.2	0.9	0.7	
• Glass/Bisphenol A	Mat + chopped fibres	90	DW	0.8	1.2	0.5	[103]
• Glass/Vinly ester		90	DW	1.9	1.0	0.6	
• Glass/Isophthalic		90	DW	2.6	0.6	0.4	
• Glass/Bisphenol B		90	DW	1.4	0.8	0.6	
All-PP	Woven fabric	65	DW	17.0	0.8	1.0	[132]
• Glass/PEI	Fabric	37	98	NA	-	0.8	[133]
• Carbon/PEI		37	98	NA		0.8	
Glass/PP	Glass mat	65	DW	2.5	0.9	0.8	[132]
Aramid49 285/Epoxy 895	• Satin weave 1/4, $[0/90]_S$	82	DW	4.8	1.0	1.0	[134]
	• Satin weave 1/4, $[\pm 45]_S$	82	DW	4.8	0.4	1.0	
Aramid49 285/Epoxy 895 (notched)	Satin weave 1/4, $[0/90]_S$	82	DW	5.4	1.0	-	[134]
Aramid49 285/Epoxy 895	Satin weave 1/4, $[0/90]_S$					-	[134]
• Impacted, 1.0 J/mm		82	DW	6.0	1.0		
• Impacted, 1.5 J/mm		82	DW	6.0	0.6		
Carbon CC201/Epoxy 895	• Satin weave 1/5, $[0/90]_S$	82	DW	2.4	1.0	-	[134]
	• Satin weave 1/5, $[\pm 45]_S$	82	DW	2.4	0.5	-	
Carbon CC201/Epoxy 895 (notched)	Satin weave 1/5, $[0/90]_S$	82	DW	3.0	1.0	-	[134]
Carbon CC201/Epoxy 895 Impacted, 0.75 J/mm	Satin weave 1/5, $[0/90]_S$	82	DW	2.4	1.0	-	[134]

Glass/Polyphenylene sulphide • AG31-60 (as received) • AG31-60 (moulded) • AG31-40 (as received) • AG31-40 (moulded)	Long satin weave fabric	 NA NA NA NA	 95, 100 95, 100 95, 100 95, 100	 28.0 15.1 18.0 10.3	 0.5 - 0.6 -	 0.4 0.5 0.6 0.7	[131]
• Glass/120°C cured epoxy • Glass/180°C cured epoxy	• 2/2 twill-weave • 8H satin-weave • 2/2 twill-weave • 8H satin-weave	70 70 70 70	95 95 95 95	2.0 NA NA NA	1.0 1.0 1.0 1.0	0.4 0.8 1.0 0.8	[104]
• Glass/120°C cured epoxy • Glass/180°C cured epoxy	• 2/2 twill-weave (in shear) • 2/2 twill-weave (in shear) • 8H satin-weave (in shear)	70 70 70	95 95 95	2.0 NA NA	0.8 0.9 0.9	0.5 0.9 0.7	[104]
Glass/Polyester	Cross-ply	30-100	DW	5.0	-	0.4	[78]
5208/T300 graphite epoxy	$[0/45/0/-45/0/\overline{\mp 45}]_S$	82	98	1.5	-	1.0	[135]
5208/T300 graphite epoxy	$[\pm 45/\mp 45]_{3S}$	82	98	1.5	-	1.0	[135]
5208/T300 graphite epoxy	$[0/\pm 45_3/0/\mp 45]_S$	82	98	1.5	-	1.0	[135]
5208/T300 graphite epoxy	$[\pm 45/90/\mp 45]_{2S}$	82	98	1.5	-	1.0	[135]
5208/T300 graphite epoxy	$[(45/90/-45/90)_2/-45/90/45/90]_S$	82	98	1.5	-	1.0	[135]
AMOCO T300-12K/Epoxy F593 (machined edges)	• $[45/90/0/-45]_S$ • $[0/90/\pm 45]_S$ • $[\pm 45/0/90/]_S$	80 80 80	95 95 95	0.8 0.8 0.8	- - -	1.0 1.0 1.0	[136]
AMOCO T300-12K/Epoxy F593 (moulded edges)	• $[45/90/0/-45]_S$ • $[0/90/\pm 45]_S$ • $[\pm 45/0/90/]_S$	80 80 80	95 95 95	0.7 0.7 0.7	- - -	1.0 1.2 1.0	[136]
Boron/AVCO 5505	$[0_2/\pm 45/\overline{90}]_S$	177	NA	0.5	1.0	0.9	[118]
Boron/Narmco 5505	$[0/\pm 45/90]_S$	177	NA	0.8	1.0	1.0	[137]
Courtaulds HMS/Hercules 3002M	$[0_2/\pm 45/\overline{90}]_S$	177	NA	0.6	1.0	1.0	[118]
Hercules AS-5/3501	$[0/\pm 45/90]_S$	27	95	1.6	1.1	1.0	[9]
Hercules AS-5/3501	$[0/\pm 45/90]_S$	129	NA	1.9	-	1.0	[120]
Hercules AS-5/3501	$[0/\pm 45/90]_S$	149	NA	1.7	-	1.0	[138]

HT-S-ERLA-4617	$[0/\pm45/90]_S$	177	NA	1.2	1.0	0.7	[137]
HT-S/Fiberite X-911	$[0/\pm45/90]_S$	177	NA	0.4	1.0	1.0	[137]
HT-S/Hysol ADX-516	$[0/\pm45/90]_S$	177	NA	1.4	1.0	1.0	[137]
HT-S/U.C.C.X-2546	$[0/\pm45/90]_S$	177	NA	2.1	1.0	0.9	[137]
Modmor II/Narmco 5206	$[0_2/\pm45/\overline{90}]_s$	177	NA	0.4	1.0	1.0	[118]
Thornel 300/Fiberite 1034	$[0/\pm45/90]_S$	149	NA	1.5	-	0.7	[124]
Thornel 300/Narmco 5208	$[0_2/\pm45/\overline{90}]_s$	177	NA	1.1	1.0	1.0	[125]
Vicotex M10/1130	$[0/\pm45/90]_s$	72	DW	≈1.3	0.8	0.4	[47]

* Values are normalised with respect to the properties at unaged condition.
T=ageing temperature, *RH*=relative humidity, *M*=corresponding moisture content, RT=room temperature, DW=demineralised water, *E*=modulus, *S*=strength, NA=not available.

Table 2.10: Temperature effects on modulus and strength of multidirectional and woven fibre composites under tensile loading.

Composite	Fibre orientation	*T*(°C)	*RH*(%)	*M*(%)	*E*	*S*	Reference
5208/T300 graphite epoxy[a]	$[0/45/0/-45/0/\overline{\mp 45}]_S$	93	DRY	-	-	1.0	[135]
5208/T300 graphite epoxy[a]	$[\pm 45/\mp 45]_{3S}$	93	DRY	-	-	1.0	[135]
5208/T300 graphite epoxy[a]	$[0/\pm 45_3/0/\mp 45]_S$	93	DRY	-	-	1.0	[135]
5208/T300 graphite epoxy[a]	$[\pm 45/90/\mp 45]_{2S}$	93	DRY	-	-	1.0	[135]
5208/T300 graphite epoxy[a]	$[(45/90/-45/90)_2/-45/90/45/90]_S$	93	DRY	-	-	1.0	[135]
Boron/AVCO 5505	$[0_2/\pm 45/\overline{90}]_S$	177	NA	0.5	1.0	0.8	[118]
Courtaulds HMS/Hercules 3002M	$[0_2/\pm 45/\overline{90}]_S$	177	NA	0.6	1.0	1.0	[118]
Hercules AS-5/3501	$[0/\pm 45/90]_S$	149	95	1.6	0.8	0.9	[9]
Hercules AS-5/3501	$[0/\pm 45/90]_S$	177	DRY	-	1.0	1.0	[128]
Hercules AS-5/3501	$[0/\pm 45/90]_S$	149	NA	1.7	-	1.0	[138]
HT-S/710 Polyimide	$[0/\pm 45/90]_S$	227	DRY	-	1.0	1.0	[128]
HT-S-ERLA-4617	$[0/\pm 45/90]_S$	177	NA	1.2	0.7	0.5	[137]
HT-S/Fiberite X-911	$[0/\pm 45/90]_S$	177	NA	0.4	1.0	1.0	[137]
HT-S/Hysol ADX-516	$[0/\pm 45/90]_S$	177	NA	1.4	0.7	0.4	[137]
HT-S/P13N Polyimide	$[0/\pm 45/90]_S$	177	-	-	0.9	0.9	[137]
HT-S/U.C.C.X-2546	$[0/\pm 45/90]_S$	177	NA	2.1	0.9	1.0	[137]
Modmor II/Narmco 5206	$[0_2/\pm 45/\overline{90}]_S$	177	NA	0.4	1.0	0.8	[118]
Thornel 300/Fiberite 1034	$[0/\pm 45/90]_S$	149	NA	1.5	-	0.7	[124]
Thornel 300/Narmco 5208	$[0_2/\pm 45/\overline{90}]_S$	177	NA	1.1	1.0	0.8	[125]
Vicotex M10/1130	$[0/\pm 45/90]_S$	72	DW	≈1.3	0.4	0.8	[47]

* Values are compared to the properties measured at room temperature at the same relative humidity and moisture content indicated. *T*=temperature, *RH*=relative humidity, *M*=corresponding moisture content, DW=demineralised water, *E*=modulus, *S*=strength, NA=not available.

[a] A combination of moisture (98%RH at 82°C) and temperature (93°C) effect reduced the strength of $[0/\pm 45_3/0/\mp 45]_S$ laminate up to 16%. For other laminates, the coupled influence was negligible.

Table 2.11: Moisture effects on modulus, strength and failure strain of multidirectional and woven composites under compressive loading.

Composite	Fibre orientation	$T(^oC)$	$RH(\%)$	$M(\%)$	E	S	ε	Reference
Aramid49 285/Epoxy 895	• Satin 1/4, $[0/90]_S$ • Satin 1/4, $[\pm45]_S$	82 82	DW DW	4.8 4.8	0.9 0.9	1.0 1.0	0.8 1.2	[134]
Aramid49 285/Epoxy 895 (notched)	Satin 1/4, $[0/90]_S$	82	DW	5.4	1.0	1.0	-	[134]
Aramid49 285/Epoxy 895 • Impacted, 1.0 J/mm • Impacted, 1.5 J/mm	Satin 1/4, $[0/90]_S$	 82 82	 DW DW	 6.0 6.0	 1.0 0.9	 1.0 0.7	 - -	[134]
Carbon CC201/Epoxy 895	• Satin 1/5, $[0/90]_S$ • Satin 1/5, $[\pm45]_S$	82 82	DW DW	2.4 2.4	1.0 0.7	0.7 1.0	- -	[134]
Carbon CC201/Epoxy 895 (notched)	Satin 1/5, $[0/90]_S$	82	DW	3.0	1.0	0.9	-	[134]
Carbon CC201/Epoxy 895 Impacted, 0.75 J/mm	Satin 1/5, $[0/90]_S$	82	DW	2.4	0.9	0.8	-	[134]
Boron/AVCO 5505	$[0_2/\pm45/\overline{90}]_S$	177	NA	0.5	1.0	-	-	[118]
Carbon T800H-12K/Epoxy 3633 [a] (compression after impact) • $< T_g$ • $>T_g$	$[45/0/-45/90]_{4S}$	 71 71	 DW DW	 1.4 1.4	 - -	 1.0 0.3	 - -	[139]
Courtaulds HMS/Hercules 3002M	$[0_2/\pm45/\overline{90}]_S$	177	NA	0.6	1.0	-	-	[118]
Hercules AS-5/3501	$[0/\pm45/90]_S$	129	NA	1.9	1.0	-	-	[120]
Modmor II/Narmco 5206	$[0_2/\pm45/\overline{90}]_S$	177	NA	0.4	1.0	-	-	[118]
Thornel 300/Narmco 5208	$[0_2/\pm45/\overline{90}]_S$	177	NA	1.1	1.0	-	-	[125]

* Values are normalised with respect to the properties at unaged condition.
T=ageing temperature, RH=relative humidity, M=corresponding moisture content, RT=room temperature, DW=demineralised water, E=modulus, S=strength, ε=failure strain, NA=not available.
[a] Similar observation for temperature effect.

2.5.4.Environmental effects on flexural and interlaminar shear strength of the composites

In addition to tensile and compressive properties, flexural and short beam properties of composite materials subjected to environmental conditions are also commonly studied to investigate the possible fibre-dominated (from flexural test) and matrix and/or interface dominated (from short beam test) properties. Gillat and Broutman [44] reported that the flexural strength is fibre dominated, and hence not affected significantly by the moisture level with or without applied stress. In their studies, slight increase of 8% in the flexural strength was found at water gain of 0.8%, which could be due to partial release of internal residual stresses [118]. Browning et al. [9] reported that the flexural properties in unidirectional composites were fibre-dominated before ageing, where brittle failure occurred with fibre breakage observed between the loading noses. After ageing, the flexural strength was mainly dominated by inter-laminar yielding, which was due to reduction in the in-plane shear strength and the nonlinear stress-strain response. This observation was supported by tensile test using $[\pm 45]_{2S}$ specimens. Fibre breakage in the aged specimens was not observed but permanent deformation was found near the loading noses where shear stress was maximum.

As for inter-laminar shear strength (ILSS) test, reduction in the short-beam strength was observed due to water ageing, which indicated interface degradation [44]. Failure mechanisms of a short beam in unidirectional carbon/epoxy composites tested under flexural loading include inter-laminar cracking, interface debonding, fibre pull-out, fibre breakage and delamination [14]. In unaged specimens, fibre breakage dominated and no fibre/matrix debonding was observed. With water immersion at 80^{o}C, fibre breakage with interface failure was noticed. Lv et al. [14] considered the reduction in ILSS as a consequence of interface deterioration. One of the causes was the existence of internal interface stresses due to water absorption, which led to crevices and lowered the interfacial strength. In addition, hydrolysing reaction between fibre and matrix also worsened the interfacial strength.

Table 2.12 and Table 2.13 summarise effects of moisture on the flexural and short beam properties of composite materials.

Table 2.12: Moisture effects on modulus and strength of composites under flexural loading.

Composite	Fibre orientation	*T*(^{o}C)	*RH*(%)	*M*(%)	*E*	*S*	Reference
Glass E-8204/Epoxy DER383 reinforced montmorillnmites (MMT)	Unidirectional						[98]
• Without MMT		80	DW	1.2	1.0	1.0	
• 3% Cloisite 30B		80	DW	1.8	1.0	0.7	
• 3% Cloisite 10A		80	DW	1.5	0.7	0.6	
• 5% Cloisite 10A		80	DW	1.4	0.8	0.5	
T300 Carbon/Polyetherimide	Unidirectional	70	85	NA	1.0	1.0	[123]
Carbon G40-800/PETU	Transverse unidirectional	90	85	0.5	-	0.8	[140]
E-glass/Polyester	• $[0/90]_{2S}$	RT	98	NA	0.5	0.8	[141]
	• $[0/90]_{4}$				0.7	1.0	
Glass/Epoxy	$[0/90]_{7S}$						[46]
• Without pre-stressed		60	DW	28.0	0.6	0.3	
• With pre-stressed		60	DW	30.0	0.3	0.2	
SP-313 graphite/epoxy	• $[90]_{8}$	60	DW	1.8	-	0.5	[44]
	• $[0/90]_{2S}$	80	DW	2.6		1.0	
Carbon/Epoxy	Plain weave fabric	71	DW	4-5	0.7	0.4	[142]
Carbon 6K HTA/Epoxy	Satin 1/5 $[(0/90)_{S}]_{3}$				-		[143]
• Autoclave		70	85	0.30		0.9	
• Quickstep		70	85	0.25		1.0	
Glass/120^{o}C cured epoxy	2/2 twill-weave	70	95	2.0	-	0.5	[104]
Glass/180^{o}C cured epoxy	• 2/2 twill-weave	70	95	NA	-	0.9	[104]
	• 8H satin-weave	70	95	NA	-	0.7	
Glass/Epoxy	Fabric	71	DW	4.0-5.0	0.7	0.5	[142]
Glass/Low styrene content DCPD orthophthalic polyester	Mats + Woven taffetas	60	SW	1.1	1.0	0.4	[115]
Glass/Low styrene emission orthophthalic polyester	Mats + Woven taffetas	60	SW	1.5	0.9	0.4	[115]
Glass/Standard orthophthalic polyester	Mats + Woven taffetas	60	SW	1.3	0.9	0.4	[115]
Glass/Vinylester	Mats + Woven taffetas	60	SW	0.5	1.0	0.5	[115]
Hexply 913C carbon/epoxy	Balanced woven	85	DW	3.0	0.6	0.7	[144]

* Values are normalised with respect to the properties at unaged condition.
T=ageing temperature, *RH*=relative humidity, *M*=corresponding moisture content, RT=room temperature, DW=demineralised water, SW=seawater, *E*=modulus, *S*=strength, NA=not available.

Table 2.13: Moisture effects on strength of composites under short-beam test.

Composite	Fibre orientation	*T*(^oC)	*RH*(%)	*M*(%)	*S*	Reference
3234/G827 carbon/epoxy	Unidirectional	80	DW	0.13g	0.5	[14]
Carbon+glass/epoxy	Unidirectional, rod	90	DW	11.7	0.8	[145]
T300 Carbon/Polyetherimide	Unidirectional	70	85	NA	0.6	[123]
E-glass/DGEBA epoxy	Quasi-unidirectional (88% in 0^o and 12% in 90^o)	50	DW	3.0	0.8	[146]
SP-313 graphite/epoxy	$[0/90]_{2S}$	80	DW	2.6	0.7	[44]
Glass/Epoxy EPON 815C	Random	45	DW	1.9	0.8	[147]
Carbon 6K HTA/Epoxy	Satin 1/5 $[(0/90)_S]_3$					[143]
• Autoclave		70	85	0.30	0.8	
• Quickstep		70	85	0.25	0.8	
Carbon/PEI	Fabric	37	98	NA	0.7	[133]
Glass/PEI	Fabric	37	98	NA	0.7	[133]

* Values are normalised with respect to the properties at unaged condition.
T=ageing temperature, *RH*=relative humidity, *M*=corresponding moisture content, RT=room temperature, DW=demineralised water, *S*=strength, NA=not available.

2.5.5.Environmental effects on interface properties of polymer composites

Due to low inter-laminar strength, delamination is generally recognised as one of the most common and early detected damage mechanism in composite materials. Moreover, the interface in the filled system is sensitive to water attack [111]. It was mentioned that moisture can affect interface and even fibre itself [13]. Even in generally recognised impermeable carbon fibres, 0.02 wt% water could be absorbed in the free fibres [34]. Progressive interface degradation is a concept of gradual reduction in the Van Der Waals's forces as the water invades the interface [111]. Besides, interface separation was found to be due to hydration weakening of oxide layer on the filler particles [111]. In addition, interface could also be destroyed due to polar bonds breakage by chemical reaction such as leaching of K_2O and Na_2O which caused glass fibres pitting [78, 148]. It was also reported that the formation of voids increased the interfacial regions in glass/polyester composites, which was harmful to the composites [78, 148]. Moreover, swelling was reported to weaken the matrix and the interface especially at high temperature [149]. Furthermore, high cross-link density was found to improve the solvent resistance but lower the fracture energy [150].

Zenasni and his co-workers [151] investigated hygrothermal and hygrothermo-mechanical effects on the fracture toughness of woven fibres reinforced polyetherimide (PEI) composites, where three reinforcements were used: 2/2 twill glass, 8-harness satin glass and 8-harness satin carbon fibres. Specimens were aged at 0, 30, 60, 120 and 180 days and then tested at constant temperature and given relative humidity. Double cantilever beam (DCB) mode I and end notched flexure (ENF) mode II tests were then performed to measure the corresponding toughness. Results showed that with moisture exposure up to 180 days, for the composites reinforced by 2/2 twill glass and 8H satin carbon fibres, G_{IC} values were reduced, but remained nearly constant in 8H satin glass fibre case. Regarding the value of G_{IIC}, at the end of the ageing, reduction was observed in 2/2 twill glass and 8H satin carbon fibres composites. On the contrary, improvement was found in 8H satin glass fibre composite.

In the studies of Huang and Sun [152], the effects of moisture absorption in 2-layer glass fabric reinforced unsaturated polyester composites were investigated at different durations of immersion. The peeling strength of the composites was found to increase with the immersion time up to 14 days. It was believed that the water molecules seeped into the cracks and voids of the laminates so as to enhance the peeling resistance. Another recent research investigated the delamination behaviour of carbon/epoxy composite reinforced by thermoplastic particulate [153]. Both dry and wet specimens were tested at low, room, elevated and high (for dry specimens only) temperatures. The specimens were tested using DCB, ENF and mixed-mode flexure (MMF) (also known as single leg bending (SLB)) tests. Results indicated that temperature and moisture absorption enhanced the ductility of the matrix, where mode I fracture toughness was improved. However, adverse effect was found on mode II fracture resistance. The mixed-mode fracture toughness increased with moisture but decreased with temperature.

In order to improve delamination behaviour of carbon/epoxy laminates under environment conditions, Walker and Hu [154] proposed to introduce Short Fibre Reinforcement (SFR) into the delamination region. It was shown that the use of SFR enhanced the inter-laminar bonding under DCB loading. The improvement of fracture toughness was observed not only in

dry specimens, but also in hot/wet specimens. In some cases, the fracture toughness of hot/wet specimens was higher than the dry ones.

A recent publication from the laboratory reported on the delamination behaviour of 8/8h satin weave glass/epoxy composites aged in demineralised water at 72^{o}C [155]. Specimens at different moisture contents were studied through DCB, ENF and MMF tests to obtain pure mode I, pure mode II and mixed-mode I+II fracture resistances, respectively. In order to investigate the effects of the orientation of adjacent fibres on the inter-laminar fracture behaviour, two series of specimens were prepared with [0//0] or [90//90] predominant fibre interface along the plane of the initial crack which was introduced at mid-thickness of specimens. Results showed that for both of [0//0] and [90//90] specimens, the influence of moisture absorption on the delamination behaviour of the composites became more significant when the participation of mode II was more important. Moreover, the toughness ratio: G_{IIC}/G_{IC}, decreased with increasing moisture content, and its reduction was more remarkable if the crack grew between [0//0] interface than that between [90//90] interface. Under pure mode I and mixed-mode I+II loadings, the fracture toughness measured at [90//90] interface was greater than that at [0//0] interface. However, an inverse effect was shown in pure mode II case. BK mixed-mode criterion [156] proposed by Gong and Benzeggagh [157-158] described by the equation:

$$G_{TC} = G_{IC} + (G_{IIC} - G_{IC})\left(\frac{G_{II}}{G_I + G_{II}}\right)^{\eta} \tag{2.47}$$

showed that η = 2/3 agreed well with the experimental results regardless the moisture content and the adjacent fibre direction. This implied that although the values of G_{IC} and G_{IIC} decreased with the moisture content, the material constant η seemed to be independent of water absorption. Regarding the behaviour of the crack growth, the increment of the resistance to delamination growth was always higher in the [90//90] specimens than that in the [0//0] ones at all moisture contents. The degradation of fibre/matrix interface caused by water absorption accelerated the formation of fibre bridging beyond the crack tip in the early crack growth, hence led to higher rate of increment in the resistance. However, the quantity of the fibre bridging decreased with the moisture content at the stable level of the resistance to delamination.

To enhance the interfacial strength, filler treatment was employed. Coupling agents (such as silane) was believed to promote stability and interfacial adhesion and protect the bond from moisture [111, 159]. However, the dissolution was enhanced and higher moisture uptake and leaching occurred, where loss in organic matter and effective damage were observed [159]. Bowditch [111] reported that the strength and modulus reduction in untreated silica reinforced epoxy system was more than silane treated silica, because there was a combination of plasticisation and interface disruption effects in untreated while the failure in treated one was dominated by plasticisation.

Environment effects do not always found to be harmful. For example, although moisture has obvious effect on delamination extension at low temperatures, G_C (especially G_{IC}) of graphite/bismaleimide (IM6/5245C) was only slightly affected by moisture below 80^{o}C [160]. Above 80^{o}C, significant matrix plasticisation was observed. Besides, toughness was enhanced by higher moisture content and damage (micro-cracking) because additional energy dissipation was created and needed [161].

Consequently, it is of great importance to better understand the environmental effects on the performance of the composite materials, which have to be included in the design to predict correctly the lifetime of the composite structures.

Table 2.14 summarises moisture effects on the fracture toughness of composite materials under different mode-mixity.

Table 2.14: Moisture effects on fracture toughness of composite materials.

Composite	Fibre orientation	*T(°C)*	*RH(%)*	*M(%)*	I	I+II	II	Reference
• AS1/3501-6 graphite/epoxy • HMS/3501-6 graphite/epoxy	Unidirectional	75 75	100 100	1.4 1.4	1.0 -	- -	1.0 1.0	[162]
Carbon/Epoxy reinforced • No reinforcement • Polyamide web • Zylon HM • Polyolefin web	Unidirectional	 95 95 95 95	 DW DW DW DW	 2.1 2.1 2.1 2.1	 2.5 0.3 3.0 4.0	-	-	[154]
IM6 Graphite/PEEK	Unidirectional	70	DW	0.2	1.0	-	-	[163]
T300/934 graphite/epoxy	• $[0]_{16}$ • $[0]_{26}$	70 70	DW DW	2.1 1.5	1.3 1.1	-	-	[164]
T300/934 graphite/epoxy	$[0_7/45//\mp45/-45_2/\pm45/45/0]$	70	DW	1.6	-	-	0.9	[164]
T800H/3900-2 carbon epoxy (T800H/3631 reinforced thermoplastic particles)	Unidirectional Test temperature: • 21°C • -43°C • 98°C	 50 50 50	 95 95 95	 0.8 0.8 0.8	 1.1 1.2 1.4	 1.0 1.1 1.1	 1.0 0.8 0.8	[153]
E-glass/DGEBA epoxy	Quasi-UD	50	DW	3.0	-	0.8	-	[146]
HTA/6376C carbon/epoxy	$[0_{12}//(\pm5/0_4)s]$ Test temperature: • -50°C • 20°C • 100°C	 70 70 70	 95 95 95	 1.2 1.2 1.2	 0.9 1.0 1.1	 0.9 0.9 0.8	 0.9 0.9 0.8	[165]
Carbon/Epoxy	Plain weave fabric	71	DW	4.0-5.0	1.2	-	0.3	[142]
E glass/Polyester[b]	Plain weave	29	DW	4.6	1.3	-	-	[152]
Carbon/Polyetherimide • Without pre-stressed • With pre-stressed	8-harness satin	 70 70	 95 95	 0.3 0.3	 0.8 0.9	-	 0.6 0.9	[151]
Glass/120°C cured epoxy[a]	2/2 twill-weave	70	95	2.0	0.3	-	0.4	[104]

Glass/Epoxy	8-harness satin • Warp dominated • Weft dominated	 72 72	 DW DW	 3.0 3.0	 0.7 0.7	 0.7 0.8	 0.7 0.8	[155]
Glass/Polyetherimide • Without pre-stressed • With pre-stressed	 • 2/2 twill • 8-harness satin • 2/2 twill • 8-harness satin	 70 70 70 70	 95 95 95 95	 0.2 0.2 0.2 0.2	 0.8 1.0 0.8 1.0	 - 	 0.7 1.3 0.8 1.2	[151]

* Values are normalised with respect to the properties at unaged condition.

T=ageing temperature, *RH*=relative humidity, *M*=corresponding moisture content, RT=room temperature, DW=demineralised water.

[a] Although the mixed-mode fracture toughness are not reported, the authors mentioned $\eta = 1.5$ using Equation (2.47).

[b] Peeling test.

2.5.6.Environmental effects on adhesive bonded joints

Advanced structural adhesives are widely used in joining primary and/or secondary structural members and manufacturing of advanced composite materials such as Glass Laminate Aluminium Reinforced Epoxy (GLARE) [166]. In addition, it is commonly applied in the repair of the structures. Advantages of adhesive bonding over traditional joining techniques such as welding and riveting include ease in assembly process, elimination of material removal and hence more uniform load distribution and thus reduced stress concentration, better fatigue resistance, higher corrosion resistance, substantial weight reduction, flexibility in joining different materials [100, 167-169]. These in turn lead to improved production and quality, and reduced production and maintenance cost.

Effects of moisture absorption on adhesive bonded joints have been studied by numerous researchers. Adhesive bonding characteristics could be studied through single-lap joint (SLJ), double-lap joint (DLJ), lap-strap, butt, thick adherend shear test (TAST), L-joint, Acran and peel tests. In addition, pre-cracked adhesive bonded tests such as DCB, ENF, MMF, wedge and notched coating adhesion (NCA) are also of interest. The degradation of bonded joints depends on type of substrate and adhesive, type of surface treatment, loading configuration and ageing environment (moisture, temperature and external loading) [170]. Moisture could enter into the bulk adhesive and the adhesive/adherend interface. Hence, there are generally two main failure modes in adhesive bonded joints, which are cohesive and interface failure. Adhesive degradation is usually caused by plasticisation, swelling and hydrolysis, whereas interface degradation is often attributed to metal oxide hydration, displacement of the adhesive by water, substrate corrosion and cathodic delamination [171]. The degradation level in the bulk adhesive and interface will determine the failure mode, which could be cohesive or adhesive. It is always desired to maintain cohesive failure or mixed cohesive/adhesive failure in adhesive joining.

Moisture effects on mild steel bonded AV119 adhesive joints were studied extensively through TAST, butt, NC, MMF and SLJ [100, 167-168, 172-173]. In general, AV119 adhesive bonded joints exhibited interfacial failure in both dry and wet conditions. All specimens showed degradation at the presence of water. Compared to the unaged specimens, the maximum percentage degradation was found in MMF specimens (80%), while the least strength drop was observed in SLJ and TAST specimens (30%). The authors suggested that coating the specimens' edges using primer paint enabled more uniform diffusion and also reduced corrosion and cathodic delamination at the edges [168, 173]. Consequently, the results were more convincing to be treated as average values, due to more uniform interfacial degradation.

Contrary to AV119, EA9321 and E32 joints showed cohesive failure regardless the type of adherend used (aluminum, composite or steel) even after subjected to ageing (although it could be shifted nearer to interface) [109-110, 174]. Cohesive failure in wet specimens was also observed in epoxy-amine bonded mild steel butt joints [175]. Ameli et al. [176] studied the irreversible effects in epoxy-aluminium joints by ageing the specimens for 5 months at 60^{o}C with 82%RH and 95%RH, and followed by drying for 6 months. It was revealed that G_{IC} was practically unchanged, but significant reduction in the R-curve and hence steady-state fracture toughness, G_R was observed, with 50% and 75% reduction in 82%RH and 95%RH, respectively. Cohesive fracture was observed in all specimens, which indicated that the interface was not degraded more severe than the adhesive.

Testing aluminium (2024-T3)-FM73 adhesive joint with peel test, doubles in three-point bending (DB), and full- and reduced-width single-lap joints (FSLJ and RSLJ) also revealed that the failure in both dry and wet specimens was mainly cohesive [166, 177]. As for aluminium (7075-T6) adherend bonded with the same type of adhesive, cohesive failure (near interface) was noticed in unaged and low moisture concentration MMF specimens, whereas high moisture content shifted the failure mode to the interface [112, 178]. Change in the failure mode from cohesive to interface due to moisture was also found in carbon steel-Hysol 3425 [179], aluminium (AA2024-T3)-epoxy/acrylic hybrid adhesive single-lap joints [180], acrylic adhesive bonded glass fibre reinforced polymer composites [181] and also aluminium adherend bonded with various different adhesives (except vinyl-phenolic) in both natural and accelerated ageing conditions [182]. Bordes et al. [105] reported that in low carbon steel (S35)-Araldite 2015 DLJ, unaged specimens showed cohesive failure near interface whereas interface failure was noticed in aged specimens. In addition, under both tensile and shear loadings (Arcan test), the failure mode changed from cohesive in dry specimens to mixed cohesive-adhesive failure in wet specimens. In the study by Moidu et al. [108], cohesive failure was noticed in the aged E04 adhesive system while interfacial failure dominated in EA 9346 adhesive system in both dry and wet specimens. Brewis found that wet joints always failed in interfacial region [106].

The difference in the failure mode could be due to various factors. Particularly, the diffusion and degradation mechanisms in adhesive bonded joints are comparatively more complicated than bulk adhesive/neat resin or even composite materials. Firstly, this is due to the difference in material properties between the adherend and the adhesive, which induces high peel and shear stresses at the free edges. Moisture could be beneficial in reducing the peel stress at the overlap end of the joint through compressive stress induced by swelling effect and reduction in the elastic modulus of the adhesive [100-101]. However, additional adherend/adhesive interface diffusion which is generally faster than the bulk adhesive could be observed due to capillary diffusion and cathodic delamination (in metal adherend) [167, 183]. Diffusion is believed to cause instability in the interface [166]. By comparing the diffusion in the bulk adhesive and laminated disc, interface diffusion was reported to be more significant [100]. Even in adhesive bonded composite joints, the diffusion in the adhesive could be higher than the diffusivity of the composite [184]. Consequently, interface degradation could occur because of the rupture of interfacial secondary bonds, the reduction of interionic forces, the hydration of oxide layer in metallic adherend and the hydrolysis and the breakage of bonds at the boundary of the adhesive layer (interface) [111, 185-187]. This could lead to the change in failure mode from cohesive to interface [182]. Hence, the adherend/adhesive interface degradation becomes one of the major factors that govern the joint strength [100] or even the dominant failure mechanism [188]. Through scanning electron micrograph (SEM) observation Loh et al. [173] discovered that there was approximately 70% reduction in the adhesive fragments on the substrate surface in aged specimens, which signified interface weakening. Ameli and his co-workers [70] reported that cohesive degradation of a rubber-toughened epoxy adhesive was due to chemical changes by the water molecules [189-190], whereas mobile molecules toughened the adhesive bonded joints.

Table 2.15 summarises the effect of moisture absorption on the adhesive joints under different testing configurations.

Table 2.15: Moisture effects on adhesive bonded joints.

Adherend	Adhesive	*T* (^oC)	*RH* (%)	*M* (%)	Test	Parameter	*S*	Reference
Low carbon steel	Araldite 2015	60	DW	8.4	• DLJ • Acran	Failure load	0.3 0.5	[105]
Carbon steel	Hysol 3425	50	100	4.5	SLJ	Failure load	0.2	[179]
Steel	Epoxy	90	DW	NA	Butt	Fracture stress	0.3	[191]
Mild steel	AV119 (Araldite 2007)	50	DW	7.6	MMF	Critical load	0.2	[167-168, 172-173]
Mild steel	AV119 (Araldite 2007)	60	DW	NA	NCA	Critical strain	0.3	[100]
Mild steel	AV119 (Araldite 2007)	60 60	DW DW	NA NA	• SLJ • Butt	Failure load	0.7 0.6	[100]
Mild steel	AV119 (Araldite 2007)	50	DW	7.6	TAST	Failure load	0.7	[167]
Mild steel	Epoxy-amine	RT	SW	NA	Butt	Failure stress	1.3	[111]
• Mild steel • Aluminium (7075-T6)	E32	22	DW	9.7	Butt	Failure load	0.6 0.5	[192]
Aluminium (AA 1100-H14)	• E04 • EA 9346	67	DW	5.9	Peel	Peel force	0.5 0.2	[108]
Aluminium (AA 2024-T3)	• SBT 9244 • SBT 9245	RT	100	2.5	SLJ	Failure load	0.8 0.8	[180]
Aluminium	Dicy cured nitride epoxy paste	52	100	NA	SLJ	Shear strength	0.1	[193]
Aluminium	Epoxy • Carbonate filled amine • Carbonate filled polyamide • Ufilled polyamide	 52 52 52	 100 100 100	 NA NA NA	SLJ	Shear strength	 1.5 0.9 1.1	[193]
Aluminium	Epoxy	90	100	NA	SLJ	Shear strength	0.8	[194]

Aluminum alloy (L165)	• Epoxy-polyamide • Vinyl-phenolic • Epoxy ME170 • Epoxy ME170g • Epoxy ME120K	35 35 35 35 35	85 85 85 85 85	NA NA NA NA NA	DLJ	Failure load	≈0 0.6 0.5 0.6 0.7	[182]
Aluminum alloy (L165)	• Epoxy-polyamide • Vinyl-phenolic • Epoxy ME170 • Epoxy ME170g • Epoxy ME120K	50 50 50 50 50	95 95 95 95 95	NA NA NA NA NA	Wedge	Failure load	0.2 0.7 0.5 0.6 0.1	[182]
Aluminium (B53L152)	DGEBA epoxy	50	100	2.1	SLJ	Failure load	0.8	[106]
Aluminium (B53L73) • etched • anodised I • degreased • anodised II • sandblasted	DGEBA epoxy	50	97-100	NA	SLJ	Failure load	 0.6 1.4 0.6 0.8 0.7	[195]
Aluminium (B53L73) • etched • anodised	FM1000	50	100	NA	DLJ	Failure load	 0.2 0.6	[196]
Aluminium (B53L73)	FM1000	50	DW	9.4	SLJ	Failure load	0.6	[113]
Aluminium (2024-T3)	FM1000	50	95	13.4	SLJ	Failure load	0.8	[185]
Aluminium (2024-T3)	FM73	50	DW	NA	Peel	Peel force	0.9	[177]
Aluminium (2024-T3)	FM73	50	DW	NA	• DB • FSLJ • RSLJ	Failure load	0.8 0.9 0.8	[166]
Aluminium (7075-T6)	FM73	50	96	2.2	• SLJ • L-joint	Failure load	0.5 0.5	[112]
• Aluminium • IM7/8552 • Al-CFRP-Al	FM73	50 50 50	96 96 96	2.2 3.2 3.2	• SLJ • SLJ • DLJ	Failure load	0.8 0.8 0.7	[178]

Aluminium (7075-T6)	Epoxy EA9321	50 50	96 96	3.9 3.9	• MMF • SLJ	Critical load Failure load	0.6 0.7	[110, 174]
IM7-8552	Epoxy EA9321	50	96	4.9	SLJ	Failure load	0.7	[110, 174]
UD 6376C/T400 carbon/ epoxy	• Redux 410 • Hysol 9321	40 40	90 90	NA NA	DLJ	Failure load/width	0.9 0.8	[114]
Carbon bismaleimide/epoxy • $[0]_{16}$ • $[(0/\mp45/0)_2]_S$	Epoxy	 90 90	 97 97	 >0.8 >0.8	Lap-strap	Fatigue threshold	 0.4 0.5	[101-102]
CFRP	Sikadur 31PBA	40	95	NA	SLJ	Shear strength	0.8	[197]
GFRP	Sikadur 31PBA	40	95	NA	SLJ	Shear strength	0.8	[197]
XAS/914 Carbon/epoxy $[\pm45/0/90]_{2S}$	BSL 319	45	92	1.7	• Tensile • 4PB	Tensile strength Flexural strength	0.5 0.8	[198]
XAS/913 Carbon/epoxy $[\pm45/0/90]_{2S}$	BSL 312/5	45	93	1.4	• Tensile • 4PB	Tensile strength Flexural strength	0.4 1.0	[198]

* Values are normalised with respect to the properties at unaged condition.
T=ageing temperature, *RH*=relative humidity, *M*=corresponding moisture content, RT=room temperature, DW=demineralised water, NA=not available.

2.6.Modelling the durability of adhesive joints by finite element approaches

As durability testings are often more costly and time consuming, there is a trend to analyse adhesive bonded joints behaviour through mathematical approaches using analytical and/or numerical methods. However, closed form solution (analytical) is not easy to be obtained due to complex geometry (especially when three-dimensional analysis is required), material property (non-linearity) and boundary conditions [199]. Hence, finite element modelling becomes a popular method. Nevertheless, some experimental tests are still generally required.

The major challenges in durability modelling are accurate consideration of various ageing effects in the model and inclusion of the complete damage initiation and propagation cycle that lead to the final failure [200]. In terms of adhesive joints modelling coupled with environment effects, the research team led by Professor Andrew Crocombre, Professor Ian Ashcroft and Professor Magd Abdel Wahab has done a lot of works since last two decades.

Generally, in the finite element analysis, the first step (although not common) is to calculate the thermal residual stress introduced by the thermal mismatch between the adherend and the adhesive during curing process. The studies of thermal residual stress effects can be found in references [201-202]. Next step is to simulate how the moisture diffuses in the joints. Generally, a two-dimensional model is sufficient to predict not only the moisture diffusion through the adherend and adhesive (through overlap end/side) separately but also the mutual diffusion between the adherend and the adhesive. However, a three-dimensional model is required when accurate prediction of the moisture concentration across the edges of the width is also desired. In addition, it was shown that the diffusion through composite needs to be modelled although its diffusion coefficient is one order lower than that of the adhesive [110, 174, 178, 203].

The following step is to conduct the stress analysis by converting the diffusion elements into continuum/cohesive elements. Hygroscopic stress can be calculated based on the moisture distribution from the diffusion analysis. The combination of the thermal and the hygroscopic stresses gives the total hygro-thermal stress. It was recognised that residual stresses at the joint centre were dominated by the mismatch of the coefficient of thermal expansion (CTE) between the adherend and the adhesive in the overlap direction, but the domination was reduced at overlap ends due to adhesive swelling in both width and transverse directions caused by the moisture absorption [178].

Subsequently, the mechanical loading (usually input as imposed displacement) is applied. Consequently, the failure in aged joints is dependent on both residual and applied mechanical loads. Different material properties which are usually determined from experiments are assigned to the elements based on their moisture concentration at defined period. The stress distribution is generally found to be well predicted. For example, high peel and shear stresses were observed at the free edge due to Poisson's ratio mismatch of substrates [178]. Upon ageing, the peel stress at overlap end was progressively lowered because the compressive stress could be introduced by swelling at the adhesive edge and the adhesive modulus could be reduced [100-101]. In addition, during ageing of the adhesive joints, shear stress at the edge changed from positive to negative due to adhesive bulging [100]. Reduction in shear stress in the wet joints was also reported by Ashcroft et al. [101]. Furthermore, the plastic strain decreased but plastic zone increased due to lower yield strength [100]. Moreover, at saturation, swelling strains were found to be uniform,

but plastic zone has increased dramatically. Hence, the adhesive plasticisation and/or the weakening of the interface would govern the joint strength. As for butt joint, peel stress at the edge was initially highly positive, then became negative due to non-uniform swelling strain, and eventually becomes positive (but still much lower than the dry one). Peel stress at the centre of wet specimens was higher than the dry one, because the modulus at the centre (which was yet to saturate) was higher, and hence the stress transferred to the region. This could explain why the strength reduction in butt joint is faster compared to that in single lap joint (SLJ). In addition, high shear stress could be induced at the edge of the dry butt specimens due to different material properties between the adherend and the adhesive. Upon water absorption, the shear stress at the edge of the wet butt specimen could be negative because the adhesive bulging could be provoked by non-uniform swelling strain, where water uptake caused the adhesive to expand, but Poisson's effect forced the adhesive to contract. The shear stress changed from negative to positive at a distance from the end of the edge when there was no bulging effect. The plastic strain was high but the plastic zone was small. When fully saturated, swelling strains was uniform, there was no local bulging and load was transferred uniformly. Although stress concentration was reduced at the edge due to low modulus, peel stress at the central area was still comparable to the dry case. The plastic zone was also extended over the whole interface at saturation. Hence, failure would be due to plasticisation and/or interface weakening.

In terms of failure analysis, there are three major approaches, which are continuum mechanics based on stress analysis, fracture mechanics using stress intensity factor or fracture energy and damage mechanics approaches [169]. Continuum mechanics approach has disadvantages of no interface consideration and end singularities. As for fracture mechanics approach, stress singularity approach (fracture mechanics approach without initial crack) is recognised to be better than linear elastic fracture mechanics (LEFM) analysis. However, both continuum and fracture mechanics approaches do not consider the damage evolution [184] and hence progressive damage modelling is usually preferred. There are two major approaches in damage mechanics modelling, which are continuum and local approaches. Generally, continuum damage modelling (CDM) (continuum approach) is applied when the adhesive fails in cohesive [109-110, 174] and the adhesive thickness is significant [204]. As illustrated in Figure 2.6, the fracture process zone is dependent on the adhesive thickness [205]. In CDM approach, the crack path does not need to be pre-defined. The damage can propagate within the adhesive layer along and/or across the thickness layer. It was reported that stress is concentrated towards the interfaces in the adhesive layer of an adhesive joint [206]. Consequently, the cohesive/adhesive mode-mix ratio will be increased during cohesive crack propagation [204].

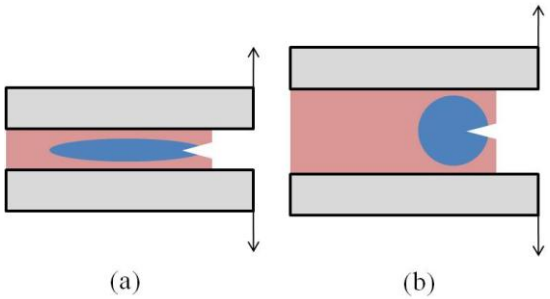

Figure 2.6: Fracture process zone dependence on adhesive thickness.

Local approach is realised through cohesive zone modelling (CZM), which is usually employed for joints with interface failure [168] (although CZM was used to simulate cohesive failure as well in certain cases [166, 177]). However, crack path needs to be pre-defined. Generally, damage mechanics approach has been widely used in recent years due to its ability to simulate major aspects in adhesive joints.

In terms of the modelling technique, displacement-based failure model was found to be better than the strain-based failure model in CDM approach due to its mesh independency [109-110]. As for CZM analysis, the process zone has to be long enough to include a few elements to avoid mesh dependency [112, 178, 207]. In addition, Drucker-Prager plasticity model was found to perform better than Von-Mises model due to incorporation of hydrostatic stress dependency of the adhesive in the former model [109, 112, 178]. Generally, the failure initiation location and subsequent propagation were found to be well predicted using those models. For example, at the joint corner in the fillet region, the moisture content was the highest and hence stress was highly concentrated. Failure was thus initiated at the respective region and progressed through overlap direction and width direction [110]. In addition, in butt joint, yielding was onset at the edges for both dry and wet joints [109]. In dry joint, damage was initiated from the edge (largest strain) to the centre, whereas in wet joint, damage was initiated from the centre and propagated to the side.

However, if cathodic delamination occurred experimentally due to ageing in tap water, the failure load could be over-predicted [178]. In addition, composite failure (especially delamination) was also found to be important to be included in the modelling [178]. Hence, the chemical degradation in the adhesive joint, the degradation of the composite properties and composite failure need to be included in the analysis for better prediction. Also, to achieve a reliable predictive model for adhesive joint, calibration of damage/cohesive parameter was needed at the first place on fracture specimens (such as MMF and NCA tests) [112, 167, 173-174, 178]. This implies that the physical meaning of some parameters is still unclear to certain extent. This could be an aspect that can be further enhanced.

Figure 2.7 schematises the analysis steps for durability prediction discussed above using finite element modelling.

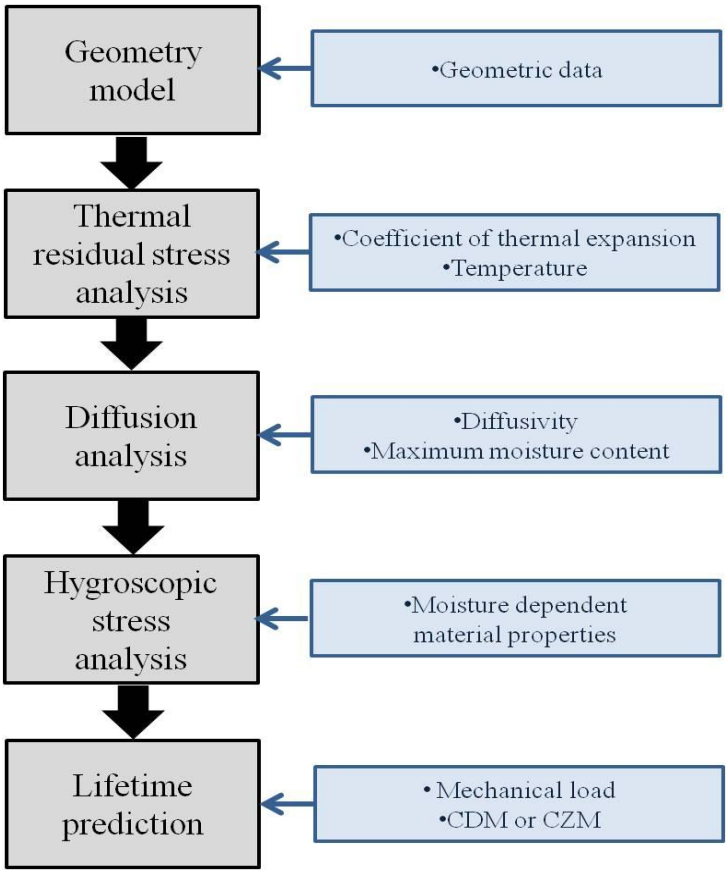

Figure 2.7: Analysis steps for lifetime prediction by finite element modelling.

2.7.Some review on circular external patches repaired composite joints

Figure 2.8 illustrates the schematic diagram of a quarter model of external patch repaired joint with some important nomenclatures generally used in the joint design. As a temporary repair, patch repair has the advantages of simple and less preparation time compared to other repair methods such as scarf and step sanded repairs. It can be implemented by removing the damaged region, followed by patches attachment using an adhesive. However, this method requires good surface preparation. Besides, external patches lead to aerodynamics disturbance and load path eccentricity that induce high shear and peel stresses at patch edges [6].

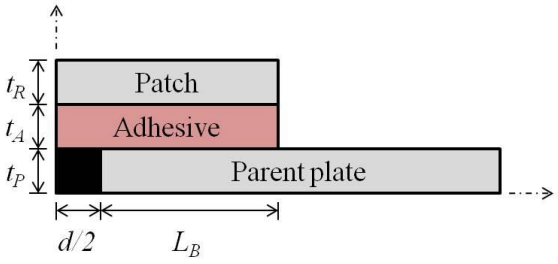

b = *width of the parent plate*
E_P = *parent plate elastic modulus*
E_R = *patch elastic modulus*

Figure 2.8: A quarter model of external patch bonded joint.

Several publications are available on external patches bonded composite-composite repair. Soutis and Hu [208] studied the compressive behaviour of double-sided patch repaired carbon/epoxy composites. The shear behaviour of the adhesive was modelled to be elastic perfectly plastic. Based on Hart-Smith's analytical method [209-210], Soutis and Hu reported that that the optimum overlap length was predicted to be approximately 12mm. Besides, the patch thickness was optimised at half of the parent plate if their membrane stiffnesses were the same. Ultimate shear strain of the adhesive has stronger effect compared to its shear strength. In addition, increasing adhesive thickness could reduce the shear strain at the overlap edge. Moreover, it was proposed that tapered end patch with spew fillet adhesive could provide the optimum design by reducing the shear and peel stresses. Through a three-dimensional finite element analysis with maximum stress failure criterion, it was found that the location of stress concentration was highly dependent on the thickness of the patch. Besides, patch was generally safe under loading. Concerning the adhesive/adherend interface, inter-laminar shear stress dominated the failure initiation, whereas peel stress could contribute to ultimate failure due to the delamination of the parent plate.

In their later work, the authors implemented a combined stress and fracture based cohesive zone fracture model to analyse the damage initiation and propagation in the patch repaired composites under compressive loading [6]. The contribution of parent plate, patch and adhesive on the stress distribution and stress intensity factor (SIF) were assessed through linear-superposition approach. The failure load and the corresponding critical buckling length could be obtained from the intersection of stress and SIF distribution curves. The predicted strengths were found to be conservative with acceptable errors (maximum of 15% lower than experimental values).

In another publication, Soutis and his co-workers [211] reported that filling the drilled hole using a plug (made from the same material as the parent plate) improved the failure strength of the repaired composites. The thickness of the patches had negligible effect on the failure strength. However, the failure mechanism was different with earlier adhesive failure observed in thicker patches. Repair system with thin patches and plugging was found to be able to retard damage propagation. Slight improvement was obtained by patches at lower stiffness. X-ray radiographs and scanning electron micrographs illustrated that damage mechanisms consisted of matrix cracking at notch edges, delamination, patch debonding at patch edges and fibre micro-buckling in 0^o layers. Finite element simulation results revealed that increasing patch thickness reduced normal stress concentration near the notch edges; however, the stress concentration especially the shear stress at patch edges was increased with patch thickness. This shear stress at both hole and patch edges could by reduced by increasing adhesive thickness. To characterise the damage, maximum stress criterion was adopted for the failure of the composite, whereas the adhesive damage and patch debonding were quantified through average stress failure criterion, using the parameters of yield shear stress and ultimate shear stress respectively. It was reported that fibre micro-buckling was always the governing failure mechanism for the ultimate failure for the cases of intermediate and high patch thicknesses, whereas patch debonding was the final failure mechanism for thin patch system. Regarding the repaired system where the membrane stiffness of the parent plate was higher than the patch, fibre micro-buckling occurred before adhesive yielding, but the order of the occurrence was reversed if their stiffness was the same.

Through experimental observation, Liu and Wang [212] reported that depending on the patch size and stacking sequence, the patches of the repaired composites could be debonded or fractured. To characterise the progressive damage numerically, they implemented stiffness degradation model for the adhesive joints. Stress based failure criteria were adopted to identify the damage onset in the composite, where Tsai-Wu criterion [213] governed the fibre breaking and matrix cracking and Ye criterion [214] for delamination detection. As for the adhesive, maximum shear stress criterion was adopted. The numerical predicted failure strengths were always lower than the experimental ones with maximum error for approximately 20%. Parametric studies revealed that optimum repair could be achieved with overlap length of 15mm, patch thickness to parent plate thickness ratio of 0.6 (with patch to parent plate stiffness ratio fixed at 0.3) and adhesive thickness between 0.2-0.3mm. For patches with the same membrane stiffness, stacking sequence did not show significant effect on the remote tensile strength.

Campilho and his co-workers [215] reported tensile behaviour of single- and double-sided patch repaired composites. Results showed that double-sided patch repairs exhibited slightly higher failure load compared to single-sided patch joints at all overlap lengths and adhesive thicknesses. Besides, double-sided repair showed improved failure load at higher overlap lengths. Improvement in the failure load was observed in double-sided repairs at all patch thicknesses with overlap length of 10mm, but not in single-sided repairs. For both single- and double-sided repairs, low overlap length led to premature patch debonding and the failure load was even lower than the notched specimen.

The same material was tested under compressive loading as well [216]. Experimental results showed that for both repairs, the failure load was increased with the overlap length and patch thickness. In both studies, numerical simulations were carried out by applying trapezoidal mixed-mode cohesive zone model in the adhesive layer. Within the studied parameters under both tensile and compressive loadings, it was concluded that double-sided repair was better than the single-sided one and the optimum repair could be achieved with double-sided repair at 15mm overlap length. Considering the weight penalty and aerodynamics disturbance, 0.5 could be optimum ratio of patch to parent plate thickness.

A recent publication from the laboratory reported that for soft patches (patches cured directly on the parent plate without using adhesive) repaired composites under tensile loading, larger bonding area could restore more residual strength [217]. Longitudinal elliptical patches were better than the transverse ones, and the use of Z-pins improved the performance as well. In later publications [218-219], Hoffmann failure criteria was adopted to predict the failure in the repaired systems. The ply of the parent plate that was the nearest to the adhesive was found to be the most critical in determining the failure of the repairs. From the plot of the normalised maximum strength ratio versus the normalised membrane stiffness, the intersection of the two most critical zones was found to give the optimum performance. Besides, patches with the same membrane stiffness but different stacking sequence did not seem to affect on the remote tensile strength. The predictions were confirmed by experimental results. Using the same analogy, parametric studies illustrated that lower adhesive stiffness provided better solution [218]. Lower patch thickness was found to improve the repaired system. However, lower maximum strength ratio was obtained for thicker adhesive. In general, it was noted that the optimised parameters were accompanied by an increment in the patch membrane stiffness. Through the parametric studies, a design parameter was introduced to correlate the stiffness and thickness of parent plate,

patch and adhesive. Optimal repair was achieved when the design parameter reached unity. This serves as a convenient guideline to design the repaired system. Acoustic emission data was presented in a later publication to predict the damage location [220]. In addition, cohesive zone model was used to analyse the damage in the repaired composites [221]. The numerical results showed a similar trend in the variation of ultimate strength with respect to the patch membrane stiffness compared to the experimental data. Furthermore, it was reported that for patches with low membrane stiffness, patch fracture was observed, and patch debonding was noticed for patches with high membrane stiffness.

Table 2.16 summarises some experimental studies on circular external patches repaired composite joints. In the table, $L_B = 0$ refers to the notched strength and normalised strength refers to the ratio of repaired to the unnotched strength. Other parameters are referred to Figure 2.8.

Table 2.16: Summary of the experimental studies on circular external patches repaired composite joints.

Test/Material/Parent/Adhesive	*d/b*	t_A (mm)	Patch	$E_R t_R / E_P t_P$	L_B (mm)	Normalised strength	Reference
Test : Compressive Material : HTA/913C Parent : $[(\pm 45/0_2)_3]_S$ Adhesive : Araldite 2011 Repair : Double-sided (DS)	0.2	0.1	$[(\pm 45/0_2)_3]_S$	1.00	 0 5 12.5	<u>Circular</u> <u>Square</u> 0.65 0.68 0.66 0.83 0.83	[222]
Test : Compressive Material : T800/924C Parent : $[(\pm 45/0_2)_3]_S$ Adhesive : Araldite 2011 Repair : Double-sided (DS)	0.2	0.1	 $[(\pm 45/0_2)]_S$ $[(\pm 45/0_2)_2]_S$ $[(\pm 45/0_2)_3]_S$	 0.33 0.67 1.00	0 12.5	0.54 0.65 (0.78)* 0.62 0.63 *Plugged with parent plate	[211]
Test : Compressive Material : T800/924C Parent : $[(\pm 45/0_2)_3]_S$ Adhesive : Araldite 2011 Repair : Double-sided (DS)	0.2	0.1	 $[(\pm 45/0/90)]_S$ $[(\pm 45/0/90)_2]_S$ $[(\pm 45/0/90)_3]_S$	 0.22 0.45 0.67	0 12.5	0.54 0.74 (0.78)* 0.67 0.67 *Plugged with parent plate	[211]
Test : Compressive Material : T800/924C Parent : $[(\pm 45/0/90)_3]_S$ Adhesive : Araldite 2011 Repair : Double-sided (DS)	0.2	0.1	 $[(\pm 45/0/90)]_S$ $[(\pm 45/0/90)_2]_S$ $[(\pm 45/0/90)_3]_S$	 0.33 0.67 1.00	0 12.5	0.49 0.70 (0.85)* 0.71 0.71 *Plugged with parent plate	[211]
Test : Compressive Material : HTA/913C Parent : $[(\pm 45/0/90)_3]_S$ Adhesive : Araldite 2011 Repair : Double-sided (DS)	0.2	0.1	$[\pm 45/0/90]_{2S}$	0.67	0 12.5	0.53 0.68	[6]

Test : Compressive Material : T800/924C Parent : $[(\pm 45/0/90)_3]_S$ Adhesive : Araldite 2011 Repair : Double-sided (DS)	0.2	0.1	$[\pm 45/0/90]_{2S}$	0.67	0 12.5	0.47 0.69	[6]
Test : Compressive Material : Texipreg HS 160 RM Parent : $[0_2/90_2/0_2/90_2]_S$ Adhesive : Araldite 2015 Repair : Single-sided (SS) and Double-sided (DS)	0.2	0.2	$[0_2/90_2]_S$ $[0/90]_S$ $[0_2/90_2/0_2]_S$ $[0_2/90_2/0_2/90_2]_S$	0.50 0.25 0.96 1.00	5 10 15 10 10 10	Normalised by notched strength: SS DS 1.08 1.11 1.12 1.38 1.20 1.63 1.12 1.30 1.15 1.33 1.19 1.40	[216]
Test : Tensile Material : T300/QY8911 Parent : $[(0/90/\pm 45/90/0)_2]_S$ Adhesive : Epoxy J159 Repair : Double-sided (DS)	0.3	0.12	$[\pm 45]$ $[0/\pm 45/90]$ $[0_2/\pm 45/90]$ $[0_2/\pm 45_2/90_2]$	0.04 0.09 0.17 0.21	10 10, 40 20, 50 30	Within the limited data reported, increasing $E_R t_R / E_P t_P$ increased the ultimate failure strength.	[212]
Test : Tensile Material : Texipreg HS 160 RM Parent : $[0_4/90_4]_S$ Adhesive : Araldite 2015 Repair : Single-sided (SS) and Double-sided (DS)	0.2	0.2	$[0_2/90_2]_S$ $[0/90]_S$ $[0_2/90_2/0_2]_S$ $[0_2/90_2/0_2/90_2]_S$	0.50 0.25 0.96 1.00	5 10 15 10 10 10	Normalised by notched strength: SS DS 0.94 0.97 1.00 1.02 1.00 1.05 0.98 1.00 1.00 1.03 0.99 1.02	[215]

Test : Tensile Material : T600S/R638-1 Parent : $[45/-45/0/90]_S$ Adhesive : Premabond ESP110 Repair : Double-sided (DS)	0.2	0.2	 $[90]_4$ $[\pm75]_S$ $[\pm45]_S$ $[0]_4$ [90/0/-45/45] [45/-45/90/0] [0/90/45/-45]	 0.09 0.09 0.14 1.31 0.36 0.36 0.36	0 12.5	0.56 0.68 0.72 0.90 0.75 0.80 0.73 0.85	[223]
Test : Tensile Material : T600S/R638-1 Parent : $[45/-45/0/90]_S$ Adhesive : Araldite 2015 Repair : Double-sided (DS)	0.2	0.2	$[90]_4$ $[\pm75]_S$ $[\pm45]_S$ $[0]_4$ [90/0/-45/45] [45/-45/90/0] [-45/45/0/90] [0/90/45/-45]	0.09 0.09 0.14 1.31 0.36 0.36 0.36 0.36	12.5	0.58 0.69 0.70 0.75 0.78 0.71 0.83 0.83	[224]

2.8.Summary

In this chapter, the moisture absorption mechanisms, diffusion models (Fickian and non-Fickian), environmental effects on the performance of the engineering materials, finite element modelling approaches for adhesive joints lifetime prediction and patch repaired composites are reviewed.

From the literature, it is obvious that the moisture ingression in the adhesives and the composites could be very complex. To understand how moisture enters the material, the first step is to propose a diffusion model that is capable to describe the mechanisms of water uptake. A good model is not only integrating different parameters that are susceptible to influence the water uptake behaviour, but also easily applied. Up to present, although many research works have been performed and very precious results and interesting discussion have been published in the literature, experiments are still needed to enrich the database in order to establish a good model.

Regarding the degradation in the material properties due to ageing, although different experimental observations were described in the literature, a general relationship between moisture uptake and the changes in material behaviour is not available, some results are even contradictory. Actually, the complexity of the environmental influence also implies different possibilities on the performance of the engineering materials. Usually, degradation is observed, however, in certain cases, improvement in the properties is signified. Therefore, it is worth to provide more experimental data in order to contribute to a more thorough understanding.

Finally, the prediction of the structure life with the ageing effect needs to be paid more attention. Specifically, in a composite system with adhesive joint, the damage and failure process are rather complicated that the prediction by finite element modelling is far from perfect, hence the improvement has to be continued.

In real life applications, there is a great variation in the design of composite laminates used in structural applications. One of the major differences is the laminate thickness (due to the difference in the prepreg thickness and ply number). Moisture absorption characterisation could be realised through accelerated ageing tests conducted in laboratory for time-saving purpose. However, thick laminates may still require long immersion time to obtain saturation even under accelerated ageing tests. If the moisture absorption behaviour of the composite laminates at low thickness could be well predicted, it could be further applied to composite laminates at any thickness, which would be greatly time-saving. Hence, this study will firstly focus on the effects of carbon/epoxy composite laminate thickness on the water ingression behaviour. In particular, the role of the laminate interface in retaining water molecules and the effects on the moisture absorption behaviour will be investigated. A moisture absorption model to describe the relevant phenomena observed through the experiment is expected. In addition, review on the external patches repair method shows that there is yet to have studies on the environmental effects on patch repaired composites. As a common temporary repair method, it is thus believed that the understanding of the performance of external patches repair composite joints is important and essential. Hence, the characterisation of the mechanical performance of the composites, adhesives and repairs under dry and wet conditions will be conducted as well. Finally, based on the experimental data, a reliable finite element modelling approach is to be proposed to provide some guidelines for future analysis with minimal experimental works.

CHAPTER 3. WATER UPTAKE BEHAVIOUR IN CARBON/EPOXY COMPOSITES

3.1.Introduction

This chapter mainly discusses the water uptake behaviour in the carbon/epoxy composites made from four different prepregs at various thicknesses. Firstly, the density and constituent's content are determined. Then the moisture transport of single-ply laminates at different thicknesses is investigated. It is followed by the analyses of laminate thickness/interface effects on the water ingression. A two-phase diffusion model is proposed based on the experimental data to characterise the water ingression behaviour in multi-ply laminates up to 1.2mm thickness. This model is then used to predict the weight gain of 8-ply coupon. Finally, moisture concentration distributions in both single- and multi-ply composites are predicted.

3.2.Experimental details

3.2.1.Fabrication of composite plates

The materials used in this study are carbon/epoxy prepregs supplied by Structil. Four different types of prepregs are used to fabricate the coupons for moisture absorption tests. The properties of the prepregs given by the manufacturer and the number of ply of prepared coupons are listed in Table 3.1. All composite laminates are fabricated using hand lay-up technique and cured using hot-press machine with the curing cycle shown in Figure 3.1. Once the polymerisation cycle is finished, the laminates are cooled down to room temperature, and then traveller coupons of $100\times100mm^2$ size are cut using diamond coated abrasive cutting blade with coolant. Edges of the coupons with thickness greater than 0.3mm are sealed with aluminium foil using Araldite 2015 adhesive to ensure one-dimensional diffusion through the surface only. For 170_S traveller coupons, one of the surfaces is sealed.

Table 3.1: Series of traveller coupons for moisture absorption test.

Prepreg	ρ (g/m^2)	T_g (^oC)	V_f (%)	Thickness per ply (mm)	Number of ply
T600S/R367-2	50	105	57±2	0.05	1, 2, 3, 4
TR50S/R368-1	110		62±2	0.10	1, 2
TR50S/R367-2	150		62±2	0.15	1, 2
T600S/R368-1	170		59±2	0.20	1, 2, 4, 6
	170_S				1, 2

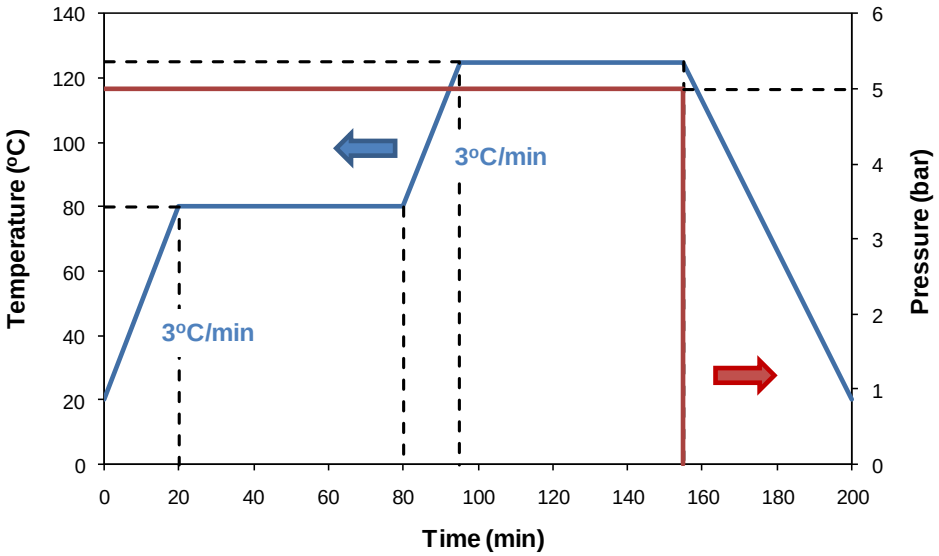

Figure 3.1: Curing cycle of the composite laminates used in this study.

3.2.2.Moisture absorption test

Firstly, the weight of each traveller coupon is measured to the accuracy of 1mg and recorded as "as-received" weight. The coupons are then heated in an oven at 70°C for approximately 18hours followed by the measurement of the dry weight after cooling down to room temperature. The oven heating process is performed to ensure that the fabrication-induced moisture is completely removed from the coupons. The corresponding weight is referred to as "oven-dry" weight.

All coupons are then immersed into an environmental chamber filled with demineralised water at 70°C. This temperature is the maximum value recommended by ASTM D5229 [225] to accelerate the ageing process for epoxy cured at 125°C. Measurements are carried out periodically to record the weight of the coupons and the corresponding exposure time until the moisture uptake saturation is reached. At least four coupons are prepared for each type of laminate.

3.2.3.Density and constituents' content measurement

The density measurement of the 170g/m^2 composite laminates is carried out using pycnometer. Specimens with the size of 30×10 mm^2 are prepared at 2, 4, 6, 8 and 16 plies. The density of 1-ply laminate is not determined due to its low weight that could easily cause significant error during the measurement. The pycnometer is filled with demineralised water and the density is determined using the balance at 1mg accuracy as well.

For constituents' content measurement, specimens at 4 and 8 plies are prepared at 30×30 mm^2. All specimens are firstly dried in an oven at 50°C for 2 hours and left to cool down to room temperature after that. Specimens are then sealed in an impermeable bag to prevent any additional moisture into the specimens before burning. Then, the muffle furnace is pre-heated at 500°C. Each specimen is placed in a desiccated crucible and is burned at 600°C for continuous two hours. This is as recommended by Procedure G in ASTM D3171 [226]. Weight before and after burning is measured using the same balance.

For both tests, at least three replicates are prepared for each series of specimens to obtain an average value.

3.3.Density and constituents' content

Figure 3.2 illustrates the density of the composite laminates at different number of plies. Results show that the average value of the density is slightly decreasing with the number of plies. Since the same prepreg is used, the decrement in the density should be attributed to the increment in the void amount at ply/ply interfaces, where the relative interface volume (interface volume over laminate volume) tends to a constant with increasing number of plies. Actually, the variation in the measured density is not significant. Moreover, the average values are falling within the upper and lower limits of the measured density at each ply number.

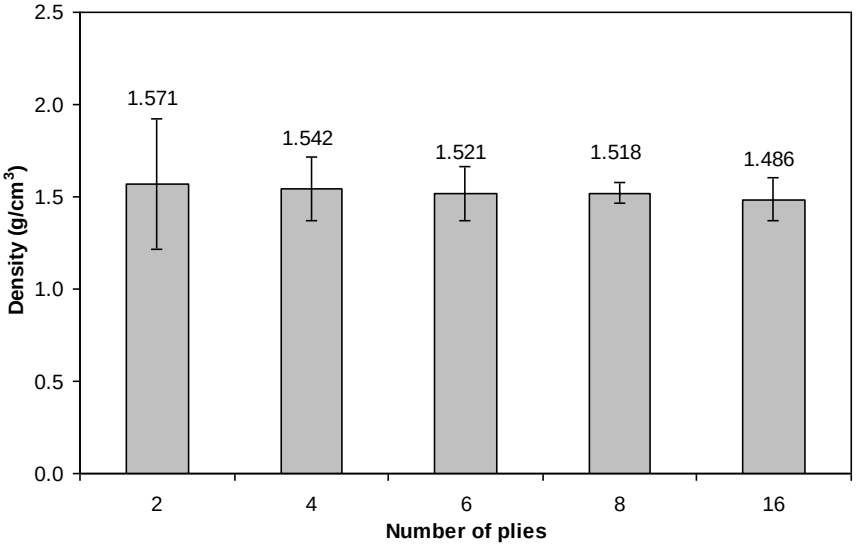

Figure 3.2: Variation of measured density with ply number of 170g/m^2 composite.

The measured fibre (V_f), matrix (V_m) and void (V_v) contents of 4- and 8-ply composites are shown in Table 3.2. The calculated fibre volume fraction agrees quite well with the manufacturer's given data (59±2%). This provides certain confidence level on the measured data. It seems that the void content increased slightly with the ply number. Negative void content for 4-ply laminate is probably due to experimental dispersion where its low weight increases the sensitivity to the variation during measurement. Hence, it is reasonably to be accepted as an average value. Similar observation has been reported by Bao and Yee [65, 91], where negative void content was obtained for low thickness composites. The variations in the measured composite density could be the reason for negative void content [91].

Table 3.2: Major physical properties of 170g/m^2 prepreg composite.

Ply number	Thickness (mm)	Density (g/cm^3)	V_f (%)	V_m (%)	V_v (%)
4	0.8	1.542±0.056	56.3±0.6	44.5±0.9	-0.8±0.3
8	1.6	1.518±0.070	56.4±0.2	42.4±0.2	1.2±0.1

According to Costa et al. [227], in fabric and unidirectional T300/F584 carbon/epoxy composites, a void content of less than 1.5% exhibited similar moisture absorption curves. Thomason [228] reported that the moisture uptake behaviour of several different types of E-glass/epoxy composites was similar to its neat resin at low void content (approximately 1%). When the void content became superior (approximately 1.4% and above), significant increment in the absorption rate and moisture content was notified. It is thus postulated that the initial difference in the void content measured in this study would have a minimal effect on the water uptake behaviour.

3.4.Moisture uptake behaviour in single-ply laminates at different thicknesses

Figure 3.3 illustrates the moisture absorption curves of all single-ply composites. The error bars refer to standard deviation values of 2σ at that respective moisture absorption level. Results indicate that for any composite, the moisture absorption varies linearly with $\sqrt{t}/h$ in the early stage and gradually decreases to a saturation level when the maximum moisture content in the material is reached. The decrement in the moisture content beyond the saturation could be attributed to the solubility of the material under hot-wet environment. Even the single-ply composites are not super-imposable, the experimental weight gain data could still be individually well fitted with the single-phase Fickian diffusion model (solid lines in Figure 3.3) using Equations (2.12) and (2.15). This suggests that the individual single-ply carbon/epoxy composite could still be assumed as a homogeneous material.

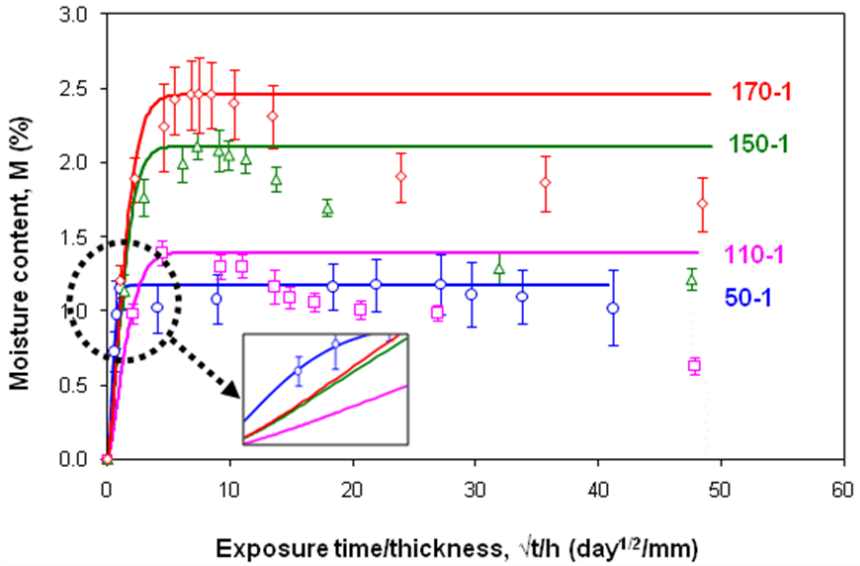

Figure 3.3: Moisture absorption curves of single-ply laminates made from the different prepregs having different thickness.

Table 3.3 displays the values of M_{m1} and D_z of all of the single-ply composites tested. Here, M_{m1} denotes the maximum moisture content only for single-ply composites. It is shown that M_{m1} and D_z are not constant, where the former increases with the ply thickness and the later seems to decrease with the ply thickness except for 110g/m^2 laminate.

Table 3.3: M_{m1} and D_z of all single-ply composites.

ρ (g/m^2)	M_{m1} (%)	D_z (10^{-7} mm^2/s)
50	1.18	29.38
110	1.40	2.71
150	2.11	3.54
170	2.46	3.09

The possible explanation of the variation of M_{m1} and D_z with laminate thickness follows two ways:

Hypothesis I: In reality, the diameter of both T600S and TR50S fibres is similar (≈7μm) and all laminates have approximately the same fibre volume fraction. Hence, the proportion of matrix, fibre as well as that of the interface should be practically the same for all single-ply laminates tested. If it can be considered that the quality of the matrix and the fibre/matrix interface of all four single-ply laminates are the same, the thickness effect on

water uptake behaviour should be attributed to non-Fickian absorption, because water uptake curves of single-ply composites are not super-imposable.

In fact, thickness effects on the moisture uptake behaviour have been highlighted in several published works. For example, to describe the anomalous moisture uptake behaviour in a rubber toughened epoxy adhesive (Araldite 2007) at 50^{o}C, Loh et al. [94] found that D_{zI} could be treated as constant at all humidity levels (81.2%RH, 95.8%RH and deionised water) and thicknesses (0.4, 0.8 and 2mm). However, since M_{mI} is not constant for all thicknesses at a particular humidity level, the initial stage of the reduced sorption curves are not the same at different thicknesses. This implies that even in the first stage, Fickian diffusion is not strictly followed. Besides, the authors reported that the maximum moisture content increased with the adhesive thickness. Similar observation was noticed for the moisture absorption behaviour of commercial epoxy mould compounds (EMCs) used in electronics packaging aged at 60^{o}C/85%RH and 85^{o}C/85%RH [95]. The authors described that the deviation of the curves indicates non-Fickian behaviour. Also, higher M_m was achieved at higher sample thickness. The coupling of diffusion and relaxation that contributes to non-Fickian behaviour was also reported to be thickness dependent elsewhere [229]. Similar phenomena in the specimens having different thickness but same material were even mentioned in the study of Shirell [230]. According to the author, the difference in the initial slope could indicate either non-Fickian behaviour or concentration dependent diffusivity according to the author.

Hypothesis II: Since the experimental data can be well fitted using Fickian equation at least in the first stage of the curves (before the postulated dissolution occurs), Fickian diffusion is believed to occur in each single-ply laminate. In this case, the change in water uptake behaviour should be provoked by different matrix behaviour and the interface quality in each laminate instead of the effect of thickness. This is reasonable because strictly speaking, these four prepregs cannot be viewed as the same material. Firstly, according to the datasheet provided by the manufacturer [231], R368-1 is a resin that is more tack than R367-2, where the polymer network in those resins would be different. The influence of the polymer nature on moisture absorption is described in Section 2.3(a). Secondly, although both carbon fibres are PAN fibres that the manufacturing process is the same, T600S is produced by Toray whereas TR50S is manufactured by Mitsubishi [232]. Generally, carbon fibres are recognised to be impermeable by water, although it was reported that free carbon fibres can absorb 0.02 wt% water [34]. However, the fibre/matrix interface quality is believed to be different when the same resin is reinforced by two different kinds of fibre. In fact, in addition to different ply thickness, none of the constituents combination of four different prepregs used in this study is the same. This is further convinced by the results obtained. For example, Figure 3.3 indicates that the initial slope of the curves is not the same, with no specific trend is observed. Furthermore, the calculated diffusivities vary at different thicknesses, which could suggest the dependence of diffusivity on certain parameters such as the resin type, fibre volume fraction of each prepreg and the quality of the fibre/matrix interface.

Moreover, it was reported that under moisture attack, the fibre/matrix interface would be degraded due to capillary action that allows rapid penetration of moisture between the fibre bundles and the matrix [230]. In composite materials, hygro-thermal stresses induced by the differential dilatation between the matrix and the fibre are mainly located at the interfaces [16]. Capillarity happens when water ingresses along the fibre/matrix interface and leads to cavities or micro-cracking through capillary action. Consequently, fibre/matrix interface debonds and crack propagates along fibre surfaces, and additional moisture transport takes place through these cracks.

The possibility of which hypothesis is more likely to occur in the carbon/epoxy prepregs used in this study will be further discussed in the next section.

3.5.Effects of ply/ply interface and total laminate thickness on moisture uptake behaviour

Figure 3.4 compares the moisture absorption behaviour of laminates with same thickness but different number of plies. It shows that for the same thickness, M_m increases with the number of ply. This observation suggests that Hypothesis II described in the previous section is more plausible. The use of Hypothesis II signifies independent water uptake behaviour of the single-ply composites made from different prepreg. Moreover, it is unable to describe the water uptake behaviour in multi-ply composites by Fickian law that always over-predicts the moisture absorption at the shoulder region. This non-Fickian observation was also reported in angle-ply graphite/epoxy laminates [64, 230, 233], woven carbon/bismaleimide composites (for short term ageing) [65] and AV119 epoxy adhesive [94]. Therefore, in non-Fickian case, the calculated D_z for the upper Fickian curves will have little or no physical significance [28] .

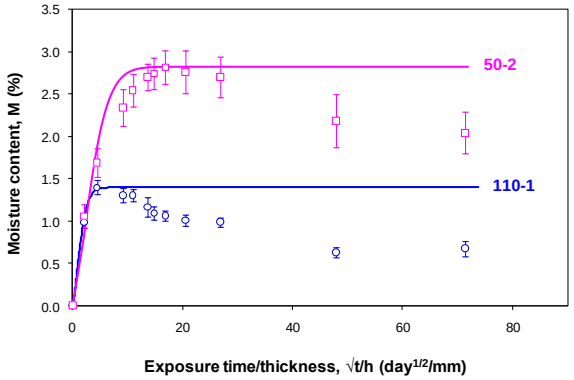

(a) Laminate thickness = 0.10mm

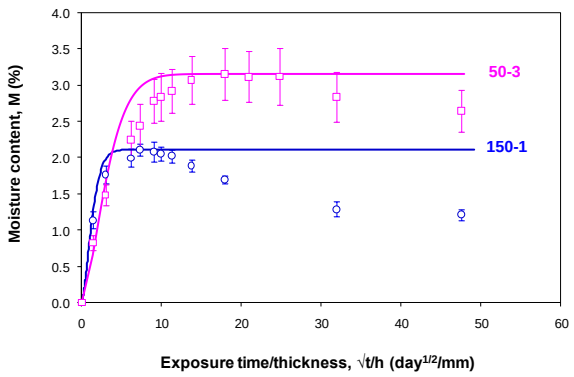

(b) Laminate thickness = 0.15mm

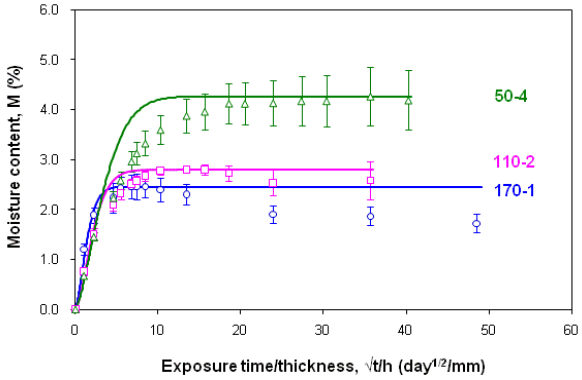

(c) Laminate thickness = 0.20mm

Figure 3.4: Moisture absorption behaviour of laminates with same thickness but different number of plies.

To give an overall view on the effects of ply and laminate thickness, Table 3.4 illustrates the moisture uptake behaviour of each type of the prepreg at various thicknesses/number of plies. It is apparent that M_m increases with both number of ply and single ply thickness.

Table 3.4: Variation of M_m (%) with laminate thickness of each type of prepreg.

Ply / Density	1	2	3	4	6
50	1.18	2.82	3.15	4.26	-
110	1.40	2.80	-	-	-
150	2.11	3.65	-	-	-
170	2.46	5.88	-	7.36	8.90
170_S	-	6.19	-	6.81	-

For the laminates made from the same prepreg, when the thickness of the multi-ply laminate changes the reduced sorption curves are not super-imposable, hence non-Fickian behaviour can be identified [63]. In order to understand non-Fickian diffusion mechanisms in the composites tested, firstly, effect of the number of ply/ply interface on water uptake behaviour is investigated by testing the specimens with different number of ply/ply interface but the same equivalent thickness. For example, a coupon made from 2 plies with one surface completely sealed has the same equivalent thickness to that from 4 plies with two free surfaces, but the former has one ply/ply interface, and the later has three interfaces.

According to the results illustrated in Figure 3.5, the water uptake behaviour is nearly the same in both unsealed and sealed coupons. This suggests that the ply/ply interface is tiny enough compared to the entire laminate that its influence to the overall water uptake behaviour in the composites is negligible.

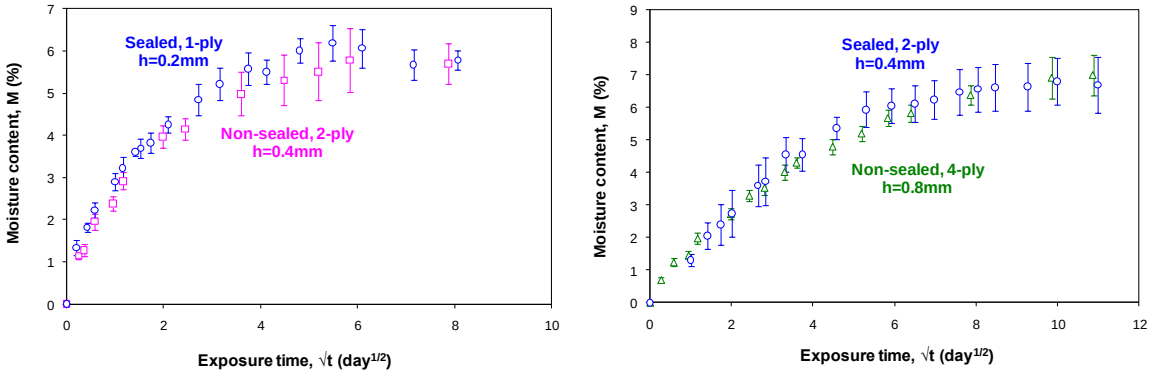

(a) Two-ply equivalent laminate (b) Four-ply equivalent laminate

Figure 3.5: Comparison of two-sided and one-sided moisture uptake behaviour.

Hence, the departure of moisture absorption from classical Fickian diffusion model should be due to other mechanisms. It is generally recognised that the weight gain due to moisture exposure is dependent on the temperature, relative humidity, material, fibre volume fraction, specimen dimensions, fibre cross-sectional shape, interphase dimensions, transport properties and types of ageing medium [8, 234]. As described in Section 3.4, the single-ply laminates made from different prepregs are not actually the same material according to the Hypothesis II. However, the laminates made from the same prepreg exhibit thickness effect due to non-Fickian absorption. In many cases, absorbed penetrant tends to induce changes to the material through relaxation and swelling, polymer-penetrant interaction, chemical degradation, internal stresses and damage [8]. As described in Section 2.2, anomalies are observed when the diffusion and relaxation rates are comparable [12]. According to Blackadder and Keniry, non-Fickian moisture sorption behaviour is highly dependent on the internal stresses and relaxation rates [235]. Internal stresses are induced when swelling occurs. Swelling by hygrothermal stresses is an effect of volumetric changes due to moisture content

as a consequence of rearrangement of the marco-molecules of the polymer to relieve the stresses and is independent of the thermal expansion [8, 29]. As the water molecules diffuse into a glassy polymer, the outer surfaces (swollen region) tend to expand and increase the area in the direction of diffusion. However, the underlying region is not or less swollen. This causes two separate effects:

Firstly, the outer sides are compressed by the inner region (or the outer region exerts tensile stress on the inner region). At the same time, the enhancement in the polymer segmental motions (polymer-penetrant interaction) reduces the relaxation times [236]. The polar water molecules interact with the polymer network and form hydrogen bonds with hydroxyl groups in the polymer chain by altering the inter-chain hydrogen bonding which subsequently interrupt the cross-linking in the polymer network, where the inter-segmental hydrogen bond length is augmented [29]. It was reported that polymers with fewer polar groups reduce moisture sensitivity and hence the M_m and T_g decrease with increased cross-linking [13]. According to Long and Thompson [30], anomalous diffusion is accentuated in the polymer that exhibits large chain-chain interactions due to small size, regular spacing and polar nature of the hydroxyl side groups. Liquid molecules that combine with the polymer molecules in the glassy state could become part of the glassy structure when equilibrium is achieved [31]. This binding effect is also known as dual-mode sorption, where some solvent molecules could diffuse freely within the polymer while others are restrained by the interaction with polymer molecules. The corresponding chemical reaction is called hydrolysis. The interaction between water and polar polymers such as epoxy is complex [18]. Generally, in a polymer, the level of the hydrolysis depends on the number of the groups available in the polymer macromolecular chains that could react chemically with water molecules. The interaction level of the penetrant-polymer pair and the interaction effect on the polymer network will affect the amount of moisture absorbed in a solvent-solute system [8]. Diamant et al. [32] suggested that higher levels of cross-linking might remove possible interaction sites, and additional linking could retard the equilibration of the polymer due to the increased difficulty for the water molecules to access to the polymer sites.

As swelling stresses lead to the change in the polymer network structure, the polymer chains fail to self-adjust fast enough at the presence of the penetrant molecules (which implies long relaxation times) that the hygrothermal stresses do not decay rapidly especially under extensive swelling. Therefore, when the penetrant molecules penetrate into the polymer, the polymer chains fail to respond instantaneously to the change in the concentration that tends to change their physical conditions. Since the stresses in the underside region are not relaxed instantaneously, the expansion will be restricted and the outer region is thus stretched and the accessibility of the polymer to the penetrant is further enhanced [37]. It is recognised that swollen layers are in the rubbery state and the swollen phase is comparatively rigid and deformation resistance, which signifies high modulus of the swollen layer [19]. The level of expansion will reach constant when the compressive stress by the lower surface is constant with time. In other words, the stress relaxation rate determines the rate of attainment of a constant degree of expansion at the upper surface [28].

Furthermore, under continuous swelling process, micro-cracks could have developed. Swelling is a reversible effect but the damage caused by significant swelling is irreversible. Damage is likely to increase the relaxation rate at the boundary between swollen and unswollen regions [7]. Moreover, solvent crazing-stress cracking leads to local weakening effect and clustering of solvent molecules [10, 42]. However, micro-cracking also leads to loss of material that enables moisture to further penetrate into the material. Hence, the net effect could be absorption or desorption. When the weight gain by the absorbed moisture is

more significant than the loss of material, the overall weight of the coupon is augmented. Otherwise, the net weight decreases [234].

Secondly, the surface concentration caused by swelling does not reach the true equilibrium immediately [235]. Consequently, the sorptive capacity will be reduced [237]. This is why the shoulder region of non-Fickian diffusion behaviour is always over-predicted using Fickian law. In this study, swelling is obvious after prolonged ageing period.

In addition, similar to the discussion for single-ply composites, the non-Fickian response in composite materials is also attributed to the low cross-link density region surrounding the fibres that generates a preferential diffusion path for the water molecules [34]. The preferential paths may not alter the diffusion mechanisms but affect the uptake curve.

Besides, mild thermal shock could be caused during the weight measurement of the specimens, leading to cavitation mechanism [230]. Surface cracks and subsurface micro-voids are thus formed, that enable the moisture to contain in the material [238].

In this study, the non-Fickian in multi-ply composites is not likely to be caused by concentration- or time-dependent diffusivity, which is in accordance to the discussion by Bao and Yee [65] using the time-dependent diffusivity model mentioned in Section 2.4.2.

3.6.A two-phase diffusion model to describe non-Fickian diffusion

Based on the discussion in the previous sections, moisture absorption is influenced by the thickness of laminates. Any single-ply composite studied in this work is found to follow Fickian law although M_{m1} and D_z for each material are different. As for multi-ply composites, results show that the moisture diffusion behaviour can be divided into two stages. Identical behaviour is displayed by coupons of different thicknesses at the initial stage. At the later stage, distinctively different behaviours are shown by the laminates. This observation indicates that Fickian diffusion model can only describe the moisture uptake of the laminates during Stage I. It is thus supposed that water uptake process of carbon/epoxy composite laminates can be described in general by a two-phase diffusion model. The total weight gain at any instant of time $M(t)$, is taken as the sum of the moisture uptake by Fickian diffusion $M_I(t)$, and by non-Fickian diffusion $M_{II}(t)$, which can be described as:

$$M(t) = M_I(t) + M_{II}(t) \tag{3.1}$$

In this study, it is proposed that:

$$\begin{aligned} M(t) &= \phi M_m G(t) + (1-\phi) M_m W(t) \\ &= \phi M_m \left\{ 1 - \exp\left[-7.3 \left(\frac{D_z t}{h^2} \right)^{0.75} \right] \right\} + (1-\phi) M_m \left[1 - \left\{ \exp - \left[\left(\alpha \left\langle t - t_o \right\rangle \right)^{\beta} \right] \right\} \right] \end{aligned} \tag{3.2}$$

where ϕ is the single- to multi-ply maximum moisture content ratio, t_o refers to the exposure time of the initiation of non-Fickian water absorption (Stage II); α and β are material parameters, which have to be determined by interpolation of experimental data. $\langle \cdot \rangle$ is the Macaulay bracket which signifies the second term equals to zero when $t<t_o$. This is based on the assumption that at Stage I, the water molecules are free and Fickian diffusion dominates (the first term). When more moisture penetrates into the specimens, the diffusion slows down due to swelling and comparable relaxation rate that more water molecules are bound to the polymer network. Hence, non-Fickian diffusion (the second term) takes place. The delay term (t-t_o) signifies that non-Fickian effect is negligible at the initial stage. A sample plot of the distribution of the Fickian, non-Fickian and total moisture absorption is illustrated in Figure 3.6 below.

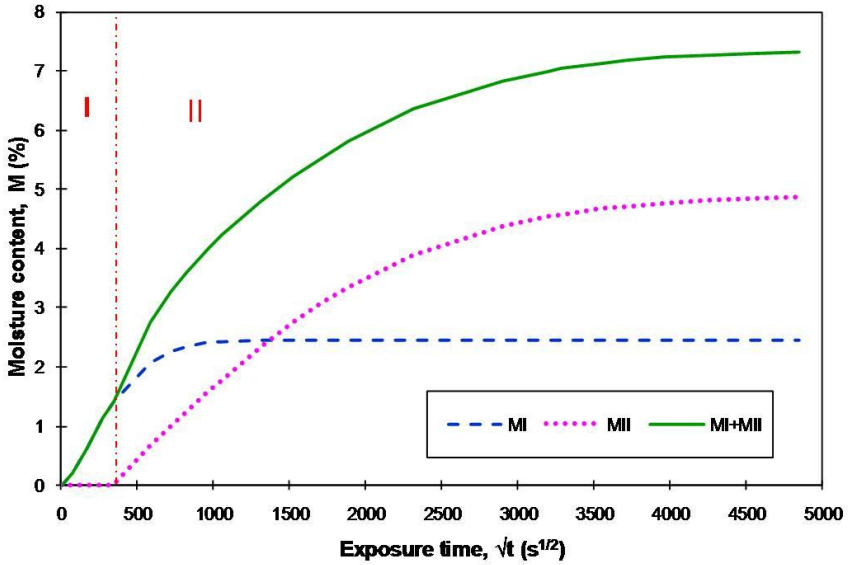

Figure 3.6: Distribution of M_I, M_{II} and $M(t)$ of the proposed two-phase model.

Since composite laminate coupons for all thicknesses follow Fickian diffusion behaviour during Stage I, both D_z and ϕM_m are assumed to be constants. They can be determined from the data obtained on single-ply composite coupons. It means that the parameters D_z is the diffusivity of single-ply composite and $\phi M_m = M_{m.1}$, while M_m and ϕ are dependent of the thickness (number of ply) of the laminate.

It is to be mentioned that this two-phase model is very similar to SDF model (Equation (2.45)) by Ameli et al. [70], if the SDF model is written in the approximated form:

$$M = M_{mI}\left\{1-\exp\left[-7.3\left(\frac{D_{zI}t}{h^2}\right)^{0.75}\right]\right\} + H(t-t_I)M_{mII}\left\{1-\exp\left[-7.3\left(\frac{D_{zII}(t-t_I)}{h^2}\right)^{0.75}\right]\right\} \qquad (3.3)$$

Ameli et al. [70] argued that SDF model is a more general two-stage moisture uptake model that relates the physical significance of Fickian diffusion and Langmuir model. However, in the current model, since the second term accounts for non-Fickian diffusion, it is firstly supposed that the exponent β does not necessary to be equal to 0.75. In addition, this studies focuses on the effects of laminate thickness on the moisture uptake behaviour, which was not considered in [70].

Figure 3.7 presents the results obtained using the current model, where excellent correlations is shown with the experimental data of multi-ply composites except slight initial slope deviation in the initial stage for 50-2 laminate. It is to be mentioned that since D_z and M_{m1} are always fixed at each prepreg at all thicknesses, PDF (Equation (2.41)) and Langmuir (Equation (2.35)) models are not able to fit well the non-Fickian behaviour in any case.

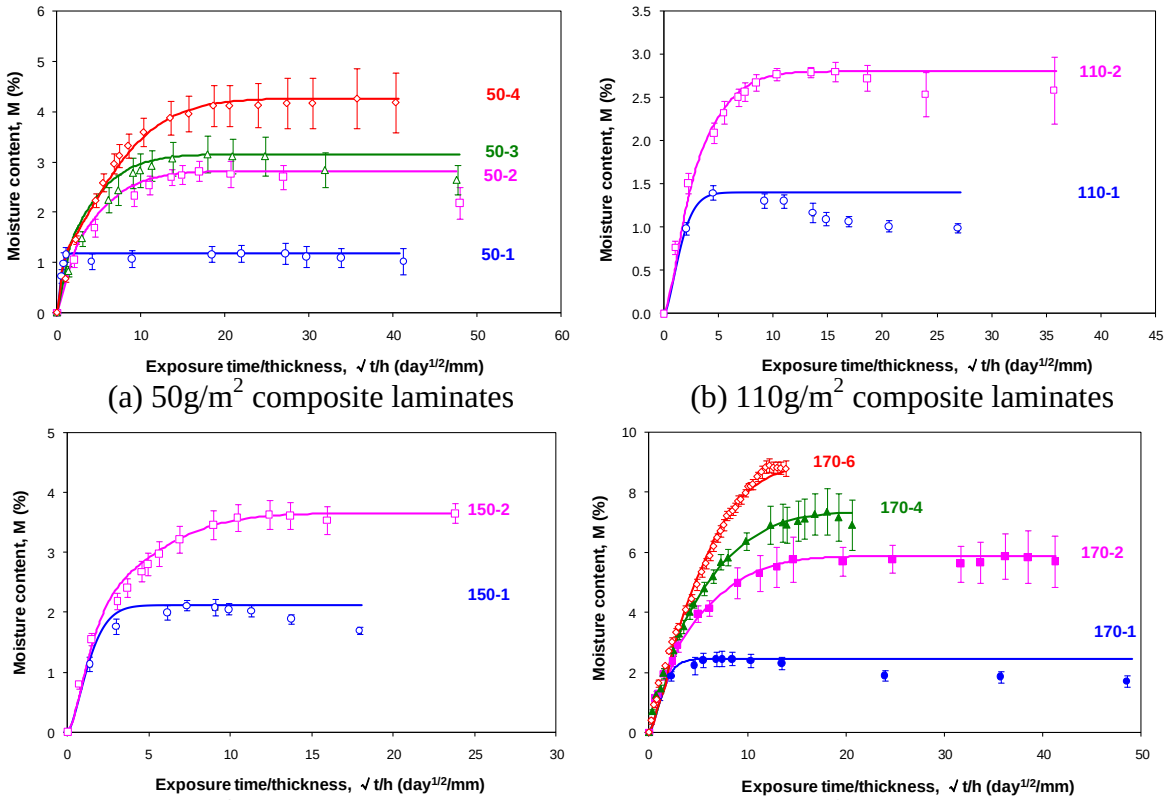

(a) 50g/m^2 composite laminates (b) 110g/m^2 composite laminates

(c) 150g/m^2 composite laminates (d) 170g/m^2 composite laminates

Figure 3.7: Moisture absorption curves of composite laminates made from different prepregs.

Table 3.5 to Table 3.8 summarise all the values of ϕ, α, β and t_o of each type of prepreg at different number of plies. Results indicate that M_m increases with both number of ply and ply thickness. Besides, it is observed that regardless the ply thickness, the values of ϕ are similar at the same number of plies. α decreases with number of plies and ply thickness, whereas β falls within the range of 0.65-0.86. In addition, t_o increases with ply thickness and number of plies. This is in accordance to the hypothesis in the proposed model that if the laminate is sufficiently thick, the moisture uptake tends to exhibit Fickian's behaviour (since t_o becomes large). The difference of t_o in one-sided and two-sided specimens at four plies could be due to the difference in the interval of measurement.

Table 3.5: Variation of ϕ with laminate thickness of each prepreg type.

Ply / Density	1	2	3	4	6
50	1	0.42	0.37	0.28	-
110	1	0.50	-	-	-
150	1	0.58	-	-	-
170	1	0.42	-	0.33	0.28
170_S	1	0.40	-	0.36	-

Table 3.6: Variation of α (10^{-7} $mm^{-1}s^{-1}$) with laminate thickness of each prepreg type.

Density \ Ply	2	3	4	6
50	321.28	195.33	43.17	-
110	121.85	-	-	-
150	36.82	-	-	-
170	13.88	-	3.52	1.86
170_S	18.25	-	6.70	-

Table 3.7: Variation of best-fitted β with laminate thickness of each prepreg type.

Density \ Ply	2	3	4	6
50	0.72	0.65	0.74	-
110	0.86	-	-	-
150	0.85	-	-	-
170	0.79	-	0.75	0.85
170_S	0.71	-	0.80	-

Table 3.8: Variation of t_o (hours) with laminate thickness of each prepreg type.

Density \ Ply	2	3	4	6
50	1	1	1	-
110	5	-	-	-
150	5	-	-	-
170	8	-	33	95
170_S	8	-	48	-

To examine the sensitivity of β, the graphs are plotted by fixing the parameter at 0.75. The comparison in between the plots are described in Figure 3.8 for 50-3 and 110-2 coupons as those two laminates are with β at the extremes (0.65 and 0.86 respectively). Results show that β = 0.75 (without varying α) is a good choice to fit the experimental data with the lowest R^2 = 0.9646. This adds one similarity to the SDF model by Ameli et al. [70] (see the simplified form in Equation (3.3)). However, it is to be emphasised that in the studies by Ameli et al., SDF model was applied to adhesives aged at different temperature and humidity levels. The application of the model to the moisture absorption at different thickness was not studied. The distinction of the current study is the generalisation of the model with respect to the laminate thickness/number of plies.

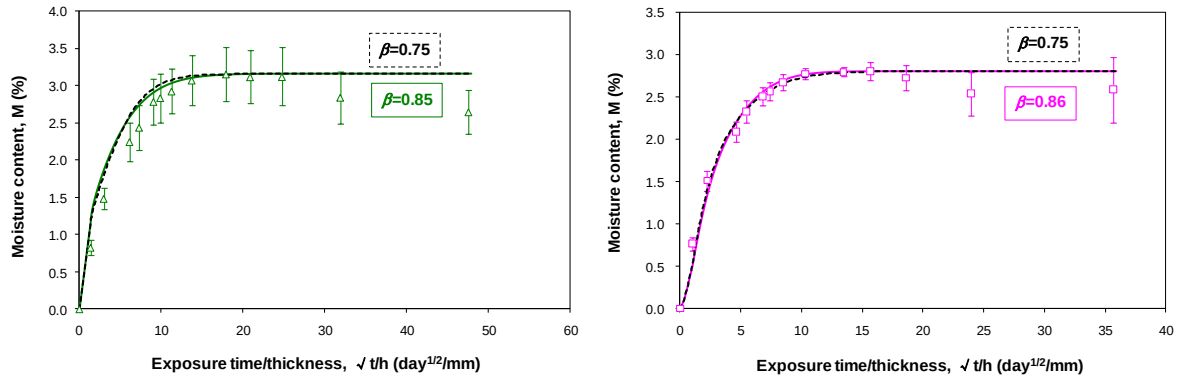

(a) 50-3 laminate (b) 110-2 laminate

Figure 3.8: Comparison of curve-fitting using best fitted β and β = 0.75.

Inspired by the simplified SDF model expressed by Equation (3.3), α could be represent as $7.3^{4/3}\cdot D_{zII}/h^2$. Based on this hypothesis, the values of D_{zII} based on the data from Table 3.6 are displayed in Table 3.9. If this postulation is true, Table 3.9 shows that for all prepregs, D_{zI} is at least one order higher than D_{zII}. This could imply that Fickian diffusion dominates in the prepregs. A one or two order higher in D_{zI} as compared to D_{zII} was also found when applying SDF model to describe the moisture uptake behaviour in epoxy adhesives [70], PDF model in epoxies [94-95] and carbon/bismaleimide composites [65], and DDF model in epoxy adhesive [99]. For more detailed information on the moisture absorption mechanisms, analysis such as deuterium nuclear magnetic resonance (NMR) studies as described in [67, 85] needs to be carried out.

Table 3.9: Calculated D_{zII} (10^{-8} mm/s) using the data of α.

Density \ Ply	2	3	4	6
50	2.27	3.10	1.22	-
110	3.44	-	-	-
150	2.34	-	-	-
170	1.57	-	1.59	1.89
170_S	2.06	-	3.03	-

Since there is no specific trend in D_{zII}, the next question is: can D_{zII} for each prepreg be treated as a constant value? If it can, the most convenient way is to take 2-ply D_{zII} as the fixed value for all thicknesses. This is because if it is true, then the water uptake behaviour at any thickness can be predicted using only single-ply and double-ply laminates. To verify this, 170s-2, 170s-4, 170-4 and 170-6 are plotted at β=0.75 and D_{zII}=1.57×10^{-8} mm/s. Figure 3.9 shows that this approach is not always applicable, where significant discrepancy is observed in 170s-4 and 170-6 laminates. Hence, fixing D_{zII} using 2-ply laminate data is not a good approach.

Since the approach fixing D_{zII} at 2-ply laminate does not work well, perhaps fitting the trend of α can be attempted (since it decreases with number of plies, see Table 3.6). Using the limited α data of 170s-2, 170-2, 170s-4, 170-4 and 170-6, Figure 3.10 shows that α is decreasing exponentially with the number of plies, with fitted equation of α=45.81exp(-0.55n), where n refers to the number of plies. This seems to be a good approach to characterise the variation of α with respect to the number of plies. Furthermore, the variation of t_o with the number of plies for 170g/m^2 composite laminates is also illustrated, see Figure 3.11. A power law is found to fit well the data, with t_o=1.66$n^{2.27}$.

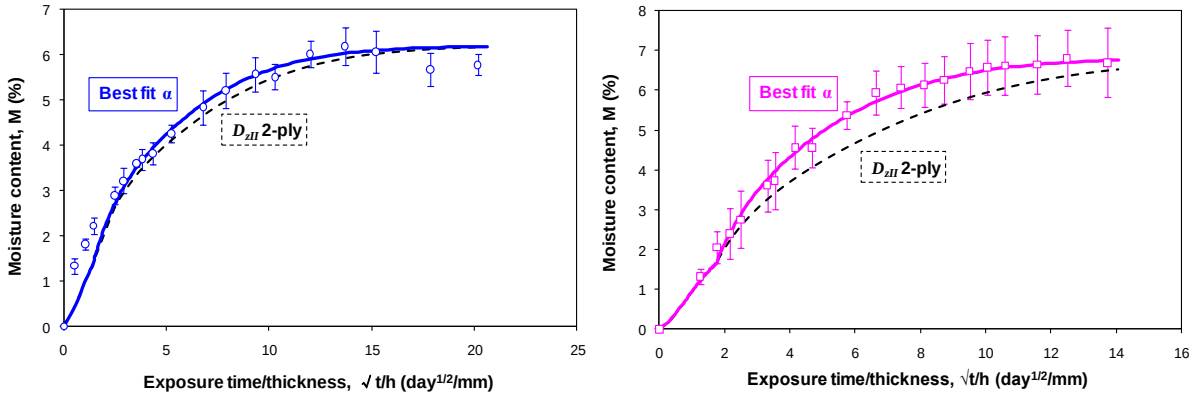

(a) 170s-2

(b) 170s-4

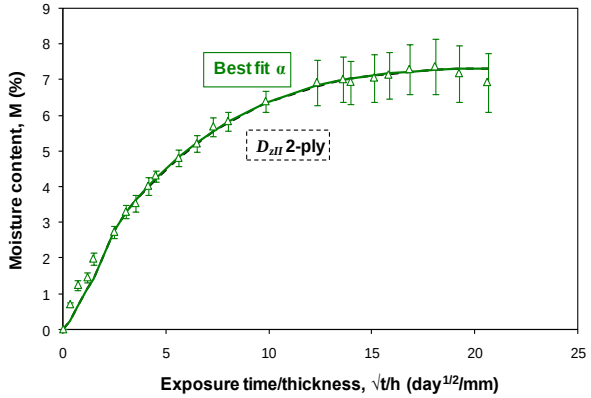

(c) 170-4

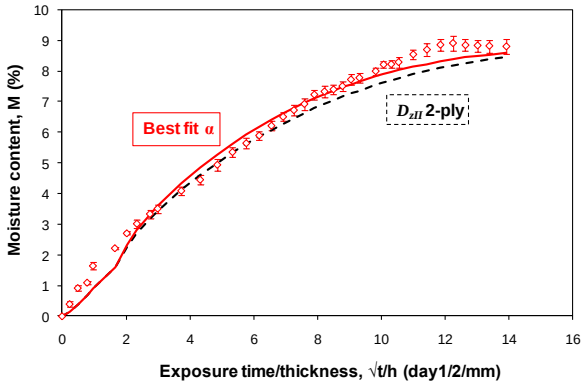

(d) 170-6

Figure 3.9: Refitting the moisture absorption curves using β=0.75 and D_{zII}=1.57× 10^{-8} mm/s.

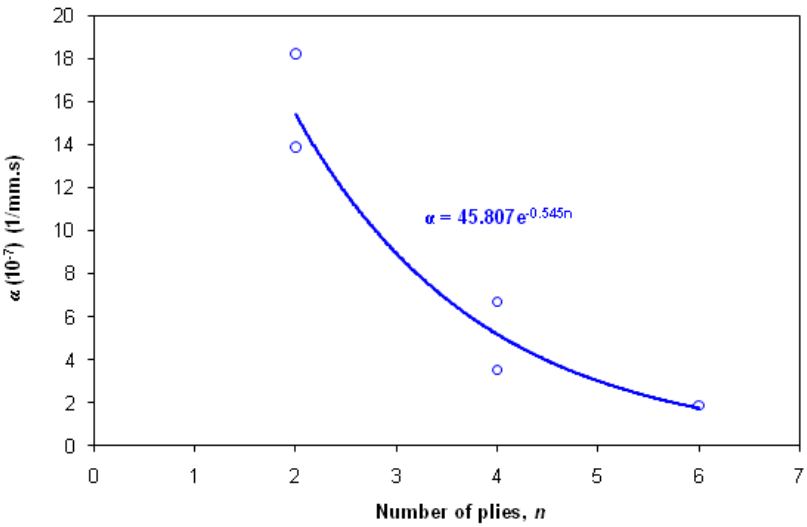

Figure 3.10: Experimental and fitted α relationship with number of plies for 170g/m^2 composite laminates.

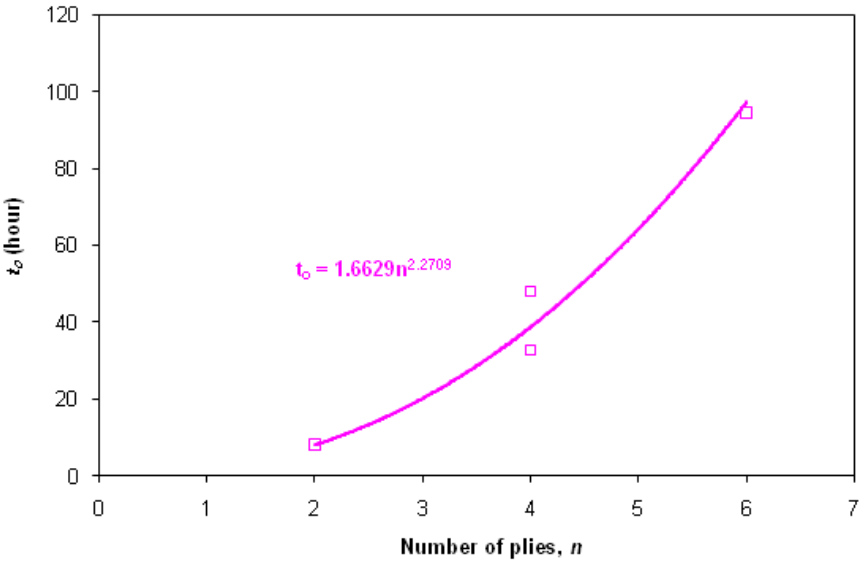

Figure 3.11: Experimental and fitted t_o relationship with number of plies for 170g/m^2 composite laminates.

Based on the previous discussion, in order to use the two-phase model proposed in this study, the following steps are to be followed:

a. Ageing of 1-ply, 2-ply and 4-ply specimens of up to water saturation;
b. Taking $\beta=0.75$ and $\phi M_m=M_{m1}$
c. Fitting the experimental water absorption data to obtain M_m, α and t_o for the specimens at each thickness;
d. Interpolating the fitted values by a suitable law. For example, in this study: bilinear for M_m, exponential for α and power for t_o

The detail steps on how to implement this two-phase diffusion model are illustrated in Appendix A. Anyhow, this fitting method needs to be confirmed by much more experimental data.

3.7.Prediction of moisture absorption at larger thickness

Based on the previous discussion, the two-phase model is used to predict the moisture absorption in 170g/m^2 8-ply laminate. Firstly, the value of the maximum moisture content M_m and the parameter ϕ for 8-ply laminate are estimated through extrapolation (saturation is not attained even after one year of ageing). The variation of M_m and ϕ with laminate thickness h (or number of plies) is illustrated in Figure 3.12. It is observed that M_m increases with h while ϕ decreases with h. The rate of change in both of them is more significant from single to 2-ply laminate, and it seems to vary linearly for multi-ply laminates. With this assumption, it is predicted that the maximum moisture concentration for 8-ply coupons will reach 10.5%, which gives ϕ=0.23. It is interesting to see that actually it is sufficient to measure M_m, and the value of ϕ can be determined by imposing $\phi M_m \equiv M_{m1}$. It means the first term in the current model, $M_1(t)$ can be completely determined by the experimental data measured on single-ply composite. The value of ϕ can be estimated from the measurement of M_m for multi-ply laminates.

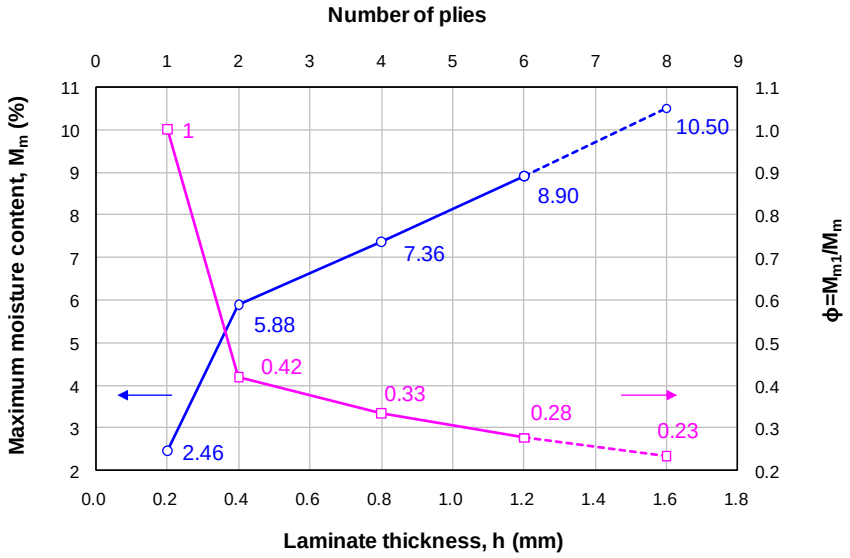

Figure 3.12: Variation of maximum moisture content M_m and maximum moisture content ratio ϕ with laminate thickness.

Secondly, capability of the two-phase model to predict moisture uptake behaviour of thicker carbon/epoxy composite laminate is assessed using measured data on moisture absorption for 8-ply laminate. Using the predicted trends of α and t_o illustrated in Figure 3.10 and Figure 3.11, respectively, the predicted values for 8-ply laminate are $\alpha=0.59\times10^{-7}mm^{-1}s^{-1}$ and t_o=187hours (t_o is measured as 190 hours from the experimental data). With β=0.75, the predicted curve is plotted in Figure 3.13 as dotted line. The best fitted curve is also shown (in solid line), with $\alpha=0.58\times10^{-7}mm^{-1}s^{-1}$ and β=0.84. Both curves show reasonably good prediction considering the phenomenological nature of the current model. Discrepancies between predicted and measured data could be due to several reasons. The predicted absorbed moisture level in the coupons represents an average value. However, the expected high local gradient of absorbed moisture at laminate interfaces is not adequately represented by the average value. In addition, effects of processing-induced non-uniform distribution and size of voids throughout the laminates by swelling on local moisture content should be quantified and incorporated into the model.

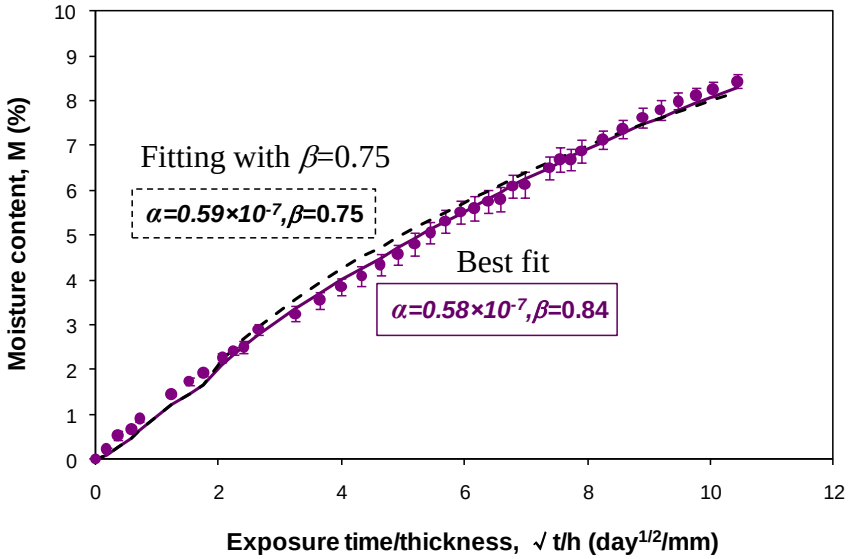

Figure 3.13: Experimental and predicted curves of 8-ply laminate.

3.8.Moisture concentration distributions across the specimen's thickness

Firstly, to illustrate moisture concentration that follows Fickian diffusion law, the concentration distribution of 170 g/m^2 single-ply composite is plotted at various time levels using Equation (2.4) and is shown in Figure 3.14. The MATLAB code for Fickian concentration distribution is shown in Appendix B1. It can be seen that the moisture concentration is initially low at the centre of the laminate, and becomes relatively uniform after approximately 18hours of continuous absorption, which corresponds to 34% of the saturation time (≈53hours).

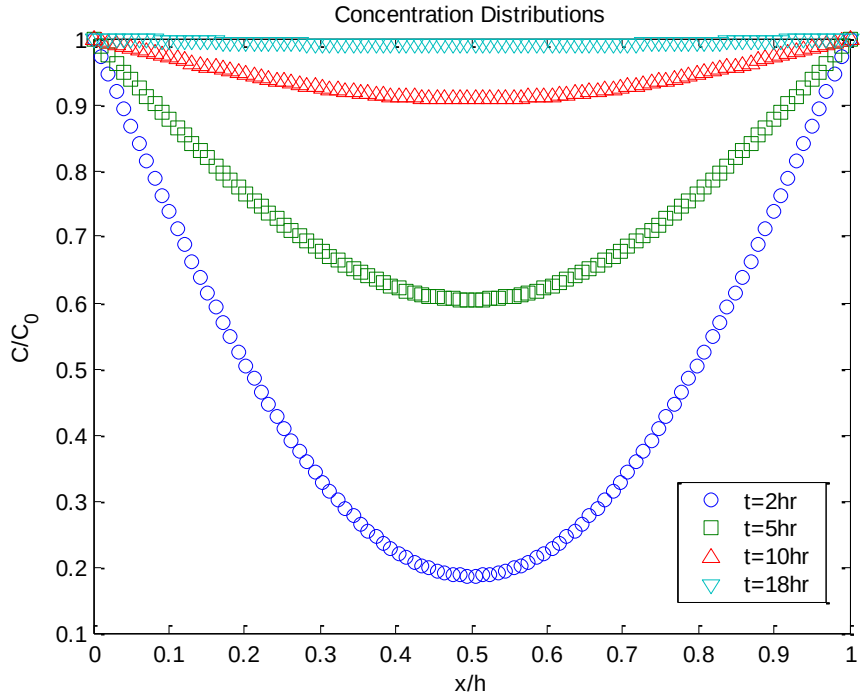

Figure 3.14: Concentration distributions of 170 g/m^2 single-ply composite.

Similar to the SDF model [70], the concentration distribution (with the absence of the initial moisture concentration) could be modelled using the following equation:

$$\frac{c(x,t)}{c_m} = \phi\left\{1-\frac{4}{\pi}\sum_{j=0}^{\infty}\frac{1}{(2j+1)}\sin\frac{(2j+1)\pi z}{h}\exp\left[-\frac{(2j+1)^2\pi^2 D_{zl}t}{h^2}\right]\right\}+ \\ (1-\phi)\left\{1-\frac{4}{\pi}\sum_{j=0}^{\infty}\frac{1}{(2j+1)}\sin\frac{(2j+1)\pi z}{h}\exp\left[-(2j+1)^2\pi^2\alpha\langle t-t_o\rangle\right]\right\} \tag{3.4}$$

A sample plot of 170g/m^2 4-ply composite is shown in Figure 3.15 and the corresponding MATLAB code is shown in Appendix B2. It is found that uniform concentration across the thickness is reached at comparatively fast interval. From the experimental water absorption data, 4-ply composite reaches saturation after 210 days of immersion, however, the prediction plotted in Figure 3.15 shows that uniform concentration is attained after 20 days of immersion, which is only approximately 10% of its saturation. This implies that even the moisture ingression is non-Fickian that the exposure time to reach saturation will be much longer; the concentration profile through the specimen thickness is still uniform [239]. Hence, beyond certain immersion period, the measured moisture content, *M* at different interval is reasonable to be treated as the average value over the whole laminate

thickness. Thus, the results from mechanical testing are also representing the average properties of the entire laminate.

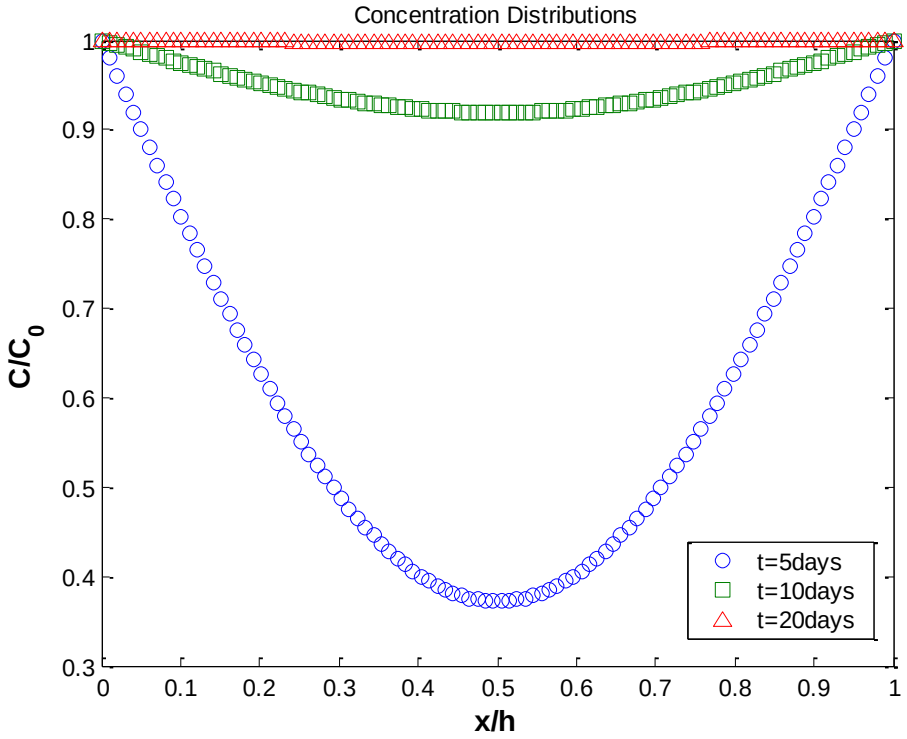

Figure 3.15: Concentration distributions of 170g/m^2 4-ply composite at various time levels.

3.9.Summary

This chapter discusses the water uptake behaviour of carbon/epoxy laminated composites at various thicknesses has been studied. Based on the results, it is summarised that:

i. The moisture ingression behaviour of the single-ply composite at all thicknesses follows the single-phase Fickian diffusion model;

ii. The maximum moisture content, M_m increases with the laminate thickness;

iii. Anomalies are observed in all multi-ply composites, which is believed to be combined effects of swelling (caused by internal stresses), relaxation rates, chemical binding of water molecules to the polymer network and damage;

iv. For multi-ply composite laminates, the average absorbed moisture content could be predicted well using the two-phase model proposed in this study which is expressed as:

$$M(t) = \phi M_m G(t) + (1-\phi) M_m W(t)$$
$$= \phi M_m \left\{1 - \exp\left[-7.3\left(\frac{D_z t}{h^2}\right)^{0.75}\right]\right\} + (1-\phi) M_m \left[1 - \left\{\exp - \left[\left(\alpha \langle t - t_o \rangle\right)^{\beta}\right]\right\}\right]$$

v. For 170g/m^2 composite laminates, the parameter α decreases exponentially with the laminate thickness and can be described using α=45.81exp(-0.55n), whereas t_o shows an increasing manner and is well fitted using a power law written as t_o=1.66$n^{2.27}$. As for β, it could be treated as a constant value of 0.75;

vi. The two-phase diffusion model predicts well the water uptake behaviour of 8-ply laminate;

vii. Based on experimental data on the carbon/epoxy composites, the parameters in the current model can be determined in an approximate manner to save the experiment time. It consists of

a. Ageing the specimens of 1-ply, 2-ply and 4-ply up to water saturation;
b. Taking $\beta=0.75$ and $\phi M_m=M_{m1}$
c. Fitting the data to obtain M_m, α and t_o for the specimens of each thickness;
d. Interpolating the fitted values by a suitable law:

For example: bilinear for M_m, exponential for α and power for t_o

This fitting method needs to be confirmed by much more experimental data. For example, moisture absorption tests could be carried out at different relative humidity and temperature levels. If non-Fickian diffusion behaviour is still observed at some or all environmental conditions, the applicability of the two phase diffusion model proposed in this study can thus be further verified.

viii. The moisture concentration through the thickness reaches a uniform level comparatively fast. Thus, beyond certain immersion period, the calculated moisture content, M is reasonable to be taken as the average value across the entire laminate thickness.

CHAPTER 4. MOISTURE EFFECTS ON ELEMENTARY AND INTERFACE PROPERTIES OF CARBON/EPOXY COMPOSITES

4.1.Introduction

This chapter summarises the effects of the moisture on the mechanical properties (longitudinal, transverse, shear and interface) of T600S/R368-1 carbon/epoxy composite. The variations in the properties are fitted using two different residual property models. The interface properties of unidirectional vacuum-bagging fabricated and multidirectional hot-press fabricated laminates are also presented. Finite element simulations are carried out on all fracture tests to analyse the delamination behaviour. To capture the fibre bridging behaviour in mode-I delamination case, a linear-exponential law is proposed to describe the traction-separation relationship. Within acceptable difference, the proposed bridging law is found to predict comparatively well the force-displacement response of the double cantilever beam (DCB) specimens.

4.2.Experimental details

All mechanical tests in this study are carried out only on the composite plates prepared from T600S/R368-1 prepreg. For tensile testing, laminates using two different stacking sequences are prepared: $[0]_8$ and $[\pm45]_{2S}$. To measure the fracture toughness, delamination tests are performed on unidirectional and multidirectional quasi-isotropic quasi-homogeneous (QIQH) laminates. Their stacking sequences are $[0_8//0_8]$ and [0/45/90/-45/90/-45/45/-45/0/90/0/45/0/45/-45/45/90/0/90/-45/90/-45/0/45//0/45/90/-45/90/-45/45/-45/0/90/0/45/0/45/-45/45/90/0/90/-45/90/-45/0/45] [240], respectively. Crack is introduced by inserting a Teflon film of 15μm thick at the mid-thickness (indicated as //). It is worth to note that the choice of this specific QIQH stacking sequence has actually some essential advantages:

a. The crack will grow at ply/ply interface. Herein, the delamination behaviour could be quite different to that of [0//0] due to fibre orientation effect. The investigation of the response of [0//45] interface to crack growth is of great importance in this study, because it represents the only interface between any two plies in the parent plate used in the repaired system studied in this work (to be discussed in Chapter 6 and Chapter 7);

b. For the entire laminate as well as any 24-ply arm separated by the insert, the stiffness matrices A_{ij}, D_{ij} and B_{ij} are not only always the same and independent of the loading direction, but also the same stiffness in tension and in bending at any direction, that means $A_{ij}/h \equiv 12D_{ij}/h^2$ where h denotes the thickness of one arm;

c. Moreover, the non-dimensional ratio $D_{12}^2/(D_{11}D_{22})$ is kept low (0.1036) to minimise the Poisson's effect;

d. Even the laminate is not symmetric, the coupling stiffness matrix **[B]** and the entries A_{16}, A_{26}, D_{16} and D_{26} in in-plane **[A]** and bending **[D]** stiffness matrices are eliminated. This avoids the perturbation on the fracture modes during delamination tests. In other

words, pure mode I, under double cantilever beam (DCB) loading and pure mode II under end notched flexure (ENF) loading can be ensured.

The curing cycle of all the laminates is the same as described in Section 3.2.1. In addition, to compare the effects of different fabrication techniques, $[0_8//0_8]$ composite plates are also fabricated using vacuum-bagging technique at 125^{o}C for 155 minutes.

For ageing tests, the composite plates with at least 250×100mm^2 size are sealed at the edges with aluminium foil and immersed in demineralised water at 70^{o}C. This is to ensure more uniform water absorption through the surfaces. In order to ensure continuous water ingression, the plates are only taken out from the environment chamber after fixed intervals of ageing period for testing. For both dry and aged specimens preparation, the composite plates are cut into longitudinal ($[0]_8$), transverse ($[90]_8$) and shear ($[\pm45]_{2S}$) specimens with dimensions as indicated in Figure 4.1. This is in accordance to the requirement by ASTM D3039 [241] and D3518 [242]. Both surface ends are then polished with fine grade sandpaper along the fibre direction, followed by cleaning with acetone. Specimens are then glued with glass/epoxy tabs. In addition, bidirectional strain gauge is attached at the centre of the surface of $[0]_8$ and $[\pm45]_{2S}$ specimens, whereas for $[90]_8$ specimens, unidirectional strain gauge is attached. Careful polishing on the area for strain gauge attachment especially the aged ones is needed to ensure good data acquisition. As for fracture test specimens, specimens with 20mm width are prepared, in accordance to the recommendation by ASTM D5528 [243]. Three different types of fracture tests are conducted, which are double cantilever beam (DCB), 3-point end notched flexure (ENF) and mixed-mode flexure (MMF) to characterise mode I, mode II and mixed-mode I+II delamination behaviour, respectively. The test configurations are as illustrated in Figure 4.2. For both ENF and MMF tests, half span length, L is always set to be 60mm. The total length of the specimens varies from 155-185mm, depending on the required initial crack length, a_o.

Table 4.1 summarises all the information about the specimens tested at different moisture contents. All tests are conducted using imposed cross-head speed of 1mm/min. Longitudinal tensile tests are conducted on the universal testing machine with load cell capacity of 100kN, whereas for all other tests are conducted using load cell capacity of 5kN. At least three replicates are tested for each series of specimens. All tests are conducted at ambient condition.

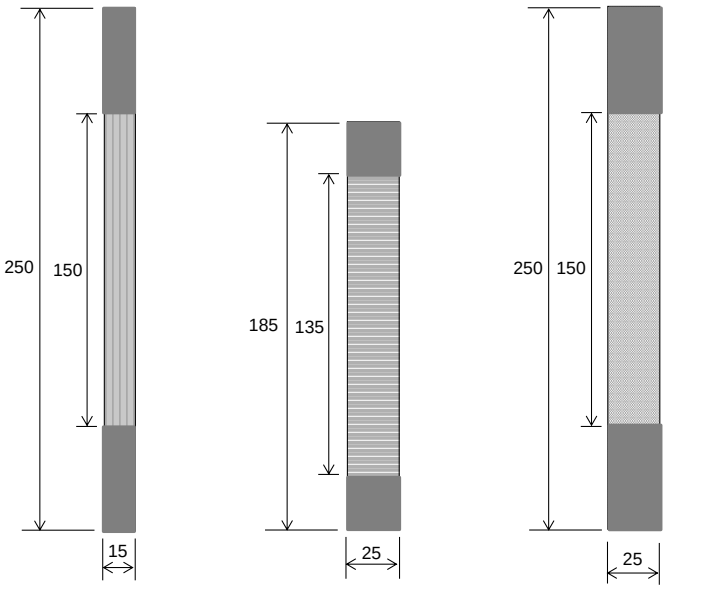

(a) Longitudinal $[0]_8$ (b) Transverse $[90]_8$ (c) Shear $[\pm 45]_{2S}$

Figure 4.1: Configurations of tensile test specimens.

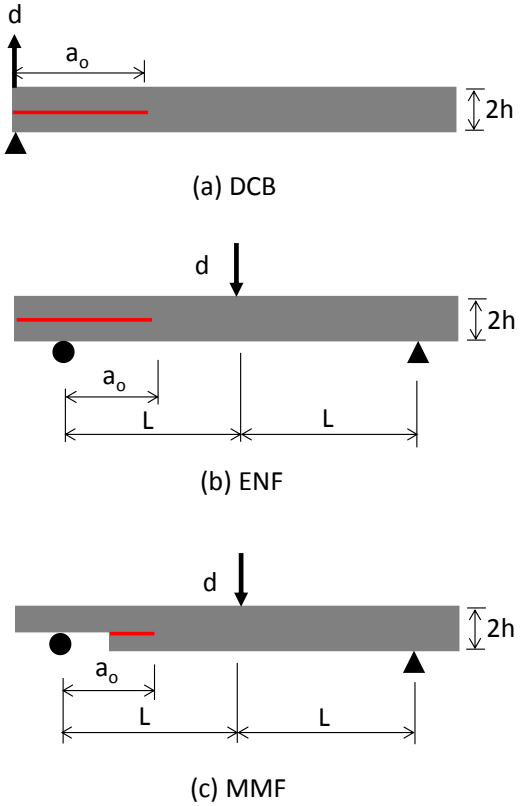

Figure 4.2: Configurations of delamination test specimens.

Table 4.1: Summary of the specimens prepared for ageing tests.

Stacking sequence	Dry	M=3%	M=5%	M=6%	M=7%
$[0]_8$	✓	✓	-	✓	✓
$[90]_8$	✓	✓	✓	✓	✓
$[\pm45]_{2S}$	✓	✓	-	✓	✓
$[0_8//0_8]$	✓	✓	✓	✓	-

* All specimens are fabricated using hot-press method.

4.3.Moisture effects on elementary tensile properties

Figure 4.3 to Figure 4.6 show some examples of typical mechanical response of longitudinal, transverse and shear specimens under tensile loading at dry and M=6%. Table 4.2 displays all the values of the elementary properties under different ageing period/moisture content with coefficient of variation indicated in bracket. For longitudinal and transverse strength, values are calculated by dividing the ultimate failure load with its nominal area. As no load drop is observed during the shear test, shear strength is taken at 5% shear strain. All longitudinal, transverse and shear modulus are taken from the initial linear slope of their respective curves. Possion's ratio is measured from the linear region of the transverse strain versus longitudinal strain graph. Considering the sensitivity of transverse properties with moisture, one additional set of experiment at M=5% is performed. Results illustrate comparatively high repeatability of all the tensile tests, with the highest coefficient of variation of approximately 12%. It should be noted that even after 278 days of ageing, saturation is yet to attain in those laminates. However, as described in Section 3.8, since the moisture concentration reaches uniformity across the thickness after a relatively short time, the measured properties can be taken as average values of the entire laminates.

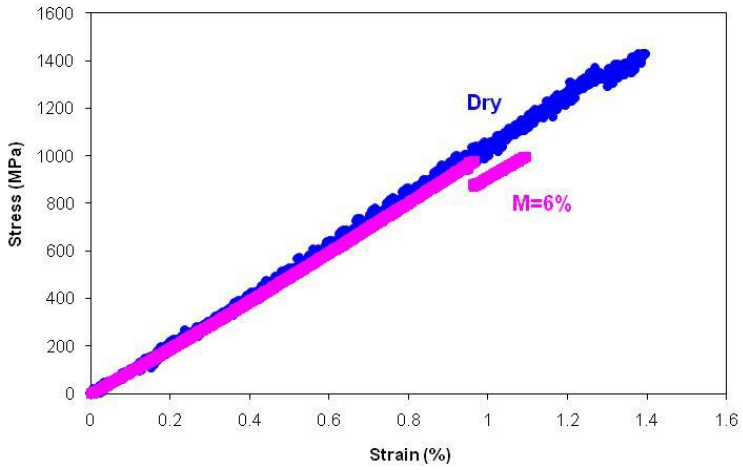

Figure 4.3: Typical stress-strain curves of longitudinal tensile specimens.

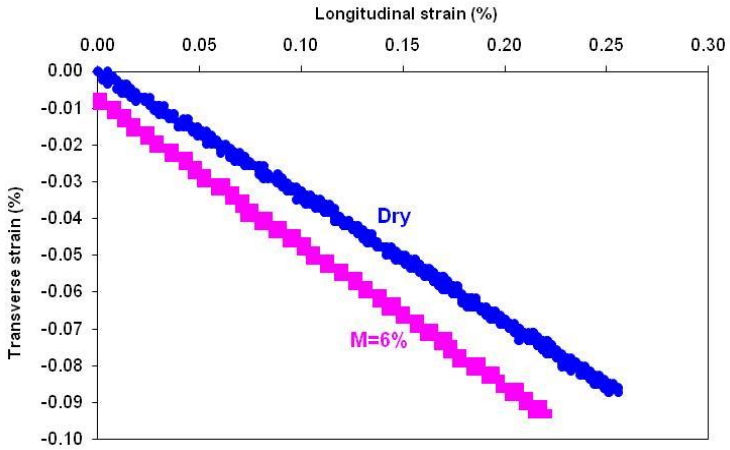

Figure 4.4: Typical transverse versus longitudinal strain curves of longitudinal tensile specimens.

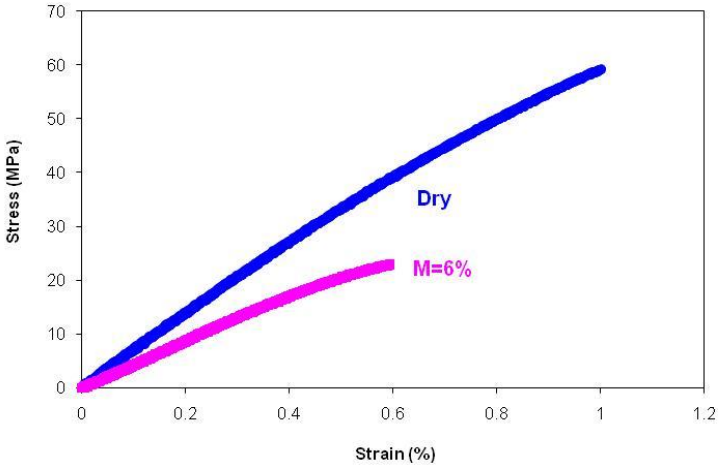

Figure 4.5: Typical stress-strain curves of transverse tensile specimens.

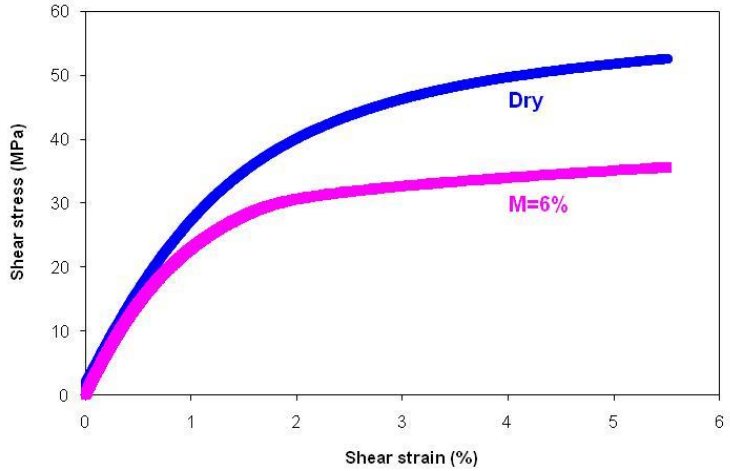

Figure 4.6: Typical shear stress-strain curves of in-plane shear tensile specimens.

Table 4.2: Elementary mechanical properties measured by tensile tests at various moisture content levels.

Ageing period (days)	M (%)	X^T (MPa)	Y^T (MPa)	S^L (MPa)	E_{11} (GPa)	E_{22} (GPa)	G_{12} (GPa)	v_{12}
0	≈0	1488.20 (3.85)	57.61 (10.17)	53.42 (5.31)	102.72 (2.70)	6.73 (7.05)	2.69 (7.13)	0.34 (5.64)
20	3	1495.40 (4.90)	33.46 (5.28)	39.57 (1.22)	97.04 (2.48)	4.65 (3.84)	2.71 (4.47)	0.34 (0.41)
71	5	-	24.73 (6.67)	-	-	4.33 (7.99)	-	-
95	6	991.25 (9.83)	22.83 (11.67)	36.00 (5.92)	95.45 (1.50)	4.52 (7.99)	2.57 (6.42)	0.37 (2.27)
278	7	1335.88 (5.95)	13.70 (10.99)	42.87 (2.37)	105.00 (1.18)	4.81 (6.71)	2.61 (5.76)	0.37 (9.69)

* X^T, Y^T, S^L refer to longitudinal tensile , transverse tensile and in-plane shear strength, E_{11}, E_{22} and G_{12} represent longitudinal, transverse and shear modulus, and v_{12} is the Poisson's ratio.

To give a clearer view on the variation of the properties with respect to the ageing period/moisture content, the normalised properties with respect to the dry condition (the values in the first row of Table 4.2) are illustrated in Figure 4.7 and Figure 4.8.

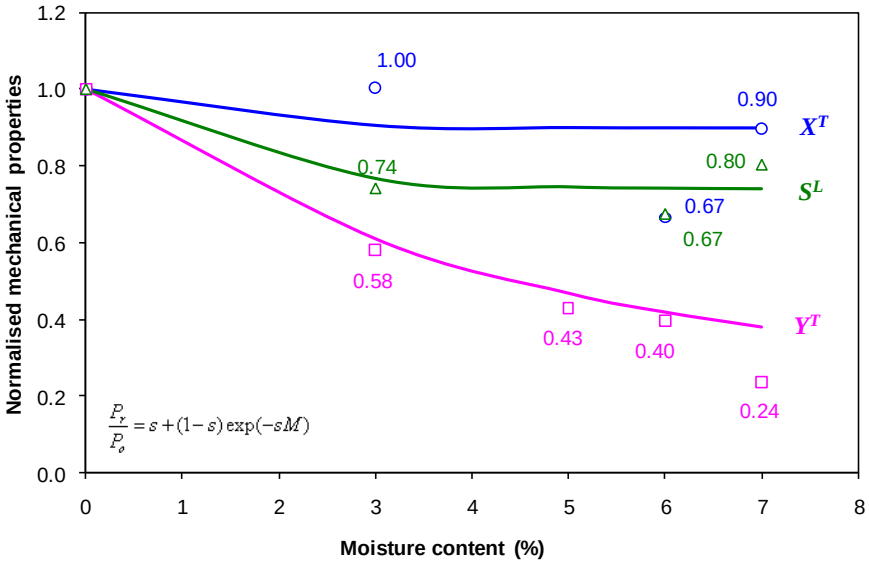

Figure 4.7: Normalised experimental and fitted tensile strength of T600S/R368-1 composite laminates at various moisture content levels.

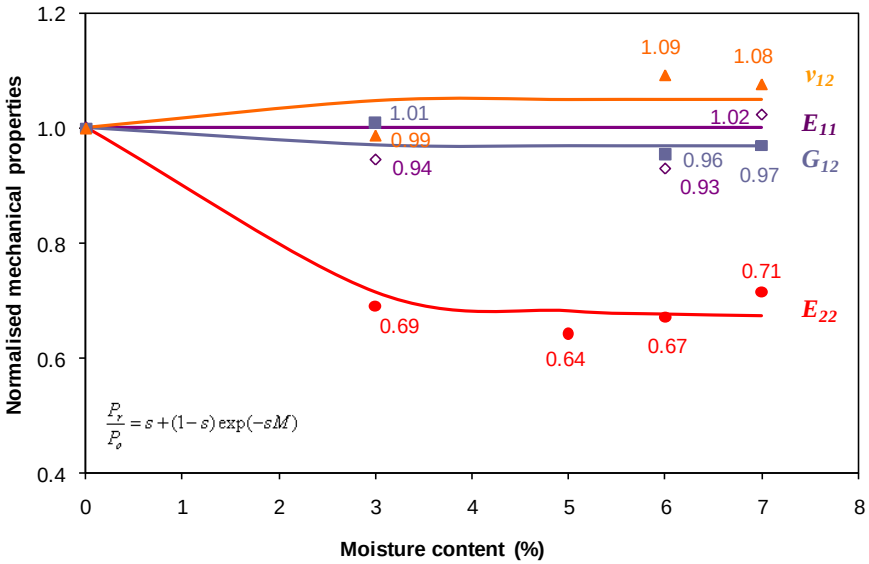

Figure 4.8: Normalised experimental and fitted tensile modulus and Poisson's ratio of T600S/R368-1 composite laminates at various moisture content levels.

As can be seen from Table 4.2, Figure 4.7 and Figure 4.8, results indicate that the longitudinal strength is invariant at the initial stage (M=3%), dropped for 30% at M=6% and recovered to 90% of its dry strength at M=7%. The reasons are unknown, however, experimental scatter should be one of the factors. Nevertheless, the residual strength falls within the general reported range listed in Table 2.6. At all moisture contents, the failure mode is always a combination of fibre splitting and fibre breakage (Figure 4.9). In addition, considering the experimental scatter, it is deduced that moisture has insignificant effect on the longitudinal modulus.

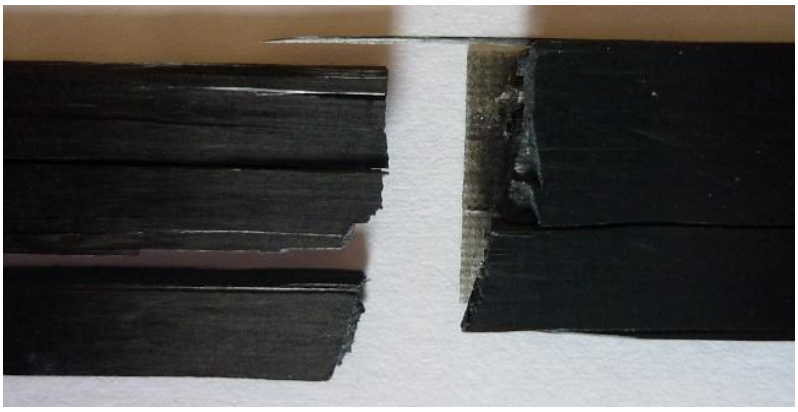

Figure 4.9: Failure mode of longitudinal specimens: fibre splitting and breakage.

Transverse strength is significantly influenced by moisture absorption. It reduces consistently with moisture content. At M=7%, only 24% of its original strength is retained. As for the transverse modulus, significant reduction (30%) is observed during the initial stage of ageing (M=3%), and remains constant after that. The percentage drop agrees with the reported values from the literature (see Table 2.6). This is in accordance to general hypothesis that matrix is sensitive to moisture attack. The major factors for the degradation are generally recognised as swelling and plasticisation. It is also noted that most of the transverse specimens fail in the central region between the grips, which implies minimal stress concentration effect near tab ends. At all moisture content levels, the failure mode is always

uniform across the width of the specimens by matrix cracking with some fibre peeling, which is illustrated in Figure 4.10.

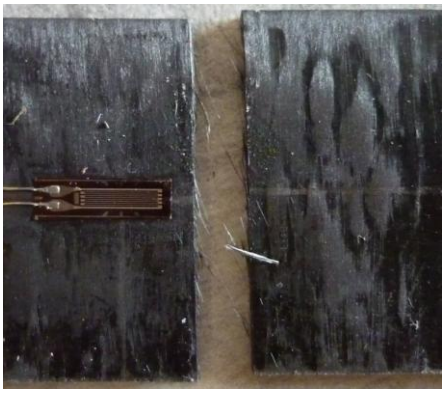

Figure 4.10: Failure mode of transverse specimens: matrix cracking across the width with some fibre peeling

Shear strength is found to decrease for approximately 30% at M=3%, and does not drop much until M=6%. Similar to the longitudinal strength, improvement is observed after that at M=7% (80% compared to the dry strength). Shear modulus is almost invariant after prolonged ageing. Even shear properties are mentioned to be sensitive to the moisture attack [13], several publications reported invariant shear properties as well [9, 123].

Besides, slight increment in the Poisson's ratio (≈10%) is observed after long ageing period (M=6% and 7%).

In order to characterise the variation of mechanical properties of the composite tested due to water absorption observed above, the residual property model (RPM) proposed by Papanicolaou et al. [29] is applied. RPM describes that the normalised residual property can be predicted using the following equation:

$$\frac{P_r}{P_o} = s + (1-s)\exp(-sM) \tag{4.1}$$

where P_r is the residual property at particular moisture content, P_o is the dry property, s is the ratio of the residual property at saturation to the dry level, and M is the moisture content.

As saturation is not really attained in this study, an approximate s value is estimated based on the residual property at high moisture content level for each property. Reasonably good fit is achieved for all measured properties, which are also shown as solid lines in Figure 4.7 and Figure 4.8. However, it should be noted that the RPM (Equation (4.1)) was intended to describe the degradation in the property that follows exponential decay form.

4.4.Moisture effects on the delamination behaviour of the carbon/epoxy composite

4.4.1.Data reduction schemes

The ply/ply interface properties are characterised firstly by fracture toughness in terms of the critical strain energy release rate (CSERR): $G_{C;}$ and secondly by R-curve which gives the variation of the resistance to the crack growth as a function of the crack extension.

G_C can be determined using the Irwin-Kies equation [244]:

$$G_C = \frac{P_C^2}{2b}\frac{dC}{da} \tag{4.2}$$

where P_C = critical load corresponding to crack initiation (in this study, it is always taken at non-liner (NL) point); b = width of the specimen; C = compliance and a = initial crack length.

If the specimen maintains a constant fracture mode during crack propagation, the compliance, C can be calibrated as a function of the initial crack length. It can be realised empirically by measuring the slope of the linear part from the load-displacement curve and the inverse of the slope gives the compliance for each specimen at different initial crack length. Then, the values of the compliance are interpolated as a function of crack length. Empirical compliance calibrated models proposed in the literature can be expressed by:

$$\text{Incomplete polynomial cubic, } C_{\exp 1} = A + Ba^3 \tag{4.3}$$

$$\text{Berry, } C_{\exp 2} = ka^n \tag{4.4}$$

where A, B, k and n are constants to be determined empirically. Substituting the derivative of Equation (4.3) or (4.4) into Equation (4.2) yields the following expressions:

$$G_{C\exp 1} = \frac{P_C^2}{2b}\cdot 3Ba^2 \tag{4.5}$$

$$G_{C\exp 2} = \frac{P_C^2}{2b}\cdot kna^{n-1} \tag{4.6}$$

It should be noted that Equation (4.5) can be applied to all different fracture modes whereas Equation (4.6) is only used for DCB case. Besides, the mode ratio, G_{II}/G_T of DCB, ENF and MMF are 0, 1 and 0.43, respectively.

These models are also applied to the crack propagation so as to determine a_p, defined as effective crack length when the crack grows and G_P, which represents the resistance to crack growth in terms of the strain energy release rate as following:

$$a_p = \left(\frac{C_p - A}{B}\right)^{\frac{1}{3}}, \qquad G_p = \frac{P_p^2}{2b}\cdot 3\cdot B\cdot a_p^2 \tag{4.7}$$

$$a_p = \left(\frac{C_p}{k}\right)^{\frac{1}{n}}, \qquad G_P = \frac{P_p^2}{2b}\cdot k\cdot n\cdot a_p^{n-1} \tag{4.8}$$

where C_p and P_p signify the measured specimen compliance and the load corresponding to an effective crack length a_p. Equation (4.7) and Equation (4.8) are deduced from Equation (4.3) and Equation (4.4), respectively.

R-curves can then be obtained in order to investigate the behaviour of crack propagation. In this study, the increment of the resistance relative to the fracture toughness, defined as $dR = G_P - G_{IC}$ is plotted as a function of the extension of the crack: $da = a_P - a_o$, where a_o is initial crack length.

Effects of fabrication techniques on ply/ply interface propertiesTable 4.3 compares the mode I fracture toughness: G_{IC}, measured on the DCB specimens fabricated by two different process: hot-press and vacuum-bagging. The results using Berry's model (Equation (4.5)) and the incomplete polynomial cubic's model (Equation (4.6)) are also given in the same table. The values in bracket refer to coefficient of variation (C.V) in percentage.

Table 4.3: Mode I fracture toughness of unidirectional carbon/epoxy composite measured on DCB specimens.

Fabrication method	Berry	Polynomial
	G_{IC} (N/m)	G_{IC} (N/m)
Hot-press	491.04 (12.98)	489.93 (13.39)
Vacuum-bagging	442.03 (11.79)	432.52 (15.69)

It can be seen that G_{IC} values calculated using Berry's method is always slightly higher than incomplete polynomial cubic's method. Hence, to be more conservative, incomplete polynomial cubic's method is adopted for all other DCB cases. Besides, 12% reduction in G_{IC} value is observed on the specimens prepared by vacuum-bagging method.

In order to establish the mixed-mode criterion necessary for numerical simulation, the fracture toughness has to be measured under pure mode I, mode II and at least one mixed-mode loading. Recall that BK mixed-mode criterion [156] proposed by Gong and Benzeggagh [157-158] is used in this study, expressed by Equation (2.47) as follow:

$$G_{TC} = G_{IC} + (G_{IIC} - G_{IC})\left(\frac{G_{II}}{G_I + G_{II}}\right)^{\eta}$$

Figure 4.11 shows all fracture toughness of unidirectional composites fabricated using hot-press and vacuum-bagging techniques, where the values in the bracket refer to coefficient of variation. Results of each fabrication technique are fitted using Equation (2.47) and their respective material parameter, η is also presented. It is obvious that the fracture toughness of the laminate fabricated using vacuum-bagging technique is always lower compared to hot-press technique: approximately 12%, 25% and 30% lower for DCB, MMF and ENF cases, respectively. This implies that different fabrication techniques do affect the interface quality. The application of higher pressure during hot-press curing process provides better bonding behaviour between neighbouring plies. Besides, the fracture toughness seems to be more sensitive to the interface quality if the participation of mode II is more important. However, the material parameter, η is shown to be insensitive to the interface quality.

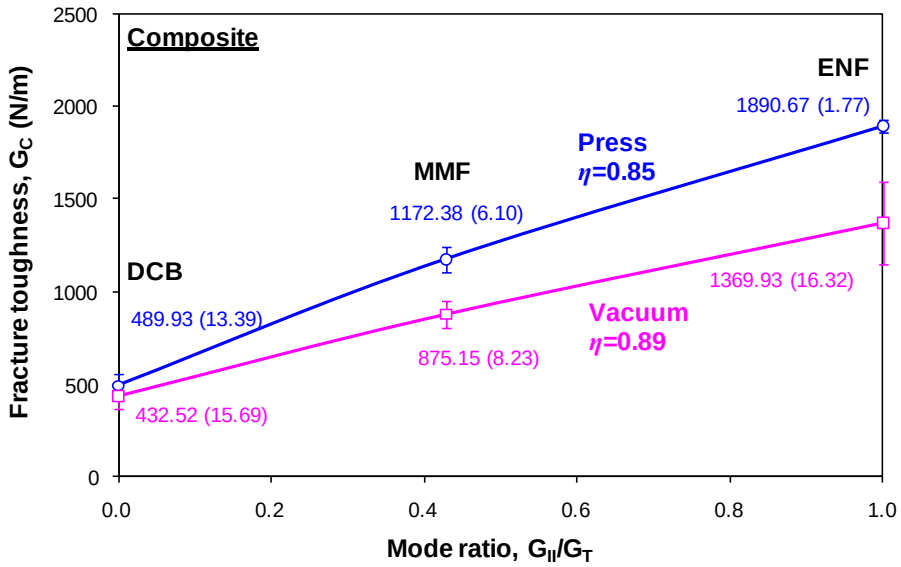

Figure 4.11: Mode I, II and mixed-mode I+II fracture toughness of unidirectional carbon/epoxy composites fabricated by hot-press and vacuum-bagging methods.

4.4.2.Effects of fibre orientation on ply/ply interface properties

Comparison of the fracture toughness of laminates with different fibre orientation ([0//0] and [0//45]) is illustrated in Figure 4.12. All laminates are prepared by the hot-press technique. It is found that mode I fracture toughness is invariant with the fibre orientation, whereas mode II and mixed-mode I+II fracture toughness of [0//0] laminate is higher than [0//45] laminate. Besides, the material parameter η (Equation (2.47)) fitted by these limited data seems to be quite different between those two interfaces.

In fact, the results shown here agree well with some observations by other researchers. In the study of Pereira and de Morais, independence of G_{IC} values with respect to fibre orientation was also reported, however, the fibre bridging behaviour was found to be different, where extensive R-curve was observed at larger angle difference between the adjacent plies [245]. Actually, similar observation in this work is obtained concerning R-curve, which will be described in detail in Section 4.4.4. In addition, under the condition of no intra-ply cracking, decrement in the mode II fracture toughness with the increment in the adjacent ply angle was also revealed [246].

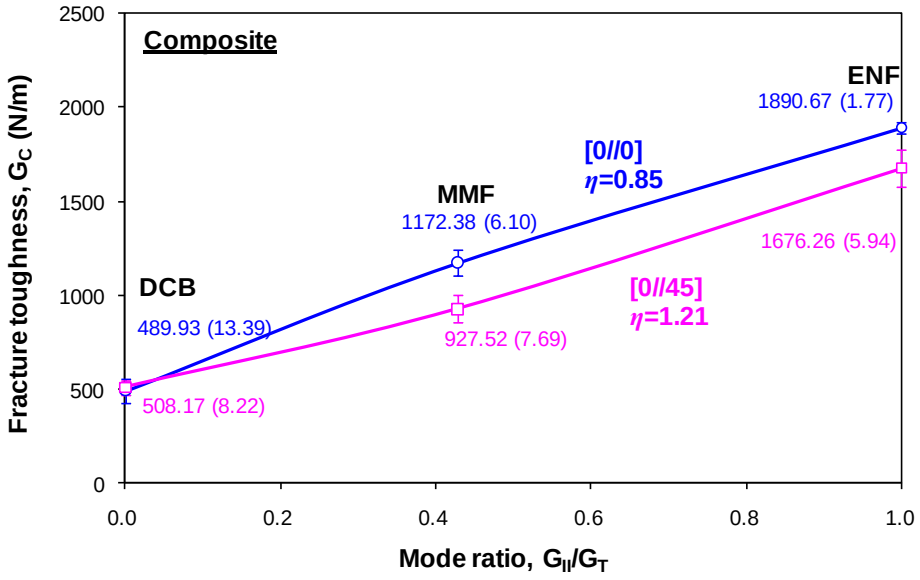

Figure 4.12: Mode I, II and mixed-mode I+II fracture toughness of unidirectional and multidirectional carbon/epoxy composites fabricated by hot-press method.

4.4.3.Moisture effects on the delamination behaviour

Figure 4.13 schematises the change in the fracture toughness of unidirectional carbon/epoxy composites at different moisture content. Similarly, the material parameter, η varies more or less with the moisture content. No clear trend of this variation is shown. The normalised fracture toughness shown in Figure 4.14 gives a clearer view on the moisture effects on the fracture toughness.

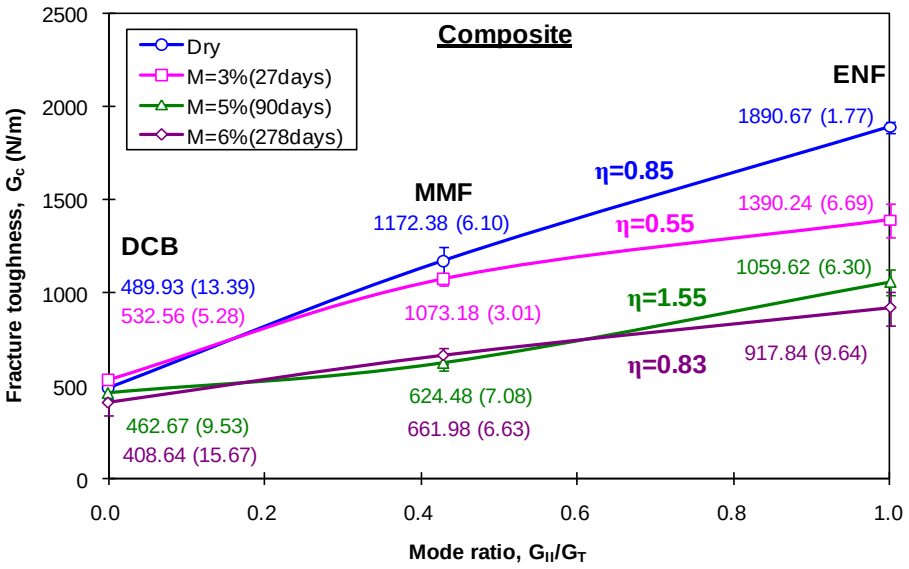

Figure 4.13: Mode I, II and mixed-mode I+II fracture toughness of unidirectional carbon/epoxy composites at different moisture content levels.

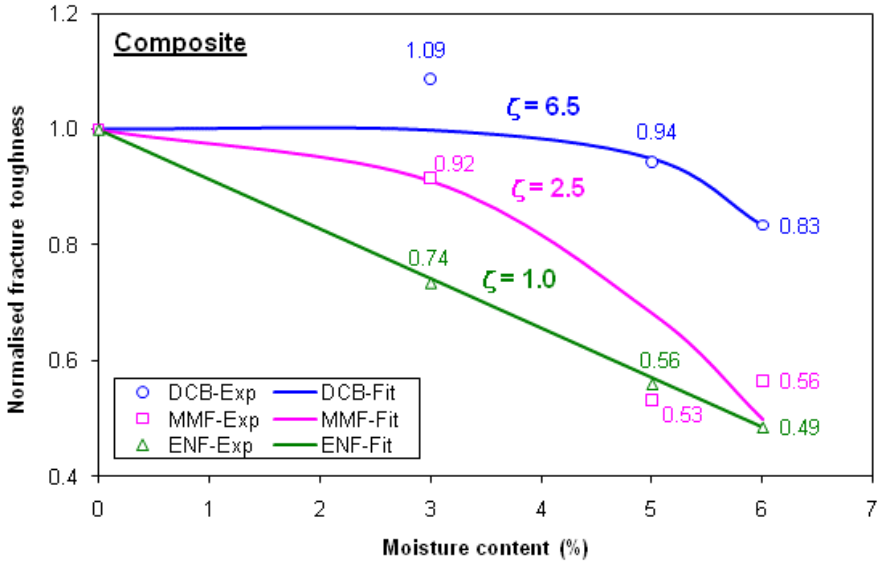

Figure 4.14: Normalised experimental and fitted fracture toughness of unidirectional carbon/epoxy composites at different moisture content levels.

Fracture results show that the mode I fracture toughness is the least influenced, with slight increment at the initial stage, and dropped after that (≈20% at M=6%). As for mixed-mode I+II fracture toughness, it is almost invariant at M=3%, and 50% reduction in the fracture toughness is observed after long ageing periods (M=5 and 6%). Mode II fracture toughness decreases consistently with the moisture content. At M=6%, only 50% of its dry value is retained. It seems that moisture effect is more significant when mode II participation increases. This implies that the shear strength at the fibre/matrix interface is more sensitive to the moisture than the peel strength. This is similar to the findings reported in another research work from the laboratory on 8/8 harness satin weave glass/epoxy composites, where upon saturation, the mode I, mixed-mode I+II and mode II fracture toughness in warp direction (0//0 pre-dominant) drop for 20, 40 and 55%, respectively [155].

Based on the results obtained, it is found that water sorption generally deteriorates the interface behaviour (which is reflected in the reduction of the fracture toughness) except for DCB case during early ageing period (at M=3%). Interface degradation could be attributed to hydrolysis of unsaturated groups within the polymer [103]. In addition, matrix plasticisation due to water absorption could separate the polymer chains apart. Consequently, the matrix becomes softer/more pliable [139], which eventually leads to decrease of fracture resistance, especially that of shear resistance. It was also reported that long immersion period is harmful to the matrix and interface, and hence the peeling strength is reduced [152]. Degradation in the interface bonding ability and thus the fracture toughness due to moisture absorption was also reported by some other researchers [104, 247-249].

On the contrary to the fracture resistance decrement, the slight increment in the mode I fracture toughness at M=3% observed in this study is not uncommon (see Table 2.14). It was reported that G_{IC} dropped due to interfacial degradation, but plasticisation by water increased it [142]. When plasticisation dominated over interfacial degradation, the net G_{IC} was improved. Huang and Sun [152] have obtained similar conclusion. It was reported that the increment in the peeling strength was probably due to matrix plasticisation by the penetrated water. Besides, the hydroxyl group of water molecules which filled the gap in the composite could also improved the bonding strength [152]. Furthermore, the increment in G_{IC} was reported to be due to matrix ductility enhancement [153, 250-251]. In addition, G_{IC} improvement could also be contributed by fibre bridging enhancement and crack tip blunting due to increment in the porosity as a result of moisture absorption [142]. The increment in the crack tip radius implied reduction in the crack tip stress concentration, which eventually leads to a higher G_{IC} value [252]. It is noteworthy that the mixed-mode I+II fracture toughness might increase with moisture [153], however, the mode II fracture toughness, G_{IIC} was always found to decrease upon water absorption [142, 153, 250-251].

As the variation of the fracture toughness does not generally follow the exponential decay form, Equation (4.1) is not suitable to describe the trend. Hence, another residual property model is proposed in this study, which is described as follow:

$$\frac{P_r}{P_o} = 1-(1-s)\left(\frac{M}{M_m}\right)^{\zeta} \tag{4.9}$$

where P_r, P_o, s and M are having the same definition as Equation (4.1), M_m and ζ are saturation moisture content and degradation parameter, respectively. In this case, since M_m is not attained, the maximum moisture content (M=6%) is considered. Results show comparatively good fit with non-constant ζ, which decreases when mode II ratio increases, as shown in Figure 4.14. It is noteworthy that Equation (4.9) is more general than Equation (4.1) that it can fit any trend of variation including exponentially decay properties. Refitting the elementary properties variation with Equation (4.9), excellent correlation is also found, which is illustrated in Figure 4.15 and Figure 4.16. For invariant properties (E_{11}, G_{12}, ν_{12}), the degradation parameter, ζ can be simply assumed to be unity.

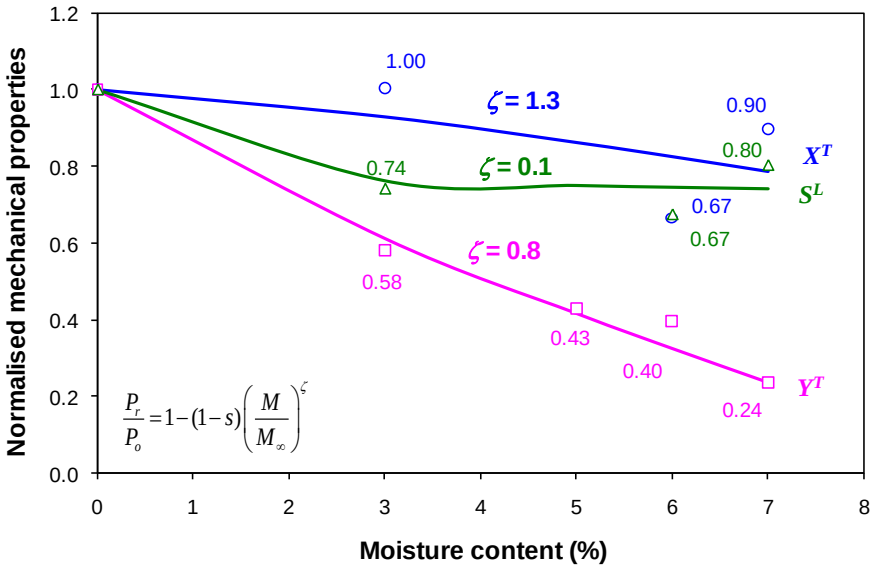

Figure 4.15: Normalised experimental and refitted (using Equation (4.9)) strengths of T600S/R368-1 composite laminates at various moisture content levels.

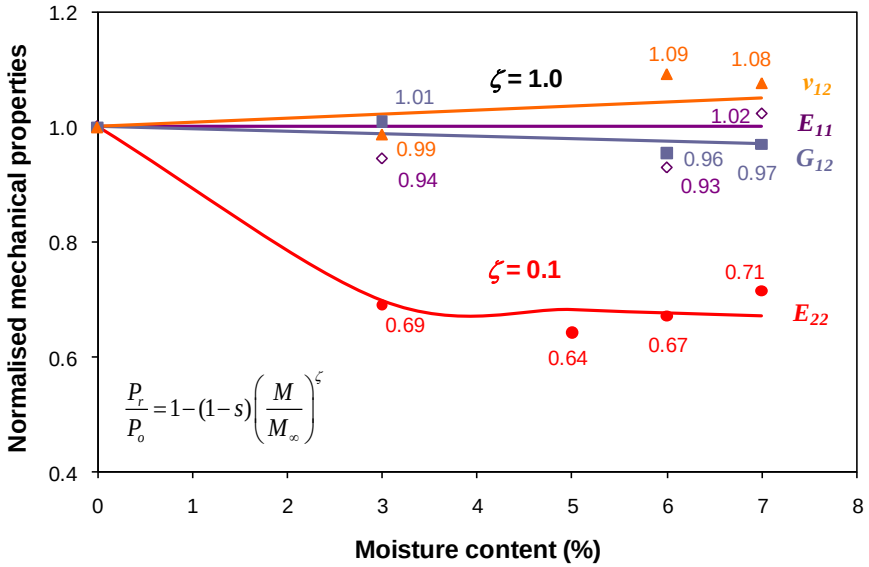

Figure 4.16: Normalised experimental and refitted (using Equation (4.9)) modulus and Poisson's ratio of T600S/R368-1 composite laminates at various moisture content levels.

4.4.4.Modelling of R-curve bridging laws for mode I delamination

In this study, R-curve behaviour is noticed in all mode I delamination cases except unidirectional composite laminated fabricated using hot-press technique. Figure 4.17 compares that the increment in the fracture energy of UD hot-press and vacuum-bagging DCB specimen. It is seen that the fracture energy increment in hot-press specimen is negligible because it is approximately only 10% of its G_{IC} value. However, the increment in the resistance to crack growth in the vacuum-bagging specimen is significant. In this case, it is hence necessary to model the R-curve effect to describe accurately the mode I delamination behaviour.

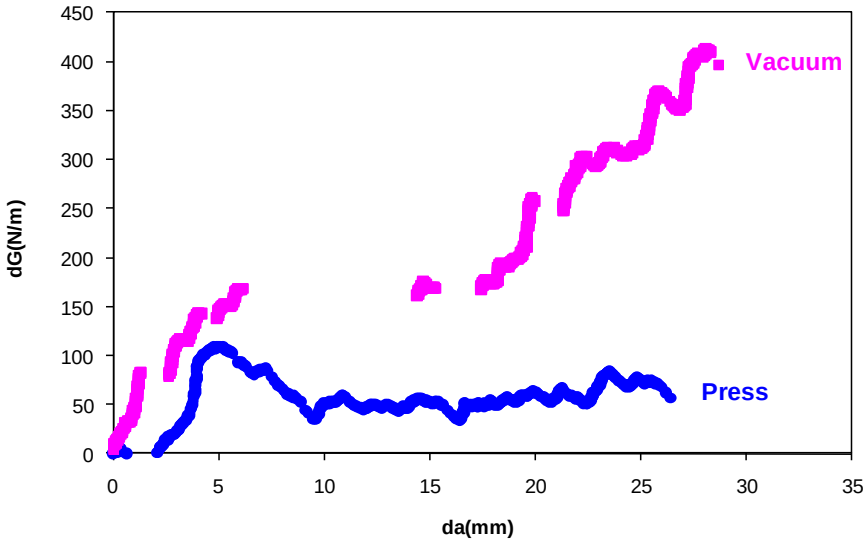

Figure 4.17: Typical R-curves of unidirectional DCB specimens fabricated by hot-press and vacuum-bagging methods.

Firstly, the R-curves at different initial crack length are shown in Figure 4.18. It is apparent that the R-curve is different only when the initial crack length is too short (24mm in this study). For initial crack length of 30mm and above, the R-curves are similar. Hence, it is reasonable to constitute the R-curves at initial crack lengths within the respective range. Actually, in all other mode I delamination tests, the initial crack length is around 40mm. Figure 4.19 shows the R-curves of mode-I delamination at M=6%. Results indicate significant R-curve effect with highly repetitive curves.

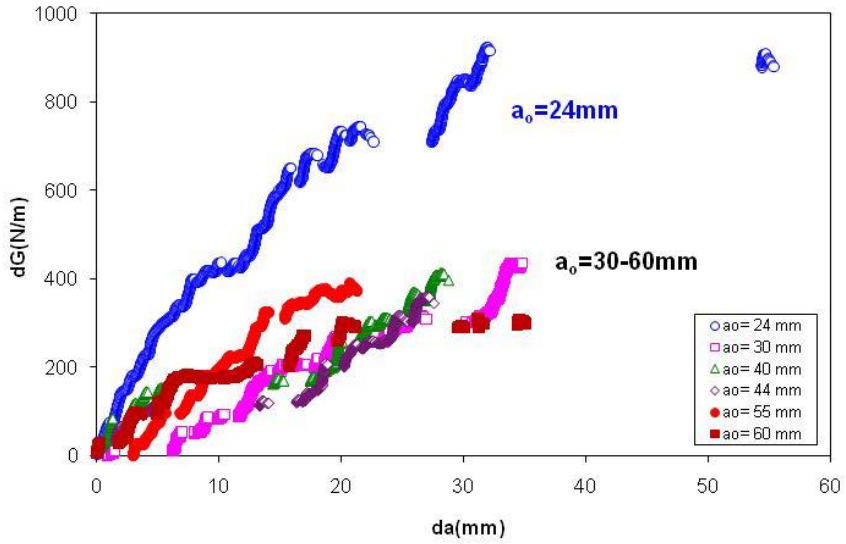

Figure 4.18: R-curves of unidirectional DCB specimens fabricated by vacuum-bagging technique at different initial crack length.

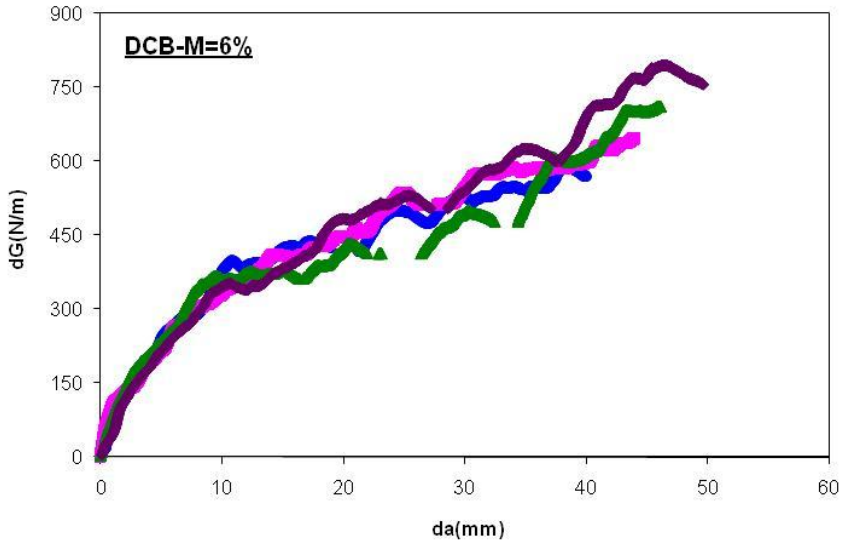

Figure 4.19: R-curves of unidirectional DCB specimens at M=6%.

To describe the R-curve behaviour, a linear-exponential traction-separation relationship as shown in Figure 4.20 is proposed in this study, which was previously found to be able to model R-curve behaviour with the advantage of a higher flexibility in the curve-fitting through the parameter γ in the equation [253]. The traction distribution of the bridging law is described in Equation (4.10).

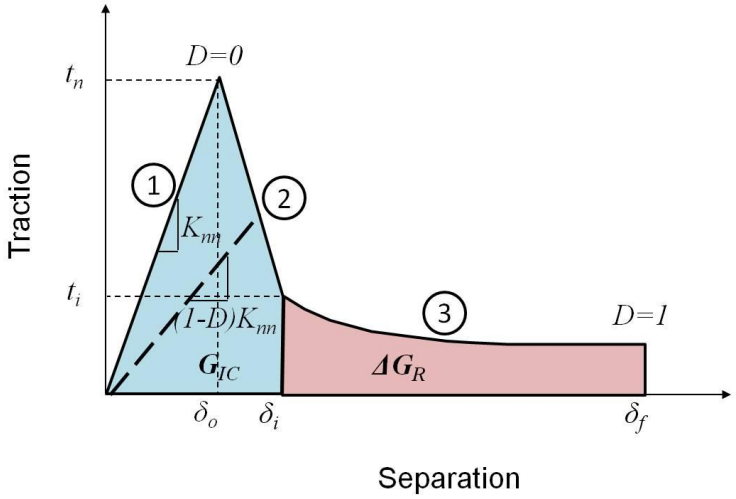

Figure 4.20: Traction-separation relationship of linear-exponential bridging law.

$$t = \begin{cases} K_{nn}\delta & \text{for } 0 \le \delta \le \delta_o \\ t_n + (t_n - t_i)\left(\dfrac{\delta - \delta_o}{\delta_o - \delta_i}\right) & \text{for } \delta_o \le \delta \le \delta_i \\ t_i \exp\left(-\gamma \dfrac{\delta - \delta_i}{\delta_f - \delta_i}\right) & \text{for } \delta_i \le \delta \le \delta_f \end{cases} \tag{4.10}$$

In the above equation, δ is the crack opening displacement (COD) and γ is the fitting parameter. Other parameters are as defined in Figure 4.20. The damage parameter D could be obtained as shown in the following equation:

$$D=\begin{cases}1-\dfrac{1}{K_{nn}\delta}\left[t_n+(t_n-t_i)\left(\dfrac{\delta-\delta_o}{\delta_o-\delta_i}\right)\right] & \text{for } \delta_o\le\delta\le\delta_i \\ 1-\dfrac{t_i}{K_{nn}\delta}\exp\left(-\gamma\dfrac{\delta-\delta_i}{\delta_f-\delta_i}\right) & \text{for } \delta_i\le\delta\le\delta_f\end{cases} \tag{4.11}$$

In the above equation, the damage value D=0 at $\delta=\delta_o$ and D=1 at $\delta=\delta_f$.

4.4.5.Analysis of experimental R-curves

Using the assumption of interface crack profile that follows a third order polynomial as shown in Figure 4.21 [254], the COD, δ could be estimated using Equation

(4.12).

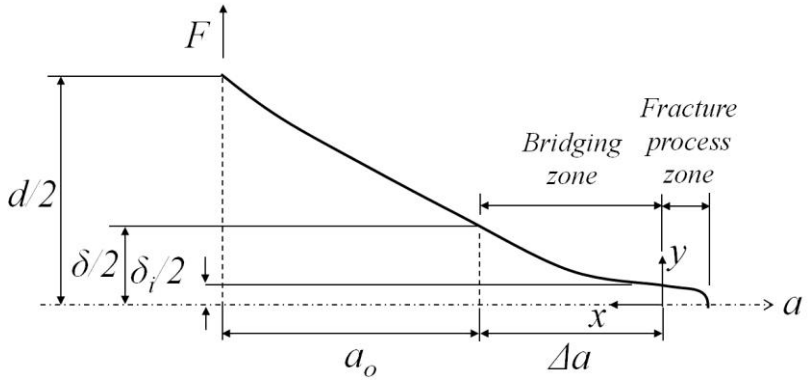

Figure 4.21: Assumed crack profile for a DCB specimen.

$$\delta=(d-\delta_i)\frac{\Delta a^2(2\Delta a+3a_o)}{(a_o+\Delta a)^3}+\delta_i \tag{4.12}$$

where d, Δa and a_o are the crack end displacement, increment in the crack length and initial crack length, respectively.

In this study, a drop in fracture energy of more than 5% from the previous maximum value is chosen as a basis for establishing representative R-curves. The sudden drop in fracture energy value is attributed to instable crack propagation. Thus, energy magnitude of lower than the previous attained maximum does not contribute to additional crack propagation. In fact, it is an energy storing process. An example of unfiltered and filtered R-curves is illustrated in Figure 4.22. In reality, except hot-press dry UD specimen that does not exhibit fibre bridging behaviour, R-curves shown in Figure 4.17 to Figure 4.19 are the filtered curves. The manipulated R-curves are then fitted with the linear-exponential law, which could be obtained through the integral of the traction term. Equation (4.13) describes the corresponding fitting equation.

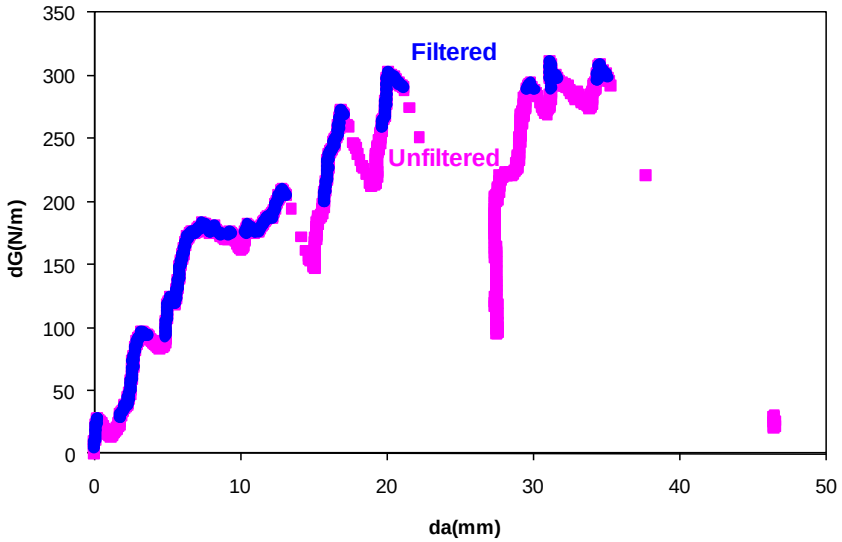

Figure 4.22: Typical unfiltered and filtered R-curves.

$$dG = \frac{t_i(\delta_f - \delta_i)}{\gamma}\left[1 - \exp\left(-\gamma \frac{\delta - \delta_i}{\delta_f - \delta_i}\right)\right] \tag{4.13}$$

The term, *dG* represents the increment in the fracture energy. The derivation and implementation of the linear-exponential traction-separation law are described in detail in Appendix C.

For illustration purpose, only one selected experimental curve is used to fit Equation (4.13). However, it should be noted that a representative curve obtained from all experimental curves through statistical method is generally more preferred instead of one selected curve. At this stage, it is yet to be attempted. Figure 4.23 and Figure 4.24 show excellent fit in between the experimental and analytical curves of vaccum-bagging fabricated unidirectional and hot-press fabricated multidirectional composite plates, respectively. It is observed that upon ageing, significant R-curve is notified. Fibre bridging enhancement is believed to be due to additional porosity when water molecules penetrate into the specimens [142]. Since G_{IC} values at each moisture content are different, for better comparison, the R-curves of aged specimens are plotted in terms of the fracture toughness ratio, dG/G_{IC}. Good correlation is also found as illustrated in Figure 4.25. In addition to that, the graphs show that the maximum increment in the fracture toughness is found at M=6% and the least at M=5%. The fitting parameter, γ seems to be decreasing with the moisture content. However, at this stage, it is difficult to conclude on the general trend of G_R and γ with respect to the moisture content.

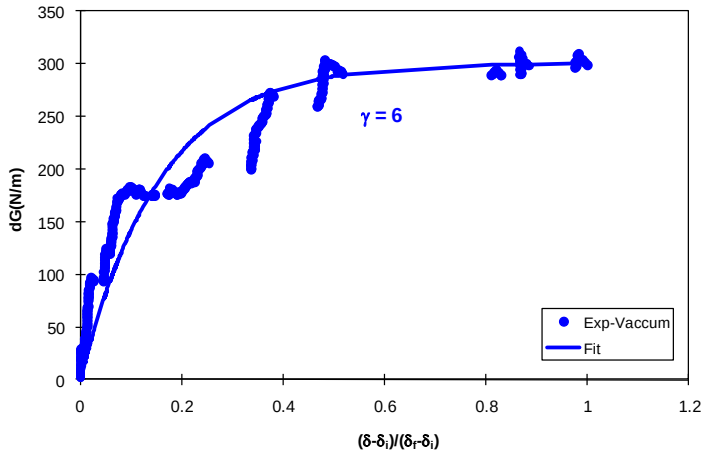

Figure 4.23: Experimental and fitted R-curves of unidirectional DCB specimens fabricated by vacuum-bagging method.

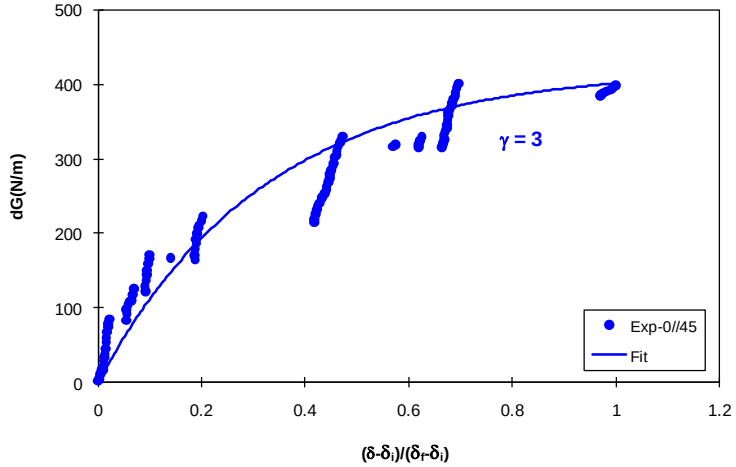

Figure 4.24: Experimental and fitted R-curves of multidirectional QIQH DCB specimens.

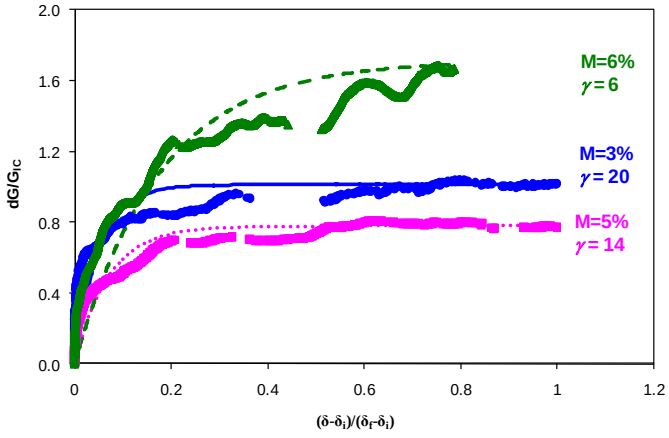

Figure 4.25: Experimental and fitted R-curves of unidirectional DCB specimens aged at various moisture content levels.

4.4.6.Delamination behaviour modelling using finite element method

To simulate the delamination between neighbouring laminas, the mid-plane interface of the composite laminate are modelled with cohesive elements proposed by Camanho and

Davila [255] based on the cohesive zone concept by Dugdale [256] and Barenblatt [257]. Before any delamination damage occurs, the traction separation behaviour is assumed to be linear elastic. For uncoupled normal and shear tractions, the constitutive behaviour is given as:

$$\begin{Bmatrix} t_n \\ t_s \\ t_t \end{Bmatrix} = \begin{pmatrix} K_{nn} & 0 & 0 \\ 0 & K_{ss} & 0 \\ 0 & 0 & K_{tt} \end{pmatrix} \begin{Bmatrix} \delta_n \\ \delta_s \\ \delta_t \end{Bmatrix} \tag{4.14}$$

A quadratic nominal stress criterion is used to indicate the initiation of interface damage, as shown in the following equation:

$$\left\{ \frac{\langle t_n \rangle}{t_{u,n}} \right\}^2 + \left\{ \frac{t_s}{t_{u,s}} \right\}^2 + \left\{ \frac{t_t}{t_{u,t}} \right\}^2 = 1 \tag{4.15}$$

The symbol $\langle \cdot \rangle$ refers to Macaulay bracket where no damage will be initiated under compressive stress state. Delamination starts to occur at a material point of the interface when the quotient of the nominal stress ratios reaches unity.

Following interface damage initiation event, subsequent damage propagation upon further loading is predicted using a mixed-mode energy-based criterion based on equation (2.47).

$$G_{IC} + (G_{IIC} - G_{IC}) \left\{ \frac{G_{II} + G_{III}}{G_I + G_{II} + G_{III}} \right\}^{\eta} = G_C \tag{4.16}$$

Given the normal and shear inter-laminar strengths ($t_{u,n}$, $t_{u,s}$, $t_{u,t}$) and penalty stiffnesses (K_{nn}, K_{ss} and K_{tt}), the damage onset displacements ($\delta_{o,n}$, $\delta_{o,s}$ and $\delta_{o,t}$) could be calculated while the failure displacements ($\delta_{f,n}$, $\delta_{f,s}$ and $\delta_{f,t}$) are obtained through the input of fracture energies (G_{IC}, G_{IIC} and G_{IIIC}).

At each time increment, the mixed-mode displacement is calculated using the following equation:

$$\delta_m = \sqrt{\langle \delta_n \rangle^2 + \delta_s^2 + \delta_t^2} = \sqrt{\langle \delta_n \rangle^2 + \delta_{shear}^2} \tag{4.17}$$

where δ_{shear} is the normal of the vector that represents the tangential relative displacement of the element.

At the same time, the mode mixity ratio, tan θ is calculated as:

$$\tan\theta = \frac{\delta_{shear}}{\delta_n} \tag{4.18}$$

For bi-linear mixed-mode softening law (without R-curve consideration), it is schematically described in Figure 4.26:

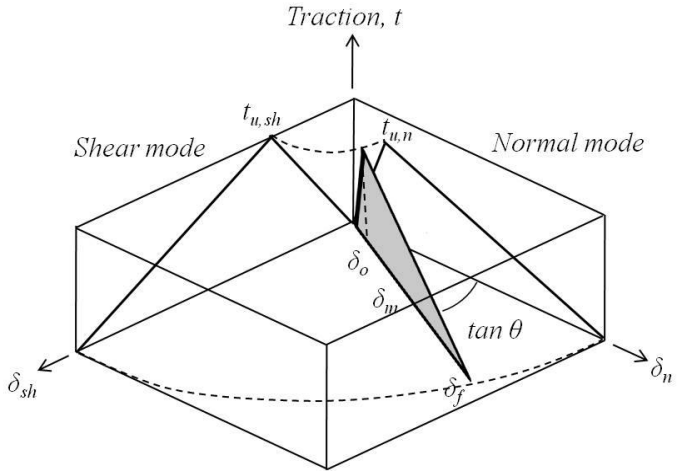

Figure 4.26: Schematic diagram of bi-linear mixed mode softening law.

For illustration purpose, consider that $K_{nn}=K_{ss}=K_{tt}=K$ and $t_{u,s}=t_{u,t}=t_{shear}$, the mixed mode damage onset displacement is calculated using

$$\delta_{o,m}=\begin{cases}\delta_{o,n}\delta_{o,shear}\sqrt{\dfrac{1+\tan^2\theta}{\delta_{o,shear}^2+\tan^2\theta\cdot\delta_{o,n}{}^2}} & \delta_n>0\\ \delta_{o,shear} & \delta_n\le 0\end{cases} \tag{4.19}$$

The mixed-mode failure displacement is

$$\delta_{f,m}=\begin{cases}\dfrac{2}{K\delta_{o,m}}\left[G_{IC}+(G_{IIC}-G_{IC})\left(\dfrac{\tan^2\theta}{1+\tan^2\theta}\right)^{\eta}\right] & \delta_n>0\\ \sqrt{\delta_{f,n}{}^2+\delta_{f,shear}{}^2} & \delta_n\le 0\end{cases} \tag{4.20}$$

The damage variable is described as follows:

$$D=\frac{\delta_{f,m}(\delta_m-\delta_{o,m})}{\delta_m(\delta_{f,m}-\delta_{o,m})} \tag{4.21}$$

The constitutive behaviour of the interface is then calculated based on the following equation.

$$\begin{Bmatrix}t_n\\ t_s\\ t_t\end{Bmatrix}=\left(\begin{bmatrix}(1-D)K_{nn} & 0 & 0\\ 0 & (1-D)K_{ss} & 0\\ 0 & 0 & (1-D)K_{tt}\end{bmatrix}+\begin{bmatrix}DK_{nn}\,H(-\delta_n)\\ 0\\ 0\end{bmatrix}\right)\begin{Bmatrix}\delta_n\\ \delta_s\\ \delta_t\end{Bmatrix} \tag{4.22}$$

where

$$H(x)=\begin{Bmatrix}0 & x<0\\ 1 & x\ge 0\end{Bmatrix}$$

The damage variable is updated into the stiffness matrix (Equation (4.22)). Subsequently, stresses/tractions are updated.

It should be noted that pure mode delamination (DCB and ENF) is mode-independent, where shear mode vanishes in DCB case and normal mode vanishes in ENF case. In other words, mixed-mode softening law is basically used in MMF case only. In addition, the

participation of mode I R-curve effect in mixed-mode delamination is also not considered in the numerical simulations. As for DCB specimens (except UD hot-press dry case), the R-curve behaviour is implemented into the finite element software using tabular function. Hence, the traction-separation relationship follows the linear-exponential law as described in Figure 4.20 instead of the bi-linear form.

Figure 4.27 shows the geometry of the finite element models along with loading and boundary conditions for the fracture specimens. To take into account the local stress state effects on the delamination behaviour, the adjacent upper and lower plies to the mid-plane are explicitly modelled for UD composites. For MD composites, the upper and lower sub-adjacent plies are also modelled, since both adjacent and sub-adjacent plies are believed to affect the delamination behaviour [253, 258-260]. Other plies are modelled as equivalent composite layer with one and two elements in thickness direction for UD and MD composites, respectively. All composite layers are modelled using 8-node continuum shell elements (SC8R). As for the mid-plane interface, 8-node cohesive elements (COH3D8) are prescribed to simulate the delamination behaviour. To well capture the delamination behaviour, elements in the fracture process zone (FPZ) are discretised with fine mesh at 0.5mm, as shown in Figure 4.28. Besides, in the width direction, 11 equal size elements are meshed (same for all models). The ply and interface properties used in the simulations are listed in Table 4.4 and Table 4.5. It is noted that G_{13} and G_{23} are assumed values. Besides, due to the lacking of experimental data at M=5% (except transverse properties), estimated properties are used. In addition, considering the insensitivity of the cohesive parameters within certain range [261], the interface stiffness and traction are assumed to be the same in all cases. Furthermore, mode III fracture toughness, G_{IIIC} is assumed to be the same as G_{IIC}.

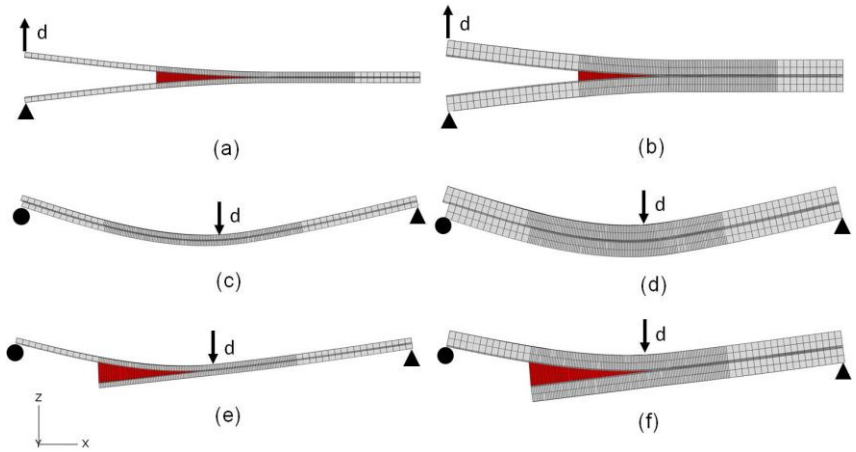

Figure 4.27: Finite element models with loading (imposed displacement at the location of arrow labelled with "d") and boundary conditions ($u_x=u_y=u_z=0$ for pinned "▲" and $u_y=0$ for roller "●") of delamination tests specimens.

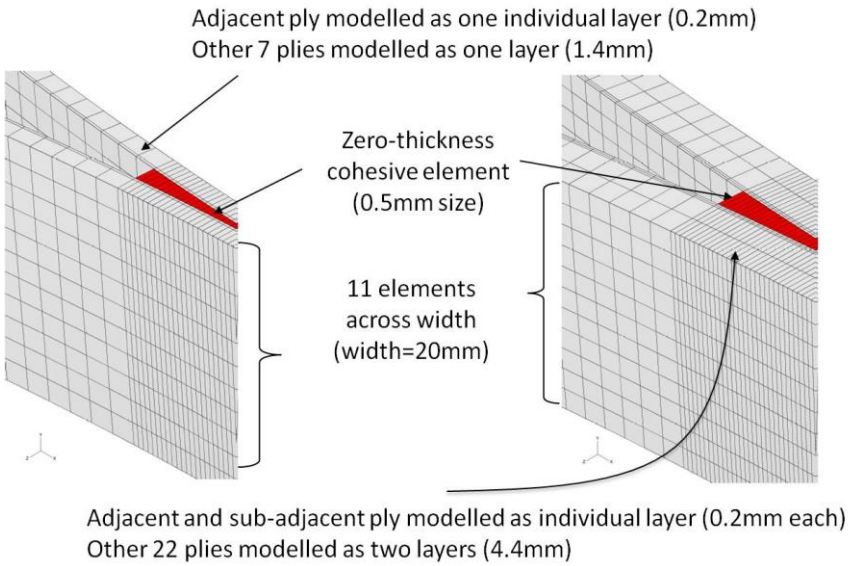

Figure 4.28: Discretisation of the finite element models of mode I DCB, mode II ENF and mixed-mode MMF tests.

Table 4.4: Lamina properties used in various DCB, ENF and MMF finite element models.

	E_1 (GPa)	E_2 (GPa)	G_{12} (GPa)	G_{13} (GPa)	G_{23} (GPa)	ν_{12}
UD Press	103.0	6.7	2.7	2.7	2.5	0.34
UD Vacuum						
MD Press						
UD M=3%	97.0	4.6	2.7	2.7	2.5	0.34
UD M=5%	96.0	4.3	2.6	2.6	2.3	0.36
UD M=6%	95.0	4.5	2.5	2.5	2.2	0.37

Table 4.5: Interface properties used in various DCB, ENF and MMF finite element models.

	$K_{nn}=K_{ss}=K_{tt}$ (N/mm^3)	t_n (MPa)	$t_s=t_t$ (MPa)	G_{IC} (N/mm)	$G_{IIC}=G_{IIIC}$ (N/mm)	η
UD Press	1×10^4	25	80	0.5	1.9	0.9
UD Vacuum				0.4	1.4	0.9
MD Press				0.5	1.7	1.2
UD M=3%				0.5	1.4	0.6
UD M=5%				0.5	1.1	1.6
UD M=6%				0.4	0.9	0.8

Figure 4.29 to Figure 4.34 compare the experimental and numerical force-displacement curves of all DCB, ENF and MMF specimens studied. In fact, it is better to plot a representative experimental curve using statistical method. However, at the current stage, it is not attempted and one selected experimental curve is presented for comparison. Nevertheless, the scatters among different experimental curves in this study are not too significant to cause obvious errors. At least, the maximum coefficient of variation (C.V) of the fracture toughness falls within 17%. For DCB specimens with fibre bridging behaviour, finite element modelling without R-curve effect (both $G_C=G_{IC}$ and $G_C=G_{RC}$) are also included for comparison. It is obvious that the inclusion of R-curve effect gives the best simulation results. The force-displacement curve of $G_C=G_{IC}$ case is always lower than the experimental one, whereas for $G_C=G_{RC}$ case, over-prediction is signified. The comparison between the experimental and numerical force-displacement curves in terms of peak load, slope and softening behaviour is summarised in Table 4.6. Results show relatively good correlation,

with negligible difference in the slope and maximum peak load difference of less than 20%. For ENF specimens, the numerical predicted peak loads are generally lower than the experimental values, which could be due to additional friction in between the sliding interfaces during experiment. However, as the difference is within an acceptable range, the inclusion of the friction in the finite element modelling is not attempted.

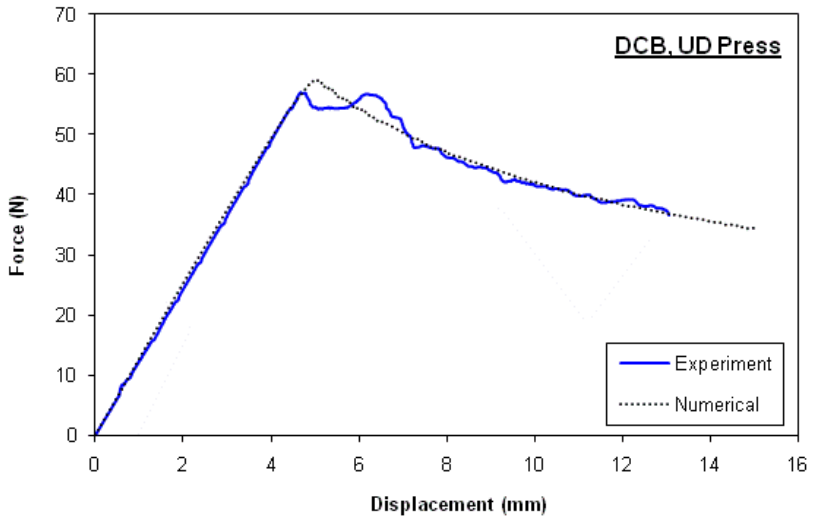

(a) DCB

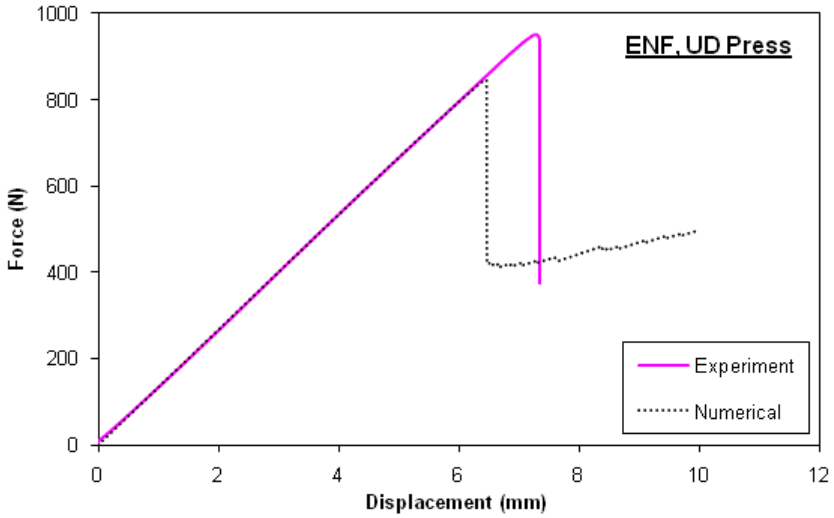

(b) ENF

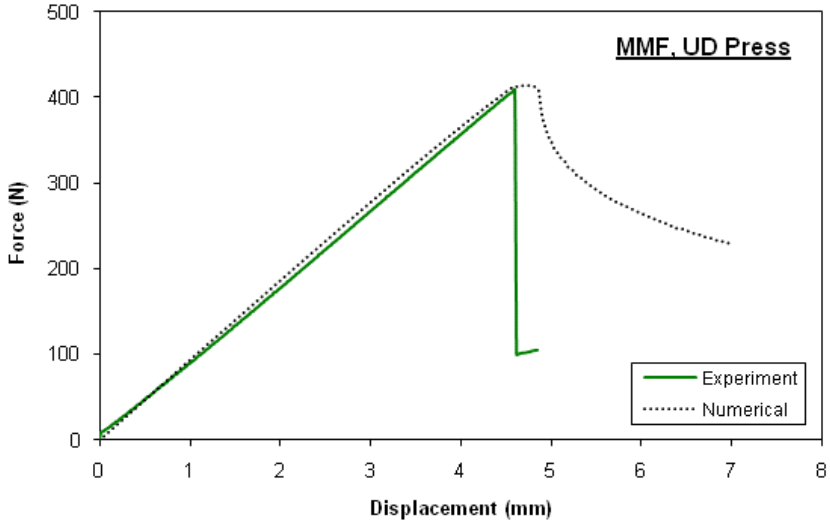

(c) MMF

Figure 4.29: Comparison of experimental and numerical force-displacement curves of unidirectional delamination tests specimens fabricated using hot-press method.

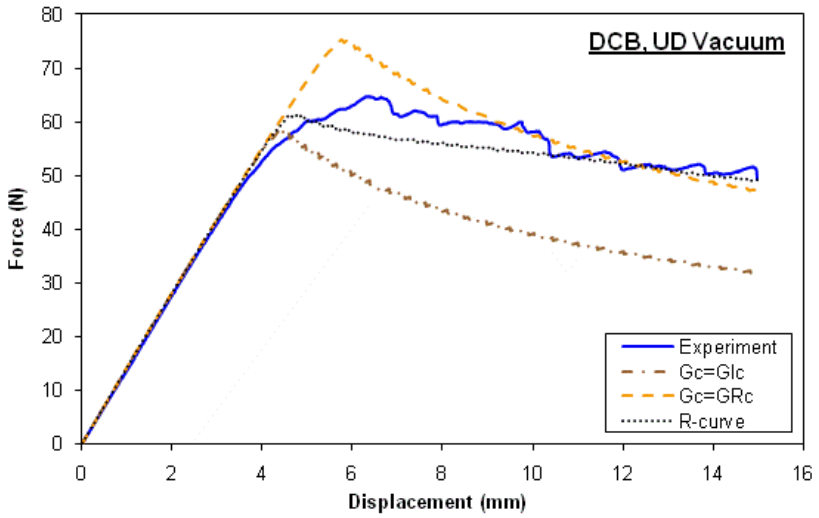

(a) DCB

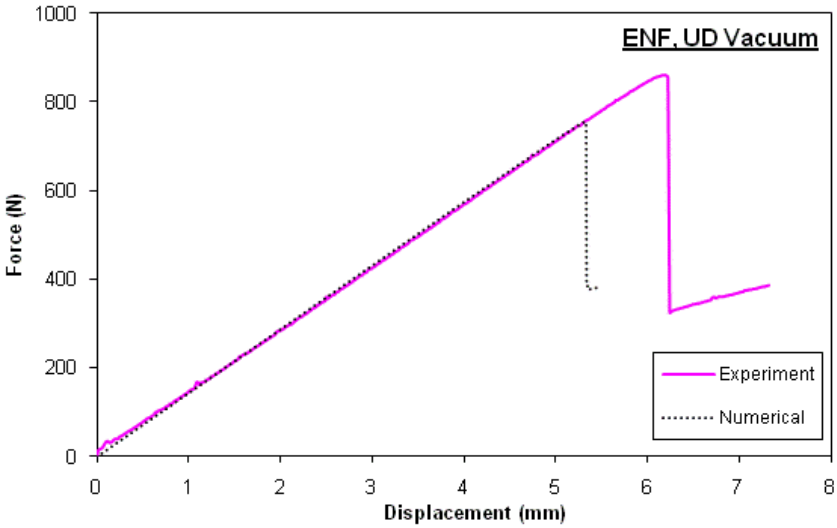

(b) ENF

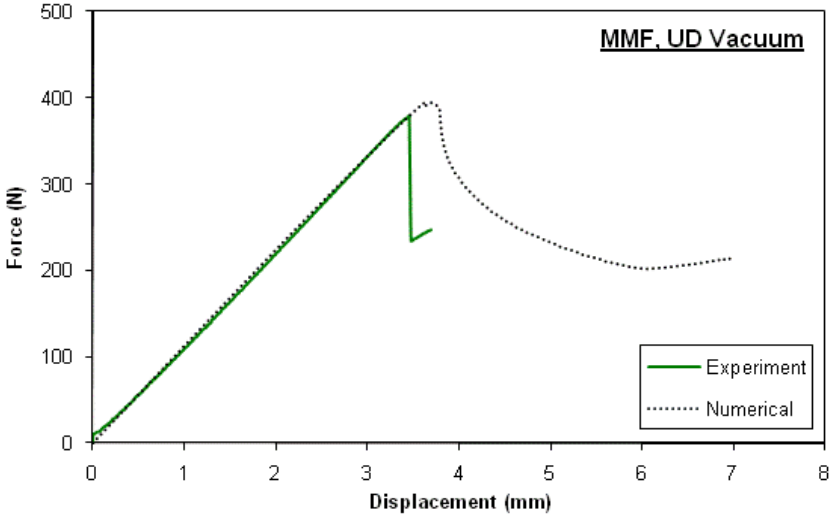

(c) MMF

Figure 4.30: Comparison of experimental and numerical force-displacement curves of unidirectional delamination tests specimens fabricated by vacuum-bagging method.

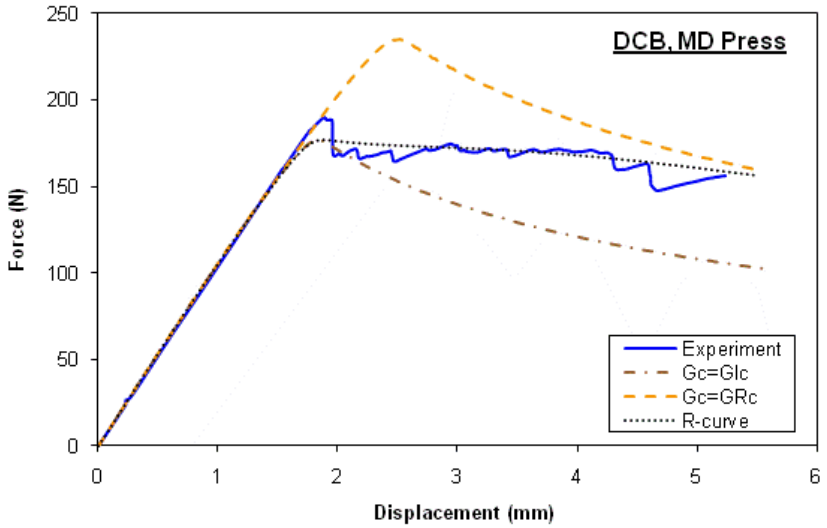

(a) DCB

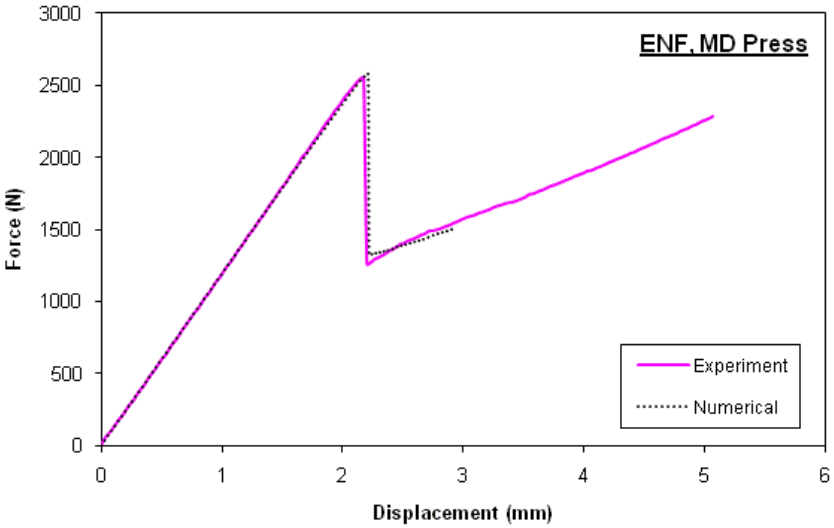

(b) ENF

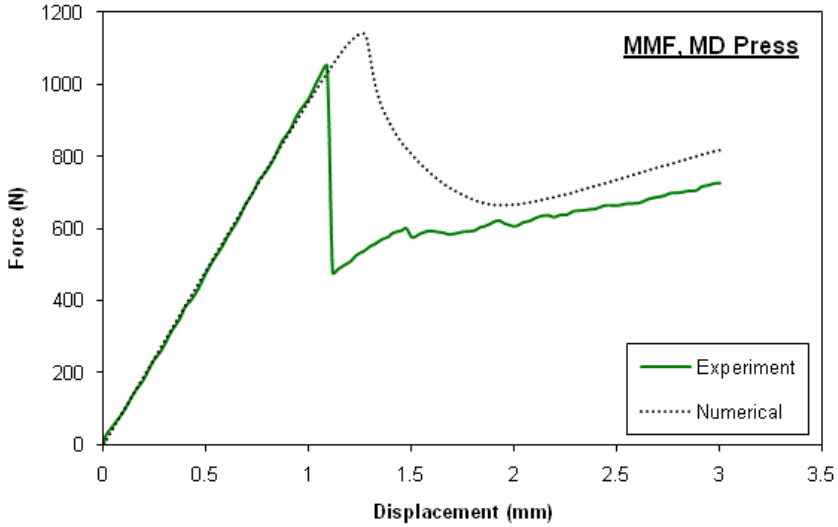

(c) MMF

Figure 4.31: Comparison of experimental and numerical force-displacement curves of multidirectional delamination tests specimens fabricated by hot-press method.

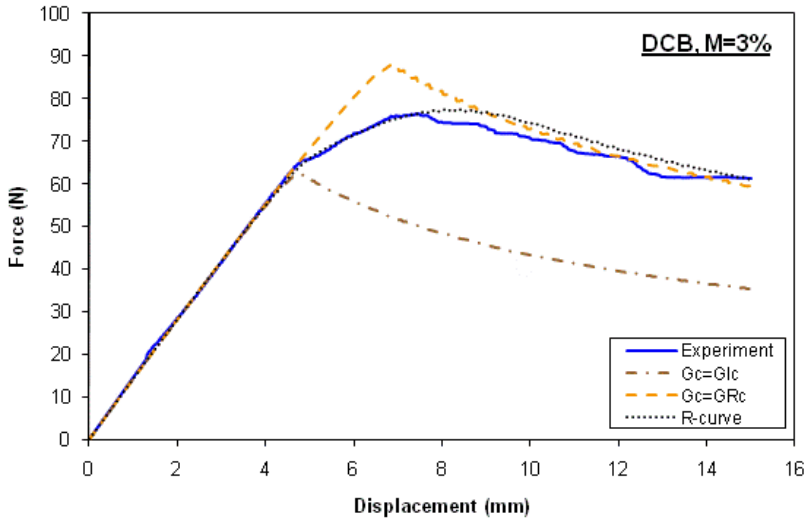

(a) DCB

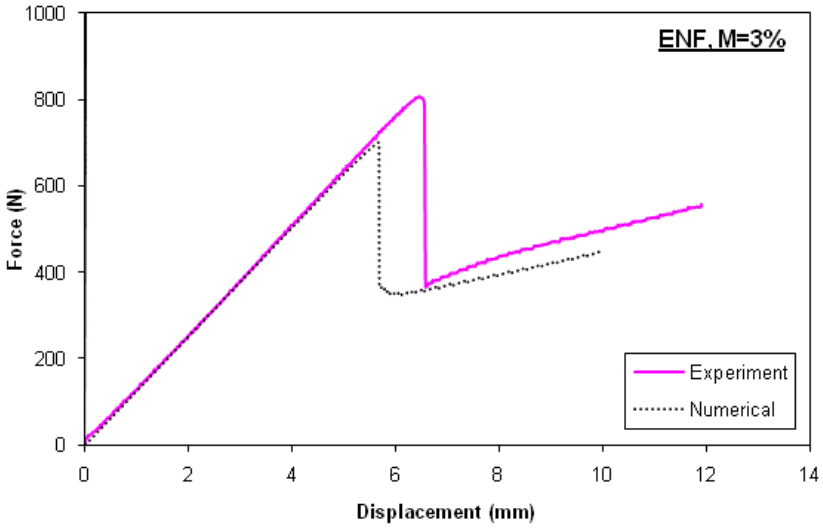

(b) ENF

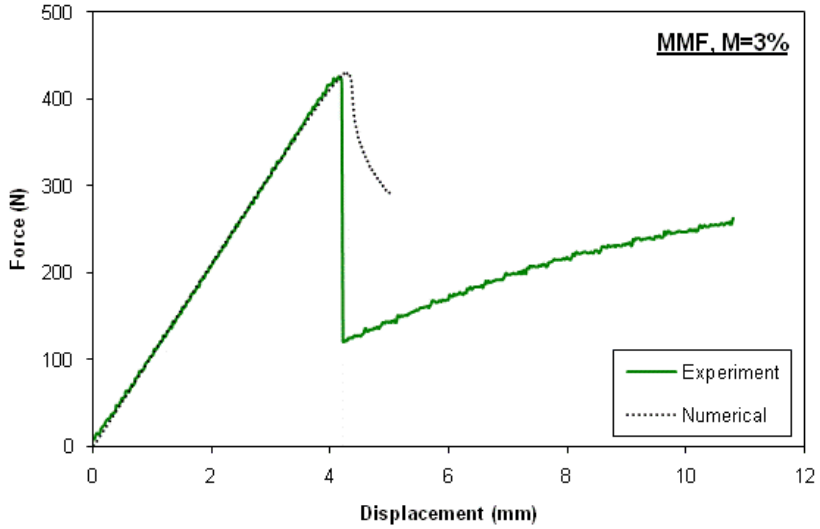

(c) MMF

Figure 4.32: Comparison of experimental and numerical force-displacement curves of unidirectional delamination tests specimens at M=3%.

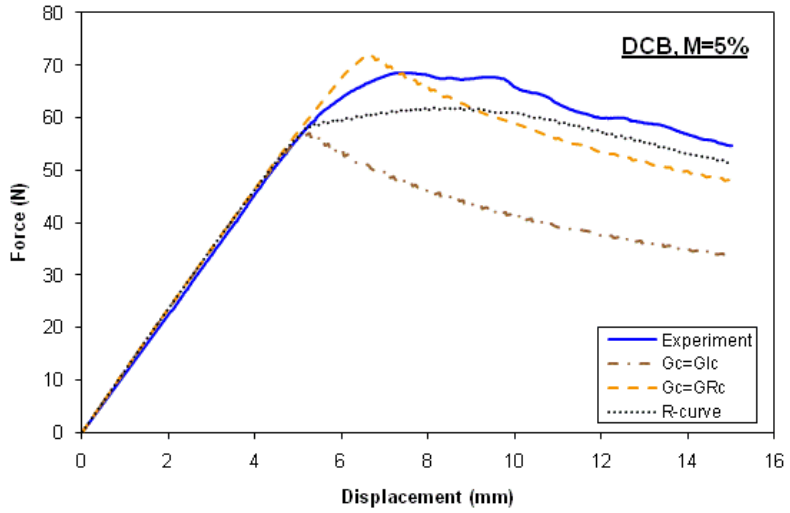

(a) DCB

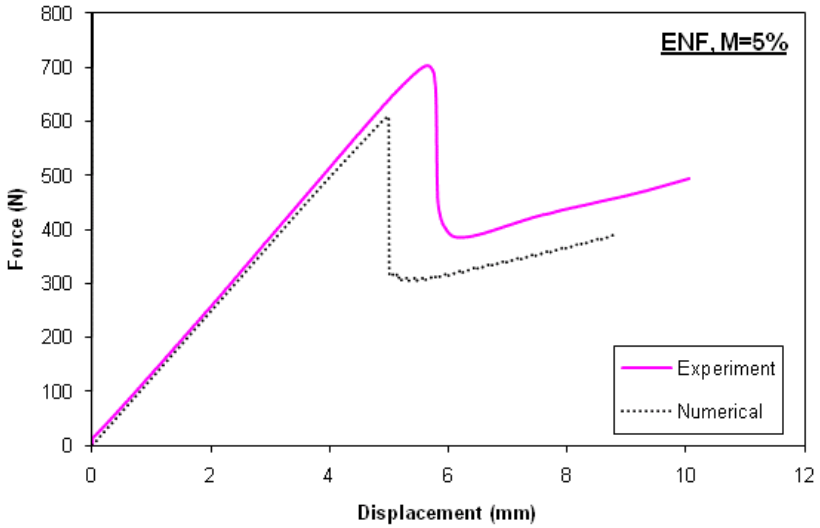

(b) ENF

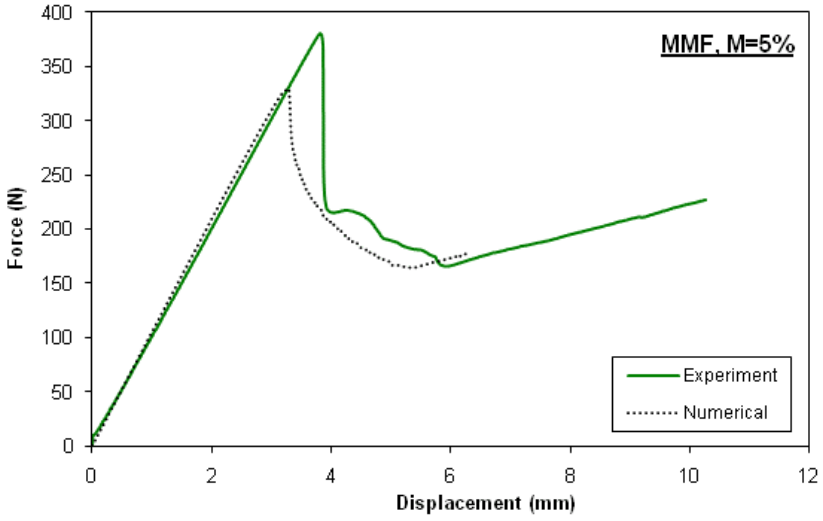

(c) MMF

Figure 4.33: Comparison of experimental and numerical force-displacement curves of unidirectional delamination tests specimens at M=5%.

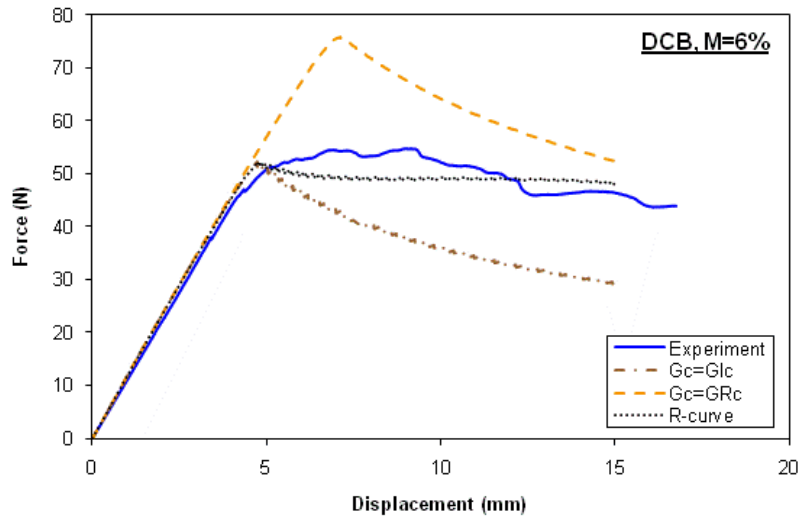

(a) DCB

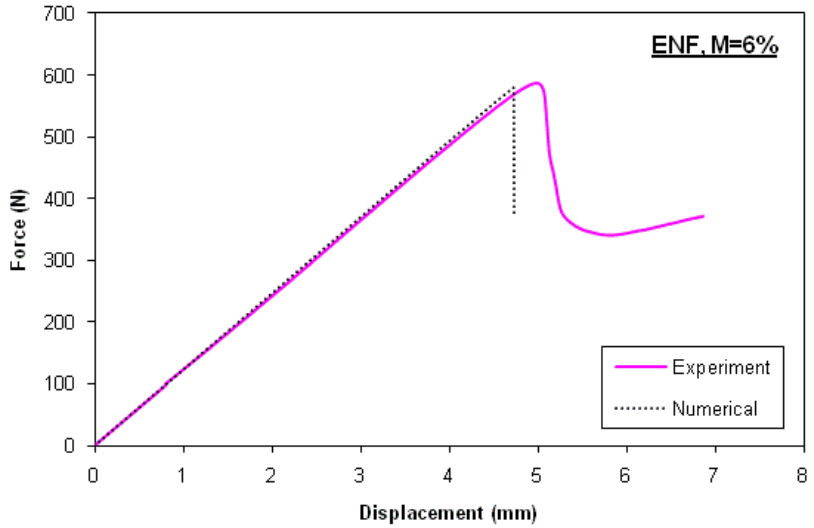

(b) ENF

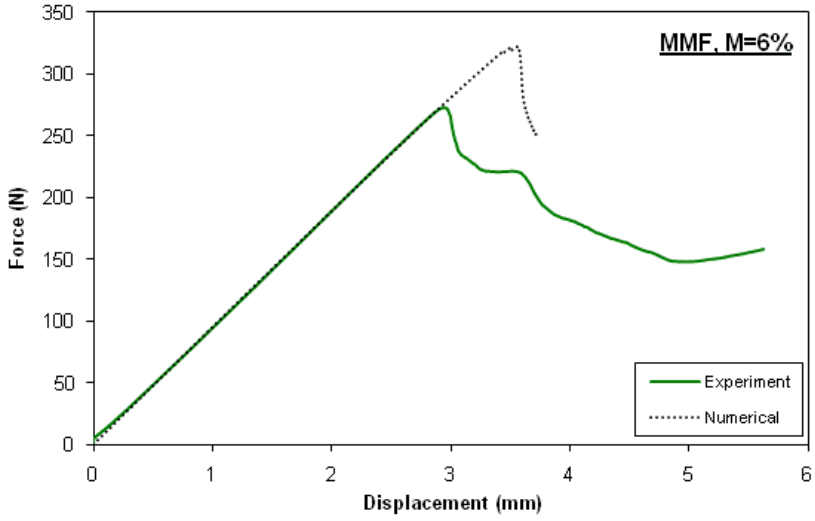

(c) MMF

Figure 4.34: Comparison of experimental and numerical force-displacement curves of unidirectional delamination tests specimens at M=6%.

Table 4.6: Summary of the comparison of experimental and numerical force-displacement curves among different composite fracture tests.

Test	DCB			ENF			MMF		
	Peak load (% diff)	Slope (% diff)	Softening behaviour	Peak load (% diff)	Slope (% diff)	Softening behaviour	Peak load (% diff)	Slope (% diff)	Softening behaviour
UD Press	3.66	3.63	Good	10.99	0.14	Good	0.96	2.53	Moderate
UD Vacuum	18.95	0.31	Moderate	15.15	6.36	Good	3.61	0.27	Moderate
MD Press	7.01	14.64	Good	1.10	11.36	Good	8.69	10.36	Moderate
UD M=3%	6.83	3.03	Good	13.08	4.88	Good	1.14	5.79	Moderate
UD M=5%	0.27	10.36	Moderate	13.36	4.22	Good	13.43	2.53	Moderate
UD M=6%	10.11	2.01	Moderate	1.12	1.65	Good	17.69	1.70	Moderate

4.5. Summary

In this chapter, the variations of the mechanical properties at different moisture contents are presented. In addition, finite element simulations are also carried out to study the delamination behaviour of DCB, ENF and MMF specimens. The mode I fibre bridging effect is studied by including R-curves constitution method, proposition of a new empirical model to fit R-curves and implementation the R-curve effect into the finite element models using linear-exponential traction separation relationship. All of these works have conduced to good correlation between experimental and numerical results.

In addition, a residual property model for aged composite is proposed and applied to all experimental results with success.

Concretely, it can be summarised that:

i. Longitudinal strength, longitudinal modulus, shear modulus and Poisson's ratio of the carbon/epoxy composite are not sensitive to water attack, whereas significant reduction in shear strength (maximum of ≈30%), transverse strength (maximum of ≈75%) and transverse modulus (maximum of ≈35%) is observed;

ii. The variation of the elementary properties measured by tensile tests (longitudinal, transverse and shear) could be fitted using the exponential decay residual property model (RPM) by Papanicolaou et al. [29] written as $P_r / P_o = s + (1-s)\exp(-sM)$;

iii. The fracture toughness of vacuum-bagging technique is always lower compared to hot-press technique, with approximately 12%, 25% and 30% lower for DCB, MMF and ENF cases, respectively;

iv. Between laminates with adjacent plies of [0//0] and [0//45], mode I fracture toughness is invariant with the fibre orientation, whereas mode II and mixed-mode I+II fracture toughness for [0//0] laminate is higher than [0//45] laminate;

v. Under moisture effects, slight increment in the mode I fracture toughness at the initial stage is observed, and dropped after that (≈20% at M=6%). As for mixed-mode I+II fracture toughness, it is almost invariant at M=3%, and 50% reduction in the fracture toughness is observed after long ageing periods (M=5 and 6%). Mode II fracture toughness decreases progressively with the moisture content. At M=6%, only 50% of its dry value is retained. It seems that moisture effect is more significant when mode II participation increases. It is expected that surface morphology analysis through scanning electron micrograph observation would provide more useful information on the delamination behaviour;

vi. A original residual property model (RPM) is proposed based on the results expressed by $P_r / P_o = 1-(1-s)\left(M/M_m\right)^{\zeta}$. It is found to fit well the variation of the interface properties with moisture content. This model has the advantage of a high flexibility in fitting various property variation trends. Good prediction is also obtained by applying this RPM to the elementary tensile properties. It would be good to carry out the mechanical testing under compressive loading to not only understand better the mechanical behaviour of the carbon/epoxy composite but also verify the applicability of the RPM to fit compressive properties;

vii. A new linear-exponential traction-separation law (shown in the equation below) is proposed to describe the fibre bridging behaviour in mode I delamination. The model fits comparatively well the experimental R-curves in various cases (unidirectional vaccum-bagging, multidirectional hot-press and all unidirectional wet DCB specimens);

$$dG = \frac{t_i(\delta_f - \delta_i)}{\gamma}\left[1-\exp\left(-\gamma\frac{\delta-\delta_i}{\delta_f-\delta_i}\right)\right]$$

viii. Through finite element simulations, good correlation is found between the experimental and numerical force-displacement curves for DCB (with R-curve modelling), ENF and MMF specimens.

CHAPTER 5. MOISTURE EFFECTS ON THE DELAMINATION BEHAVIOUR OF ADHESIVE BONDED CARBON/EPOXY COMPOSITE JOINTS

5.1.Introduction

This chapter deals with the moisture effects on the delamination behaviour of adhesive bonded composite joints. The tests of double cantilever beam (DCB), 3-point end notched flexure (ENF) and mixed-mode flexure (MMF) are performed on dry and wet specimens to characterise mode I, mode II and mixed-mode I+II delamination behaviour, respectively. The first series of the experiments compares the ductile Araldite2015 and brittle ESP110 adhesive bonded joints. Then, fracture tests on the plasma treated adherend surfaces bonded with Araldite2015 adhesive are carried out. Next, the fracture behaviour of Araldite2015 bonded composite joints aged at various moisture levels is studied. It is followed by R-curve analyses of the fracture specimens. Finally, finite element simulations are carried out on all delamination cases. Specifically, continuum damage modelling (CDM) is employed to simulate the delamination behaviour of the adhesive with water effects. The CDM parameters are calibrated and some guidelines in choosing the parameters are suggested.

5.2.Experimental details

For the adhesive bonded composite joints tested in this chapter, all specimens are prepared using T600S/R368-1 carbon/epoxy composite with stacking sequence of $[0]_8$ as adherends. The composite plates are fabricated using the same procedure as described in Section 3.2.1. Two types of adhesives are used, one of them is a two-part ductile adhesive Araldite2015 and another one is a single-part brittle adhesive ESP110. The major mechanical properties of both adhesives are listed in Table 5.1. It should be noted that ESP110 adhesive is not perfectly brittle. Nevertheless, it is comparatively stiffer and more brittle than Araldite2015. Besides, two surface preparation methods: sandpaper polishing and plasma treatment, are employed to investigate their effects. For sandpaper polished specimens, surfaces are first polished with fine grade sandpaper and followed by cleaning with acetone before bonding. As for plasma treated samples, the bonding surfaces are cleaned by iso-propanol before the treatment using plasmatreat PT60 at 3m/min. Composite plates with $200\times130mm^2$ size are bonded immediately after the treatment. The pre-crack is initiated by placing a 15μm Teflon film on the upper substrate. To ensure uniform and consistent adhesive thickness of 0.2mm across the bonding surfaces, the adhesive bonded composites are clamped with steel plates with controlled thickness bars on both sides of the plates. Composite plates bonded with Araldite2015 are heated at 50^oC for 2 hours, whereas for ESP110 bonded specimens, 120^oC for 1 hour is applied for adhesive curing.

Table 5.1: Major mechanical properties of Araldite2015 and ESP110 adhesives.

Properties	Araldite2015 [262-263]	ESP110 [264-265]
Young's modulus, E (MPa)	1850	6000
Poisson's ratio, v	0.33	0.33
Tensile yield strength, σ_y (MPa)	13	40
Tensile failure strength, σ_f (MPa)	22	64
Tensile failure strain, ε_f (%)	4.77	2.33

Ageing tests are carried out only on sandpaper polished composite plates bonded with Araldite2015. To ensure more uniform water absorption through the surfaces, the adhesive bonded composite plates are sealed with aluminium foil at whole edges before being immersed in demineralised water at 70^{o}C. In order to ensure continuous water ingression, the plates are only taken out from the environment chamber after fixed intervals of ageing period for testing. The intervals are the same as the fracture tests for composite plates, which correspond to moisture content of M=3%, 5% and 6%. All dry and wet adhesive bonded plates are cut into specimens with 20mm width using diamond coated abrasive cutting blade with coolant to obtain DCB, ENF and MMF specimens. The configurations of the specimens are schematised in Figure 5.1. Similarly, the half span length, L is always set to be 60mm for both ENF and MMF tests.

All tests are conducted at imposed cross-head speed of 1mm/min on Shimazdu testing machine with load cell capacity of 5kN. At least three replicates are tested for each series of specimens except plasma treated specimens (two for DCB and ENF respectively due to the limitation in the specimens). All tests are conducted at ambient condition.

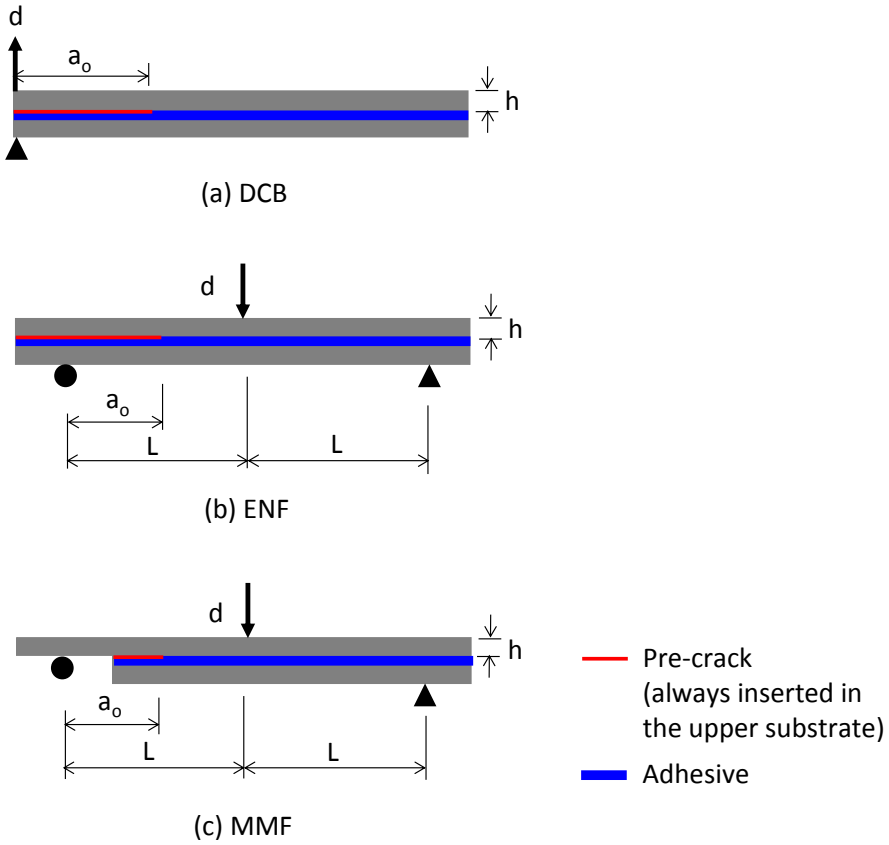

Figure 5.1: Configurations of adhesive bonded delamination tests specimens.

5.3.Determination of fracture toughness values

Similar to Section 4.4, the fracture toughness of the adhesive bonded joints is also determined at non-linear (NL) point. This point is easy to be determined in DCB and MMF cases due to the existence of comparatively initial linear region. However, due to significant non-linear region observed in aged ENF specimens (M=3%, 5% and 6%), it is thus necessary to verify whether the departure of non-linearity in ENF specimens indicates or not the delamination initiation. In this study, a unidirectional strain gauge is attached at the crack tip location of the upper substrate of the ENF specimens, as shown in Figure 5.2, to help the determination of the critical load. Figure 5.3 displays typical force/strain versus imposed displacement curves of ENF specimens at M=3%, 5% and 6%, respectively. Results verify that the peak load is the corresponding value for the initiation of the crack propagation. Hence, the calculation for the mode II fracture toughness will be based on the peak load values.

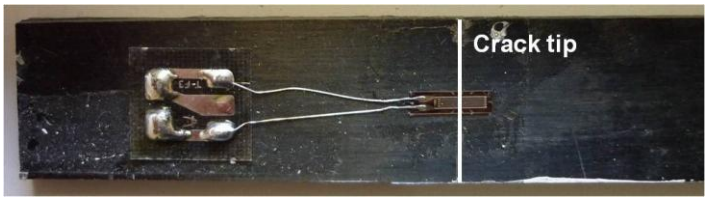

Figure 5.2: Location of strain gauge attached on upper adherend of an ENF specimen.

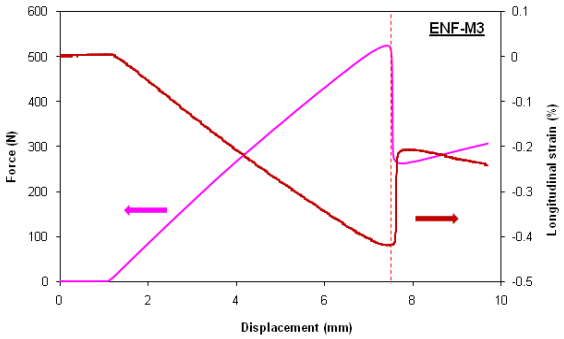

(a) M=3%

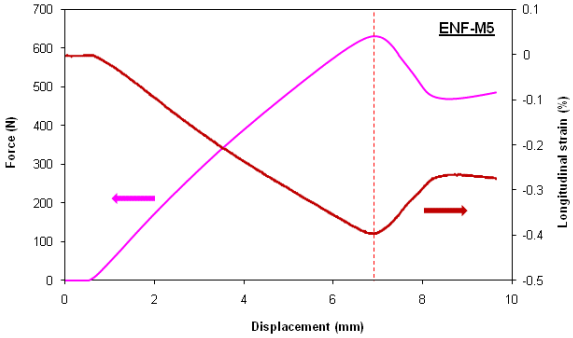

(b) M=5%

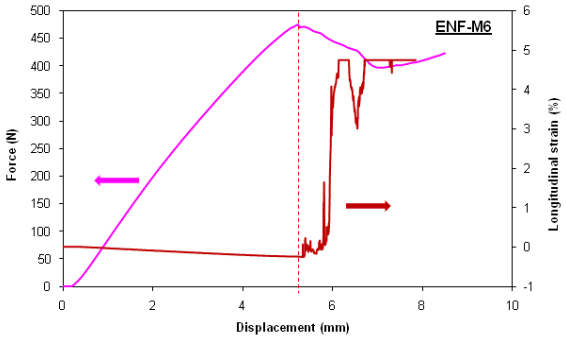

(c) M=6%

Figure 5.3: Force/strain- versus imposed displacement curves of ENF specimens at various moisture levels.

5.4.Effects of adhesive type on delamination behaviour

Figure 5.4 illustrates mode I, mode II and mixed-mode I+II fracture toughness of Araldite2015 and ESP110 bonded composite joints without ageing. In order to establish the mixed-mode criterion necessary to numerical simulation, the fitted material parameter, η in

the mixed-mode criterion (Equation (2.47)) [157-158] expressed by $G_{TC} = G_{IC} + (G_{IIC} - G_{IC})\left(\frac{G_{II}}{G_I + G_{II}}\right)^{\eta}$ is also given in the same figure.

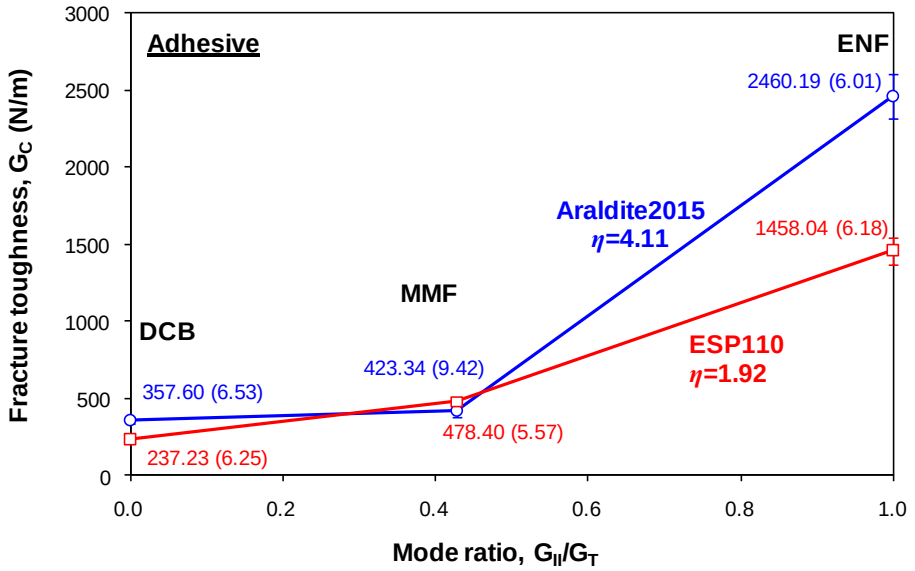

Figure 5.4: Fracture toughness of Araldite2015 and ESP110 bonded composite joints.

Results show that the mode I and mode II fracture toughness of ESP110 bonded joints are 35% and 40% lower than Araldite2015 joints. It signifies that high ductility of bulk adhesive leads to high toughness of the adhesive bonded joint under pure mode I and II. Lower G_{IIC} value in brittle adhesive (Araldite AV128/HV998) compared to ductile adhesive (Araldite2015) was also reported elsewhere [266]. However, it is surprising to see that the mixed-mode fracture toughness measured under MMF loading on ESP110 bonded joints are 13% higher than that of Araldite2015 joint, in which the order of the performance of these two adhesives is inversed.

Figure 5.5 displays the photographs of the fractured surfaces of both adhesives at all fracture mode ratio. The upper substrate is always referring to the adherend where the Teflon film is placed. It also indicates the position of the specimen during testing (the substrate with Teflon film is always facing upward, see Figure 5.1). In addition, the crack propagation path is always from the left to the right and the left side refers the initial crack tip location. It is observed that the failure in Araldite2015 bonded joints at all fracture modes is mainly cohesive towards the upper substrate, which could be due to the influence of the pre-crack. This also implies that the measured values are the fracture toughness of the adhesives (rather of the adherend/adhesive interface). As in ESP110 bonded adhesive joints, a mixture of cohesive and interface failure is observed, with more interface failure noticed at the upper adherend. Even the failure mode of the MMF specimen seems to be interface dominated, a very tiny ESP110 adhesive layer can still be seen at close view.

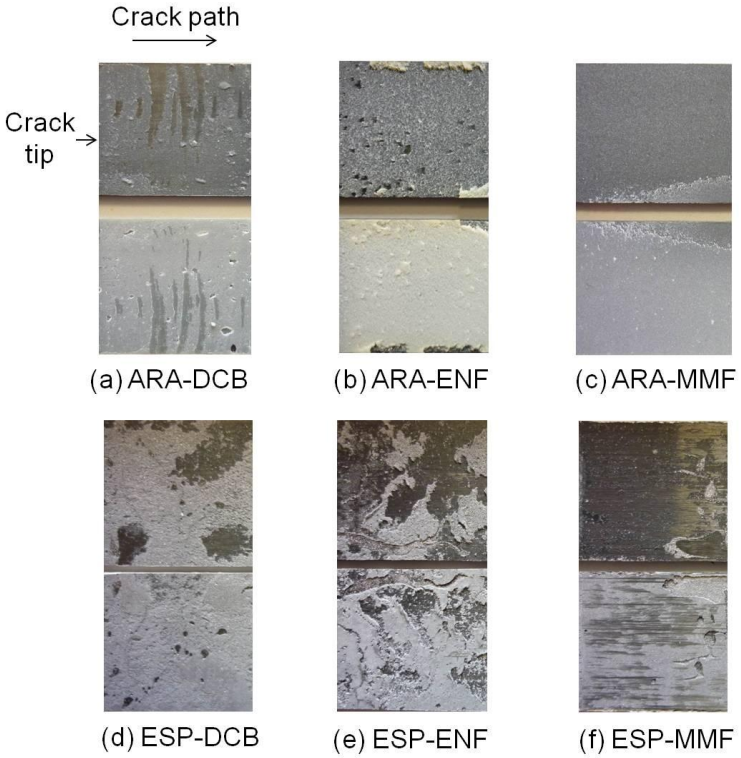

Figure 5.5: Delaminated surfaces of the adhesive bonded delamination tests specimens, where ARA and ESP refer to Araldite2015 and ESP110 adhesive, respectively.

Comparison of mode I and II toughness values of bonded joints with similar adhesives from the published works is illustrated in Table 5.2. Results show that the fracture toughness values determined in this study are generally lower compared to the reported values in the literature. For Araldite2015, even the mode II plateau value determined in this study is lower than the published G_{IIC} value [267]. The most significant difference is observed in G_{IC} values of ESP110 bonded joints, where the reported value is almost four times higher than that of the present study [268]. The actual reasons for the difference in the toughness values could be due to the difference in the substrate, surface preparation method (different grit size, number of passes and pressure applied), adhesive curing temperature and bondline thickness (for ESP110 case) [269].

Table 5.2: Comparison of mode I and II fracture toughness values of Araldite2015 and ESP110 bonded adhesive joints reported in the literature and the current study.

Adhesive	Adherend	Adhesive thickness (mm)	G_{IC} (N/m) [Ref]	G_{IIC} (N/m) [Ref]
Araldite2015	T600S/R368-1 Carbon/epoxy	0.2	358±23	2460±148[a] 3453±294[b]
	HS 160 RM Carbon/epoxy	0.2	400±40[c] [270]	4600±270[c] [267]
ESP110	T600S/R368-1 Carbon/epoxy	0.2	237±15	1458±90[a] 2354±132[b]
	T300/924 Carbon/epoxy	0.4	945±28[d] [268]	2107±274[a,c] [268] 3925±393[b,c] [268]

[a] initiation value, [b] plateau value, [c] calculated using polynomial cubic compliance calibration method. For ESP110, G_{IIC} is defined at Max/5% [268], [d] calculated using corrected beam theory.

5.5.Effects of surface treatment method on delamination behaviour

Despite the general discussion on the benefits of plasma treatment through surface cleaning, polymer chains degradation, surface material removal, surface radicals formation and polymer chains tacticity change [271] that subsequently improve the surface adhesion properties [272], contrary results are obtained in this study. Table 5.3 shows that both mode I and II fracture toughness of plasma treated specimens are approximately 80% lower compared to the sandpaper polished specimens. This could be because sandpaper polishing promotes better mechanical interlocking between the adherend and the adhesive through adhesive penetration into the crevices and pores on the surfaces of the adherend [273]. It was also reported that sandpaper abrasion exhibited better wetting behaviour compared to corona treatment and led to higher failure strength in single lap joints [274]. The authors postulated that the bonding behaviour is greatly influenced by the surface topology, where slight surface roughening through sandpaper polishing improved the mechanical interlocking between the adherend and adhesive. Figure 5.6 shows that the failure of the plasma treated specimens is mainly cohesive towards the upper substrate as well, with some crack path deflection in the adhesive, where adhesive patches are observed. Detailed surface analyses need to be carried out to verify the reasons of the difference in toughness, especially at the crack tip.

Table 5.3: Comparison of mode I and mode II fracture toughness of Araldite2015 bonded composite joints using sandpaper and plasmatreat methods.

Surface treatment method / Fracture toughness	Sandpaper	Plasmatreat	$\frac{G_{C,plasmatreat}}{G_{C,sandpaper}}$
G_{IC} (N/m)	357.60 (6.53)	55.83 (6.07)	0.16
G_{IIC} (N/m)	2460.19 (6.01)	505.03 (12.11)	0.21

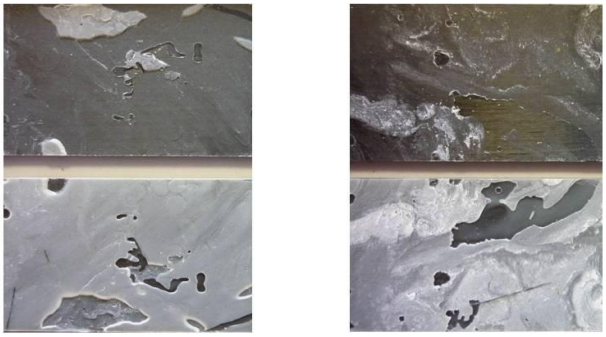

(a) Plasma-DCB (b) Plasma-ENF

Figure 5.6: Delaminated surfaces of plasma treated delamination tests specimens.

5.6.Effects of moisture absorption on delamination behaviour

The variations of mode I, mode II and mixed-mode I+II fracture toughness at different moisture content levels are displayed in Figure 5.7. The material parameter, η dropped from 4 (dry) to 2 (M=3% and 5%), and increased back to 4 (M=6%). Hence, at this stage, no specific trend in the material parameter variation could be deduced. The normalised fracture toughness presented in Figure 5.8 gives a clearer view. It is shown that regardless the loading mode, the fracture toughness decreases during the early ageing (M=3%), and increases after that at M=5%, The mixed-mode fracture toughness at M=5% is even higher than the dry value while the fracture toughness of another two modes remain lower than the dry ones. The lowest values are obtained at the highest moisture level (M=6%). Besides, at both M=3% and 5%, it

can be observed that the residual fracture toughness ratio is the highest for MMF, followed by DCB and the lowest for ENF. In addition, the moisture degradation parameter, ζ defined in the residual property model (Equation 4.9) follows the similar trend. However, it should be noted that due to the non-consistent decrement in the normalised fracture toughness, the moisture degradation parameters are merely approximated values. Additional tests at different moisture levels should be carried out in order to obtain more reliable fitting parameters. Nevertheless, it is noteworthy that at M=6%, the residual fracture toughness ratio is found to be the same at all loading modes.

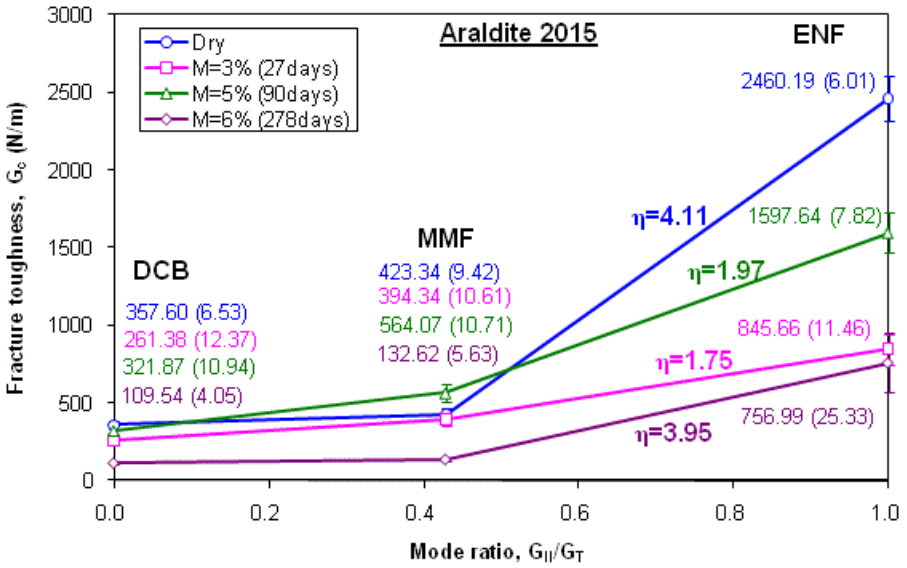

Figure 5.7: Fracture toughness of Araldite2015 bonded composite joints at various moisture content levels.

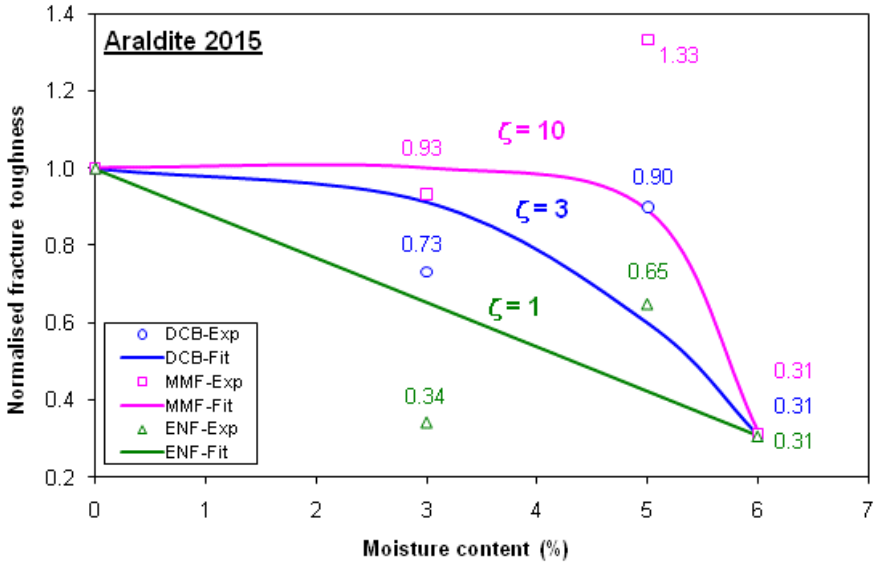

Figure 5.8: Normalised fracture toughness of Araldite2015 bonded composite joints at various moisture content levels.

In the literature, the phenomenon of "the decrement in the failure load during the early ageing period followed by subsequent increment" was commonly observed in adhesive lap joints [99, 110, 174, 178, 275-276]. In certain cases, the increment in the lap shear strength during the early ageing was even noticed [193, 197, 277]. Generally, this phenomenon is

believed to be attributed to the relief of residual stresses or stress concentration due to plasticisation that dominated over the degradation effect [111, 277-278]. Nevertheless, an overall reduction in adhesive joint strength was generally observed after prolonged ageing (see Table 2.15).

Figure 5.9 displays the fractured surfaces of DCB, ENF and MMF specimens at different moisture content levels. It could be noticed that the colour of the adhesive changed from white to slightly yellowish upon ageing. Besides, the failure mode at early ageing period (M=3%) is still mainly cohesive, despite the adhesive does not seem to be entirely uniform through the surfaces in the DCB specimen. At prolonged ageing period (M=5% and 6%), the fractured surfaces generally exhibit a mixture of cohesive and interface failure.

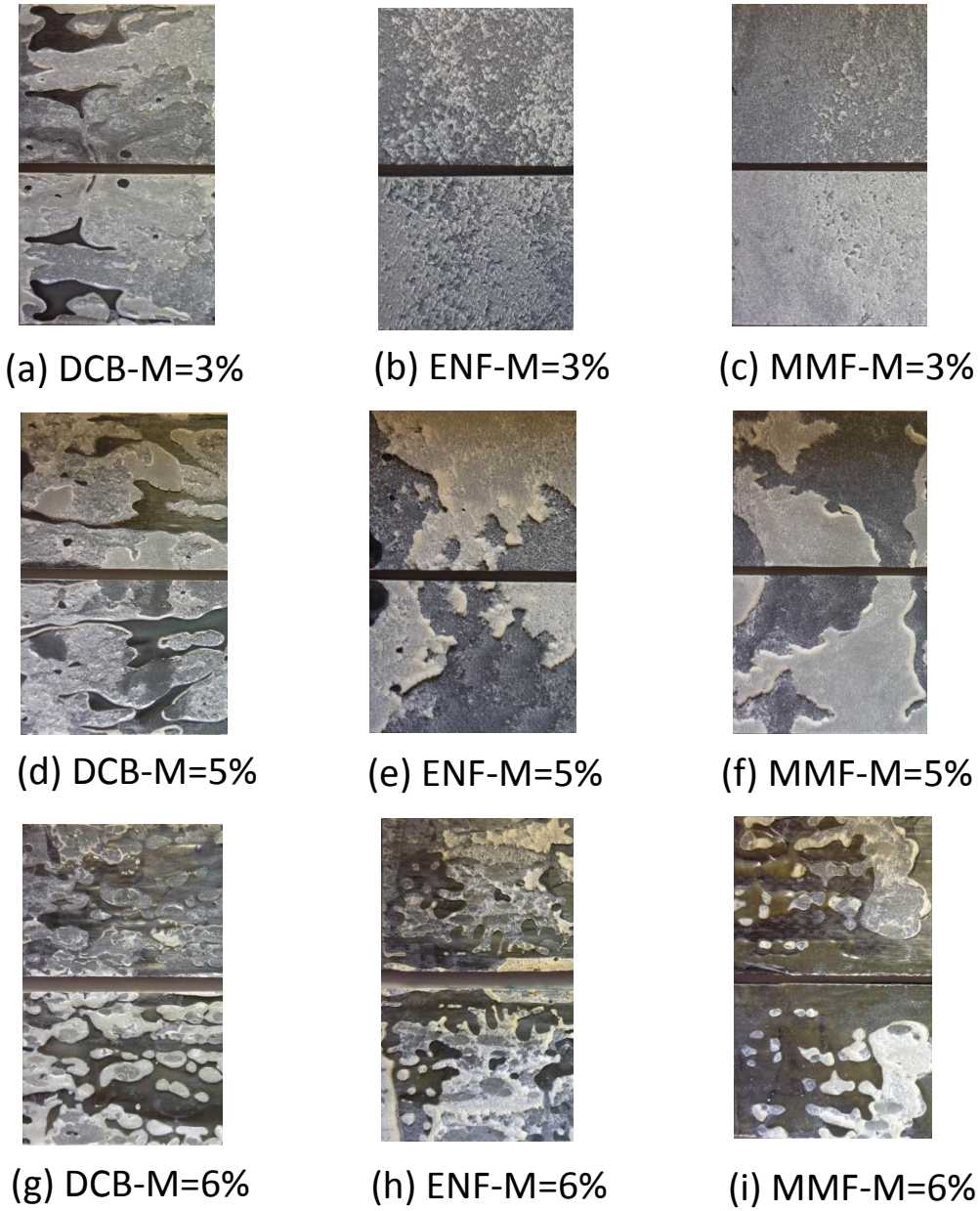

Figure 5.9: Delaminated surfaces of delamination tests specimens at various moisture content levels.

5.7.R-curve effect in adhesive bonded joints

Based on the results obtained, it is found that for mode I delamination, R-curve effect is noticed only in M=6% case, and is not observed in all MMF cases. As in mode II delamination, R-curve effect is exhibited in all cases. It is therefore necessary to quantify the mode II R-curve effect.

5.7.1.R-curve effect in mode I delamination

Figure 5.10 illustrates the R-curve behaviour of mode I DCB specimens at M=6%. The experimental R-curves are not filtered, because the drop in the fracture energy may indicate change in the crack propagation path which leads to mixed-mode delamination behaviour. The fitted R-curve using linear-exponential bridging law (Section 4.4.4) with γ=25 is also illustrated. Results show comparatively good fit within the experimental scatter.

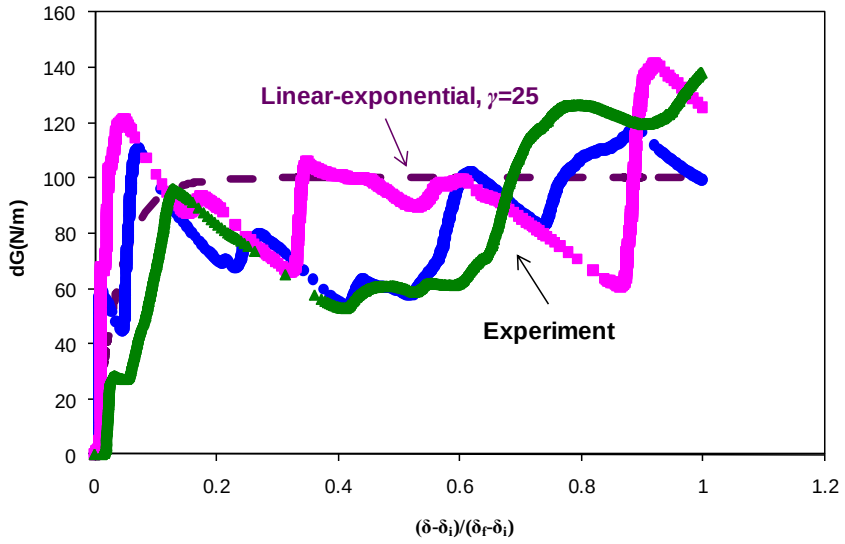

Figure 5.10: Experimental and fitted R-curves of DCB specimens at M=6%.

5.7.2.R-curve effect in mode II delamination

Figure 5.11 illustrates the experimental mode II R-curves of unaged Araldite2015 bonded composite joints prepared using sandpaper polishing method. Results show comparatively good repeatability, with maximum increment in mode II fracture energy (the plateau value) of approximately 900N/m, which corresponds to approximately 35% of augmentation. For better comparison, all other R-curves are plotted as the normalised value with their own G_{IIC}. Brittle adhesive exhibits similar initial normalised R-curve behaviour as the ductile adhesive, and becomes higher at the later stage (approximately twice of Araldite2015 at plateau), see Figure 5.12. Besides, Figure 5.13 depicts that the percentage increment in the fracture energy of plasma treated surfaces is also approximately double of the one with sandpaper polishing method. It should be noted that the G_{IIC} values exhibit the opposite trend, where the G_{IIC} of plasma treated specimens is only 20% compared to the sandpaper polished specimens. This signifies that different surface preparation method leads to different delamination behaviour (both crack initiation and propagation). Figure 5.14 compares the normalised fracture toughness increment at various moisture contents. It is observed that the percentage increment in the fracture toughness increases with the moisture content, and the value dG/G_{IIC} at plateau is approximately 0.35, 0.60, 0.70 and 1.00 for dry, M=3%, 5% and 6%, respectively. This could be due to increasing adhesive plasticisation with

the moisture content level. To confirm this, fractographic analysis through SEM observation is needed. However, it is yet to be carried out at this stage.

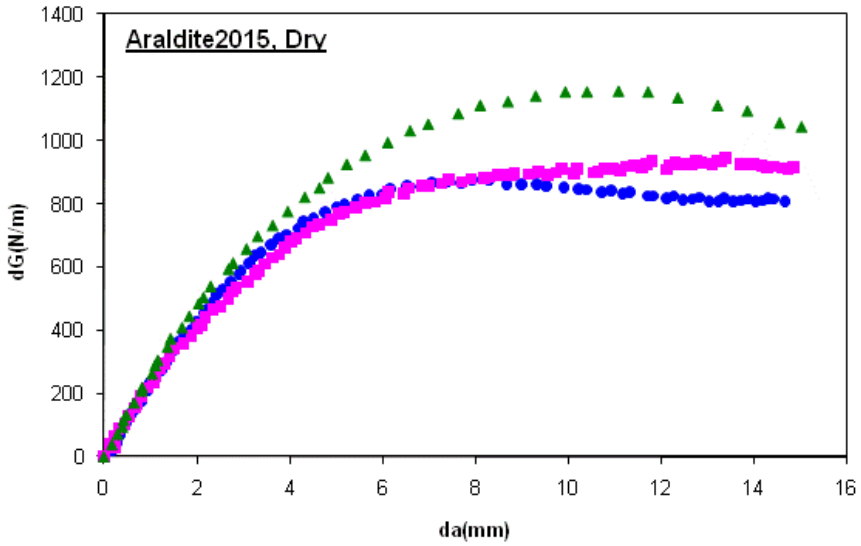

Figure 5.11: Experimental R-curves of mode II delamination of dry Araldite2015 bonded composite joints prepared using sandpaper polishing method.

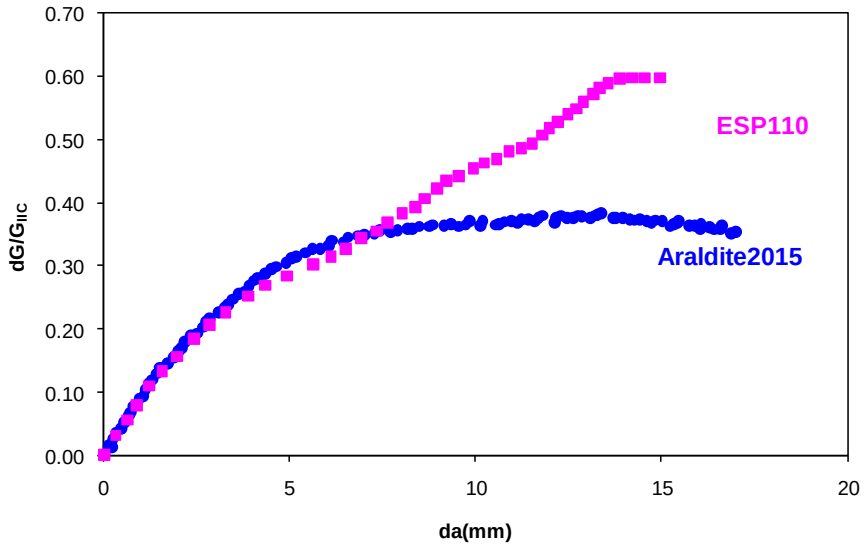

Figure 5.12: R-curves of mode II delamination of Araldite2015 and ESP110 bonded composite joints without ageing.

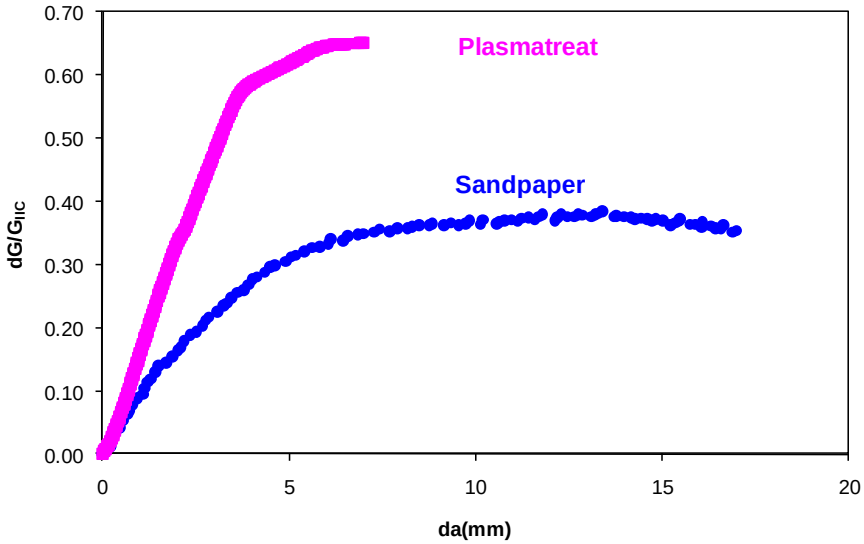

Figure 5.13: R-curves of mode II delamination of Araldite2015 bonded composite joints with sandpaper polished and plasma treated bonding surfaces.

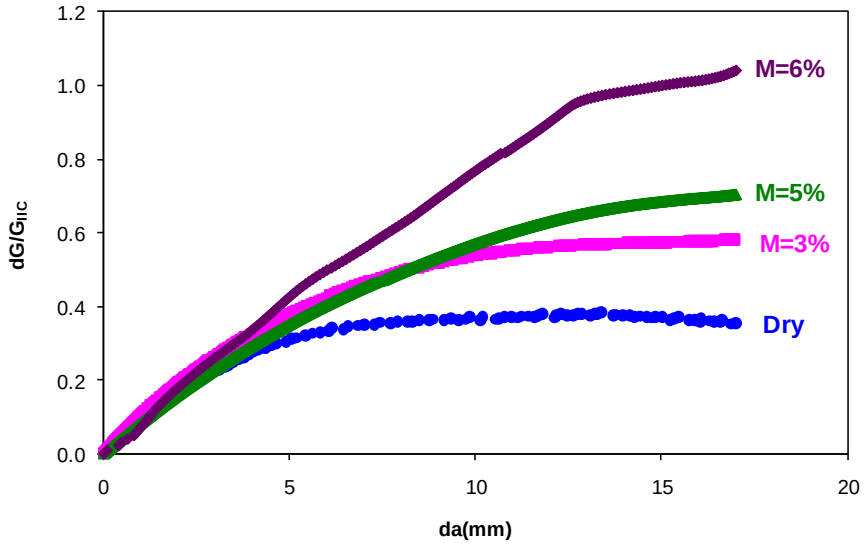

Figure 5.14: R-curves of mode II delamination of Araldite2015 bonded composite joints with sandpaper polished at various moisture content levels.

5.7.3.R-curve modelling for mode II delamination

Since there is no crack opening in mode II case, the R-curve modelling approach for mode I delamination cannot be used to describe the R-curve behaviour in mode II delamination. The linear bridging law by Anyfantis and Tsouvalis [279] which contributes to a general trapezoidal traction-separation relationship is thus adopted. This model has been reported to better predict the mode II delamination behaviour in glass/epoxy composites as compared to the power law described in the same reference. Figure 5.15 describes the corresponding linear bridging law, where the plateau region before softening includes the plasticity of the adhesive. In addition, the entire softening region represents the R-curve effect. Different notations are used as compared to Figure 4.20. This is because this bridging law will be implemented through continuum damage modelling (CDM) instead of cohesive zone modelling (CZM). The nomenclatures will be explained in detail in the following section.

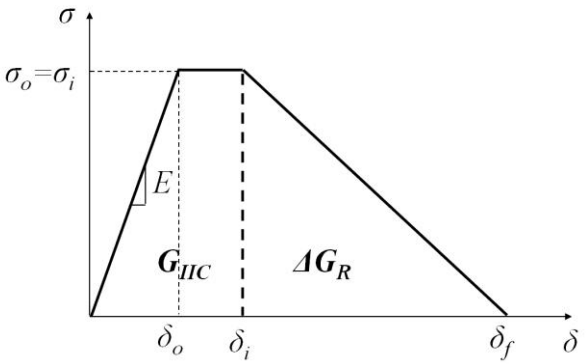

Figure 5.15: Linear bridging law for mode II R-curve modelling.

5.8.Finite element modelling of delamination behaviour in adhesive bonded joints

As the failure mode of the adhesive bonded joints is mainly cohesive or cohesive-interface mixture, it is better to model the delamination behaviour using continuum damage modelling (CDM) instead of cohesive zone modelling (CZM). In this way, the dependence of the fracture process zone (FPZ) on the adhesive thickness can be taken into account, which is discussed in Section 2.6 and illustrated in Figure 2.6.

5.8.1.Continuum damage modelling

Continuum damage modelling (CDM) utilises cohesive elements to model the adhesive layer with finite thickness using conventional material models. In other words, the constitutive behaviour of the adhesive layer is defined using its mechanical properties (such as stiffness, strength and Poisson's ratio). Cohesive elements based on CDM approach use true stress and strain measures instead of nominal stress and strain measures in CZM approach. Nevertheless, in both approaches, cohesive elements are only subjected to the through-thickness strain and two transverse shear strains. Assuming that the thickness direction is in z-axis, it means that the corresponding calculated strains are ε_{33}, ε_{13} and ε_{23}. However, it should be noted that for three-dimensional case using CDM, the other two normal stress components are not zero due to Poisson's effect. Hence, five stress components are calculated in CDM approach: σ_{11}, σ_{22}, σ_{33}, τ_{13} and τ_{23}. In CZM approach, there are only three stress components: σ_{33}, τ_{13} and τ_{23}. Besides, due to the dependency of the FPZ on the adhesive thickness, the constitutive response may not be entirely the same as the one determined using the bulk adhesive specimens. Hence, calibration may need to be carried out to accurately characterise the macroscopic material properties of the adhesive layer. In this study, von Mises yielding is assumed for the adhesive layer. A typical constitutive response of a material using the CDM approach is described in Figure 5.16. The model allows the inclusion of both elastic and plastic deformation before damage onset (at the point of D=0). The region of $0 \leq D \leq 1$ describes how the damage evolutes from the initiation (D=0) until total failure (D=1). The stress state is thus expressed as:

$$\sigma = (1-D)\sigma^* \tag{5.1}$$

To alleviate the mesh dependency during the material softening, a characteristic length, L_c, is introduced, that the fracture energy is given as:

$$G = \int_{\varepsilon_i}^{\varepsilon_f} L_c \sigma d\varepsilon = \int_{\delta_i}^{\delta_f} \sigma d\delta \tag{5.2}$$

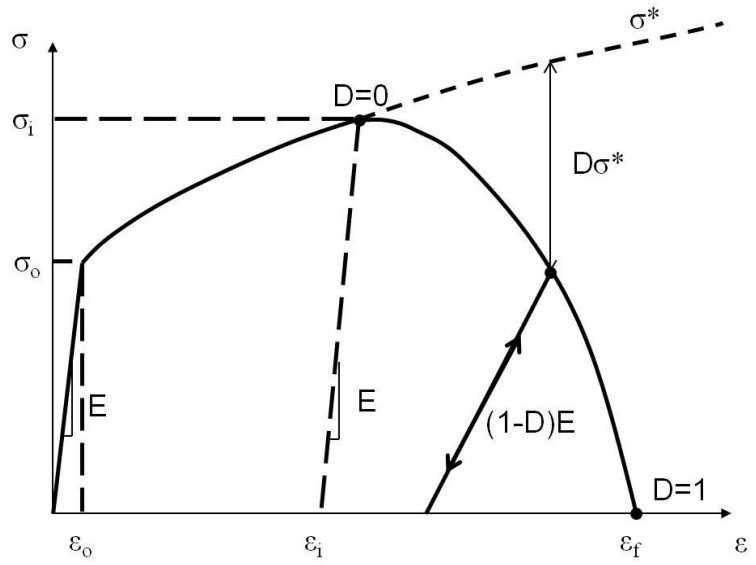

Figure 5.16: Typical constitutive response of a material using continuum damage model.

5.8.2.Determination of continuum damage parameters

The finite element models of DCB, ENF and MMF are the same as those shown in Figure 4.27 for unidirectional laminates. The only difference is that an adhesive layer with finite thickness of 0.2mm is modelled. The properties of the lamina at different moisture levels are also the same as illustrated in Table 4.4. As for the adhesives, the mechanical properties from the literature are referred ([262-263] for Araldite2015, and [264-265] for ESP110). The damage parameters are then calibrated by adjusting δ_i and σ_o, see Figure 5.15. This is based on the assumption that the thickness (adhesive layer compared to the bulk adhesive) affects the failure but not the elastic behaviour. For simplicity, σ_o is always equal to σ_i. δ_f is calculated by equalising the total area under the curve as the measured fracture toughness at each case. Besides, the R-curve effects for DCB at M=6% and ENF at all cases are always implemented using the bridging laws described in Figure 4.20 and Figure 5.15, respectively.

In addition, the stiffness and strength of Araldite2015 at different moisture content levels are estimated based on the results reported on the same adhesive aged in distilled water at 60^{o}C [105]. It should be noted that the residual normalised values, *s* are referred instead of the exact values. From the results by Bordes et al. [105], both residual stiffness and strength are estimated to be 0.2. The variations of the stiffness and strength are then estimated using the exponential decay residual property model described in Equation (4.1), which is the similar degradation trend observed by Bordes et al. [105]. For simplicity, the Poisson's ratio is assumed to be the same at all moisture levels. All continuum damage modelling parameters are shown in Table 5.4. It is worth to be mentioned that for sandpaper polished Arladite2015 bonded dry specimens, failure strength of 13MPa corresponds to the tensile yield strength reported by other researchers [263], and 43MPa corresponds to the flexural failure strength as given by the manufacturer [280]. Furthermore, the mode I (and also mixed-mode I+II) to mode II strength ratio in all cases are similar, with $\sigma_{o,DCB}/\sigma_{o,ENF}\approx 0.3$. This could provide some guidelines and convenience in the calibration of the CDM parameters, which add some physical senses to the values as well.

Table 5.4: Adhesive properties for continuum damage modelling.

	E (MPa)	ν	$\sigma_o=\sigma_i$ (MPa)	δ_i (mm)	δ_f (mm)
Araldite2015, Sandpaper polished					
DCB	1850	0.33	13	0.007	0.055
MMF			13	0.007	0.065
ENF			43	0.069	0.115
ESP110, Sandpaper polished					
DCB	6000	0.33	10	0.002	0.047
MMF			10	0.002	0.096
ENF			33	0.047	0.101
Araldite2015, Plasma treated					
DCB	1850	0.33	4	0.002	0.028
ENF			13	0.042	0.112
Araldite2015, M=3%					
DCB	1200	0.33	8	0.007	0.065
MMF			8	0.007	0.099
ENF			27	0.043	0.080
Araldite2015, M=5%					
DCB	900	0.33	6	0.007	0.107
MMF			6	0.007	0.188
ENF			21	0.088	0.145
Araldite2015, M=6%					
DCB	800	0.33	5	0.006	0.042
MMF			5	0.006	0.053
ENF			18	0.053	0.081

5.8.3.Comparison of experimental and numerical force-displacement curves

Figure 5.17 to Figure 5.22 compare the experimental and numerical force-displacement curves of DCB, ENF and MMF tests. In fact, for a better comparison, a representative experimental force-displacement curve obtained by statistical method should be plotted instead of one selected curve. However, it is not attempted at this stage. The comparison of the experimental and numerical force-displacement curves (peak load, slope and softening behaviour) is summarised in Table 5.5. Results show comparatively satisfactory correlation, with the maximum peak load difference in ESP-DCB case and maximum stiffness difference in MMF-M6% case. In addition, significant non-linear region is also observed in the numerical curve of MMF-M5%. The main reason for the discrepancies could be due to the dynamic effect in the explicit FEM analysis (CDM is only available in the explicit analysis). Besides, it could be due to the variation in the mechanical properties of the carbon/epoxy composite (particularly the longitudinal stiffness) among different plates. Nevertheless, considering the general good prediction in most of the cases and the generalisation of the mode I and II strength ratio ($\sigma_{o,DCB}/\sigma_{o,ENF}\approx 0.3$) which adds the physical significance of the parameters, the CDM parameters are not further modified.

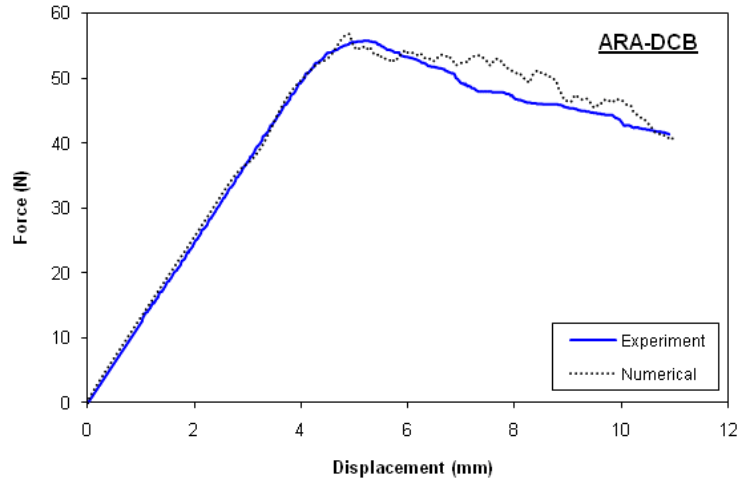

(a) DCB

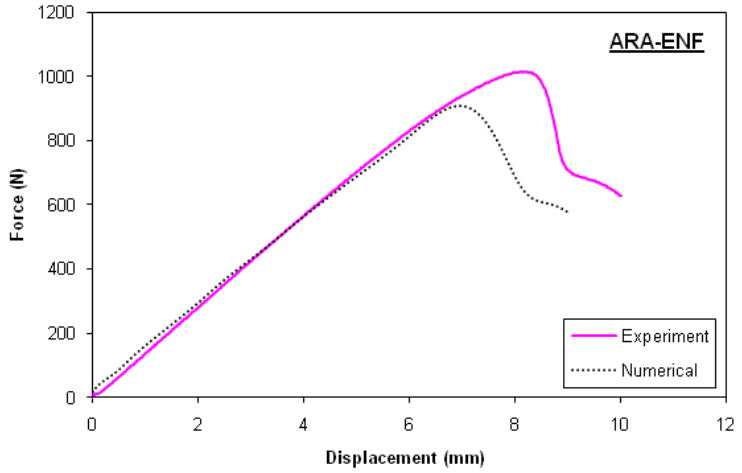

(b) ENF

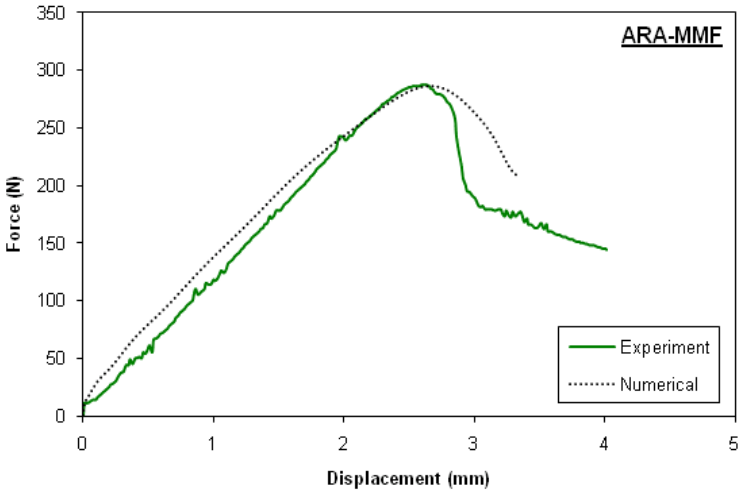

(c) MMF

Figure 5.17: Experimental and numerical force-displacement curves of Araldite2015 bonded dry specimens with sandpaper polished surfaces.

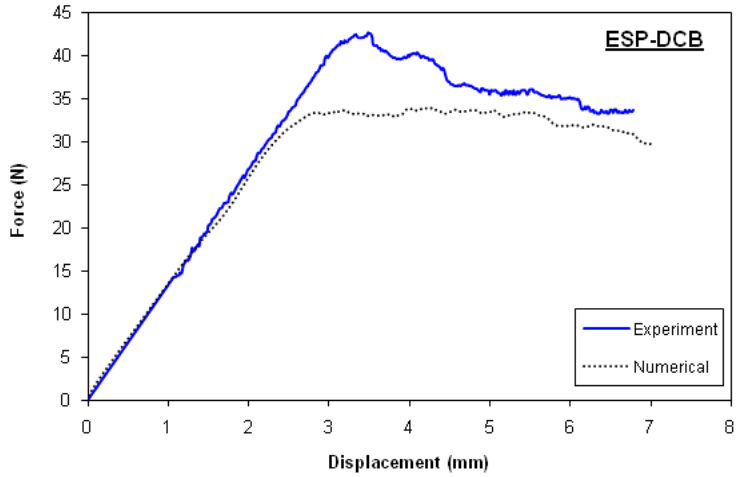

(a) DCB

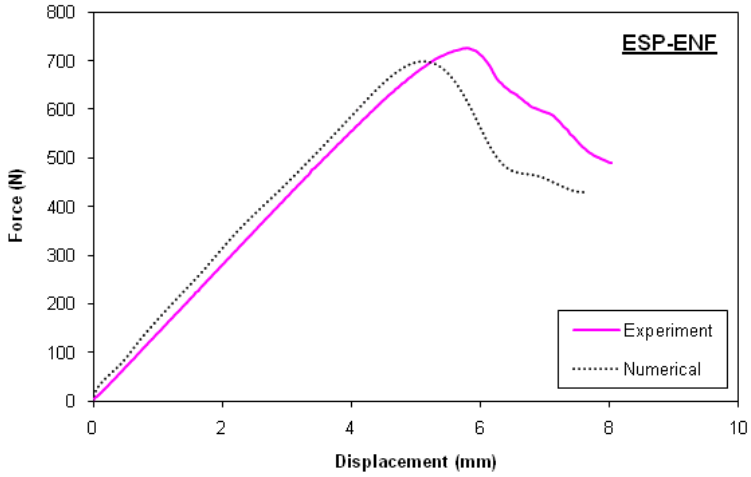

(b) ENF

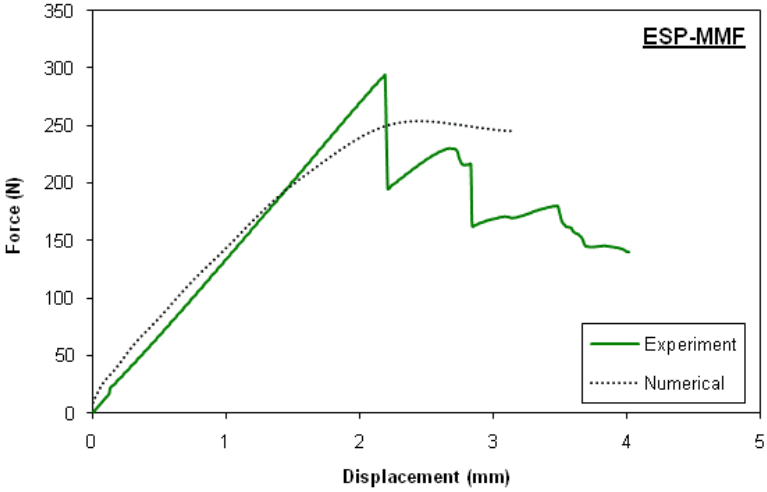

(c) MMF

Figure 5.18: Experimental and numerical force-displacement curves of ESP110 bonded dry specimens with sandpaper polished surfaces.

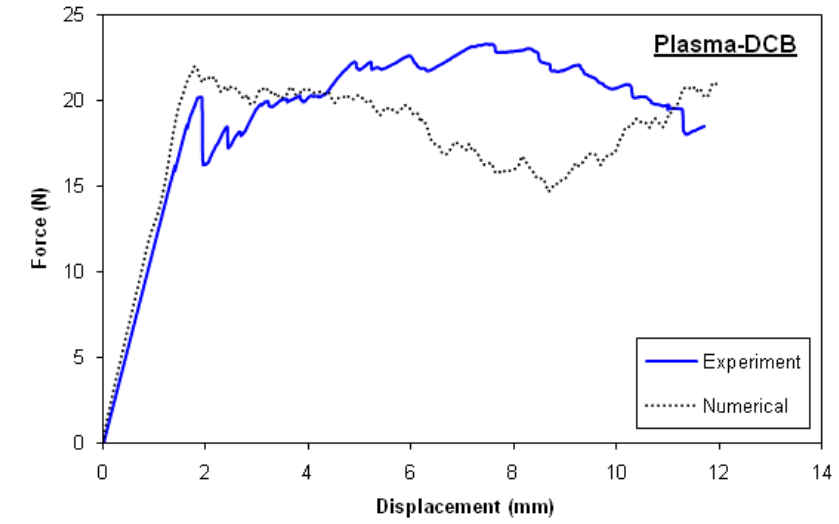

(a) DCB

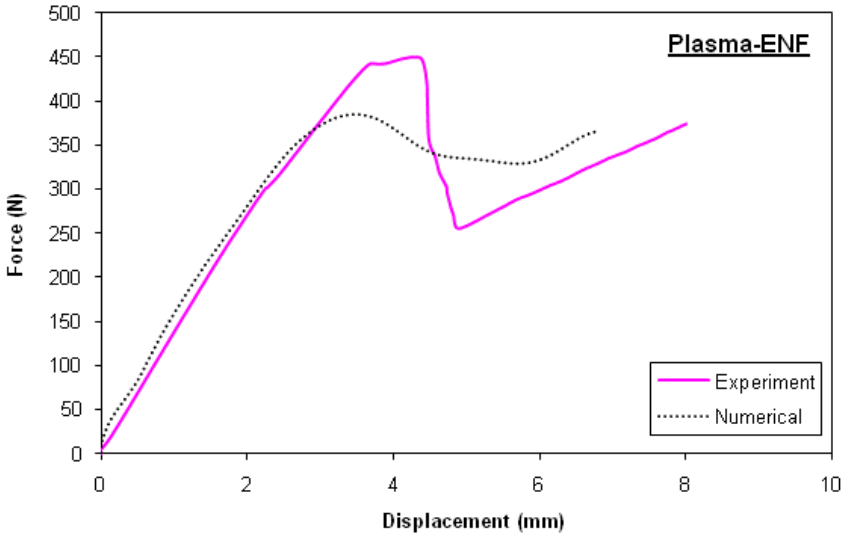

(b) ENF

Figure 5.19: Experimental and numerical force-displacement curves of Araldite2015 bonded specimens with plasma treated surfaces.

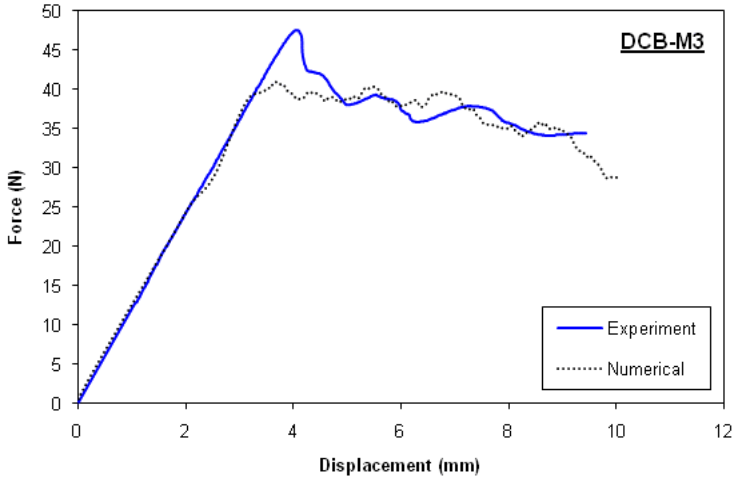

(a) DCB

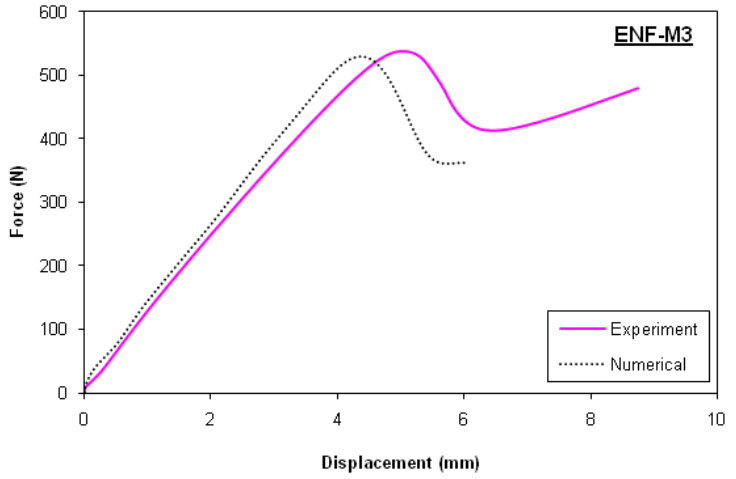

(b) ENF

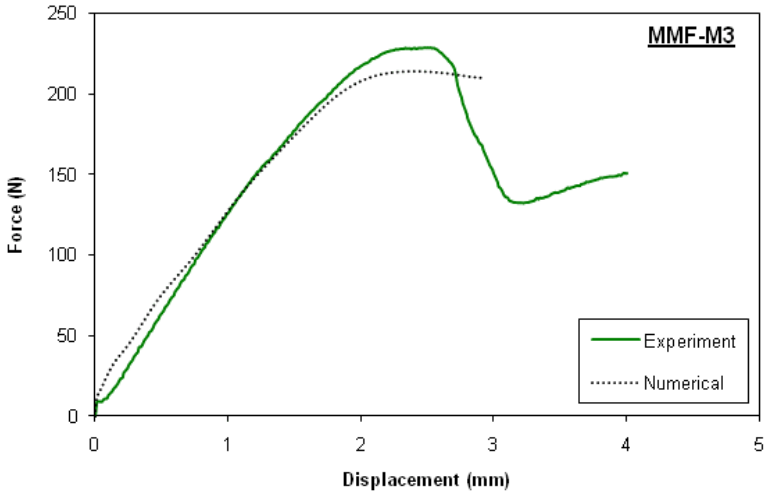

(c) MMF

Figure 5.20: Experimental and numerical force-displacement curves of Araldite2015 bonded specimens at M=3%.

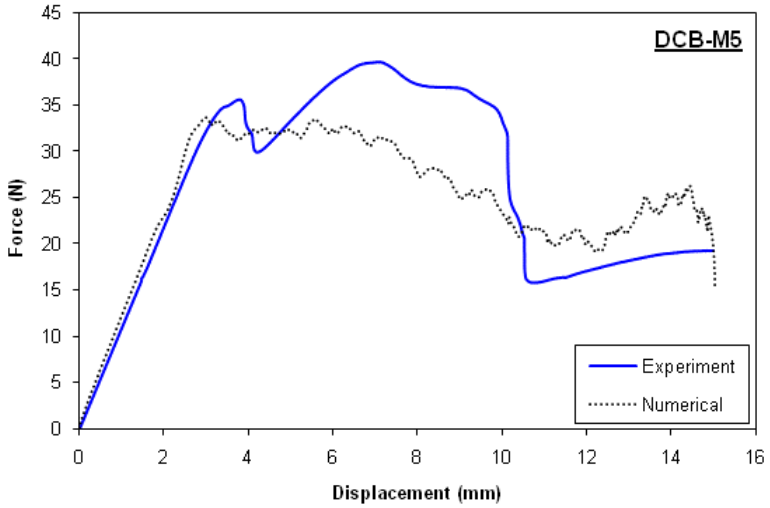

(a) DCB

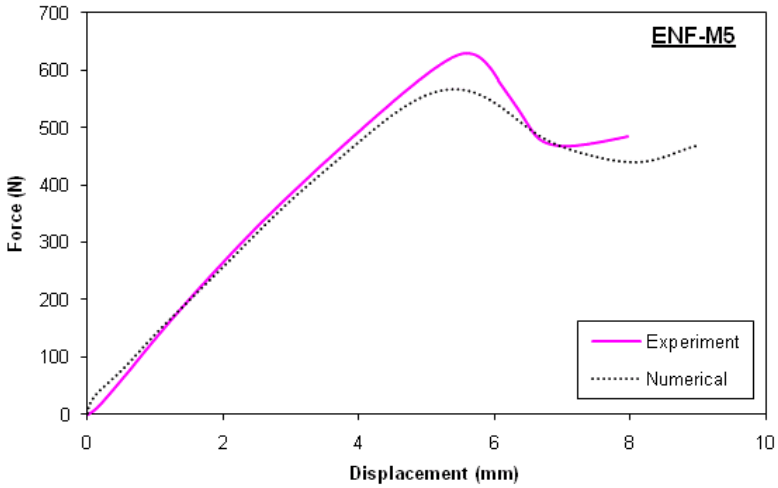

(b) ENF

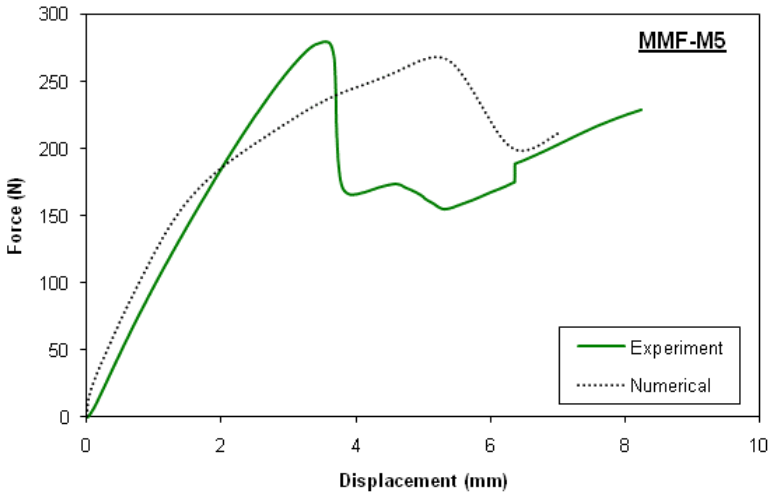

(c) MMF

Figure 5.21: Experimental and numerical force-displacement curves of Araldite2015 bonded specimens at M=5%.

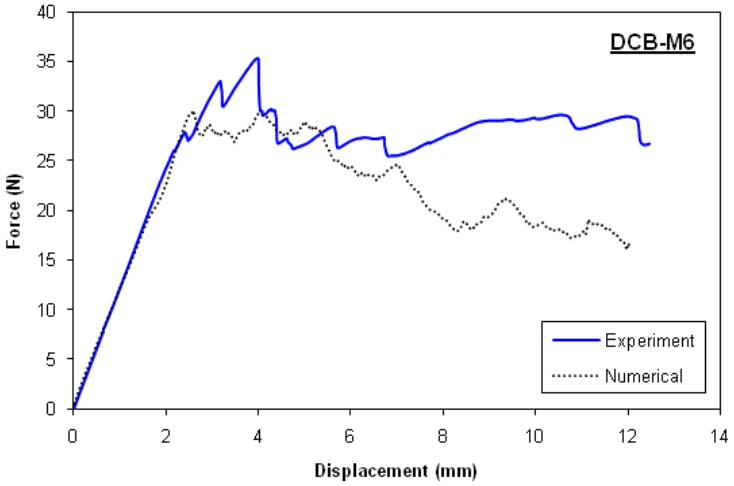

(a) DCB

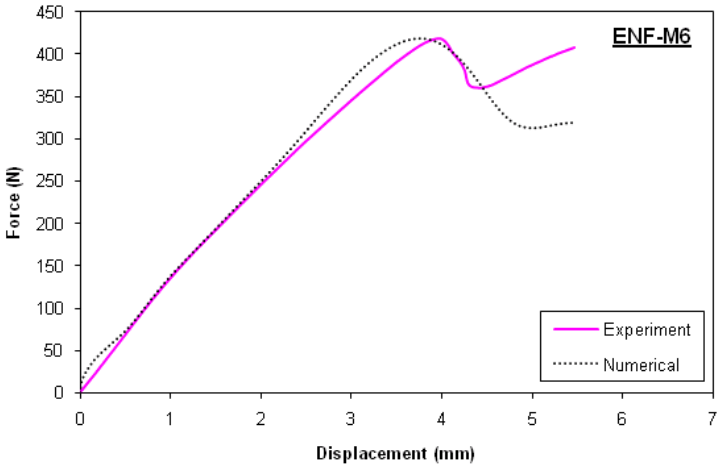

(b) ENF

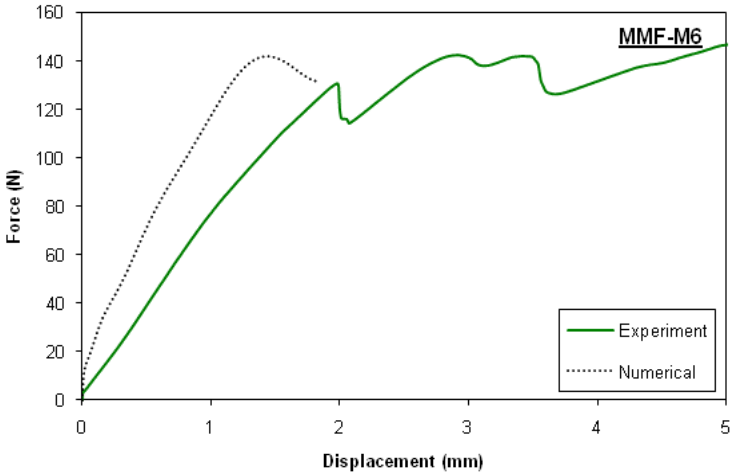

(c) MMF

Figure 5.22: Experimental and numerical force-displacement curves of Araldite2015 bonded specimens at M=6%.

Table 5.5: Summary of the comparison of experimental and numerical force-displacement curves among different adhesive fracture tests.

Test	DCB			ENF			MMF		
	Peak load (% diff)	Slope (% diff)	Softening behaviour	Peak load (% diff)	Slope (% diff)	Softening behaviour	Peak load (% diff)	Slope (% diff)	Softening behaviour
ARA	2.05	0.27	Good	10.48	6.08	Good	0.30	3.65	Good
ESP	20.61	4.31	Moderate	3.68	1.16	Good	13.73	8.39	Moderate
Plasma	8.68	8.53	Moderate	12.86	12.40	Moderate	-	-	-
M=3%	13.86	2.65	Good	1.59	13.05	Good	6.50	6.72	Good
M=5%	5.64	5.37	Moderate	10.21	5.95	Good	3.93	14.36	Poor
M=6%	8.19	6.72	Moderate	0.00	7.57	Good	8.80	49.62	Moderate

5.9.Summary

In this chapter, the delamination behaviour of different adhesive types (ductile Araldite2015 and brittle ESP110), surface treatment methods (sandpaper polished and plasma treated) and moisture content levels (dry, M=3%, 5% and 6%) are studied. The experimental results are further complemented by the numerical results. Based on the results, it can be summarised that:

i. The composite joints bonded by ductile adhesive shows higher mode I and mode II fracture toughness compared to those by the brittle adhesive. However, inversed trend is observed in mixed-mode I+II fracture toughness. The material parameter, η, defined in BK mixed-mode criterion, of the ductile adhesive is about twice of the brittle adhesive;

ii. The mode I and mode II fracture toughness of plasma treated adhesive joints are approximately 80% lower compared to the sandpaper polished joints bonded with the same adhesive. It is postulated that mechanical interlocking dominates the bonding quality of the adhesive joints;

iii. Regardless the loading mode, the fracture toughness is decreased at early ageing (M=3%), and then increased with water uptake (M=5%), finally dropped after prolonged ageing (M=6%). Approximately 30% of the residual fracture toughness is retained in all DCB, ENF and MMF cases at M=6%. No specific trend is observed in the moisture degradation parameter, ζ with the mixed-mode loading ratio;

iv. In the cases of DCB mode I delamination, detectable R-curve effect is observed only in M=6% case, whereas it is noticed in all mode II delamination cases. Mixed-mode I+II delamination does not exhibit R-curve effect. The normalised fracture toughness (dG/G_{IIC}) of both sandpaper polished ESP110 and plasma treated Araldite2015 joints is twice higher compared to sandpaper polished Araldite2015 bonded joints. Furthermore, the dG/G_{IIC} ratio increases with the moisture content. Mode I R-curve is quantified using the linear-exponential traction-separation law, and mode II R-curve is characterised through linear bridging law (trapezoidal traction-separation relationship) available in the literature;

v. Continuum damage modelling (CDM) is employed to simulate the damage of the adhesive layer in the finite element modelling, where both of the moisture effect and the R-curve effect have taken into account. The correlation between experimental and numerical results is in general quite good. Through CDM parameters calibration, it is proposed that satisfactory results could be obtained with $\sigma_{o,DCB}/\sigma_{o,ENF}\approx 0.3$;

vi. Fractographic analysis through scanning electron micrograph observation is needed to better understand the fractured surfaces, such as the plastic deformation in the adhesive.

CHAPTER 6. PROGRESSIVE DAMAGE ANALYSES OF PATCH REPAIRED COMPOSITES

6.1.Introduction

This chapter discusses the tensile behaviour of unnotched, notched and repaired quasi-isotropic laminates. Specifically, composite repairs are prepared using two different adhesives (Araldite2015 and ESP110), two patch stacking sequences ($[\pm 45]_S$ and $[\mp 45]_S$) and two different surface treatment methods (sandpaper polished and plasma treated). Experimental characterisation is accompanied by acoustic emission. In the numerical analyses, the lamina, interface and adhesive are modelled by Hashin damage model, cohesive zone model (CZM) and continuum damage model (CDM), respectively. Analyses of the acoustic emission (AE) data and the numerical simulation results lead to establishment of the relationship between the damage mechanisms (matrix cracking, adhesive failure, delamination and fibre breakage) and the amplitude ranges of AE.

6.2.Experimental details

6.2.1.Fabrication of composite plates

The material used for both parent plate and patch is T600S/R368-1 carbon/epoxy prepreg supplied by Structil. Similarly, the composite laminates are fabricated using hand lay-up technique with curing cycle as described in Figure 3.1. The stacking sequences of the quasi-isotropic parent plates are $[45/-45/0/90]_S$ and $[45/90/-45/0]_S$, and composite plates of $[0/90]_S$ are fabricated for patches.

6.2.2.Preparation of testing coupons

The cured plates are cut into specimens of $250\times50mm^2$ size in both longitudinal and transverse directions to obtain samples with stacking sequences $[45/-45/0/90]_S$, $[-45/45/90/0]_S$, $[45/90/-45/0]_S$ and $[-45/0/45/90]_S$. To study the specimen's width influence, $[-45/0/45/90]_S$ specimens at 25mm width are also prepared. For notched and repaired specimens, a central hole of 10mm diameter was drilled, which gives the diameter to width ratio as 0.2. For the repaired specimens, the parent plate is always at the stacking sequence of $[45/90/-45/0]_S$. Circular patches of 35mm diameter are prepared through milling. This provides a constant overlap length of 12.5mm, which is in the range of the generally reported values to obtain the optimum repaired strength (see Table 2.16).

The surface preparation procedure for both sandpaper polishing and plasma treated methods is as described in Section 5.2. Similarly, two types of adhesives are used, which are two part ductile adhesive Araldite2015 and single part brittle adhesive ESP110. For the patches, two stacking sequences are employed, which are $[\pm 45]_S$ and $[\mp 45]_S$, to ensure same membrane stiffness of the patch. The respective stiffness was found to be optimal for composite repair in the previous studies at the laboratory [223]. Adhesive curing procedure is also the same as mentioned in Section 5.2.

All specimens are then bonded with glass/epoxy tabs of 50mm length on both ends of the specimens. The configurations of unnotched, notched and repaired specimens are shown in Figure 6.1. Table 6.1 and Table 6.2 summarise all the tests conducted for unnotched, notched and repaired specimens.

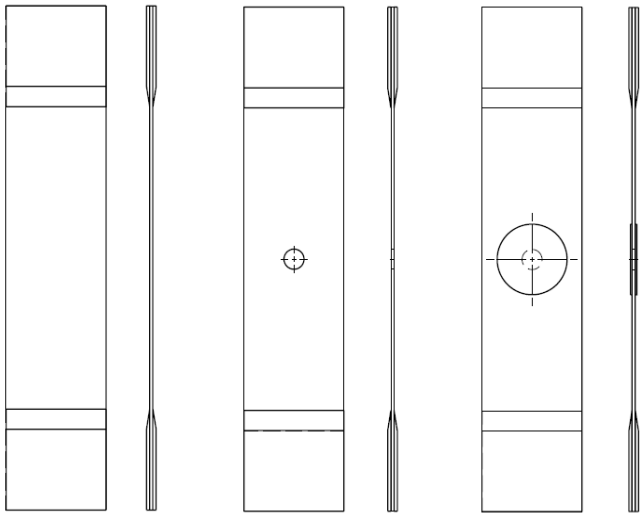

Figure 6.1: Configurations of unnotched, notched and repaired specimens.

Table 6.1: Series of unnotched and notched specimens tested.

Type	Width (mm)	Stacking sequence
Unnotched	25	$[-45/0/45/90]_S$
Unnotched and Notched	50	$[45/-45/0/90]_S$,$[-45/45/90/0]_S$, $[-45/0/45/90]_S$, $[45/90/-45/0]_S$

Table 6.2: Series of repaired specimens tested.

Adhesive	Surface treatment	Patch stacking sequence	Name
Araldite2015	Sandpaper	$[\pm 45]_S$	ARA+sp
		$[^{\mp}45]_S$	ARA-sp
	Plasma	$[^{\mp}45]_S$	ARA-pl
ESP110	Sandpaper	$[\pm 45]_S$	ESP+sp
		$[^{\mp}45]_S$	ESP-sp
	Plasma	$[^{\mp}45]_S$	ESP-pl

6.2.3.Testing and data acquisition

Tensile test is carried out on MTS DY-36 universal testing machine with load cell capacity of 100kN at crosshead speed of 1mm/min. At least three replicates are tested for each type of specimens. All tests are conducted at ambient condition. In addition, acoustic emission equipment is used for repaired specimens. The threshold value is set to be 45dB, which is the general practice at the laboratory on the acquisition of carbon/epoxy composites [281]. In order to identify the location of damage events in the repairs, three transducers are attached to the specimen, located at the centre (on the patch) and 40mm on both sides from the centre on the parent plate (Figure 6.2).

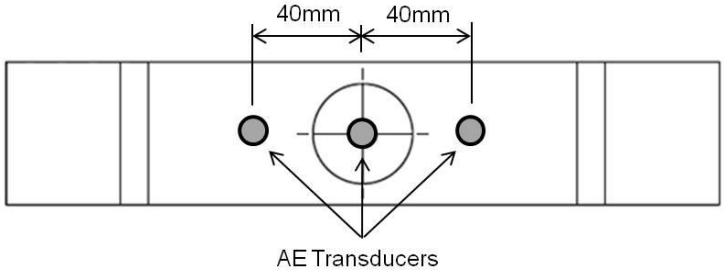

Figure 6.2: Location of acoustic emission transducers on repaired specimens.

6.3.Finite element modelling

6.3.1.Lamina damage model

Similar to the modelling approaches described in Section 4.4.6 and Section 5.8, cohesive zone model (CZM) is employed in the ply/ply interface of the composite, whereas continuum damage model (CDM) is implemented in the adhesive joint. In addition, the continuum damage model based on Hashin's criterion [282-283] is adopted to predict the damage initiation and progression in the layers of composite laminates. Each layer is modelled by continuum shell elements, where the state of the stresses is considered as in-plane stresses. The different failure modes are treated separately and failure conditions are described by the following equations:

Fibre tensile mode ($\hat{\sigma}_{11} \geq 0$), $F_{ft} = \left(\frac{\hat{\sigma}_{11}}{X^T}\right)^2 + \alpha\left(\frac{\hat{\sigma}_{12}}{S^L}\right)^2 = 1$ (6.1)

Fibre compressive mode ($\hat{\sigma}_{11} < 0$), $F_{fc} = \left(\frac{\hat{\sigma}_{11}}{X^C}\right)^2 = 1$ (6.2)

Matrix tensile mode ($\hat{\sigma}_{22} \geq 0$), $F_{mt} = \left(\frac{\hat{\sigma}_{22}}{Y^T}\right)^2 + \left(\frac{\hat{\sigma}_{12}}{S^L}\right)^2 = 1$ (6.3)

Matrix compressive mode ($\hat{\sigma}_{22} < 0$), $F_{mc} = \left(\frac{\hat{\sigma}_{22}}{2S^T}\right)^2 + \left[\left(\frac{Y^C}{2S^T}\right)^2 - 1\right]\frac{\hat{\sigma}_{22}}{Y^C} + \left(\frac{\hat{\sigma}_{12}}{S^L}\right)^2 = 1$ (6.4)

where X^T, X^C, Y^T, Y^C, S^L and S^T denote the longitudinal tensile strength, longitudinal compressive strength, transverse tensile strength, transverse compressive strength, longitudinal (in-plane) shear strength and transverse (out-of-plane) shear strength, respectively. α is the coefficient that relates the shear stress contribution to the fibre tensile initiation criterion. In this study, the fibre tensile failure is assumed to be independent of the shear stress, hence α=0.

Before any damage occurs, the constitutive model is given as below:

$$\begin{Bmatrix} \sigma_{11} \\ \sigma_{22} \\ \sigma_{12} \end{Bmatrix} = \mathbf{C} \begin{Bmatrix} \varepsilon_{11} \\ \varepsilon_{22} \\ \varepsilon_{12} \end{Bmatrix} \quad (6.5)$$

where **C** is the composite stiffness matrix, defined as:

$$\mathbf{C} = \begin{bmatrix} \dfrac{E_1}{1-\nu_{12}\nu_{21}} & \dfrac{\nu_{12}E_2}{1-\nu_{12}\nu_{21}} & 0 \\ \dfrac{\nu_{12}E_2}{1-\nu_{12}\nu_{21}} & \dfrac{E_2}{1-\nu_{12}\nu_{21}} & 0 \\ 0 & 0 & G_{12} \end{bmatrix} \tag{6.6}$$

Stresses are computed during each load increment and updated accordingly. Damage is initiated in any of the failure modes whenever the criterion given by Equations (6.1) to (6.4) is satisfied. Upon further loading, damage evolves and the stiffness matrix is substituted by:

$$\mathbf{C_d} = \frac{1}{1-(1-d_f)(1-d_m)\nu_{12}\nu_{21}} \begin{pmatrix} E_1(1-d_f) & (1-d_f)(1-d_m)E_2\nu_{21} & 0 \\ (1-d_f)(1-d_m)E_1\nu_{12} & E_2(1-d_m) & 0 \\ 0 & 0 & [1-(1-d_f)(1-d_m)\nu_{12}\nu_{21}](1-d_s)G \end{pmatrix} \tag{6.7}$$

The shear damage state is quantified as follows:

$$d_s = 1-(1-d_{ft})(1-d_{fc})(1-d_{mt})(1-d_{mc}) \tag{6.8}$$

The stress state in the damaged material point is updated for the current load increment such that:

$$\begin{Bmatrix} \hat{\sigma}_{11} \\ \hat{\sigma}_{22} \\ \hat{\sigma}_{12} \end{Bmatrix} = \begin{bmatrix} \dfrac{1}{(1-d_f)} & 0 & 0 \\ 0 & \dfrac{1}{(1-d_m)} & 0 \\ 0 & 0 & \dfrac{1}{(1-d_s)} \end{bmatrix} \begin{Bmatrix} \sigma_{11} \\ \sigma_{22} \\ \sigma_{12} \end{Bmatrix} \tag{6.9}$$

Damage evolution is described by the linear softening law, and hence it is similar to Equation (4.21). In Hashin lamina damage model, D could refer to d_f or d_m. The damage variable, d_s starts to evolve whenever there is matrix or fibre failure, as shown in Equation (6.8). All damage variables vary from zero (onset of damage) to unity (complete failure).

6.3.2.Finite element model

Finite element modelling is only carried out on repaired composites. Figure 6.3 describes the finite element model used in this study, with the loading condition, boundary condition, modelling approach and nomenclature of the repaired composites. Patch interface damage is not considered as a first run of the simulation reveals that the stresses are very low and hence patch delamination is negligible. Only the region of 150mm within the tabs is modelled. Besides, due to the symmetric about the mid-thickness plane, only half-thickness specimen is modelled. It means that the interface failure between those two 0^o layers is not considered. For the composite laminate, each layer is modelled as one single ply and meshed with continuum shell elements. The stiffness and Poisson's ratio values are referred to Table 4.4 for dry specimen. Strength values are referred to Table 4.2 whereas X^C, Y^C and S^T are assumed due to lack of experimental data and are presented in Table 6.3. Besides, the matrix fracture energy, G_{mc} is taken as the G_{IC} value of T600S/R368-1 carbon/epoxy composite, which is approximately 0.5N/mm. This is based on the assumption that the mode I delamination is mainly dominated by matrix cracking. However, it should be noted that the appropriate test to obtain G_{mc} is by compact tension (CT) test on $[0]_{30}$ specimens.

Nevertheless, the values of G_{mc} and G_{IC} may not differ much. For example, it was reported that for AS4 carbon/PEEK composite, G_{mc}=1.20N/mm and G_{IC}=0.97N/mm [284]. In addition, G_{fc} is assumed to be similar to the value obtained from CT test of $[0/90]_{15}$ AS4 carbon/PEEK specimens [284] since both AS4 and T600S have similar mechanical properties. Zero-thickness cohesive elements are inserted into each interface between two plies of the parent plate to model the interface failure. BK criterion [158] proposed by Gong and Benzeggagh [159, 160] is used to simulate the mixed-mode damage evolution and the CZM parameters are referred to Table 4.5. Since mixed-mode delamination is anticipated, R-curve effect is not considered in the interface delamination. Adhesive is modelled using continuum damage model (CDM) to illustrate the cohesive or cohesive/interface mixture failure. Similarly, since mixed-mode fracture is expected, the CDM parameters of MMF specimens are used, which are indicated in Table 5.4. This is similar to the approach employed in [112, 167, 173-174, 178], where CDM parameters are first calibrated in MMF specimens and then applied in lap joints modelling. However, it should be noted that at current stage, the built-in CDM in Abaqus 6.9EF does not consider the participation of mode-mixity in the damage evolution process. In addition, mixed-mode fracture toughness of plasma treat Araldite2015 joints are estimated by fitting the mode I and II plasma treat fracture toughness using the same material parameter as the sandpaper polished joints (η=4). Hence, G_{I+IIC} is estimated to be 70N/m. As for ESP110, since none of the plasma treat fracture toughness is determined, it is estimated by taking the ratio of $G_{I+IIC,ESPpl}=G_{I+IIC,ARApl}/G_{I+IIC,ARAsp}\times G_{I+IIC,ESPsp}$, which gives the value of 80N/m. Based on the similar approach described in Section 5.8.2, other parameters can thus be calculated and are listed in Table 6.4.

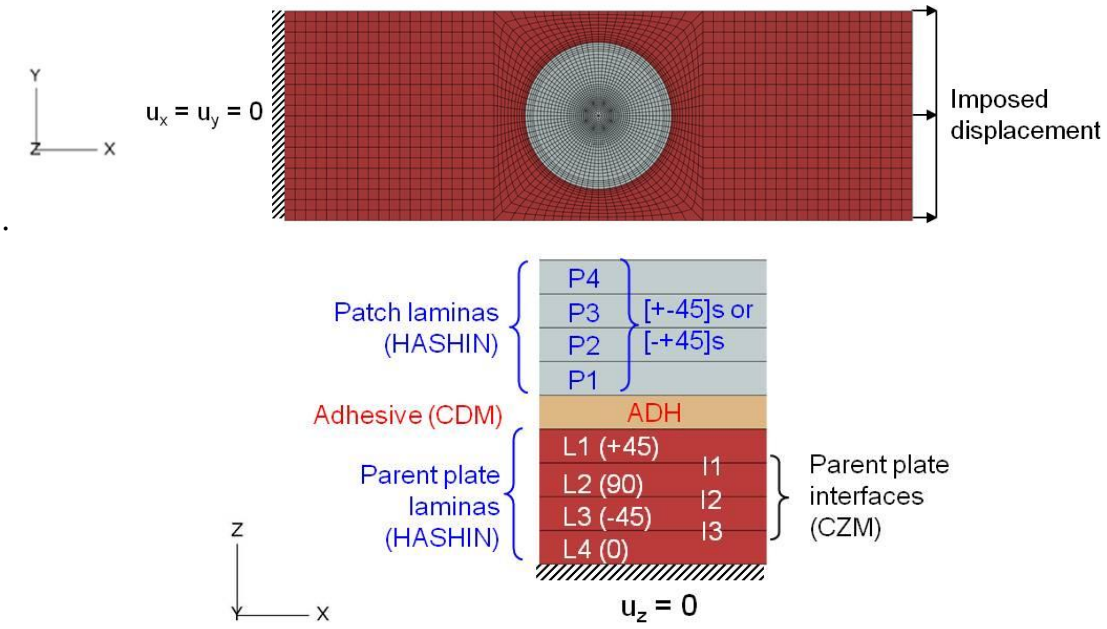

Figure 6.3: Finite element model and modelling approach of repaired composite.

Table 6.3: Lamina strength and fracture energy values.

X^T (MPa)	X^C (MPa)	Y^T (MPa)	Y^C (MPa)	S^L (MPa)	S^T (MPa)	G_{mc} (N/mm)	G_{fc} (N/mm)
1500	1000	58	140	53	30	0.5	3.5

Table 6.4: Estimated MMF CDM parameters for plasma treated Araldite2015 and ESP110 bonded joints.

Adhesive	*E (MPa)*	ν	$\sigma_o=\sigma_i$ *(MPa)*	δ_i *(mm)*	δ_f *(mm)*
Araldite2015	1850	0.33	4	0.002	0.035
ESP110	6000	0.33	3	0.001	0.051

6.4.Effects of specimens' width on failure strength

Table 6.5 compares the ultimate tensile strength of $[-45/0/45/90]_S$ unnotched composites at specimens' width of 25mm and 50mm. Results reveal that the average failure strength of specimens with 25mm width is approximately 8% lower compared to specimens with 50mm width. Figure 6.4 suggests that the edge effect in a multidirectional laminate could explain this difference. Supposing that the edge delamination zone: t_d is constant at a given stress level, its effect on the performance of the laminate of width b can be represented by the ratio (t_d/b), which is more important for a narrower specimen than that for a wider one. Hence, for better strength comparison with notched and repaired composites, unnotched specimens at other stacking sequences are prepared at 50mm width.

Table 6.5: Ultimate tensile strength of $[-45/0/45/90]_S$ unnotched composites.

Specimen's width (mm)	Strength (MPa) (C.V %)
25	526.26 (2.81)
50	571.02 (1.35)

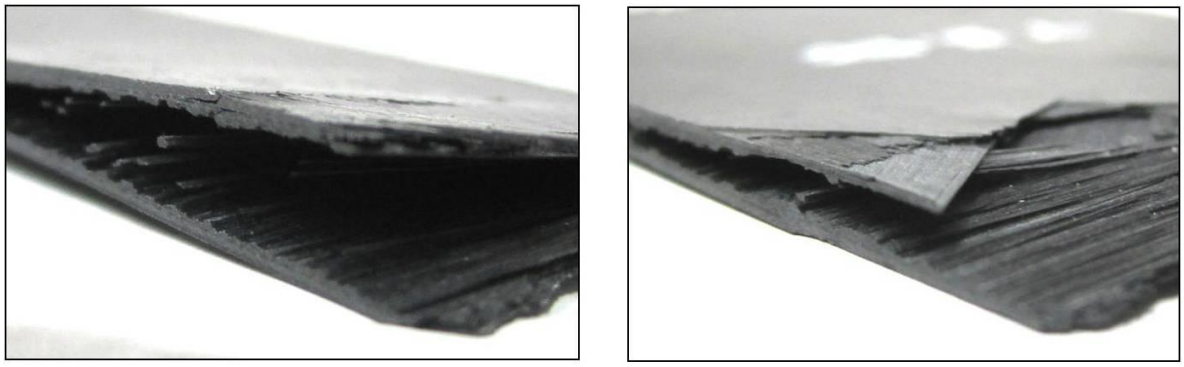

(a) 25mm (b) 50mm

Figure 6.4: Edge delamination in $[-45/0/45/90]_S$ unnotched composites.

6.5.Effects of stacking sequence of the remote tensile strength of unnotched and notched specimens

Figure 6.5 compares the remote tensile strength of unnotched and notched specimens at stacking sequences of $[45/-45/0/90]_S$, $[-45/0/45/90]_S$, $[-45/45/90/0]_S$, and $[45/90/-45/0]_S$. All values are calculated based on the peak load divided by the nominal area (width×thickness) of the specimen. The blue values refer to the normalised strength as compared to $[45/90/-45/0]_S$ unnotched specimens (the highest), whereas the underlined red values indicate the residual strength as compared to its own unnotched strength.

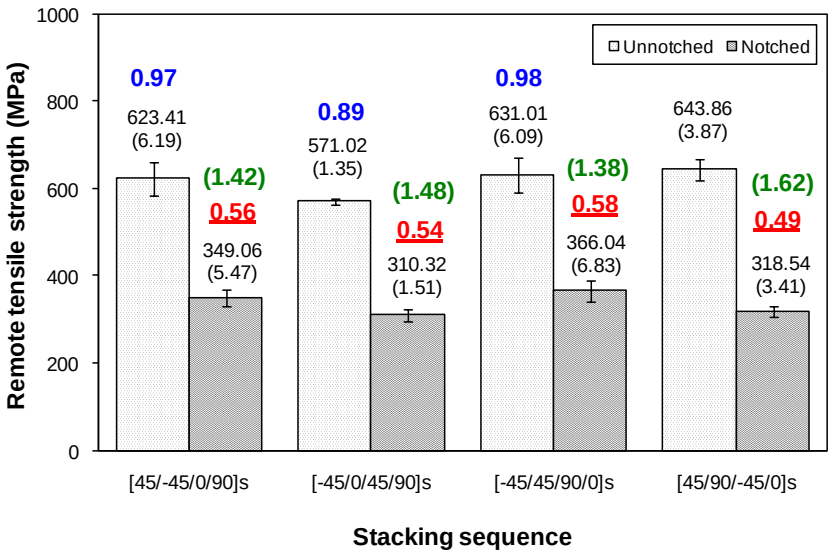

Figure 6.5: Comparison of unnotched and notched remote tensile strength at various stacking sequences.

It is seen that the average unnotched strengths are similar except for $[-45/0/45/90]_S$ composite, which is 11% lower than $[45/90/-45/0]_S$ composite. Difference in unnotched quasi-isotropic laminate strength was also reported by some researchers [285-286]. It was discussed that the major reason is the variation in the inter-laminar stress distribution at different laminate stacking sequence [286]. Figure 6.6 suggests that the reason for lower strength could be due to more significant edge delamination in $[-45/0/45/90]_S$ composite. Obvious but less edge delamination is also observed in $[45/-45/0/90]_S$ composite and is not noticeable in $[-45/45/90/0]_S$ and $[45/90/-45/0]_S$ composites. In other words, quasi-isotropic with 0^o plies at the mid-thickness could reduce the edge delamination. In addition, the failure mode also differs with stacking sequence. $[45/-45/0/90]_S$ composite shows failure path in 90^o and $\pm 45^o$ directions (which is believed to be attributed to significant delamination), $[-45/0/45/90]_S$ and $[45/90/-45/0]_S$ composites depict a combination of failure in 90^o and -45^o directions, whereas $[-45/45/90/0]_S$ composite exhibit brittle failure (failure path in 90^o direction). Notched specimens show different strength order, with the highest obtained in $[-45/45/90/0]_S$, followed by $[45/-45/0/90]_S$, $[45/90/-45/0]_S$ and the lowest in $[-45/0/45/90]_S$ composite. Compared to its own unnotched strength, generally only 50-60% of failure strength is retained after removal of 20% cross-sectional area because of the local stress concentration at the transverse edges of the hole. Consider that the effect of local stress concentration (*ELSC*) on the average strength which can be represented using the following equation:

$$ELSC = \frac{\sigma_{un} / (b \cdot t)}{\sigma_n / [(b-d) \cdot t]} = \frac{\sigma_{un}}{\sigma_n}\left(1 - \frac{d}{b}\right) \tag{6.10}$$

where σ_{un}, σ_n, are the remote strength of unnotched and notched specimens, and b, d and t are corresponding to the width, hole diameter and thickness of the parent plate. The *ELSC* is indicated in Figure 6.5 as green values in bracket. The highest *ELSC* is noted as 1.62 for $[45/90/-45/0]_S$ laminate.

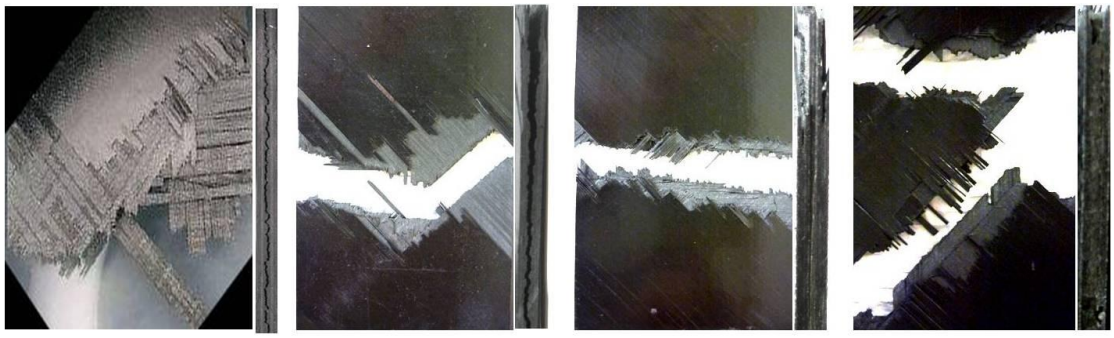

[45/-45/0/90]s [-45/0/45/90]s [-45/45/90/0]s [45/90/-45/0]s

Figure 6.6: Fractured unnotched specimens at various stacking sequences. Photograph of $[45/-45/0/90]_S$ specimen is taken from [223].

Besides, edge delamination is not observed in all notched specimens, see Figure 6.7. $[45/-45/0/90]_S$ and $[-45/45/90/0]_S$ composites show comparatively brittle failure, whereas $[-45/0/45/90]_S$ and $[45/90/-45/0]_S$ composites fail in 90^o and -45^o directions. Compared to the unnotched specimens, the only major difference in the failure mode is $[45/-45/0/90]_S$. Nevertheless, generally two different failure modes could be identified: brittle failure in quasi-isotropic laminates with larger inter-ply angle difference ($[45/-45/0/90]_S$ and $[-45/45/90/0]_S$), and a combination of brittle and pull-out failure in quasi-isotropic laminates with consistent 45^o inter-ply angle difference ($[-45/0/45/90]_S$ and $[45/90/-45/0]_S$).

[45/-45/0/90]s [-45/0/45/90]s [-45/45/90/0]s [45/90/-45/0]s

Figure 6.7: Fractured notched specimens at various stacking sequences. Photograph of $[45/-45/0/90]_S$ specimen is taken from [223].

6.6.Comparison among experimental, theoretical and numerical stiffness of the parent plate

Table 6.6 compares the experimental, theoretical and numerical global stiffness of the parent plate. Experimental stiffness is obtained through strain gauge measurement and the theoretical value is calculated using classical laminate theory (CLT). The numerical stiffness is obtained from the stress-strain response at the similar location where the strain gauge is attached. Results show good agreement among different analyses. This serves as a partial validation on the experimental procedure and numerical model.

Table 6.6: Experimental, theoretical and numerical stiffness values of the parent plate.

	E_x (GPa) (C.V %)	% difference
Experimental	41.02 (5.55)	-
Theoretical	38.73	5.59
Numerical	37.32	9.02

6.7.Experimental remote tensile strength and fracture modes of repaired specimens

Since the average unnotched strength of $[45/90/-45/0]_S$ is the highest compared to other stacking sequences, the parent plate of all repaired specimens is prepared using that stacking sequence. Figure 6.8 compares the remote tensile strength of unnotched, notched and repaired specimens using different methods, where the name of each series of the specimens is explained in Table 6.2. Similarly, the values are calculated based on the nominal area of the parent plate (width×thickness). Values in red refer to the residual strength as compared to the unnotched specimens. It is shown that at least 72% of strength is recovered with external patches repair, which is comparable to the strength recovery reported elsewhere, see Table 2.16. Repaired with ESP110 adhesive exhibits better performance compared to Araldite2015 (13% and 7% for the systems repaired by patches $[\pm 45]_S$ and $[\mp 45]_S$ respectively). It means that the behaviour of the adhesive used could influence the performance of the repaired system. However, regardless the type of adhesive used, the variation with the patch stacking sequence is not significant, with maximum of 3% difference. Previous study has also reported that effect of patch membrane stiffness dominates over the patch lay-up sequence if the damage in the adhesive/adherent interface is not the major failure mode [223]. Moreover, negligible effect is found between different surface treatments, although delamination tests show that the fracture toughness of plasma treated composite joints is approximately 80% lower than the sandpaper polished joints. These observations allow concluding that the behaviour of adhesive/adherend interface does not play an essential role in the failure of the repairs in this study. Further analyses will be presented in the following section through finite element modelling.

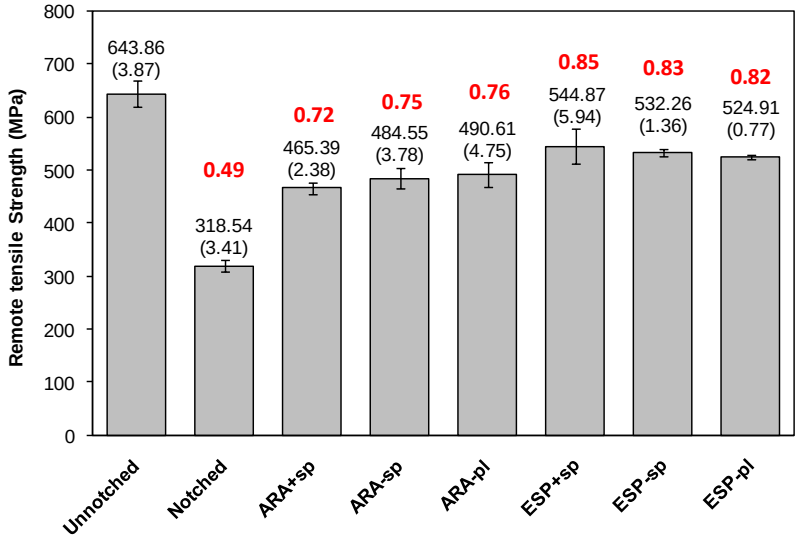

Figure 6.8: Remote tensile strength of all series of [+45/90/-45/0]s specimens.

The fracture surfaces of tested repairs are presented in Figure 6.9. The fracture mode of the repaired composites is mainly influenced by the material behaviour of the adhesive, but not by the patch stacking sequence and surface treatment method. For ductile adhesive (Araldite2015) repaired systems, partial patch debonding is always observed for sandpaper polished specimens, whereas one-side total patch debonding could be observed occasionally on plasma treated specimens. Two-side total patch debonding is noticed for brittle adhesive bonded joints (ESP110) in all cases. All these fracture modes are similar to Mode A failure mentioned in [212, 223], where patches are strong enough and debonding occurs due to high

shear and peel stresses in the adhesive layer which are generally recognised to be at the region near the edges of the patch. Besides, the fracture pattern of all parent plates is the same, where the fracture path is in the 90^o and -45^o directions.

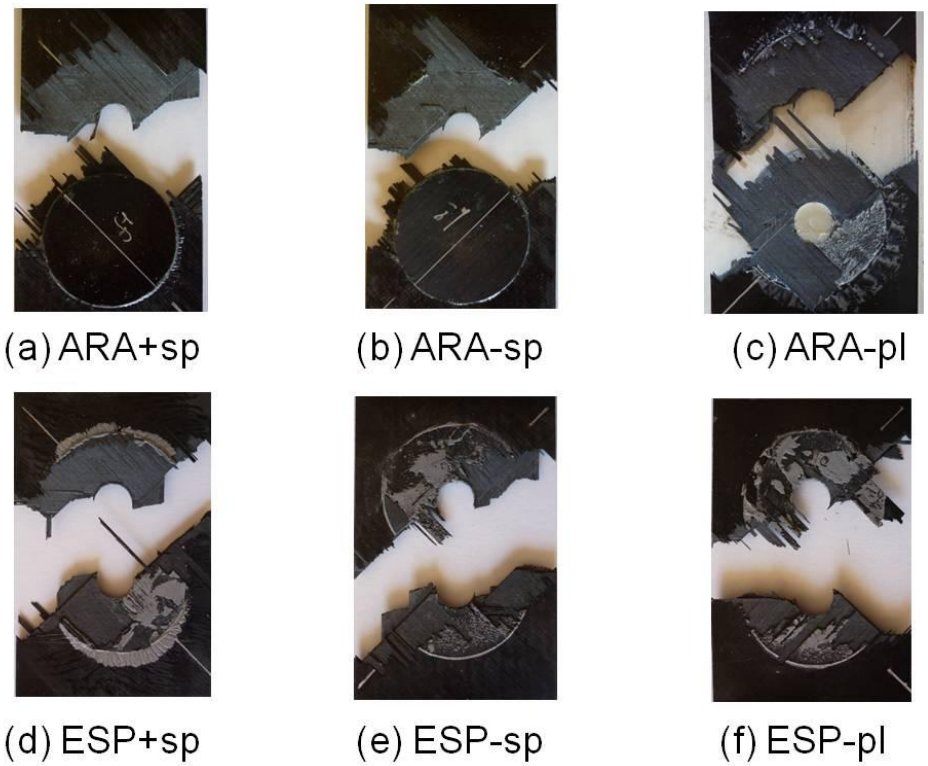

Figure 6.9: Fractured surface of all series of composite repairs.

Figure 6.10 shows the optical micrographs of the fracture surfaces for the cases with debonded patches. It is obvious that some parent plate material pieces are attached on the patches, and patch debonding is resulted from the delamination of the parent laminate and a mixture of interface and cohesive failure. This implies strong adhesive/adherend interface. Patches seem to be still intact or with minimal damage.

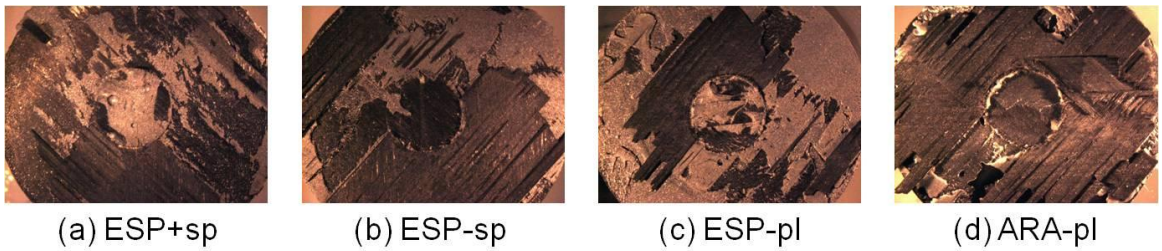

Figure 6.10: Optical micrographs of debonded patches from repaired systems.

6.8.Experimental and numerical remote tensile strengths of repaired composites

Figure 6.11 compares the experimental and numerical remote tensile strength of repaired composites. Results indicate that the numerical predicted strengths are always lower compared to the experimental values. Similar observation has also reported in reference [212]. The first reason could be due to different failure mode in unidirectional and multidirectional laminates. As described in Figure 4.9, the failure mode in $[0]_8$ specimens is a combination of fibre splitting and fibre breakage. However, in quasi-isotropic laminate, generally fibre breakage is the dominant failure mode observed in 0^o plies. To improve the finite element model, a stacking sequence factor, *m* could be introduced such that the longitudinal strength is

expressed as mX^T, where $m \geq 1$ (m=1 when the composite is unidirectional). Secondly, the CDM parameters used in the numerical simulations are for MMF case. However, in repaired composites, the mode mixity is not always fixed at 0.43. In fact, due to the loading configuration, mode II participation could be generally higher. This is the current limitation of CDM in Abaqus 6.9EF, where mode-mixity during crack propagation is not considered. Thirdly, the finite element model considers only the region of interest (150mm between the tabs), and hence the boundary and loading conditions are imposed on the tab end region. This could induce stress concentration and partially contribute to early failure.

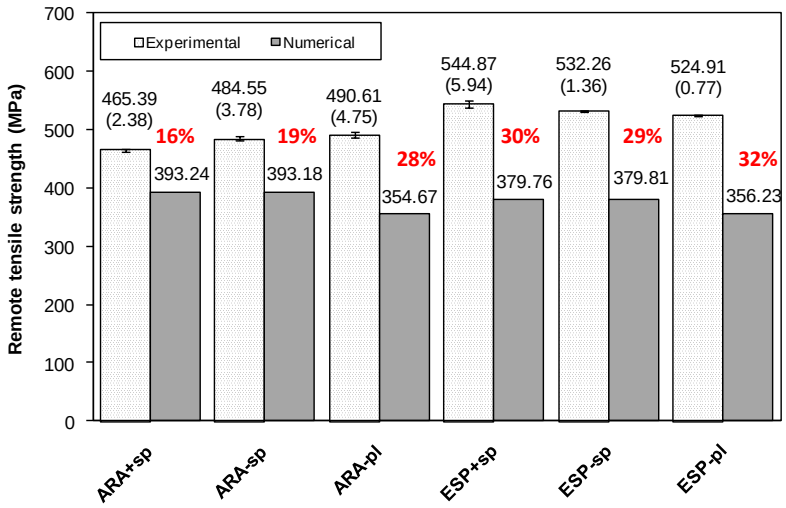

Figure 6.11: Comparison of experimental and numerical remote tensile strength of repaired composites.

In addition, the trend of the experimental and numerical remote tensile strength of Araldite2015 and ESP110 repairs contradicts to one another. Experimental results show that ESP110 repairs exhibit higher remote tensile strength than Araldite2015 repairs, but the numerical results show the opposite trend. Consequently, the experimental and numerical strength difference in ESP110 repairs is higher than Araldite2015 ones. However, it should be noted that the CDM parameters used are those already calibrated for MMF case. It is possible that under different joint configuration, the adhesive behaves differently [169]. Further analysis such as fractographic analysis on the fractured specimens is needed to understand the failure behaviour of both adhesives and improve the finite element model. For example, if the local stress state in the adhesive layer plays an important role in the failure behaviour of the repair, the out-of-plane stress in the adjacent lamina to the adhesive may need to be modelled. One possible approach is by adding cohesive elements between the parent plate and the adhesive.

6.9.Occurence of first damage initiation in repaired composites

In order to observe the order of damage initiation, Figure 6.12 illustrates two examples of numerical results obtained from finite element analysis. ARA-sp and ESP-sp are chosen for comparison since experimental results show that the adhesive type has a more significant influence on the remote tensile strength compared to the patch stacking sequence and surface treatment method. Herein, the normalised elongation is given at the damage initiation in each ply, interface and the adhesive. Normalised elongation of 1.0 corresponds to the final failure of the specimen. The damage initiation in the layers L1-L3 indicates only the matrix tensile fracture, where Equation (6.3) is fulfilled and the dominated damage could be matrix cracking

and fibre/matrix interface cracking. For layer 4, fibre tensile breakage is referred as the damage mechanism, which corresponds to Equation (6.1), due to its significance compared to matrix cracking. It is obvious that the order of the damage initiation is quite different in the systems repaired by two adhesives. For ARA-sp repair, adhesive damage occurs after matrix tensile fracture in layers L1-L3, whereas adhesive damage is the first damage occurred in ESP-sp repair. This is logical since the calibrated MMF CDM parameters indicate that ESP110 adhesive is much stiffer but less resistant than Araldite2015 adhesive. To give a clearer comparison, the order of the damage occurrence is listed in Table 6.7. It can be seen that other than the adhesive, the damage initiation follows the same order regardless the adhesive used: layer 2 (L2 with 90^o fibres), layers 1 and 3 (L1 and L3 with $\pm 45^o$ fibres), interface 3 (I3:$-45^o/0^o$), interface 1 (I1:$45^o/90^o$) and 2 (I2:$90^o/-45^o$), and finally layer 4 (L4 with 0^o fibres). No damage is observed in the patch up to the total failure of the repairs.

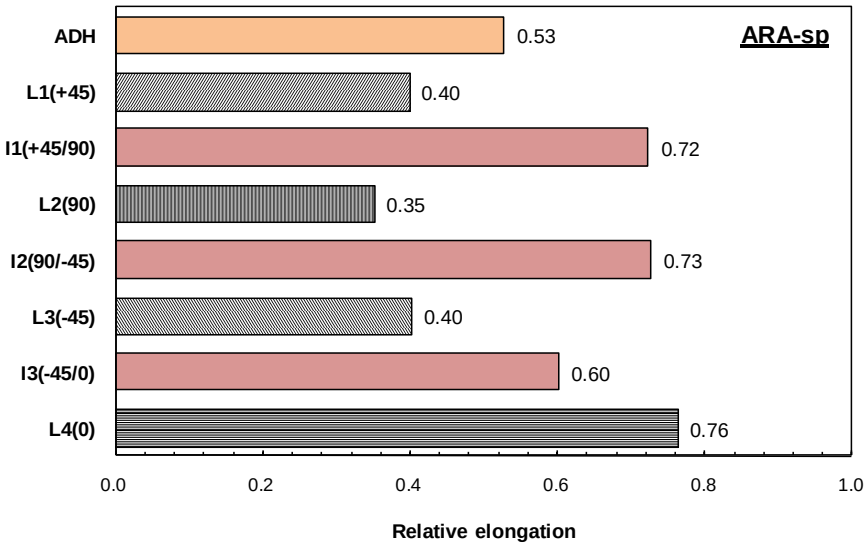

(a) Araldite2015, $[\mp 45]_S$ patch, sandpaper polished

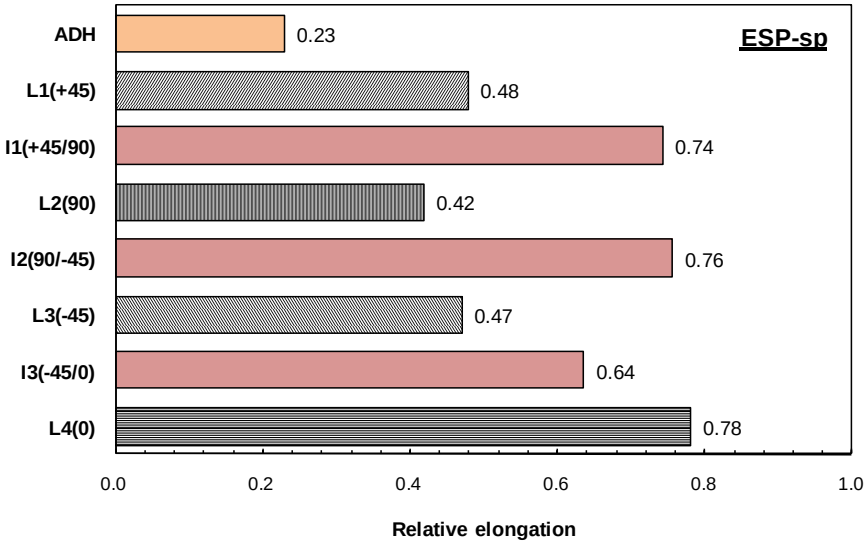

(b) ESP110, $[\mp 45]_S$, sandpaper polished

Figure 6.12: Normalised elongation at damage initiation in repaired composites.

Table 6.7: Comparison of damage initiation sequence in ARA-sp and ESP-sp repairs.

Sequence	1	2	3	4	5	6	7	8
ARA-sp	L2(90)	L1, L3 (±45)		ADH	I3(-45/0)	I1(+45/90)	I2(90/-45)	L4(0)
ESP-sp	ADH	L2(90)	L3(-45)	L1(+45)	I3(-45/0)	I1(+45/90)	I2(90/-45)	L4(0)

6.10.Damage initiation and progression in repaired composites

Figure 6.13 to Figure 6.16 illustrate how the damage evolutes as the remote applied displacement increases in the laminas of ARA-sp repaired composite. Region in red (value of 1) implies that damage has initiated. For other colours, they indicate intact region. Nevertheless, different colours provide the information of the stress level in the element (index with value closer to 1 means that the corresponding element is closer to damage initiation). It should be noted that in each lamina, there is only one damage mode presented, either matrix tensile fracture for layers L1-L3 (in which Equation (6.3) is fulfilled), or fibre tensile breakage for layer L4 (which corresponds to Equation (6.1)). The damage evolution is only shown when there is a significant change in the damage pattern, hence the interval may not be the same. Nevertheless, the pattern (d) is always taken at the point of peak load. Besides, the same legend and coordinate system is used in all laminas, interfaces and adhesive. Figure 6.13 to Figure 6.15 show the matrix tensile fracture patterns in the layers L1, L2 and L3 in the parent plate, respectively. Matrix tensile fracture is first detected near the transverse edges of the notch, followed by slight propagation in the transverse direction and patch edge region, and finally evolutes towards the specimen's edges. Matrix tensile fracture is more severe in layer L2 (90^o), due to its weak strength (Y^T) in the loading direction. Besides, in layers L1-L3, the longitudinal notch edges region is generally less stressed. As for layer L4 (0^o), Figure 6.16 shows that the tensile failure in the fibre direction is also initiated at the transverse hole edges, and subsequently propagated towards the specimen's edges in $\pm 45^o$ directions.

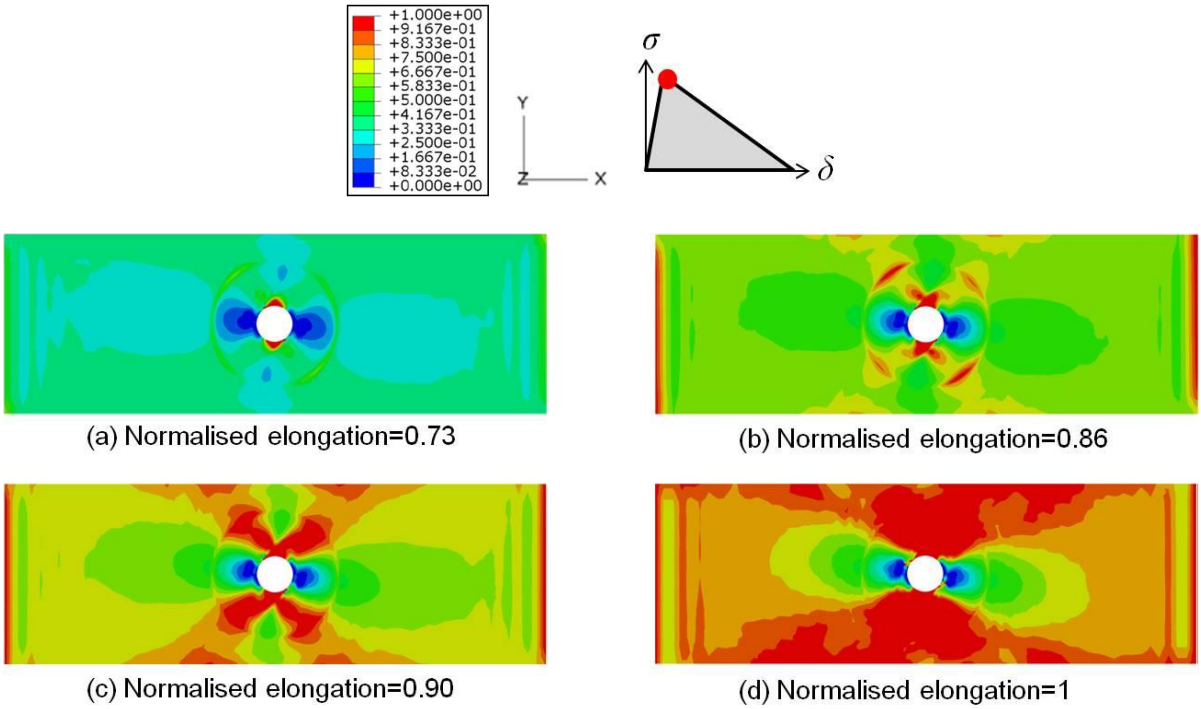

Figure 6.13: Progression of matrix cracking initiation in layer 1 (L1 with $+45^o$ fibres).

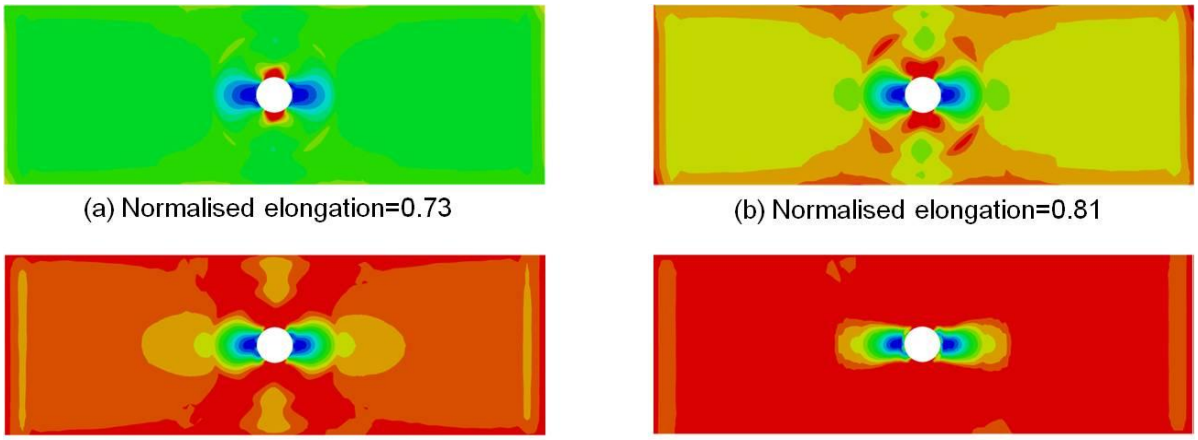

(a) Normalised elongation=0.73 (b) Normalised elongation=0.81

(c) Normalised elongation=0.86 (d) Normalised elongation=1

Figure 6.14: Progression of matrix cracking initiation in layer 2 (L2 with 90^o fibres).

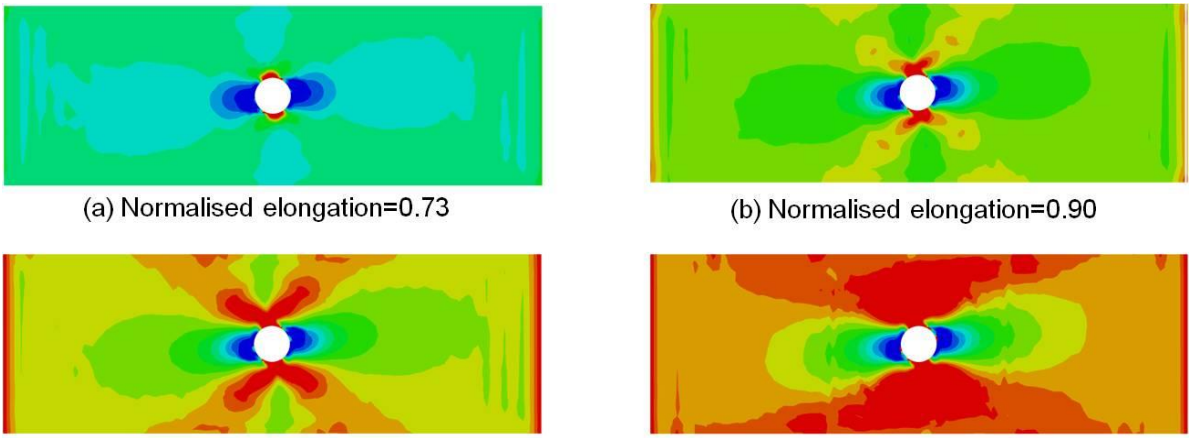

(a) Normalised elongation=0.73 (b) Normalised elongation=0.90

(c) Normalised elongation=0.94 (d) Normalised elongation=1

Figure 6.15: Progression of matrix cracking initiation in layer 3 (L3 with -45^o fibres).

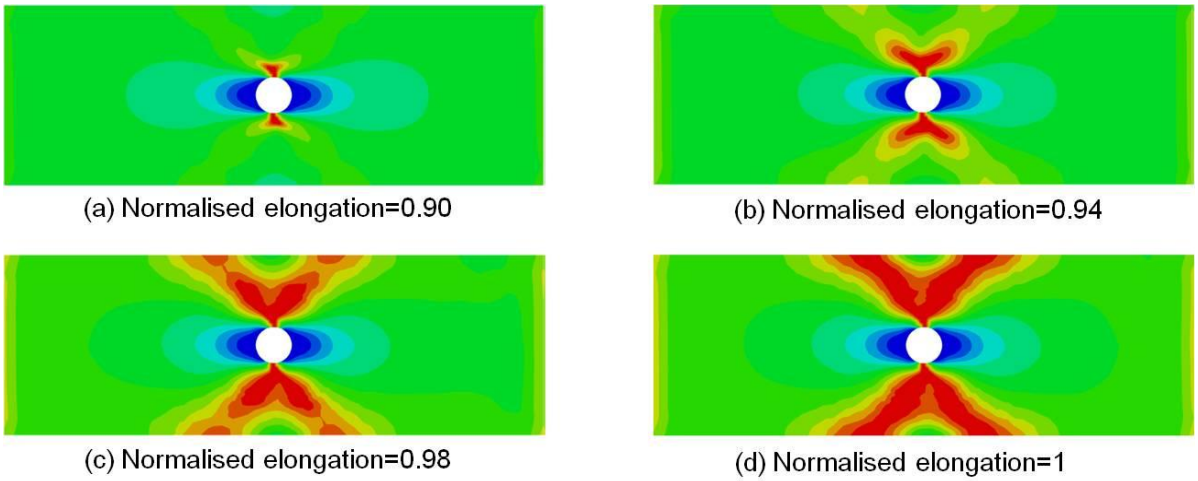

(a) Normalised elongation=0.90 (b) Normalised elongation=0.94

(c) Normalised elongation=0.98 (d) Normalised elongation=1

Figure 6.16: Progression of fibre breakage initiation in layer 4 (L4 with 0^o fibres).

The delamination in the parent plate is not significant, and hence only the damage pattern at the peak load is shown. Figure 6.17 shows that interface delamination mainly occurs at a small region at the transverse notch edges. Hence, it is not a dominant damage mode in this case.

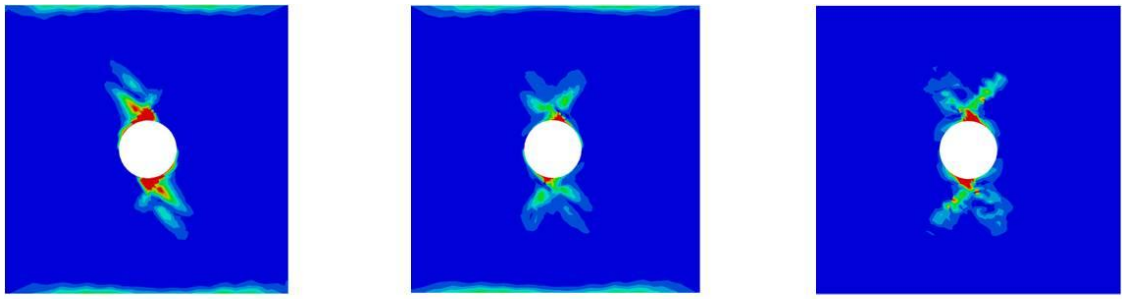

(a) I1 (+45/90) (b) I2 (90/-45) (c) I3 (-45/0)

Figure 6.17: Interface delamination at peak load.

Figure 6.18 shows that the adhesive damage is first noticed at the longitudinal edges of the patch, and then the longitudinal notch edges are affected. As load increases, the damage zones at both locations are then propagated towards each other and eventually "joined". Finally, at the peak load, damage has initiated in the entire bonded region. In fact, damage initiation in the adhesive layer occurs almost simultaneously in the thickness direction, and hence only x-y view is shown. However, it is interesting to note that the total failure (D=1) may differ among the repaired composites. Figure 6.19 shows that the failure pattern in ARA+sp and ARA-sp repairs are similar, where major total damage is concentrated near the parent plate. As for ESP+sp and ESP-sp repairs, total element failure is only noticed on the right side of the elements near the parent plate. Similar total failure pattern is identified in both plasma treated composites (ARA-pl and ESP-pl), where damage is seen on one side of both surfaces of the adhesive. This seems to contradict with the experimental observations shown in Figure 6.9 and Figure 6.10, where partial patch debonding is observed in ARA+sp and ARA-sp, whereas one-side total patch debonding is observed in ARA-pl (occasionally) and two-side total patch debonding in all ESP repairs. Further detail in the analysis of the fractured surface is needed to explain these contradictions.

(a) Norm. elong.=0.73 (b) Norm. elong.=0.81 (c) Norm.elong.=0.90 (d) Norm. elong.=1

Figure 6.18: Progression of damage initiation in the adhesive.

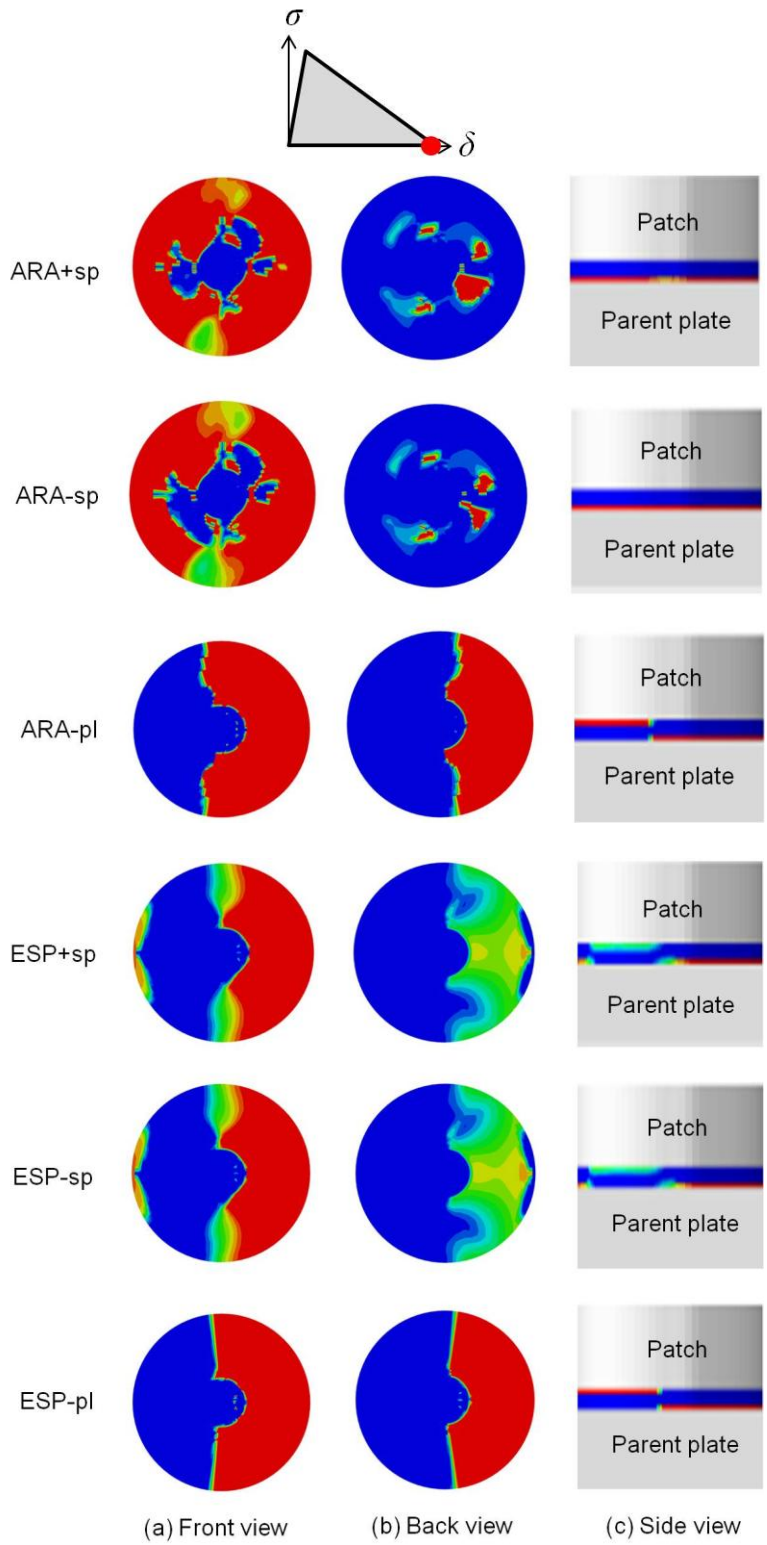

Figure 6.19: Total failure region (D=1) in adhesive joint of repaired composites.

Since mode II participation could be expected to be high in the adhesive joint configuration used in this study, one simulation is also carried out on ARA-sp repair using ENF CDM parameters (see Table 5.4). Results reveal that there is an increment of 10% (435.87MPa) in the peak load compared to the one with MMF CDM parameters, which reduces the difference in the remote tensile strength compared to the experimental result.

However, Figure 6.20 shows that upon peak load is attained, there is no damage in the adhesive, and matrix tensile fracture is noticed in the patch laminas (all laminas exhibit similar damage pattern). This damage pattern does not seem to correlate well with the experimental observations, where adhesive damage is clearly observed. Hence, the use of MMF CDM parameters seems to be more appropriate.

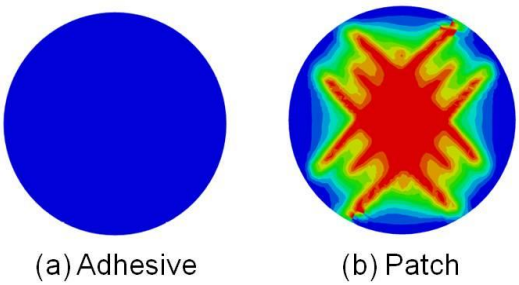

(a) Adhesive (b) Patch

Figure 6.20: Damage in the adhesive and the patch of ARA-sp repair using ENF CDM parameters.

Figure 6.21 displays the damage energy in the laminas, interfaces and adhesive of ARA-sp repaired composite. Herein, the damage energy refers to the total dissipated fracture energy in each lamina, interface or adhesive, which corresponds to its respective damage mode. The interfaces damage energy is much lower than that in the laminas. It is observed that energy dissipated in layer L2 (90^o) is higher than $\pm45^o$ layers (L1 and L3), which is due to more severe damage as seen in Figure 6.14. Besides, larger damage energy is dissipated in layer L4 (0^o), because of higher fibre fracture energy (refer Table 6.3). In addition, higher total energy is dissipated in the adhesive compared to the interfaces. Furthermore, even Figure 6.12 shows that delamination is observed first in interface 3 (I3:$-45^o/0^o$), more energy is dissipated in interface 1 (I1:$+45^o/90^o$), which indicate larger delaminated area. The lowest total damage energy is noted in interface 2 (I2:$90^o/-45^o$).

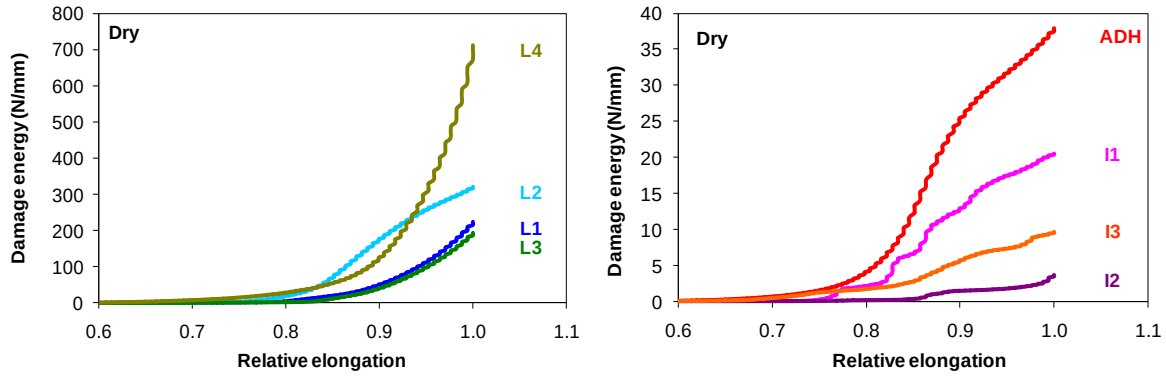

(a) Lamina (b) Interface and adhesive

Figure 6.21: Damage energy in the laminas, interfaces and adhesive of ARA-sp repair.

6.11.Analyses of acoustic emission (AE) data on the damage in repaired composites

For the purpose of following the damage evolution in the repairs, acoustic emission (AE) data is taken at several intervals throughout the tensile test. Figure 6.12 presents the AE amplitude versus the event position at different loading level: from small load (a) to the peak load (d) of ARA-sp repair. The energy level of the events is represented by different colour. It can be seen that damage first occurs in the amplitude range of 45-60dB with energy less than 5J and concentrated at the right region (Figure 6.12(a)). This is most probably corresponding

to matrix cracking. Later on, damage events within the amplitude range of 60-70dB at energy level less than 35J are observed and located around the edge of the notch (Figure 6.12(b)). Compared to the numerical prediction, the corresponding amplitude range (60-70dB) could indicate adhesive damage, but it has to be at the longitudinal edges of the patches. Delamination initiation could fall in the range of 60-80dB, which is shown in Figure 6.12(c). Finally, damage events at high energy level within the amplitude range of 80-100dB are observed, as depicted in Figure 6.12(d). This is believed to be corresponding to fibre breakage.

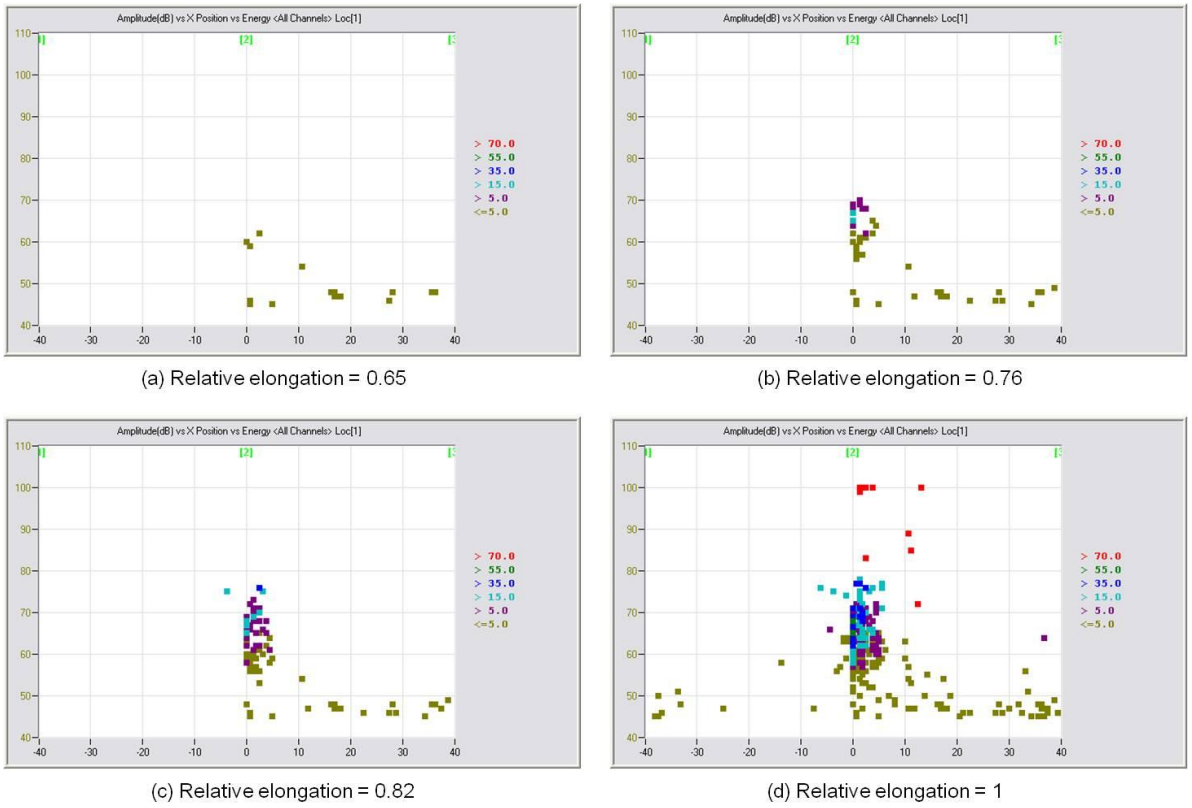

(a) Relative elongation = 0.65

(b) Relative elongation = 0.76

(c) Relative elongation = 0.82

(d) Relative elongation = 1

Figure 6.22: Acoustic emission amplitude and energy versus position of events at various damage occurrence levels of ARA-sp repair.

AE data of ESP-sp at the same normalised elongation is shown in Figure 6.23. Contrary to the repair ARA-sp, Figure 6.23(a) shows that some high energy events (>5J) are noticed. The one near the centre location has an amplitude value close to 60dB, which may indicate the adhesive damage. Another two damage events with energy level greater than 5J should not be related to the adhesive damage, since they fall outside the repair zone (±17.5mm). However, it should be noted that AE data is different from the FE contour such that AE data is a cumulative representation of all damage events, however, FE contour displays only one individual damage process (matrix tensile cracking, fibre tensile breakage, adhesive damage or delamination). The early damage events in the adhesive (as predicted from the numerical results) may not be significant to AE data acquisition in the beginning, and hence not easily detected. Nevertheless, based on the occurrence of the damage events (Figure 6.23(a)-(d)), it is still reasonable to use the same categorisation of the amplitude range for ARA-sp repair, where: 45-60dB for matrix cracking, 60-70dB for adhesive damage, 60-80dB for interface delamination and 80-100dB for fibre breakage.

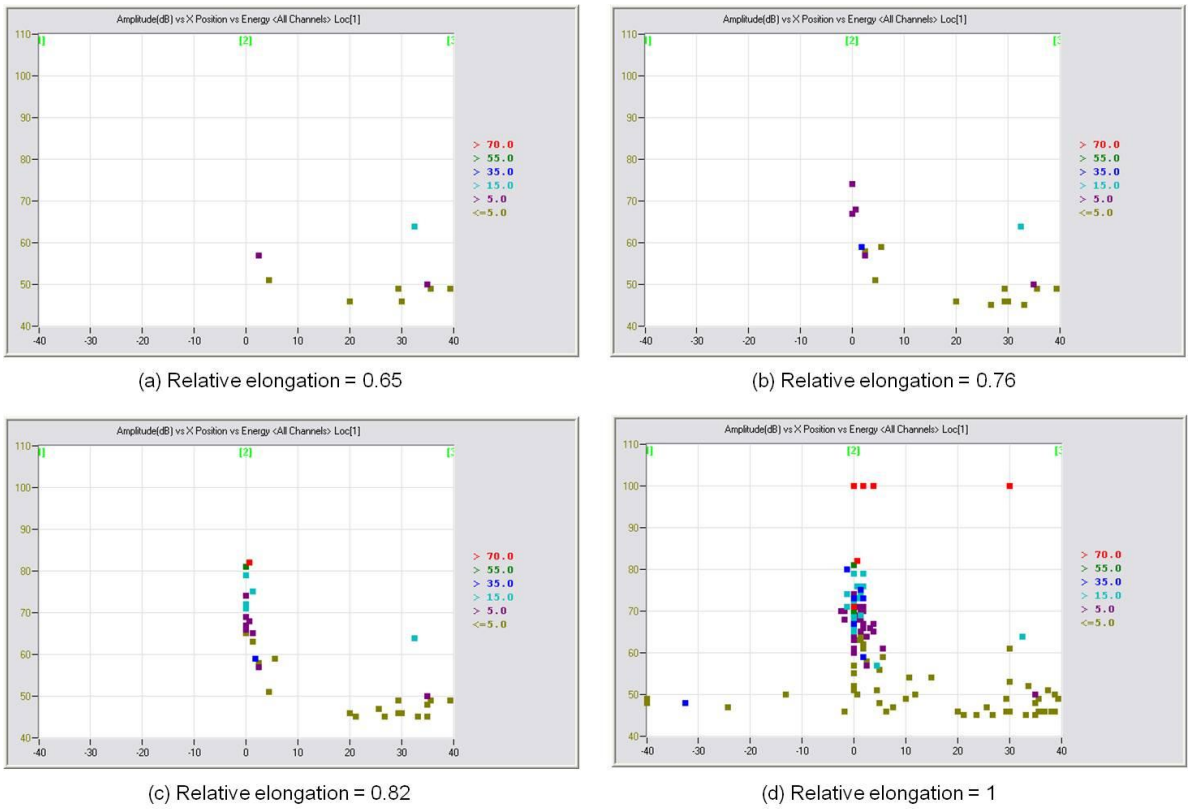

(a) Relative elongation = 0.65 (b) Relative elongation = 0.76

(c) Relative elongation = 0.82 (d) Relative elongation = 1

Figure 6.23: Acoustic emission amplitude and energy versus position of events at various damage occurrence levels of ESP-sp repair.

The distribution of amplitudes with respect to the damage mechanisms is described in Table 6.8. These propositions compare well with the classification by other researchers [287-289]. However, it should be aware that the numerical simulation in this study is limited to the macromechanics damage prediction (matrix tensile fracture, adhesive damage, delamination and fibre breakage), where the role of fibre/matrix debonding and pull-out (micromechanics failure) could not be identified by the macroscopic criterion (see Equations (6.1) to (6.4)).

Table 6.8: Amplitude ranges with respect to the damage mechanisms in repaired composites.

Reference	Matrix cracking	Fibre/matrix interface debonding	Adhesive failure	Delamination	Fibre pull-out and/or breakage
Current study	45-60 dB	-	60-70 dB	60-80 dB	80-100 dB
[287]	40-60 dB	50-70 dB	-	60-80 dB	80-100 dB
[288]	50 dB	-	-	62 dB	-
[289]	40-70 dB	-	-	-	60-100 dB

6.12.Summary

In this chapter, the tensile behaviour of quasi-isotropic laminates is investigated., and the repaired composites are studied using two different adhesives (ductile Araldite2015 and brittle ESP110). The effects of patch stacking sequences ($[\pm 45]_S$ and $[\mp 45]_S$) and surface treatments (sandpaper and plasma) are also investigated. Damage evolution in the repaired composites are analysed by acoustic emission method, and the numerical simulation by finite element model also provides interesting information. Based on the results obtained, the following summaries are drawn:

i. In $[-45/0/45/90]_S$ composite, the tensile strength of 25mm width specimens is 8% lower than the one with 50mm width due to the edge delamination;

ii. Tensile strength in both unnotched and notched quasi-isotropic laminates with different stacking sequence is not the same. Laminates with 0o as mid-plies could reduce edge delamination in unnotched specimens. In both unnotched and notched specimens, brittle failure is identified in laminates with larger inter-ply angle difference ($[45/-45/0/90]_S$ and $[-45/45/90/0]_S$), whereas a combination of brittle and pull-out failure is observed in laminates with consistent 45o inter-ply angle difference ($[-45/0/45/90]_S$ and $[45/90/-45/0]_S$);

iii. The stiffness of $[-45/0/45/90]_S$ laminate measured experimentally and predicted numerically agrees well with the theoretical value, with maximum 6% difference;

iv. The repairs using brittle adhesive ESP110 have better performance than those using ductile adhesive Araldite2015: at least 82% strength recovery is attained in the former and 72% in the later. However, finite element models predict the inversed effect. Further analysis is needed to understand the adhesive behaviour and improve the finite element model;

v. In general, a mixture of cohesive and adhesive failure is observed in the adhesive joints. Two-side total patch debonding is always observed in all ESP110 bonded repairs, but not in Araldite2015 bonded repairs. The final fracture in ESP110 bonded repairs should be caused by unstable crack propagation at peak load due to dynamical effects, as generally happened in most of the brittle materials. These observations cannot be predicted by the finite element model used in this study;

vi. For the composites repaired using ductile Araldite2015 adhesive, according to the numerical simulation, matrix tensile fracture is first initiated in the 90^o and $\pm 45^o$ laminas of the parent plate, followed by the adhesive joint damage; and then the interface delamination in the parent plate. The final fracture is reached after fibre breakage in 0^o ply. Patches remain intact until the end of the test;

vii. Numerical simulation reveals that in brittle ESP110 bonded repairs, the order of damage initiation could be different to that in ductile Araldite2015 bonded repairs. The calibrated MMF CDM parameters of ESP110 adhesive which show higher modulus and lower strength seem to lead to the early damage in the adhesive joint. After that, the damage order in parent plate follows the same order than that in ductile Araldite2015 bonded repairs. This prediction is not really confirmed experimentally;

viii. The effects of patch stacking sequence and surface treatment on the performance of the repairs are negligible if the damage at the adhesive/adherend interface is not the dominant mechanism;

ix. By comparing the acoustic emission data with numerical results, a correlation between each damage mode and the AE amplitude is established as: 45-60dB for matrix cracking, 60-70dB for adhesive damage, 60-80dB for interface delamination and 80-100dB for fibre breakage, respectively.

CHAPTER 7. MOISTURE EFFECTS ON PATCH BONDED COMPOSITE REPAIRS

7.1.Introduction

In this chapter, the effects of water absorption on tensile behaviour of the unnotched, notched and repaired specimens are discussed. Finite element simulations are also carried out to characterise the damage behaviour in the repaired composites. Simulation results are further correlated with acoustic emission (AE) data.

7.2.Experimental details

Ageing tests on $[45/90/-45/0]_S$ parent plate with $[\mp 45]_S$ patch repairs are carried out on sandpaper polished surfaces bonded with Araldite2015 adhesive. Unnotched and notched specimens are also prepared for comparison. The preparation of repaired specimens is the same as described in Section 6.2. For the ageing test, the edges of the parent plate (all unnotched, notched and repaired) are sealed with aluminium foil before immersing in demineralised water at 70^{o}C. Specimens are taken out from the environmental chamber at similar period of the specimens for elementary tensile property tests, which corresponds to M=3%, 6% and 7%.

Similarly, tensile test is carried out on a universal testing machine with load cell capacity of 100kN at crosshead speed of 1mm/min. At least three replicates are tested for each series of specimens. All tests are conducted at ambient condition. Acoustic emission equipment is also used for repaired specimens, with the same setup shown in Figure 6.2.

7.3.Finite element modelling

Similar to the modelling approaches in Section 6.3, lamina, interface and adhesive damage are modelled using Hashin damage model, CZM and CDM, respectively. The elementary, interface and adhesive properties are referred to Table 4.4, Table 4.5 and Table 5.4, respectively. Table 7.1 to Table 7.4 list all the properties used in the finite element modelling.

Table 7.1: Stiffness and Poisson's ratio of lamina at various moisture content levels.

M (%)	E_1 (GPa)	E_2 (GPa)	G_{12} (GPa)	G_{13}*(GPa)	G_{23}*(GPa)	v_{12}
Dry	103.0	6.7	2.7	2.7	2.5	0.34
3	97.0	4.6	2.7	2.7	2.5	0.34
6	95.0	4.5	2.5	2.5	2.2	0.37
7	105.0	4.8	2.6	2.6	2.3	0.38

* Assumed values.

Table 7.2: Lamina strength and fracture energy at various moisture content levels.

M (%)	X^T (MPa)	$X^{C,a}$ *(MPa)*	Y^T *(MPa)*	$Y^{C,a}$ *(MPa)*	S^L *(MPa)*	$S^{T,a}$ *(MPa)*	$G_{mc}{}^b$ *(N/mm)*	$G_{fc}{}^c$ *(N/mm)*
Dry	1500	1000	58	140	53	30	0.5	3.5
3	1500	1000	34	82	40	23	0.5	3.5
6	1000	670	23	56	36	20	0.4	3.5
7	1400	930	14	34	43	24	0.3	3.5

[a] Assumed values based on the same proportion of reduction compared to its longitudinal strength.
[b] Refer to Table 7.3.
[c] The fibre breakage fracture energy, G_{fc} is assumed to be insensitive to the moisture attack.

Table 7.3: Ply/ply interface parameters at various moisture content levels.

M (%)	$K_{nn}=K_{ss}=K_{tt}$ *(N/mm^3)*	t_n *(MPa)*	$t_s=t_t$ *(MPa)*	G_{IC} *(N/mm)*	$G_{IIC}=G_{IIIC}$ *(N/mm)*	η
Dry	1×10^4	25	80	0.5	1.9	0.9
3				0.5	1.4	0.6
6				0.4	0.9	0.8
7				0.3*	0.8*	0.3*

* Values obtained by assuming $G_{IC,M7}=0.7G_{IC,dry}$, $G_{IIC,M7}=0.4G_{IIC,dry}$ and $G_{I+IIC,M7}=0.4G_{I+IIC,dry}$, based on the extrapolated trend from Figure 4.14.

Table 7.4: Adhesive CDM parameters at various moisture content levels.

M (%)	*E (MPa)*	ν	$\sigma_o=\sigma_i$ *(MPa)*	δ_i *(mm)*	δ_f *(mm)*
Dry	1850	0.33	13	0.007	0.065
3	1200	0.33	8	0.007	0.099
6	800	0.33	5	0.006	0.053
7	700[a]	0.33	5[a]	0.007[b]	0.034[b]

[a] Values estimated using Equation (4.1), which is the similar approach as mentioned in Section 5.8.2.
[b] Values obtained by assuming the mixed-mode I+II fracture toughness of the adhesive at M=7% is 20% of the dry condition, see Figure 5.8.

7.4.Comparison among experimental, theoretical and numerical stiffness of the quasi-isotropic parent plate with stacking sequence of $[45/90/-45/0]_S$

Table 7.5 compares the experimental, theoretical and numerical tensile stiffness of $[45/90/-45/0]_S$ quasi-isotropic (QI) laminates at various moisture content levels. Experimental stiffnesses are obtained through strain gauge measurement. Generally, the experimental stiffness value is almost invariant with respect to moisture content. This is consistent with some results published in literature on carbon/epoxy composites (refer Table 2.9). Theoretical values are calculated using classical laminate theory (CLT) by inputting the experimentally measured elementary tensile properties (see Table 4.2). Numerical stiffness is measured on the parent plate at the similar location of strain gauge. Results show comparatively good comparison, with maximum difference of 16% for numerical M=3% case. Besides, it is normal to see that the numerical predicted values are varying consistently with the theoretical values, as the outcome is based on the elementary tensile properties input to the calculation/simulation. Within the acceptable scatter, the experimental results and numerical models are thus believed to be partially validated.

Table 7.5: Comparison among experimental, theoretical and numerical global stiffness at various moisture content levels.

M (%)	Experimental	Theoretical		Numerical	
	(MPa) (C.V %)	(MPa)	% difference	(MPa) (C.V %)	% difference
Dry	41.02 (5.55)	38.73	5.59	39.92	9.02
3	41.00 (4.65)	36.11	11.93	34.60	15.61
6	39.31 (9.60)	35.29	10.23	33.62	14.47
7	39.99 (7.67)	38.75	3.10	36.79	8.00

7.5.Comparison among remote tensile strength of unnotched, notched and repaired specimens

Figure 7.1 displays the effects of water absorption on the remote tensile strength of unnotched, notched and repaired specimens. Dry values are also shown for comparison. The red value indicates the normalised strength with respect to its dry strength. Results show that even after prolonged ageing, the unnotched and notched strength are almost invariant, with approximately 10% strength decrement in unnotched specimens and 15% strength increment in notched composites. Invariant tensile strength in quasi-isotropic carbon/epoxy laminate is generally observed by researches, as listed in Table 2.9. It is due to the strength of quasi-isotropic laminate is fibre-dominated [9]. Slight increment in the failure strength in notched composites could be due to relaxation of stress concentration at the edges of the notch upon moisture absorption. This effect is noticed even during the early ageing period (M=3%), which is believed to be due to unsealed hole edges that the respective region is directly exposed to moisture since the beginning of immersion. Figure 7.2 illustrates the effect of local stress concentration (*ELSC*) of the notched specimens at different moisture content level calculated using Equation (6.10). It could be seen that the *ELSC* decreases linearly with the moisture absorption level, which confirms the argument of stress concentration relief upon ageing. Concerning the remote tensile strength of the repairs, 12% reduction is noticed during early ageing (M=3%). This is obvious to be attributed to adhesive degradation, since both unnotched and notched specimens do not exhibit strength reduction. Beyond M=3%, the failure strength almost levels off. This is similar to the strength reduction trend of Adhesive2015, where the adhesive degrades in exponential decay form upon ageing [105]. If the repaired strength at M=7% is normalised with the unnotched dry strength, approximately 36% of strength reduction is noted. Nevertheless, compared to the strength reduction in the adhesive joints listed in Table 2.15, the performance of the repairs in this study is still comparatively stable under water attack. Besides, the normalised strength of unnotched, notched and repaired specimens is also fitted using Equation (4.9). Figure 7.3 illustrates the experimental and fitted normalised strength, where comparatively good fitting is observed.

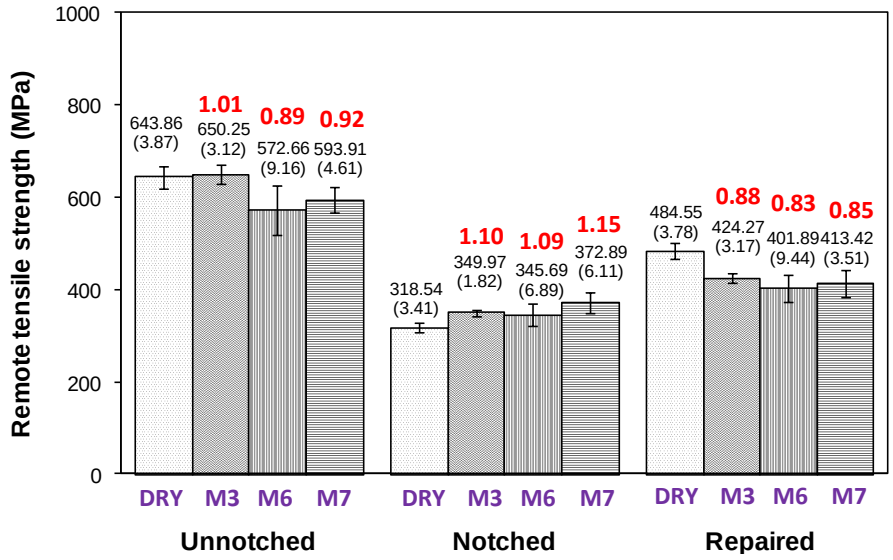

Figure 7.1: Remote tensile strength of unnotched, notched and repaired specimens at various moisture content levels.

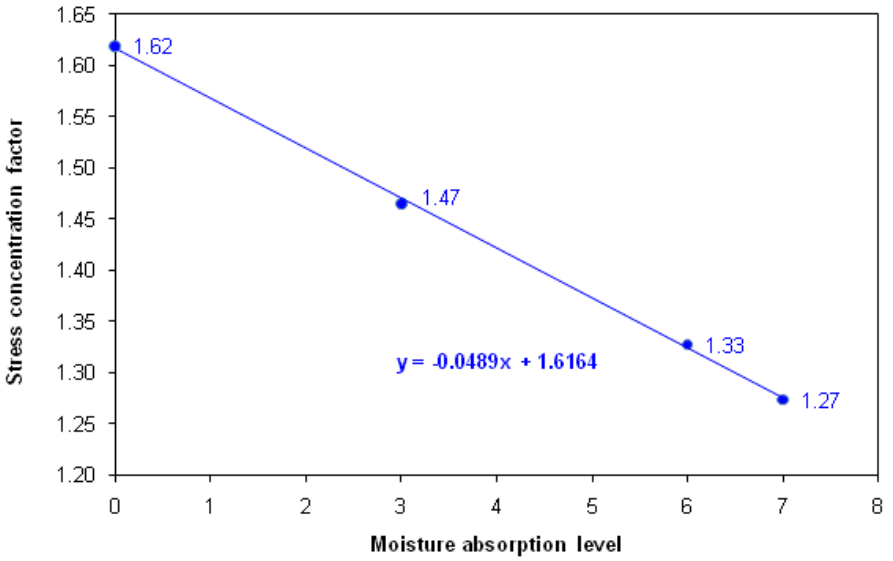

Figure 7.2: Effect of local stress concentration (*ELSC*) of notched specimens at various moisture content levels.

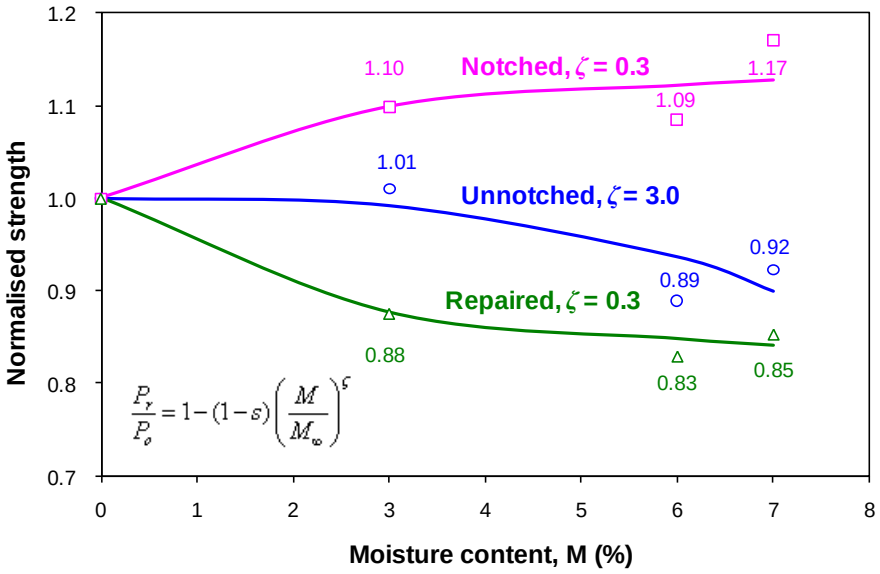

Figure 7.3: Experimental and fitted normalised strength of unnotched, notched and repaired specimens at various moisture content levels.

Figure 7.4 to Figure 7.6 show the fractured surfaces at different moisture content levels including dry condition of unnotched, notched and repaired specimens, respectively. It can be observed that in unnotched specimens, delamination and fibre splitting in quasi-isotropic laminate are observed to be increasingly significant with the ageing level. This implies significant ply/ply interface degradation, which is in accordance to the results reported in Section 4.4.3. Besides, ageing also enhances the possibility of failure in $+45^{o}$ direction in addition to -45^{o} and 90^{o} directions. This could be due to weakening of $+45^{o}$ plies which are located on the surfaces of the specimen that are subjected to more swelling and plasticisation. As for notched specimens, Figure 7.5 shows that the failure mode at M=3% appears similar to the dry specimen, where the final failure is in -45^{o} and 90^{o} directions. Similar to unnotched specimens, significant delamination and fibre splitting are observed at high moisture levels (M=6% and 7%), which is believed to be due to the similar weakening effects to those in unnotched ones. Figure 7.6 indicates that in repaired specimens, partial patch debonding is noticed at all moisture content levels with more or less adhesive failure at the longitudinal edges of the patch. This suggests good bonding behaviour even after prolonged ageing. Besides, the failure mode of the parent plate is similar to the notched specimens.

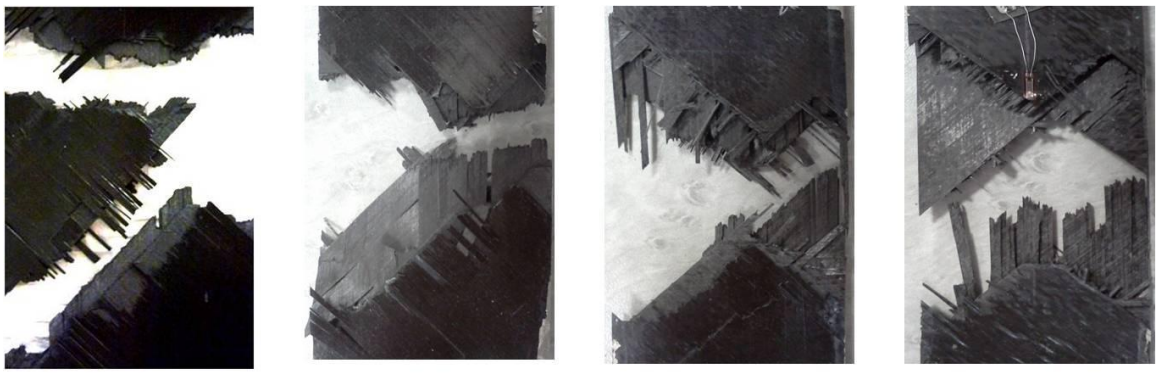

Figure 7.4: Fractured unnotched specimens at various moisture content levels.

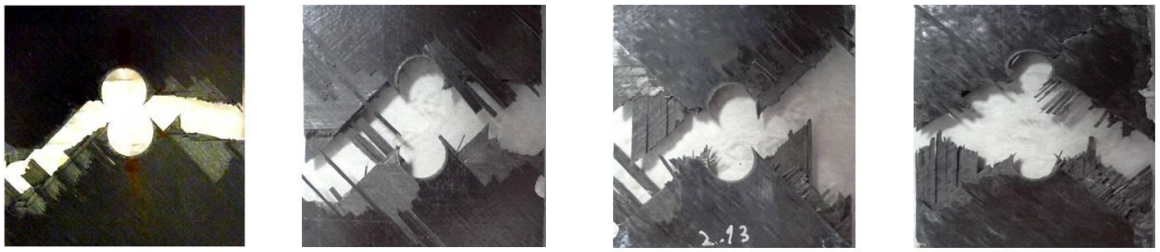

(a) Dry (b) M=3% (c) M=6% (d) M=7%

Figure 7.5: Fractured notched specimens at different moisture content levels.

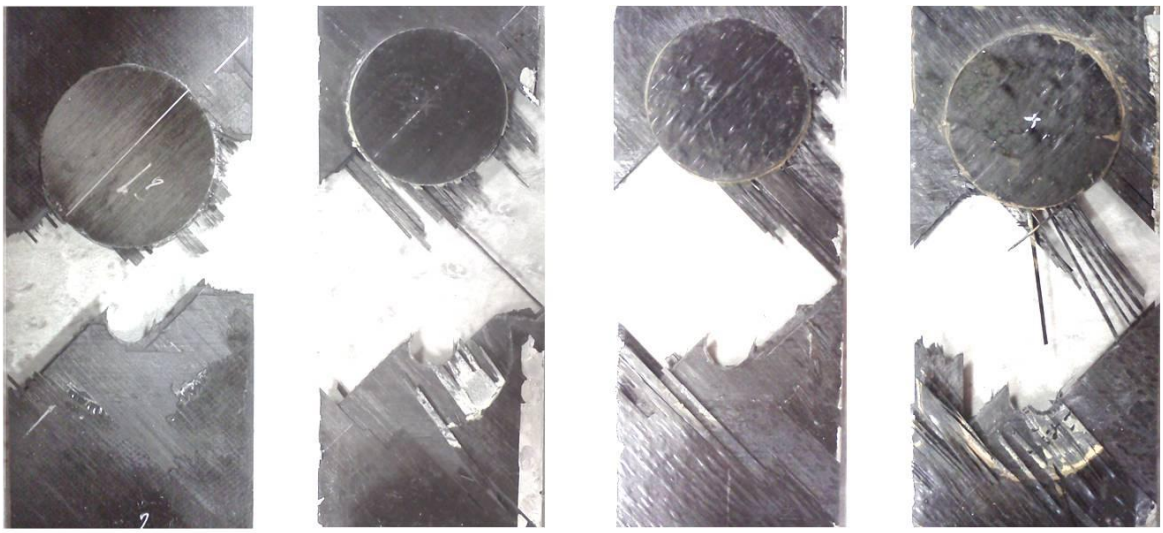

(a) Dry (b) M=3% (c) M=6% (d) M=7%

Figure 7.6: Fractured repaired specimens at various moisture content levels.

7.6.Comparison of experimental and numerical remote tensile strength under moisture ageing

Figure 7.7 compares the experimental and numerical remote tensile strength at various moisture levels. Similar to the dry cases (see Figure 6.11), the numerical values are always lower compared to the experimental ones. However, it is noteworthy that the experimental and numerical remote tensile strengths follow the same trend, which is decreasing with the moisture content level. Within the possible errors discussed in Section 6.8, these results are accepted.

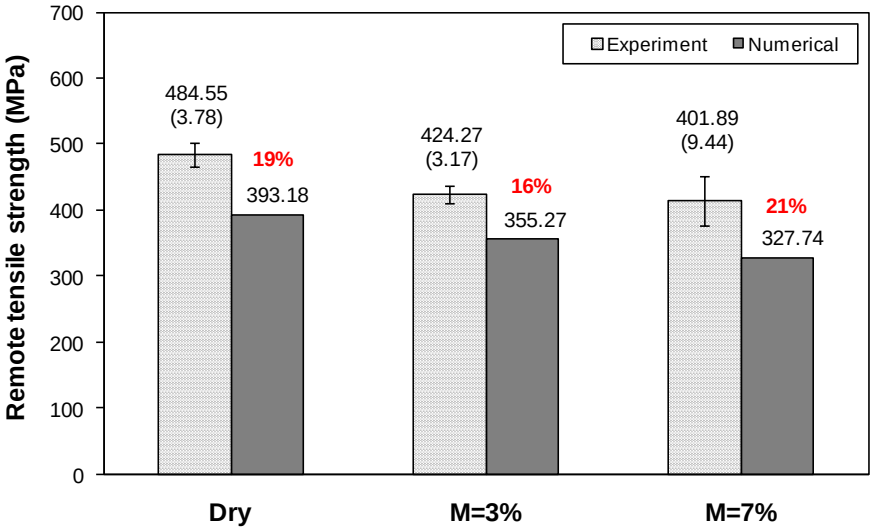

Figure 7.7: Comparison of experimental and numerical predicted remote tensile strength.

7.7.Comparison of first damage initiation in composite repairs at various water content levels

Figure 7.8 compares the first damage initiation in the laminas, interfaces and adhesive of the repairs at various water content levels. Table 7.6 shows the sequence of first damage initiation in the repairs at each moisture level. Generally, it can be seen that matrix tension damage in layer L2 (90^o) occurs first, followed by matrix tension damage in layers L1 and L3 ($\pm 45^o$), adhesive failure and interface delamination in interface I3 ($-45^o/0^o$). The moisture uptake can inverse the damage order between layers L1 (45°) and L3 (-45°). In addition, the damage order from the step 6 is seen influenced by moisture absorption. In dry and M=3% repairs, the step 6 and step 7 indicate the delamination in interface I1 ($45^o/90^o$) and interface I2 ($90^o/-45^o$). Fibre breakage in layer L4 (0^o) is the last damage initiation before final failure of the repairs. As for the moisture level at M=7%, fibre breakage in layer L4 (0^o) is noted before interface delamination in interfaces I1 ($45^o/90^o$) and I2 ($90^o/-45^o$). This could be due to lower X^T at higher water content level.

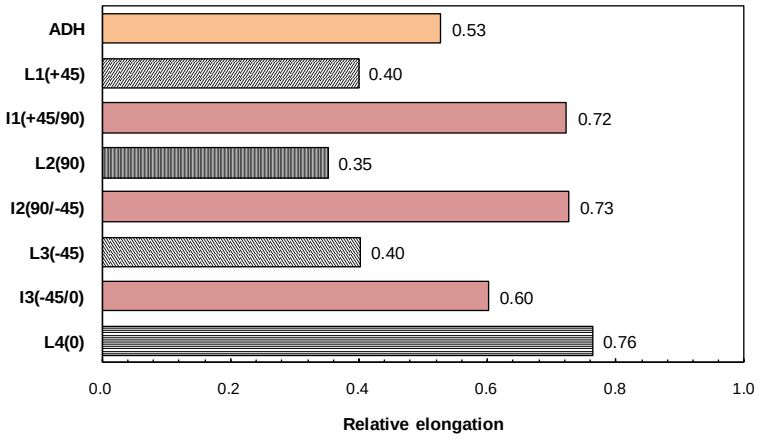

(a) Dry

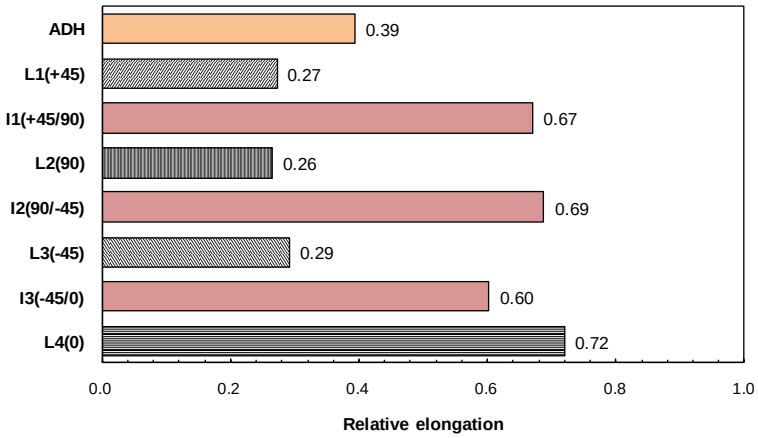

(b) M=3%

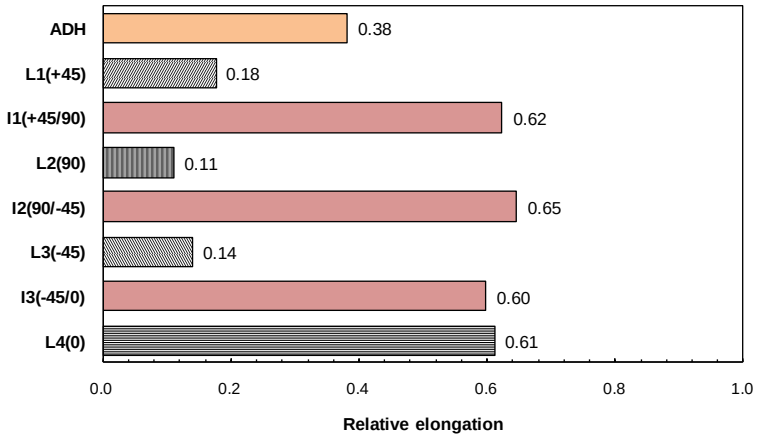

(c) M=7%

Figure 7.8: Comparison of first damage initiation in repaired composites at various water content levels.

Table 7.6: Comparison of damage initiation sequence in the repair composites at various moisture levels.

Sequence	1	2	3	4	5	6	7	8
Dry	L2(90)	L1(+45)	L3(-45)	ADH	I3(-45/0)	I2(90/-45)	I1(+45/90)	L4(0)
M=3%	L2(90)	L1(+45)	L3(-45)	ADH	I3(-45/0)	I1(+45/90)	I2(90/-45)	L4(0)
M=7%	L2(90)	L3(-45)	L1(+45)	ADH	I3(-45/0)	L4(0)	I1(+45/90)	I2(90/-45)

7.8.Numerical comparison of damage level in repaired composites at different moisture content levels

Since the initiation of the damage and its evolution in all the dry and wet repaired composites are similar, this section presents only the numerical results of their damage initiation level when the peak load is attained. Similar categorisation of the contour colours as described in Figure 6.13 is represented here.

It is shown that the least damage in $\pm 45^{o}$ plies is found at dry condition, whereas M=7% case exhibits the most severe damage level (see Figure 7.9 to Figure 7.11). Besides, the damage severity in layer L2 (90^{o}) is in accordance to the moisture exposure level, as depicted in Figure 7.10. Fibre breakage level is approximately the same in all dry and wet repairs (see Figure 7.12). In addition, Figure 7.13 illustrates that minimal interface

delamination concentrated near the transverse notch direction is always observed. Based on the experimental observations (Figure 7.6), the interface delamination is obviously underestimated. Recall that the toughness measured on 0/45 ply/ply interface of multidirectional laminate is smaller than that on 0/0 ply interface (Figure 4.12), it should be better to take into account of the effect of fibre orientation in the numerical simulation. However, in this study, the ageing test on QIQH MD laminate is not conducted because much longer ageing period is anticipated for 48-ply thick laminate. As for the initiation of adhesive damage, Figure 7.14 also illustrates similar damage level in all dry and wet specimens, where damage has initiated in the entire bonded region through the adhesive thickness. However, the contour of the total failed adhesive elements differs with the ageing condition (Figure 7.15). At low moisture levels (dry and M=3%), the region of the adhesive bonded to the parent plate has reached total failure. The elements away from the parent plate are almost intact. However, at high moisture level (M=7%), anti-symmetric failure pattern is noticed. Damage is found on each side of the joint near to the parent plate or to the patch.

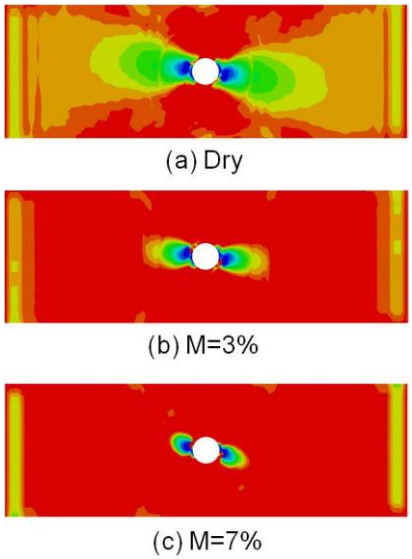

Figure 7.9: Extension of matrix tension damage initiation at peak load in layer 1 (L1 with 45^{o} fibres) at different moisture levels.

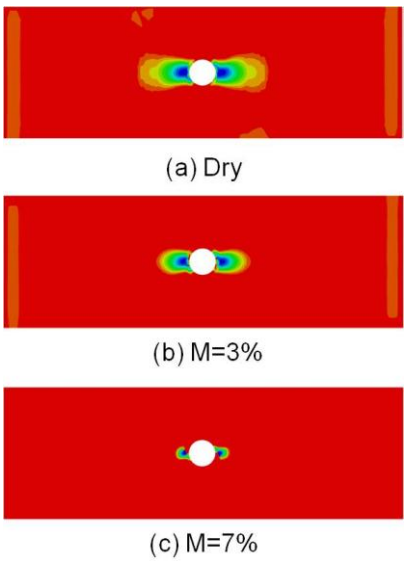

Figure 7.10: Extension of matrix tension damage initiation at peak load in layer 2 (L2 with 90^{o} fibres) at different moisture levels.

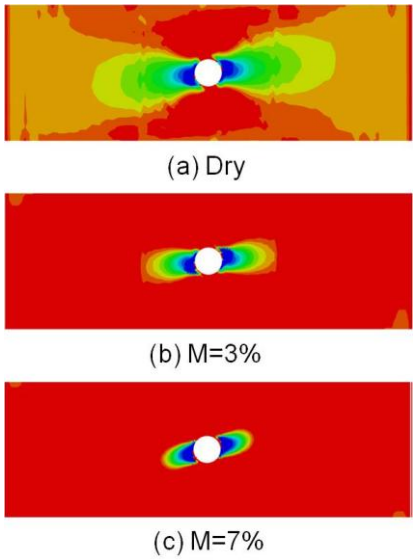

Figure 7.11: Extension of matrix tension damage initiation at peak load in layer 3 (L3 with -45^{o} fibres) at different moisture levels.

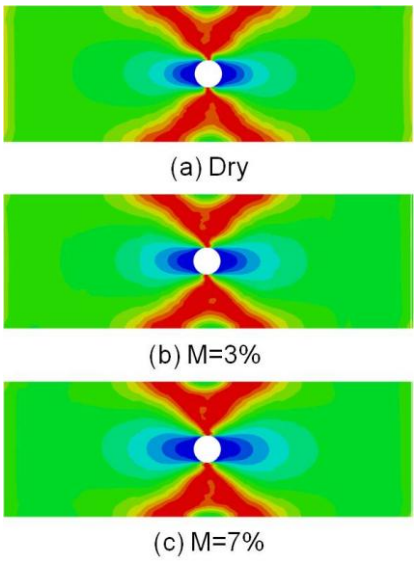

Figure 7.12: Extension of fibre tension fracture initiation at peak load in layer 4 (L4 with 0^{o} fibres) at different moisture levels.

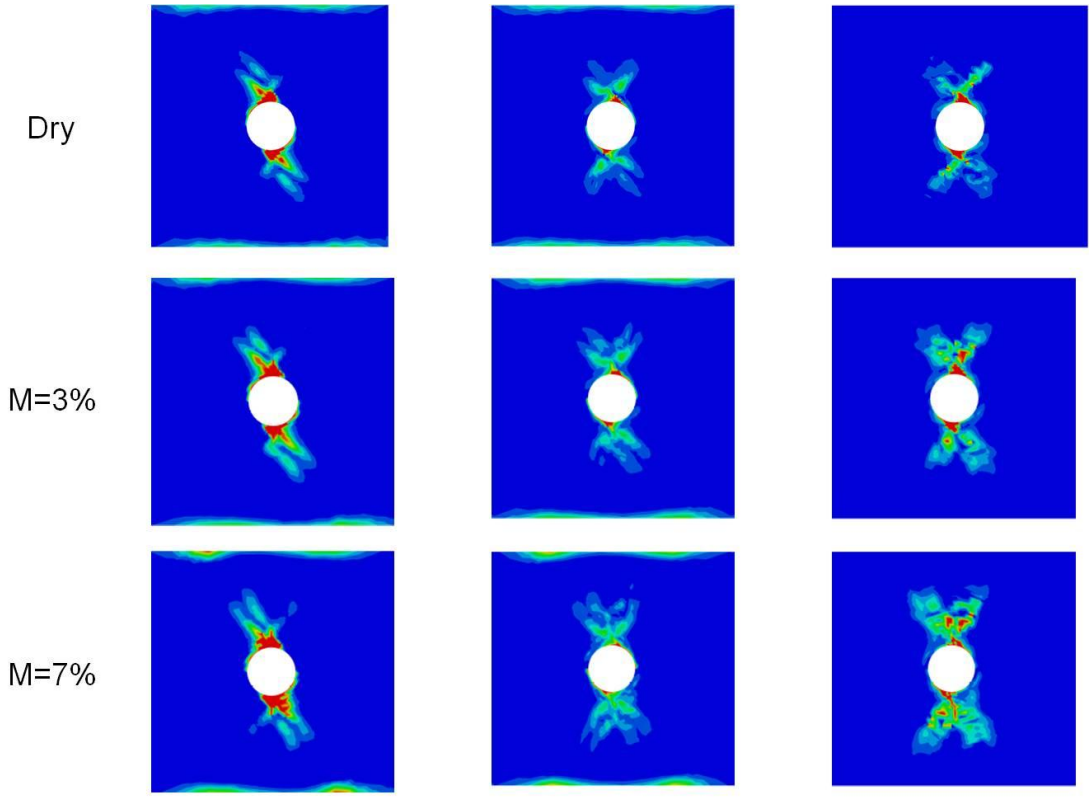

Figure 7.13: Extension of interface delamination initiation at peak load at various moisture content levels.

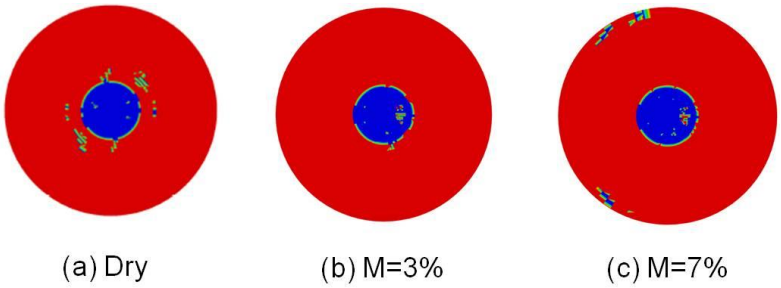

Figure 7.14: Extension of adhesive damage initiation at peak load in adhesive joint at various moisture content levels.

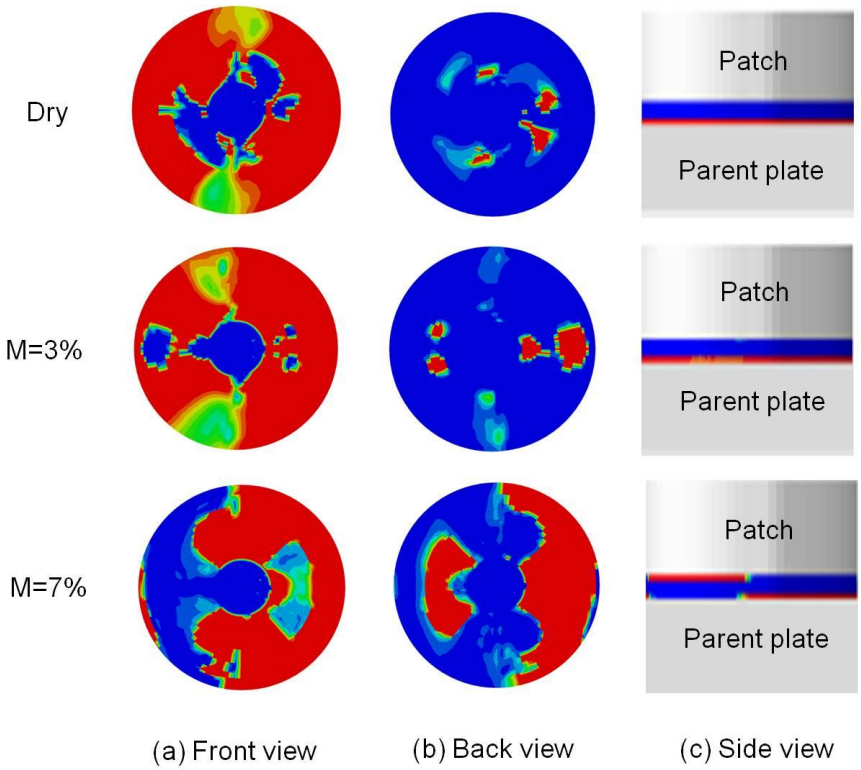

Figure 7.15: Extension of total adhesive damage (D=1) at peak load in adhesive joint at various moisture content levels.

7.9.Comparison of damage energy in composite repairs at various moisture content levels

Figure 7.16 presents the cumulative damage energy dissipated rate by damage process in each ply and interface of the parent plate, as well as the adhesive joint for the tested repairs that is obtained by numerical simulation. These curves give substantial information not only about the evolution of each damage mode as a function of the applied load, but also its changes with moisture uptake. It can be deduced that for a given moisture level, the damage energy dissipated in layer L4 (0^o) due to fibre breakage is always the largest, but its value at failure load, E_{Dmax} increases with moisture uptake level. Energy dissipated in layers L1 and L3 ($\pm 45^o$) is the same and is higher than layer L2 (90^o) except for the dry case. The maximum damage energy (E_{Dmax}) in layers L1 and L3 ($\pm 45^o$) varies with moisture content level but there is no clear trend; whereas the value of E_{Dmax} in layer L2 (90^o) decreases with moisture content level. Adhesive joint generally dissipates more energy than the interfaces. In all cases, the interface damage energy (and hence the damage region) in interface I1 ($+45^o/90^o$) is the largest among the interfaces, followed by interfaces I3 ($90^o/-45^o$) and I2 ($90^o/-45^o$) is the least. The E_{Dmax} value in adhesive joint seems to decrease with moisture content level. At M=7%, it is nearly 50% of that in dry repairs. Besides, the changes of E_{Dmax} value with moisture content level in all of interfaces are quite small.

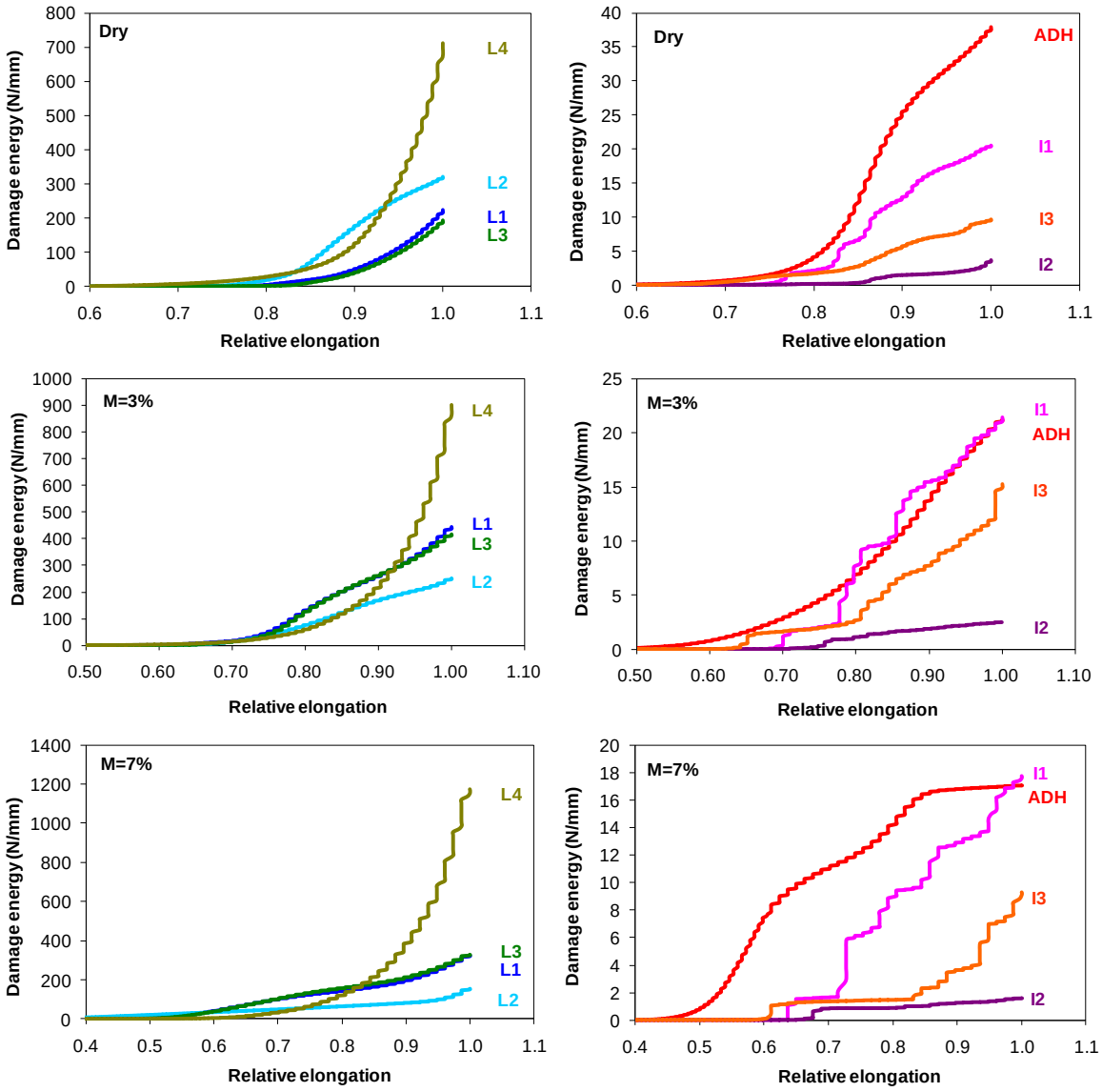

(a) Laminas (b) Interfaces and adhesive

Figure 7.16: Damage energy of each damage mode in laminas, interfaces and adhesive at various moisture content levels.

7.10.Analyses of acoustic emission data on the damage in repaired composites

Figure 7.17 displays the acoustic emission data at the peak load of repaired composites at various moisture content levels. It is apparent that more damage events are recorded upon ageing. Notably, matrix cracking which is postulated to fall within the amplitude range of 45-60dB (see Table 6.8) is observed to increase with the moisture content level. However, in aged specimens, amplitude range of 60-70dB does not seem to limit to the adhesive failure. Considerable damage events are also noticed outside the repaired zone (±17.5mm). This could be due to swelling of specimens lead to the difference in the AE signal transfer. Based on the experimental observation (Figure 7.6), it is supposed that the amplitude range of 60-80dB could refer to a mixture of both adhesive and interface delamination. However, this does not seem to agree with the finite element results, where only very minimal interface delamination at the transverse notch region is noticed. Amplitude range of 80-100dB is still reasonable to be regarded as fibre breakage.

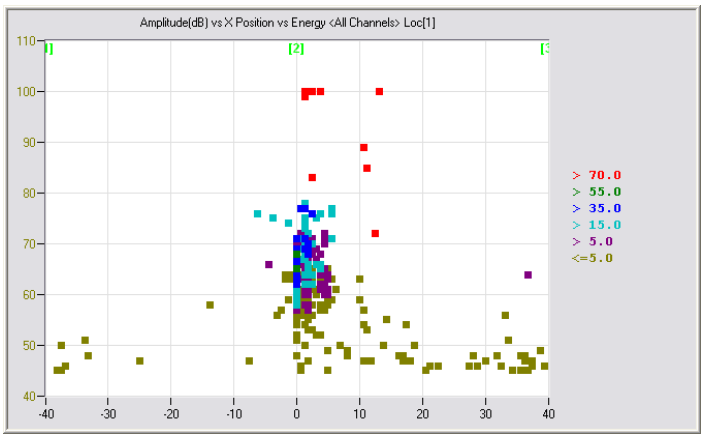

(a) Dry

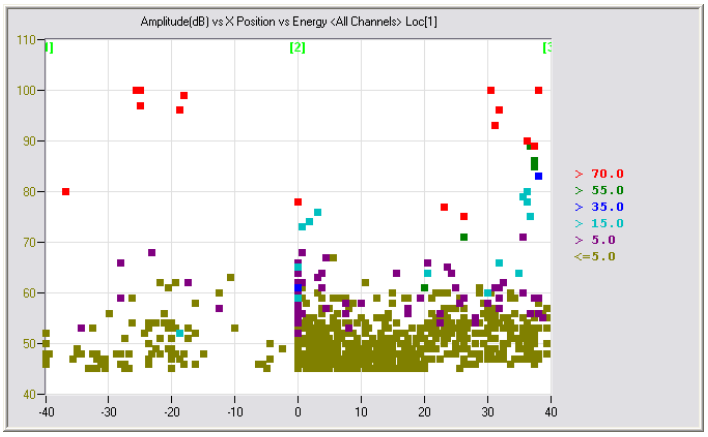

(b) M=3%

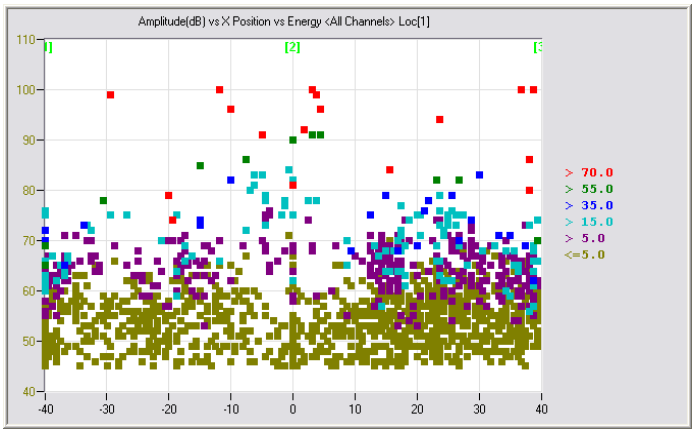

(c) M=7%

Figure 7.17: Acoustic emission amplitude and energy versus position of events in repaired composites at various moisture content levels.

7.11.Summary

This chapter reports the studies of water ingression influences on the tensile failure strength and damage process in the unnotched, notched and repaired specimens. Based on the results obtained, it can be summarised that:

i. The stiffness of the quasi-isotropic parent plate at different moisture content level is measured experimentally and also predicted by classical laminate theory and numerical simulation. The results obtained from these methods show a good agreement, with maximum difference of 16% for numerical M=3% case;

ii. Even after prolonged ageing, the remote tensile strength of unnotched specimens is almost invariant (approximately 10% reduction). A 17% of strength increment is noticed in notched specimens at M=7%, which is believed to be attributed to stress relief at the region of the notch. As for repaired specimens, approximately 15% of strength reduction is observed after long ageing period. The major reason of the weakening effect is possibly adhesive degradation;

iii. Experimental observations show that compared to dry repaired specimens, more severe delamination is observed in the aged specimens. Besides, in addition to -45^{o} and 90^{o} directions, final failure is also observed in $+45^{o}$, which is probably due to degradation of the outer most plies as a consequence of swelling and plasticisation. Partial patch debonding is always observed at all ageing level, which suggests good adhesive bonding behaviour;

iv. Numerical results show that there are two damage initiation sequences in the repairs under ageing:

- Dry and M=3%: L2 → L1, L3 → ADH → I3 → I1, I2 → L4
- M=6% and 7%: L2 → L1, L3 → ADH → I3 → L4 → I1, I2

v. Finite element results show that in general, damage initiation zone at peak load increases with moisture content in the laminas, interfaces and adhesive joint, although the severity may be different that can be estimated by damage energy data. However, the total failure elements in the adhesive could be different:

- Dry and M=3%: total adhesive failure in the bonded region near the parent plate
- M=6% and 7%: total adhesive failure on one side of the bonded region of both parent plate and patch

vi. Acoustic emission data suggests that the amplitude range of the damage mechanisms in the aged specimens could be classified as: 45-60dB for matrix cracking, 60-80dB refers to a mixture of adhesive failure and interface delamination, and 80-100dB indicates fibre breakage.

CHAPTER 8. CONCLUSIONS AND PERSPECTIVES

8.1. Concluding remarks

The objective of the study presented in this thesis is to investigate the water ingression behaviour in carbon/epoxy composites and the effects of the moisture content on their mechanical performance and bonded joints. Integration of these physical phenomena in the numerical modelling is of great importance in the prediction of structure life in their real environmental conditions. Therefore, this work consists of not only experimental observations, but also numerical simulations. Correlation between the results obtained aims, on the one hand to better understand what happened in an aged composite system under loading, what are their damage processes up to failure; on the other hand, to validate a robust numerical model for the purpose of structure design.

Firstly, the moisture absorption behaviour in T600S/R367-2, TR50S/R368-1, TR50S/R367-2 and T600S/R368-1 carbon/epoxy composites is studied. Under continuous demineralised water immersion at 70°C, water absorption in single-ply composites is well fitted using Fickian law, whereas the water uptake behaviour in multi-ply composites can be characterised using two-phase diffusion model proposed in this work expressed as:

$$\begin{aligned} M(t) &= \phi M_m G(t) + (1-\phi) M_m W(t) \\ &= \phi M_m \left\{ 1 - \exp\left[-7.3 \left(\frac{D_z t}{h^2} \right)^{0.75} \right] \right\} + (1-\phi) M_m \left\{ 1 - \exp\left[-\left(\alpha \left\langle t - t_o \right\rangle^{\beta} \right) \right] \right\} \end{aligned}$$

All constants necessary in applying this model have been discussed. Based on the results, it is worth to note that by conducting the moisture absorption test for 1-, 2- and 4-ply specimens, the moisture absorption behaviour at larger thickness can be predicted. Specifically, for T600S/R368-1 composite laminate, α=45.81exp(-0.55n), t_o=1.66$n^{2.27}$ and β=0.75. Besides, in all cases, $\phi=M_{m1}/M_m$, where M_{m1} and M_m are the maximum moisture content of single-ply and multi-ply, respectively. D_z is the diffusivity of single-ply composite.

Next, the elementary tensile and interface properties of T600S/R368-1 carbon epoxy composite are characterised at different moisture content levels. The elementary tensile properties that are more sensitive to water attack are shear strength (maximum of ≈30% reduction), transverse strength (maximum of ≈75% reduction) and transverse modulus (maximum of ≈35% reduction), whereas longitudinal strength, longitudinal stiffness, shear stiffness and Poisson's ratio are comparatively stable with moisture content level. Besides, after prolonged ageing, 20% in the reduction of the fracture toughness of DCB specimens is noticed, and 50% degradation is found in ENF and MMF specimens. The variation of both elementary tensile properties and fracture toughness with moisture content can be described by a newly proposed residual property model as: $\frac{P_r}{P_o} = 1 - (1-s)\left(\frac{M}{M_m} \right)^{\zeta}$.

R-curve effect is significant in mode I delamination of aged specimens. To describe the mode I fibre bridging behaviour, linear-exponential bridging law is proposed in the current study, where the increment in the fracture energy can thus be represented as: $dG = \frac{t_i(\delta_f - \delta_i)}{\gamma}\left[1 - \exp\left(-\gamma \frac{\delta - \delta_i}{\delta_f - \delta_i}\right)\right]$. This model is able to describe any R-curve by fitting the parameter γ.

The delamination behaviour of the laminated composites is well described using cohesive zone model (CZM). Inclusion of R-curve effect through linear-exponential law in mode I delamination has significantly improved the simulation results. It is found that the cohesive parameters are not sensitive to the moisture content level, where $K_{nn}=K_{ss}=K_{tt}=1\times10^4$ N/mm^3, t_n=25MPa and $t_s=t_t$=80MPa are suitable to be used in all delamination cases.

Subsequently, the fracture toughness of Araldite2015 bonded T600S/R368-1 carbon/epoxy composite joints at various moisture content levels is measured through DCB, ENF and MMF tests. Results show that the fracture toughness is decreased during the early ageing period, and increased after that at M=5%. At M=6%, only 31% of their dry toughness is retained. In addition, water absorption causes the change in the failure mode from cohesive fracture to a mixture of cohesive and interface fracture.

R-curve effect is observed in all mode II adhesive specimens. The linear bridging law proposed by Anyfantis and Tsouvalis [279] is adopted to include the R-curve behaviour during finite element simulation. Continuum damage modelling (CDM) is employed to simulate adhesive damage. Through CDM parameters calibration, it is suggested that strength ratio of $\sigma_{o,DCB}/\sigma_{o,ENF}\approx0.3$ is a good choice to obtain comparatively good simulation results.

This study is then continued by investigating the water absorption effects on the tensile behaviour of $[45/90/-45/0]_S$ quasi-isotropic laminate. Experimental results reveal that the remote tensile strength of unnotched and notched (with 10mm diameter central notch) specimens is comparatively stable under moisture ageing. Approximately 10% reduction and 15% of increment are noticed in unnotched and notched specimens, respectively. Repaired specimens are prepared by bonding 35mm diameter circular patches with stacking sequence of $[\mp45]_S$ on both sides of notched specimens using Araldite2015 adhesive. Approximately 15% of strength reduction is observed in aged repairs, which is possibly due to adhesive degradation. In all specimens, it is observed that delamination is more severe in the quasi-isotropic parent plates upon ageing. Besides, partial patch debonding is always observed in the repaired composites at all ageing levels, which suggests good adhesive bonding behaviour.

For the finite element modelling of composite repairs, cohesive zone model (CZM) is employed in the ply/ply interface of the composite, whereas continuum damage model (CDM) is implemented in the adhesive joint. In addition, the continuum damage model based on Hashin's criterion is adopted to predict the damage initiation and progression in the layers of composite laminates. Numerical results suggest that at all moisture absorption levels, damage initiation in the adhesive always occurs after matrix tension damage and before interface delamination and fibre breakage. The progression of damage initiation in the laminas, interfaces and adhesive is similar in the dry and wet repairs, although the severity may be different. Two different total adhesive failure (D=1) patterns are noted: in the bonded region near the parent plate for dry and M=3% cases, and on one side of the bonded region of both parent plate and patch for M=6% and 7% repairs.

Furthermore, from the acoustic emission data, it is postulated that the amplitude range of the damage mechanisms in the repaired specimens at all moisture content levels could be

classified as: 45-60dB for matrix cracking, 60-70dB for adhesive damage in dry repairs whereas 60-80dB for wet repairs, 60-80dB for interface delamination, and 80-100dB for fibre breakage.

In addition to the conclusions mentioned above which contribute to the major studies of this thesis, some additional works are also carried out on unaged specimens to verify some design parameters of the composite. One of them is the comparison between the fracture toughness of vacuum-bagging and hot-press fabricated laminates. Results indicate that the mode I, mixed-mode I+II and mode II fracture toughness of vacuum-bagging fabricated unidirectional laminate are 12%, 25% and 30% lower compared to the laminate fabricated using hot-press technique. However, fibre bridging is found in vacuum-bagging fabricated DCB specimens.

Besides, in order to understand the fibre orientation effects in delamination behaviour, composite laminates with adjacent plies of [0//0] (unidirectional laminate) and [0//45] (multidirectional QIQH laminate) are prepared. Between both stacking sequences, invariant G_{IC} values is observed, and approximately 20% lower in G_{IIC} and G_{I+IIC} values is noticed in [0//45] laminate. DCB specimens with [0//45] adjacent fibre orientation exhibit fibre bridging effect.

As for the quasi-isotropic laminates, the influence of stacking sequence is also studied. It is shown that the stacking sequence of quasi-isotropic laminates affects the ultimate tensile strength and failure mode. For unnotched specimens, edge delamination is observed in specimens with 90^o as mid-plies. Delamination is not observed in all notched specimens. Generally, two different failure modes could be identified: brittle failure in quasi-isotropic laminates with larger inter-ply angle difference ($[45/-45/0/90]_S$ and $[-45/45/90/0]_S$), and a combination of brittle and pull-out failure in quasi-isotropic laminates with consistent 45^o inter-ply angle difference: $[-45/0/45/90]_S$ and $[45/90/-45/0]_S$.

In addition to Araldite2015 adhesive, fracture tests are also carried out on adhesive joints bonded with ESP110 adhesive. It is found that the failure in Araldite2015 bonded composite joints is mainly cohesive, whereas a mixture of cohesive and interface failure is noticed in ESP110 bonded joints. Besides, mode I and II fracture toughness of ESP110 joints are 35% and 40% lower compared to Araldite2015 joints. However, the mixed-mode fracture toughness measured under MMF loading on ESP110 bonded joints are 13% higher than that of Araldite2015 joint. In the composite repairs with $[\pm 45]_S$ and $[\mp 45]_S$ patches, and $[45/90/-45/0]_S$ parent plate, ESP110 bonded repairs exhibit slightly higher remote tensile strength (6-13%) compared to Araldite2015 bonded repairs. However, two-side total patch debonding is always observed in ESP110 composite joints but not in Araldite2015 repairs.

For the adhesive joints, comparison is also done between sandpaper polished and plasma treated surface treatment methods. Compared to the sandpaper polished method, approximately only 20% of mode I and II fracture toughness is retained in plasma treated adhesive joints. Besides, crack deflection within the adhesive layer is observed in plasma treated specimens. However, it is surprising to see that the surface treatment method does not incur significant effect on the remote tensile strength of repaired composites. Furthermore, one-side total patch debonding is only occasionally observed in plasma treated repairs and partial patch debonding is always occurred in sandpaper polished repaired specimens.

It is also noteworthy that the stacking sequence of the patch ($[\pm 45]_S$ and $[\mp 45]_S$) has negligible influence on the remote tensile strength of both Araldite2015 and ESP110 bonded composite repairs.

Numerical results of the dry repaired composites using the same modelling approach as in the aged repairs reveal that in brittle ESP110 bonded repairs, the order of damage initiation can be different to that in ductile Araldite2015 bonded repairs, where early damage is observed in the adhesive joint of ESP110 repairs. However, this prediction is not really confirmed experimentally.

8.2.Suggestions for future work

As a continuation from the works presented in this thesis, it is first suggested that continuous moisture absorption tests on T600S/R368-1 carbon/epoxy composite could be carried out at different relative humidity and temperature levels. Tests could also be conducted on different engineering materials. If non-Fickian diffusion behaviour is still observed at some or all environmental conditions, the applicability of the two phase diffusion model proposed in this study could be further verified. In addition, it may be also worth to conduct cyclic moisture absorption tests on both the carbon/epoxy composite and the adhesive, since the moisture and temperature levels are generally fluctuating in real life applications. Cyclic environmental conditions could lead to different effects on the materials due to moisture and/or thermal shocks. Determination of the glass transition temperature, T_g of both composite and adhesive under dry and wet conditions is also necessary to ensure the ageing temperature is always above the T_g of the materials. Furthermore, considering the structural components are always subjected to external loadings, the study on the consequences of external mechanical loads on the diffusive behaviour is also important to investigate the possible hydro-mechanical couplings effects on the performance of the materials.

Besides, fractographic analysis on the tested specimens is essential. For the traveller coupons, fractographic analysis could provide the information of the void content at different thicknesses, heterogeneity of fibre distribution, ply integrity and possible reasons for decrement in the moisture content after the maximum moisture content, M_m is attained. Micrographic surface observation on the fractured surfaces would help to understand the damage mechanisms in the composites and composite joints. Based on the surface morphology analysis, it is expected that some information about the adhesive behaviour in the composite repairs could be obtained. It is then possible to improve the finite element model of the composite repairs, where current study shows that the experimental and numerical observations are contradicting each other for Araldite2015 and ESP110 bonded composite repairs.

In addition, characterisation of the mechanical behaviour of the dried composite and adhesive after ageing would be interesting to study the irreversible effect of moisture absorption on the properties of the materials. For the delamination tests, testing the specimens using more stable crack propagation tests such as four point end notched flexure (4-ENF), end-loaded split (ELS) and mixed-mode bending (MMB) tests could be attempted, in which R-curve may be obtained for the composite.

Moreover, in the finite element models of this study, the moisture concentration in the finite element models of the composite repairs is always assumed to be uniform at each moisture content level. It would be good to implement the two phase diffusion model in the finite element software to predict the three-dimensional moisture diffusion in the composite joints. This could in turn improve the local stress state prediction especially during the initial stage of moisture absorption. Also, improvement in the residual property model (RPM) to predict the variation of the property of the adhesive bonded joints is needed since the diffusion and thus the residual property of the composite and the adhesive are different at the same instantaneous.

For the acoustic emission (AE), it would be more convincing to verify the proposed amplitude range for the different damage mechanisms through isolated controlled tests. Measurements are to be carried out separately for the matrix breakage, ply delamination, fibre/matrix debonding, fibre breakage and adhesive failure to calibrate the triggered AE amplitude range for the failure mechanisms.

Furthermore, since the loading in the structures is generally complex, to better understand the behaviour of the composite repairs under different loading mode, quasi-static compression test on the composite and its bonded joints could be the next attempt. Compressive behaviour is interesting to be studied due to instability of the delaminated plies and micro-buckling behaviour, which could not be observed in tensile test. Also, fatigue test on the composite and patch bonded repairs is worth to be studied. Fatigue loading could better imitate the actual loading on the structural components. Fatigue behaviour could be different from the quasi-static behaviour and hence is important to be investigated.

APPENDIX A. IMPLEMENTATION OF THE TWO-PHASE DIFFUSION MODEL

To implement the two-phase diffusion model proposed in this study shown in Equation (3.2), which is written as:

$$\begin{aligned} M(t) &= M_I(t) + M_{II}(t) \\ &\phi M_m G(t) + (1-\phi) M_m W(t) \\ &= \phi M_m \left\{ 1 - \exp\left[-7.3 \left(\frac{D_z t}{h^2} \right)^{0.75} \right] \right\} + (1-\phi) M_m \left[1 - \left\{ \exp - \left[\left(\alpha \left\langle t - t_o \right\rangle \right)^{\beta} \right] \right\} \right] \end{aligned}$$

Firstly, the moisture absorption plot of the single-ply composite, $M_I(t)$ which corresponds to the first term in Equation (3.2), is plotted based on the single-ply experimental data. Then, t_o is identified at the point when significant difference ($M(t)$-$M_I(t)$≥0.2%) is noted. Next, the experimental $W(t)$ (denoted as $W_{exp}(t)$) can be plotted by:

$$W_{\exp}(t) = \frac{M(t) - M_I(t)}{M_m - M_{m1}}$$

Since $W(t) = 1 - \left\{ \exp - \left[\left(\alpha \left\langle t - t_o \right\rangle \right)^{\beta} \right] \right\}$, taking logarithms of both sides for two times yields:

$$\ln\{-\ln[1 - W(t)]\} = \beta \ln \left\langle t - t_o \right\rangle + \beta \ln \alpha$$

Plotting the curve of $\ln\{-\ln[1 - W_{\exp}(t)]\}$ versus $\ln \left\langle t - t_o \right\rangle$, a straight line is obtained. The slope of the straight line gives the value of β. From the intersection which is equal to $\beta \cdot \ln\alpha$, α can be determined.

APPENDIX B. MATLAB CODE FOR MOISTURE CONCENTRATION ACROSS LAMINATE THIEKNESS

B1. Single-ply laminates: Fickian diffusion

From Equation (2.4), the one-dimensional moisture concentration distribution across the laminate thickness is written as:

$$\frac{c-c_i}{c_m-c_i}=1-\frac{4}{\pi}\sum_{j=0}^{\infty}\frac{1}{(2j+1)}\sin\frac{(2j+1)\pi z}{h}\exp\left[-\frac{(2j+1)^2\pi^2 D_z(T)t}{h^2}\right]$$

The corresponding MATLAB code is as follows:

```
%%%%%%%%%%%%%%%%%%%%%%%%%%%%%%%%%%%%%%%%%%%%%%%%%%%%%%%%%%%%%%%%%%%%%%%
% Moisture concentration distribution of 170-1 single-ply composite
%%%%%%%%%%%%%%%%%%%%%%%%%%%%%%%%%%%%%%%%%%%%%%%%%%%%%%%%%%%%%%%%%%%%%%%

h=0.2; % laminate thickness [mm]
ts=189900; % Saturation time [s]
D=3.08507*10^-7; % Diffusivity [mm2/s]
x=linspace(0,h); % [mm]
t=linspace(0,ts); % [s]
i=1; j=1;
C=[];
for i = 1:length(t) % Loop for time
for j = 1:length(x) % Loop for position

% Determine the transient component for each t and x
for n = 0:100;
Ci = 1/(2.*n+1).*exp(-(2.*n+1).^2*pi^2*D.*t(i)/h^2).*sin((2.*n+1)*pi.*x(j)/h);
if n==0;
   Cn = Ci;
else
   Cn = Cn + Ci;
end
end
C(j,i) = 1-4/pi*Cn;
end
end

%%%%%%%%%%%%%%%%%%%%%%%%%%%%%%%%%%%%%%%%%%%%%%%%%%%%%%%%%%%%%%%%%%%%%%%
% View Results
%%%%%%%%%%%%%%%%%%%%%%%%%%%%%%%%%%%%%%%%%%%%%%%%%%%%%%%%%%%%%%%%%%%%%%%

% Plot the concentration gradient
figure
plot(x./h,C(:,4),x./h,C(:,9),x./h,C(:,19),x./h,C(:,34))
grid
title('Concentration Distributions');grid
xlabel('x/h'); ylabel('C/C_0')
legend('t=2hr','t=5hr','t=10hr','t=18hr')
%%%%%%%%%%%%%%%%%%%%%%%%%%%%%%%%%%%%%%%%%%%%%%%%%%%%%%%%%%%%%%%%%%%%%%%
```

B2. Multi-ply laminates: Two-phase diffusion

The moisture concentration of two-phase diffusion model proposed in this study described by Equation (3.4) is expressed as:

$$\frac{c(x,t)}{c_m} = \phi\left\{1-\frac{4}{\pi}\sum_{j=0}^{\infty}\frac{1}{(2j+1)}\sin\frac{(2j+1)\pi z}{h}\exp\left[-\frac{(2j+1)^2\pi^2 D_{zI}t}{h^2}\right]\right\}+$$

$$(1-\phi)\left\{1-\frac{4}{\pi}\sum_{j=0}^{\infty}\frac{1}{(2j+1)}\sin\frac{(2j+1)\pi z}{h}\exp\left[-(2j+1)^2\pi^2\alpha\left\langle t-t_o\right\rangle\right]\right\}$$

The MATLAB code for the concentration distribution is as follows:

```
%%%%%%%%%%%%%%%%%%%%%%%%%%%%%%%%%%%%%%%%%%%%%%%%%%%%%%%%%%%%%%%%%%%%%%%%%%%%
% Moisture concentration distribution of 170-4 multi-ply composite
%%%%%%%%%%%%%%%%%%%%%%%%%%%%%%%%%%%%%%%%%%%%%%%%%%%%%%%%%%%%%%%%%%%%%%%%%%%%

h=0.8; % thickness for absorption through both surfaces [mm]
ts=18052800; % saturation time [s]
ti=117600; % time at
DzI=3.08507*10^-7; % [mm2/s]
alpha=3.52*10^-7; % [mm-1s-1]
phi=0.33;
x=linspace(0,h); % [mm]
t=linspace(0,ts); % [s]
i=1; j=1;
C=[];

for i = 1:length(t) % Loop for time
for j = 1:length(x) % Loop for position

% Determine the transient component for each t and x
for n = 0:1000
CiI = 1/(2.*n+1).*exp(-(2.*n+1).^2*pi^2*DzI.*t(i)/h^2).*sin((2.*n+1)*pi.*x(j)/h);
if t<ti
   heavyside=0;
else
   heavyside=1;
end
CiII = heavyside.*1/(2.*n+1).*exp(-(2.*n+1).^2*pi^2*alpha.*t(i)).*sin((2.*n+1)*pi.*x(j)/h);
if n==0;
   CnI = CiI;
   CnII = CiII;
else
   CnI = CnI + CiI;
   CnII = CnII + CiII;
end
end
CI(j,i) = (1-4/pi*CnI)*phi;
CII(j,i) = (1-4/pi*CnII)*(1-phi);
C(j,i) = CI(j,i) + CII(j,i);
end
end
%%%%%%%%%%%%%%%%%%%%%%%%%%%%%%%%%%%%%%%%%%%%%%%%%%%%%%%%%%%%%%%%%%%%%%%%%%%%
% View Results
%%%%%%%%%%%%%%%%%%%%%%%%%%%%%%%%%%%%%%%%%%%%%%%%%%%%%%%%%%%%%%%%%%%%%%%%%%%%
% Plot the concentration gradient
figure
plot(x./h,C(:,2),'o',x./h,C(:,5),'s',x./h,C(:,10),'^')
grid
title('Concentration Distributions');grid
xlabel('x/h'); ylabel('C/C_0')
legend('t=5days','t=10days','t=20days')
%%%%%%%%%%%%%%%%%%%%%%%%%%%%%%%%%%%%%%%%%%%%%%%%%%%%%%%%%%%%%%%%%%%%%%%%%%%%
```

APPENDIX C. DERIVATION AND IMPLEMENTATION OF LINEAR-EXPONENTIAL TRACTION-SEPARATION LAW

From Figure 4.20 which describes the proposed linear-exponential traction-separation low as follows:

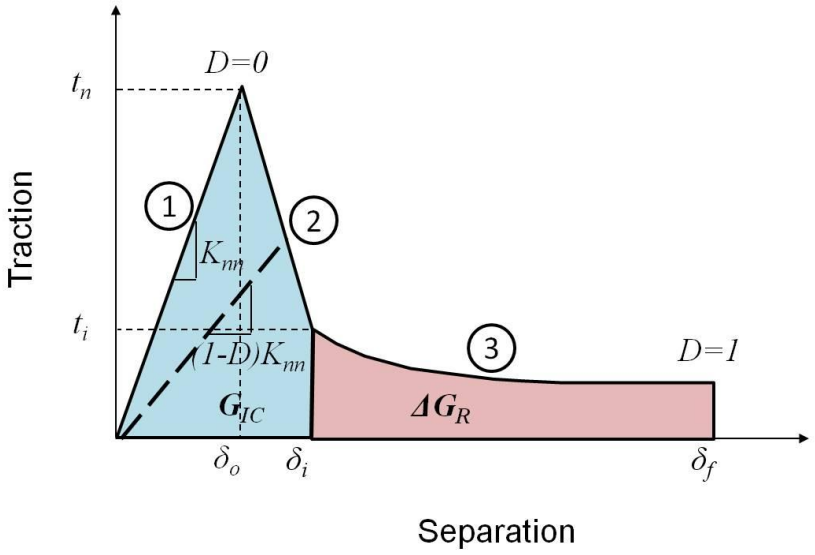

C1. DERIVATION:

TRACTION

Line ①: $t = K_{nn}\delta$

$$t = \left(\frac{t_n - t_i}{\delta_o - \delta_i}\right)\delta + c$$

B.C: at $\delta = \delta_o, t = t_n$

Line ②: $$c = t_n - \left(\frac{t_n - t_i}{\delta_o - \delta_i}\right)\delta_o$$

$$\therefore t = \left(\frac{t_n - t_i}{\delta_o - \delta_i}\right)\delta + t_n - \left(\frac{t_n - t_i}{\delta_o - \delta_i}\right)\delta_o$$

$$= t_n + (t_n - t_i)\left(\frac{\delta - \delta_o}{\delta_o - \delta_i}\right)$$

$$t = \kappa \exp\left(-\alpha \frac{\delta - \delta_i}{\delta_f - \delta_i}\right)$$

Line ③: B.C: at $\delta = \delta_i, t = t_i \Rightarrow \kappa = t_i$

$$\therefore t = t_i \exp\left(-\alpha \frac{\delta - \delta_i}{\delta_f - \delta_i}\right)$$

ENERGY

Initiation zone (blue):

$$\begin{aligned} G_{IC} &= \frac{1}{2} t_n \delta_o + \frac{1}{2}(t_n - t_i)(\delta_i - \delta_o) + t_i(\delta_i - \delta_o) \\ &= \frac{1}{2} t_n \delta_o + \frac{1}{2} t_n \delta_i - \frac{1}{2} t_i \delta_i - \frac{1}{2} t_n \delta_o + \frac{1}{2} t_i \delta_o + t_i \delta_i - t_i \delta_o \\ &= \frac{1}{2} t_n \delta_i + \frac{1}{2} t_i \delta_i + \frac{1}{2} t_i \delta_o \\ &= \frac{1}{2}[(t_n + t_i)\delta_i + t_i \delta_o] \end{aligned}$$

Bridging zone (red):

$$\begin{aligned} G &= \int_{\delta_i}^{\delta} t d\delta \\ &= \int_{\delta_i}^{\delta} \left[t_i \exp\left(-\alpha \frac{\delta - \delta_i}{\delta_f - \delta_i}\right)\right] d\delta \\ &= \frac{-t_i(\delta_f - \delta_i)}{\alpha} \exp\left(-\alpha \frac{\delta - \delta_i}{\delta_f - \delta_i}\right)\Bigg]_{\delta_i}^{\delta} \\ &= \frac{t_i(\delta_f - \delta_i)}{\alpha}\left[1 - \exp\left(-\alpha \frac{\delta - \delta_i}{\delta_f - \delta_i}\right)\right] \end{aligned}$$

DAMAGE PARAMETER (D)

Line ②:

$$(1-D)K_{nn}\delta = t_n + (t_n - t_i)\left(\frac{\delta - \delta_o}{\delta_o - \delta_i}\right)$$

$$D = 1 - \frac{1}{K_{nn}\delta}\left[t_n + (t_n - t_i)\left(\frac{\delta - \delta_o}{\delta_o - \delta_i}\right)\right]$$

Line ③:

$$(1-D)K_{nn}\delta = t_i \exp\left(-\alpha \frac{\delta - \delta_i}{\delta_f - \delta_i}\right)$$

$$D = 1 - \frac{t_i}{K_{nn}\delta} \exp\left(-\alpha \frac{\delta - \delta_i}{\delta_f - \delta_i}\right)$$

C2. IMPLEMENTATION:

From the derivation, the fracture energy in the initiation zone reads $G_{IC} = 0.5[(t_n + t_i)\delta_i + t_i\delta_o]$, where there are five parameters in the equation. The value of G_{IC} is obtained from the experiment data. Besides, based on the user predefined cohesive parameters: K_{nn} and t_n, δ_o is thus obtained. Hence, there are still two unknowns: t_i and δ_i. To obtain the solution, iteration is performed using MATLAB. The MATLAB code is displayed in the following:

```
%%%%%%%%%%%%%%%%%%%%%%%%%%%%%%%%%%%%%%%%%%%%%%%%%%%%%%%%%%%%%%%%%%%%%%%%
clear all; clc
error = 100;
K=1E4; %N/mm3
tn=25; %MPa
do=tn/K; %mm

ti=1; %MPa
di=0.00005;%mm
GIC=0.5; %N/mm
e=[];
while error>=1;
   di=di+0.0001;
   ti=ti-0.0001;
   GIC_with_error = 0.5*tn*do+0.5*(tn+ti)*(di-do);
   error = abs(GIC_with_error-GIC)/GIC*100;
   e = [e error];
end
di
ti
GIC_with_error
error
%%%%%%%%%%%%%%%%%%%%%%%%%%%%%%%%%%%%%%%%%%%%%%%%%%%%%%%%%%%%%%%%%%%%%%%%
```

Next, the crack opening displacement (COD), δ at each increment in the crack length, Δa can be calculated using Equation (4.12), which is expressed as $\delta = (d - \delta_i)\dfrac{\Delta a^2(2\Delta a + 3a_o)}{(a_o + \Delta a)^3} + \delta_i$, the final displacement, δ_f corresponds to the final point of the experiment R-curve, where the maximum increment in the fracture energy is obtained. The experimental R-curve in function of COD can thus be plotted. The fitting parameter, γ can be determined using Trust-Region curve fitting algorithm in MATLAB.

REFERENCES

1. Soutis C. Carbon fiber reinforced plastics in aircraft construction. Materials Science and Engineering: A. 2005; 412(1-2): 171-176.
2. Soutis C. Fibre reinforced composites in aircraft construction. Progress in Aerospace Sciences. 2005; 41(2): 143-151.
3. How old is too old? The impact of aging aircraft on aviation safety. Aviation Research and Analysis Report. No: B20050205. Canberra: Australian Transport Safety Bureau (ATSB); 2007.
4. Robinson Helicopter Company, Model R22 Mariner, Bents Basin State Recreation Area, NSW, 20 June 2003. Aviation Safety Investigation Report. No: 200302820. Canberra: Australian Transport Safety Bureau (ATSB); 2005.
5. Nugroho AM. A preliminary study of thermal environment in Malaysia's terraced houses. Journal of Economics and Engineering. 2011; 2(1): 25-28.
6. Hu FZ, Soutis C. Strength prediction of patch-repaired CFRP laminates loaded in compression. Composites Science and Technology. 2000; 60(7): 1103-1114.
7. Hopfenberg HB, Frish HL. Transport of organic macromolecules in amorphous polymers. Polymer Letters. 1969; 7: 405-409.
8. Bond DA, Smith PA. Modeling the transport of low-molecular-weight penetrants within polymer matrix composites. Applied Mechanics Reviews. 2006; 59(5): 249-268.
9. Browning CE, Husman GE, Whitney JM. Moisture effects in epoxy matrix composites. In: Davis Jr JG, editor. Composite Materials: Testing and Design (Fourth Conference), ASTM STP 617; 1977.
10. Pogany GA. Anomalous diffusion of water in glassy polymers. Polymer. 1976; 17(8): 690-694.
11. Sarbolouki MN. Probing the state of absorbed water by diffusion technique. Journal of Applied Polymer Science. 1973; 17(8): 2407-2414.
12. Alfrey T, Gurnee EF, Lloyd WG. Diffusion in glassy polymers. Journal of Polymer Science Part C: Polymer Symposia. 1966; 12(1): 249-261.
13. Wolff EG. Moisture effects on polymer matrix composites. SAMPE Journal. 1993; 29(3): 11-19.
14. Lv XJ, Zhang Q, Li XF, Xie GJ. Study of the influence of immersion on the carbon fiber/epoxy composites. Journal of Reinforced Plastics and Composites. 2008; 27(6): 659-666.
15. Castaing P, Mallard H. Effect of plasticization with water on the behaviour of long-term exposed filament wounded composites. In: Cardon AH, Fukuda H, Reifsnider K, editors. Progress in Durability Analysis of Composite Systems. Taylor and Francis; 1996. p. 233-239.

16. Vautrin A. Absorption de l'humidité : Synthèse pour les composites à matrice polymères, comportements mécaniques des composites à fibres. [In French]. Comptes Rendus du Colloque Greco 92; 1990.

17. Chateauminois A, Chabert B, Soulier JP, Vincent L. Hygrothermal ageing effects on viscoelastic and fatigue behaviour of glass/epoxy composites. In: Tsai SW, Springer GS, editors. Proceedings of Eighth International Conference on Composite Materials (ICCM8); 1991; Honolulu.

18. Manson JA, Chiu EH. Permeation of liquid water in a filled epoxy resin. Journal of Polymer Science: Polymer Symposia. 1973; 41(1): 95-108.

19. Frisch HL, Wang TT, Kwei TK. Diffusion in glassy polymers. II. Journal of Polymer Science Part A-2: Polymer Physics. 1969; 7(5): 879-887.

20. Crank J. A theoretical investigation of the influence of molecular relaxation and internal stress on diffusion in polymers. Journal of Polymer Science. 1953; 11(2): 151-168.

21. Frisch HL. Anomalous polymer-penetrant permeation. The Journal of Chemical Physics. 1962; 37(10): 2408-2413.

22. Harogoppad SB, Aminabhavi TM. Diffusion and sorption of organic liquids through polymer membranes. 5. Neoprene, styrene-butadiene-rubber, ethylene-propylene-diene terpolymer, and natural rubber versus hydrocarbons (C8-C16). Macromolecules. 1991; 24(9): 2598-2605.

23. Mensitieri G, Del Nobile MA, Apicella A, Nicolais L. Moisture-matrix interactions in polymer based composite materials. Revue de L'Institut Francais du Petrole. 1995; 50(4): 555-571.

24. Lucas JP, Zhou J. Moisture interaction characteristics and fracture in polymer composites. In: Poursartip A, Street K, editors. Proceedings of Tenth International Conference on Composite Materials (ICCM10); 1995; Canada.

25. Chateauminois A, Chabert B, Soulier JP, Vincent L. Effects of hygrothermal aging on the durability of glass/epoxy composite - physico/chemical analysis and damage mapping in static fatigue. Proceedings of Ninth International Conference on Composite Materials (ICCM9); 1993; Spain.

26. Rogers CE, Stannett V, Szwarc M. The sorption, diffusion, and permeation of organic vapors in polyethylene. Journal of Polymer Science. 1960; 45(145): 61-82.

27. Crank J, Park GS, editors. Diffusion in polymers. Oxford, London: Academic Press; 1968.

28. Blackadder DA, Keniry JS. Difficulties associated with the measurement of the diffusion coefficient of solvating liquid or vapor in semicrystalline polymer. I. Permeation methods. Journal of Applied Polymer Science. 1973; 17: 351-363.

29. Papanicolaou GC, Kosmidou TV, Vatalis AS, Delides CG. Water absorption mechanism and some anomalous effects on the mechanical and viscoelastic behavior of an epoxy system. Journal of Applied Polymer Science. 2006; 99(4): 1328-1339.

30. Long FA, Thompson LJ. Diffusion of water vapor in polymers. Journal of Polymer Science. 1955; 15: 413-426.

31. Adamson M. Thermal expansion and swelling of cured epoxy resin used in graphite/epoxy composite materials. Journal of Materials Science. 1980; 15: 1736-1745.

32. Diamant Y, Marom G, Broutman LJ. The effect of network structure on moisture absorption of epoxy resins. Journal of Applied Polymer Science. 1981; 26(9): 3015-3025.

33. Rider AN, Arnott DR. The influence of adherend topography on the fracture toughness of aluminium-epoxy adhesive joints in humid environments. The Journal of Adhesion. 2001; 75(2): 203-228.

34. Woo M, Piggott MR. Water absorption of resins and composites: IV. Water transport in fiber reinforced plastics. Journal of Composites Technology and Research. 1988 10(1): 20-24.

35. Robeson LM. Environmental stress cracking: A review. Polymer Engineering and Science. 2012: 1-15.

36. Nogueira P, Ramirez C, Torres A, Abad M, Cano J, Lopez J, Lopez-Bueno I, Barral L. Effect of water sorption on the structure and mechanical properties of an epoxy resin system. Journal of Applied Polymer Science. 2001; 80: 71-80.

37. Bao L-R, Yee AF, Lee CYC. Moisture absorption and hygrothermal aging in a bismaleimide resin. Polymer. 2001; 42(17): 7327-7333.

38. Li Y, Miranda J, Sue H-J. Hygrothermal diffusion behavior in bismaleimide resin. Polymer. 2001; 42(18): 7791-7799.

39. Guenther M, Sahre K, Suchaneck G, Gerlach G, Eichhorn KJ. Influence of ion-beam induced chemical and structural modification in polymers on moisture uptake. Surface and Coatings Technology. 2001; 142-144(0): 482-488.

40. Weitsman Y. Moisture in composites: sorption and damage. In: Reifsnider KL, editor. Fatigue of composite materials. Elsevier Science; 1990. p. 385.

41. Asmussen F, Ueberreiter K. Velocity of dissolution of polymers. Part II. Journal of Polymer Science. 1962; 57: 199-208.

42. Barrer RM, Barrie JA. Sorption and diffusion in ethyl cellulose. Part IV: Water in ethyl cellulose. Journal of Polymer Science. 1958; 28: 377-386.

43. Spurr OK, Niegisch WD. Stress crazing of some amorphous thermoplastics. Journal of Applied Polymer Science. 1962; 6(23): 585-599.

44. Gillat O, Broutman LJ. Effect of an external stress on moisture diffusion and degradation in a graphite-reinforced epoxy laminates. In: Vinson JR, editor. Advanced Composite Materials-Environmental Effects, ASTM STP 658; 1978.

45. Henson MC, Weitsman Y. Stress effects on moisture transport in an epoxy resin and its composite. In: Kawata K, Umekawa S, Kobayashi A, editors. Proceedings of the Third Japan-US Conference on Composite Materials; 1986; Tokyo, Japan.

46. Elsami S, Taheri-Behrooz F, Taheri F. Long-term hygrothermal response of perforated GFRP plates with/without application of constant external loading. Polymer Composites. 2012; 33(4): 467-475.

47. Gong XJ. Comportement mécanique et hygrothermique des composites stratifies: Ruptures interlaminaires et assemblage collé. [HDR Thesis, In French]. Université de Bourgogne; 2012.

48. George SC, Thomas S. Transport phenomena through polymeric systems. Progress in Polymer Science. 2001; 26(6): 985-1017.

49. Bueche F. Physical properties of polymers. New York: Interscience; 1962.

50. Prager S, Bagley E, Long FA. Diffusion of hydrocarbon vapors into polyiso-butylene. II1. Journal of the American Chemical Society. 1953; 75(5): 1255-1256.

51. Fujita H, Kishimoto A, Matsumoto K. Concentration and temperature dependence of diffusion coefficients for systems polymethyl acrylate and n-alkyl acetates. Transaction of Faraday Society. 1960; 56: 424-437.

52. Berens AR, Hopfenberg HB. Diffusion of organic vapors at low concentrations in glassy PVC, polystyrene, and PMMA. Journal of Membrane Science. 1982; 10(2): 283-303.

53. Yi-Yan N, Felder RM, Koros WJ. Selective permeation of hydrocarbon gases in poly(tetrafluoroethylene) and poly(fluoroethylene-propylene) copolymer. Journal of Applied Polymer Science. 1980; 25: 1755-1774.

54. Kwei TK, Kumins CA. Polymer-filler interaction: vapor sorption studies. Journal of Applied Polymer Science. 1964; 8: 1483-1490.

55. Varghese S, Kuriakose B, Thomas S, Joseph K. Effect of adhesion on the equilibrium swelling of short sisal fiber reinforced natural rubber composites. Rubber Chemistry and Technology. 1995; 68(1): 37-49.

56. Das B. Restricted equilibrium swelling - A true measure of adhesion between short fibers and rubber. Journal of Applied Polymer Science. 1973; 17: 1019-1030.

57. Lawandy SN, Helaly FH. Diffusion of a volatile liquid in polychloroprene rubber. Journal of Applied Polymer Science. 1986; 32: 5279-5286.

58. Kaushal S, Tankala K, Rao R, Kishore. Some hygrothermal effects on the mechanical behaviour and fractography of glass-epoxy composites with modified interface. Journal of Material Science. 1991; 26(23): 6293-6299.

59. Frish HL. Sorption and transport in glassy polymers - A review. Polymer Engineering and Science. 1980; 20(1): 2-13.

60. Ritger PL, Peppas NA. A simple equation for description of solute release II. Fickian and anomalous release from swellable devices. Journal of Controlled Release. 1987; 5(1): 37-42.

61. Fick A. Über diffusion. Poggendorff's Annalen der Physik und Chemie. 1855; 94: 59-86.

62. Jost W. Diffusion in solids, liquids, gases. London: Academic Press Inc; 1960.

63. Fujita H. Diffusion of organic vapours in polymers above the glass temperature. In: Crank J, Park GS, editors. Diffusion in Polymers. New York: Academic Press; 1968. p. 75-106.

64. Whitney JM, Browning CE. Some anomalies associated with moisture diffusion in epoxy matrix composite materials. In: Vinson JN, editor. Advanced Composite Materials-Environmental Effects. ASTM STP 658; 1978.

65. Bao L-R, Yee AF. Moisture diffusion and hygrothermal aging in bismaleimide matrix carbon fiber composites. Part II: Woven and hybrid composites. Composites Science and Technology. 2002; 62(16): 2111-2119.

66. Roy S, Xu WX, Park SJ, Liechti KM. Anomalous moisture diffusion in viscoelastic polymers: modeling and testing. Journal of Applied Mechanics. 2000; 67(2): 391-396.

67. LaPlante G, Ouriadov AV, Lee-Sullivan P, Balcom BJ. Anomalous moisture diffusion in an epoxy adhesive detected by magnetic resonance imaging. Journal of Applied Polymer Science. 2008; 109: 1350-1359.

68. Chen X, Zhao S, Zhai L. Moisture absorption and diffusion characterization of molding compound. Journal of Electronic Packaging. 2005; 127(4): 460-465.

69. Celik E, Guven I, Madenci E. Experimental and numerical characterization of non-Fickian moisture diffusion in electronic packages. Electronic Components and Technology Conference, Proceedings 57th; 2007.

70. Ameli A, Dalta NV, Papini M, Spelt JK. Hygrothermal properties of highly toughened epoxy adhesives. Journal of Adhesion. 2010; 86: 698-725.

71. Fernandez-Garcia M, Chiang MYM. Effect of hygrothermal aging history on sorption process, swelling, and glass transition temperature in a particle-filled epoxy-based adhesive. Journal of Applied Polymer Science. 2002; 84: 1581-1591.

72. Cai LW, Weitsman Y. Non-Fickian moisture diffusion in polymeric composites. Journal of Composite Materials. 1994; 28(2): 130-154.

73. Long FA, Richman D. Concentration gradients for diffusion of vapors in glassy polymers and their relation to time dependent diffusion phenomena1,2. Journal of the American Chemical Society. 1960; 82(3): 513-519.

74. Crank J. The mathematics of diffusion. Oxford: Oxford Science Publications; 1975.

75. Chiang MYM, Fernandez-Garcia M. Relation of swelling and T_g depression to the apparent free volume of a particle-filled, epoxy-based adhesive. Journal of Applied Polymer Science. 2003; 87: 1436-1444.

76. Berens AR, Hopfenberg HB. Diffusion and relaxation in glassy polymer powders: 2. Separation of diffusion and relaxation parameters. Polymer. 1978; 19(5): 489-496.

77. Berens AR, Hopfenberg HB. Induction and measurement of glassy-state relaxations by vapor sorption techniques. Journal of Polymer Science. 1979; 17: 1757-1770.

78. Pritchard G, Speake SD. The use of water absorption kinetic data to predict laminate property changes. Composites. 1987; 18(3): 227-232.

79. Barrer RM, Barrie JA, Slater J. Sorption and diffusion in ethyl cellulose. Part III. Journal of Polymer Science. 1958; 27: 177-197.

80. Vieth WR, Sladek KJ. A model for diffusion in a glassy polymer. Journal of Colloid Science. 1965; 20(9): 1014-1033.

81. Carter HG, Kibler KG. Langmuir-type model for anomalous moisture diffusion in composite resins. Journal of Composite Materials. 1978; 12(2): 118-131.

82. Gurtin ME, Yatomi C. On a model for two phase diffusion in composite materials. Journal of Composite Materials. 1979; 13(2): 126-130.

83. Bonniau P, Bunsell AR. A comparative study of water absorption theories applied to glass epoxy composites. Journal of Composite Materials. 1981; 15(3): 272-293.

84. Lee MH, Peppas NA. Water transport in graphite/epoxy composites. Journal of Applied Polymer Science. 1993; 47: 1349-1359.

85. Popineau S, Rondeau-Mouro C, Sulpice-Gaillet C, Shanahan MER. Free/bound water absorption in an epoxy adhesive. Polymer. 2005; 46(24): 10733-10740.

86. La Saponara V. Environmental and chemical degradation of carbon/epoxy and structural adhesive for adhesive for aerospace applications: Fickian and anomalous diffusion, Arrhenius kinetics. Composite Structures. 2011; 93: 2180-2195.

87. Bond DA. Moisture diffusion in a fiber-reinforced composite. Part I: Non-Fickian transport and the effect of fiber spatial distribution. Journal of Composite Materials. 2005; 39(23): 2113-2141.

88. Jacobs PM, Jones FR. Diffusion of moisture into two-phase polymers. Part 1: The development of an analytical model and its application to styrene-ethylene/butylene-styrene block copolymer. Journal of Materials Science. 1989; 24: 2331-2336.

89. Jacobs PM, Jones FR. Diffusion of moisture into two-phase systems. Part 2: Styrenated polyester resins. Journal of Materials Science. 1989; 24: 2343-2348.

90. Maggana C, Pissis P. Water sorption and diffusion studies in an epoxy resin system. Journal of Polymer Science: Part B: Polymer Physics. 1999; 37: 1165-1182.

91. Bao L-R, Yee AF. Moisture diffusion and hygrothermal aging in bismaleimide matrix carbon fiber composites. Part I: Uni-weave composites. Composites Science and Technology. 2002; 62(16): 2099-2110.

92. Shen C-H, Springer GS. Moisture absorption and desorption of composite materials. Journal of Composite Materials. 1976; 10(1): 2-20.

93. Dewimille B, Bunsell AR. The modelling of hydrothermal aging in glass fibre reinforced epoxy composites. Journal of Physics D: Applied Physics. 1982; 15(10): 2079-2091.

94. Loh WK, Crocombe AD, Abdel Wahab MM, Ashcroft IA. Modelling anomalous moisture uptake, swelling and thermal characteristics of a rubber toughened epoxy adhesive. International Journal of Adhesion and Adhesives. 2005; 25(1): 1-12.

95. Placette MD, Fan X, Zhao J-H, Edwards D. Dual stage modeling of moisture absorption and desorption in epoxy mold compounds. Microelectronics Reliability. 2012; 52(7): 1401-1408.

96. Shirangi MH, Auerspeg J, Koyuncu M, Walter H, Müller WH, Michel B. Characterization of dual-stage moisture diffusion, residual moisture content and hygroscopic swelling of epoxy molding compounds. Proceedings of the 9th EuroSime2008; 2008; Freibury, Germany.

97. Karbhari VM, Xian G. Hygrothermal effects on high V_f pultruded unidirectional carbon/epoxy composites: Moisture uptake. Composites Part B: Engineering. 2009; 40(1): 41-49.

98. Manfredi LB, Santis HD, Vázquez A. Influence of the addition of montmorillonite to the matrix of unidirectional glass fibre/epoxy composites on their mechanical and water absorption properties. Composites Part A: Applied Science and Manufacturing. 2008; 39(11): 1726-1731.

99. Mubashar A, Ashcroft IA, Critchlow GW, Crocombe AD. Moisture absorption-desorption effects in adhesive joints. International Journal of Adhesion and Adhesives. 2009; 29(8): 751-760.

100. Abdel Wahab MM, Crocombe AD, Beevers A, Ebtehaj K. Coupled stress-diffusion analysis for durability study in adhesively bonded joints. International Journal of Adhesion and Adhesives. 2002; 22(1): 61-73.

101. Ashcroft IA, Abdel Wahab MM, Crocombe AD. Predicting degradation in bonded composite joints using a semi-coupled finite-element method. Mechanics of Advanced Materials and Structures. 2003; 10(3): 227-248.

102. Ashcroft IA, Abdel Wahab MM, Crocombe AD, Hughes DJ, Shaw SJ. The effect of environment on the fatigue of bonded composite joints. Part 1: Testing and fractography. Composites: Part A. 2001; 32: 45-58.

103. Apicella A, Migliaresi C, Nicolais L, Iaccarino L, Roccotelli S. The water ageing of unsaturated polyester-based composites: influence of resin chemical structure. Composites. 1983; 14(4): 387-392.

104. Scida D, Aboura Z, Benzeggagh ML. The effect of ageing on the damage events in woven-fibre composite materials under different loading conditions. Composites Science and Technology. 2002; 62(4): 551-557.

105. Bordes M, Davies P, Cognard JY, Sohier L, Sauvant-Moynot V, Galy J. Prediction of long term strength of adhesively bonded steel/epoxy joints in sea water. International Journal of Adhesion and Adhesives. 2009; 29(6): 595-608.

106. Brewis DM, Comyn J, Raval AK, Kinloch AJ. The effect of humidity on the durability of aluminium-epoxide joints. International Journal of Adhesion and Adhesives. 1990; 10(4): 247-253.

107. Apicella A, Nicolais L. Effect of water on the properties of epoxy matrix and composite. In: Dusek K, editor. Advances in Polymer Science: Epoxy Resins and Composites I. Springerlink; 1985. p. 69-77.

108. Moidu AK, Sinclair AN, Spelt JK. Adhesive joint durability assessed using open-faced peel specimens. The Journal of Adhesion. 1998; 65(1-4): 239-257.

109. Hua Y, Crocombe AD, Abdel Wahab MM, Ashcroft IA. Continuum damage modelling of environmental degradation in joints bonded with E32 epoxy adhesive. Journal of Adhesion Science and Technology. 2007; 21(2): 179-195.

110. Hua Y, Crocombe AD, Abdel Wahab MM, Ashcroft IA. Continuum damage modelling of environmental degradation in joints bonded with EA9321 epoxy adhesive. International Journal of Adhesion and Adhesives. 2008; 28(6): 302-313.

111. Bowditch MR. The durability of adhesive joints in the presence of water. International Journal of Adhesion and Adhesives. 1996; 16(2): 73-79.

112. Liljedahl CDM, Crocombe AD, Abdel Wahab MM, Ashcroft IA. Modelling the environmental degradation of the interface in adhesively bonded joints using a cohesive zone approach. The Journal of Adhesion. 2006; 82(11): 1061-1089.

113. Brewis DM, Comyn J, Shalash RJA. The effect of moisture and temperature on the properties of an epoxide-polyamide adhesive in relation to its performance in single lap joints. International Journal of Adhesion and Adhesives. 1982; 2(4): 215-222.

114. John SJ, Kinloch AJ, Matthews FL. Measuring and predicting the durability of bonded carbon fibre/epoxy composite joints. Composites. 1991; 22(2): 121-127.

115. Maurin R, Perrot Y, Bourmaud A, Davies P, Baley C. Seawater ageing of low styrene emission resins for marine composites: Mechanical behaviour and nano-indentation studies. Composites Part A: Applied Science and Manufacturing. 2009; 40: 1024-1032.

116. Bowditch MR, Stannard KJ. The interaction of water with a barytes-filled polyurethane. International Journal of Adhesion and Adhesives. 1984; 4(4): 175-178.

117. Garden H, Hollaway LC. Environmental durability of composites. Internal Report. 1997.

118. Hofer Jr KE, Rao N, Larsen D. Development of engineering data on the mechanical and physical properties of advanced composites materials. Technical Report. No: AFML-TR-72-205, Part II. Dayton, Ohio: Air Force Materials Laboratory, Air Force Systems Command, Wright-Patterson Air Force Base; 1974.

119. Abdel-Magid B, Ziaee S, Gass K, Schneider M. The combined effects of load, moisture and temperature on the properties of E-glass/epoxy composites. Composite Structures. 2005; 71(3-4): 320-326.

120. Verette RM. Temperature/humidity effects on the strength of graphite/epoxy laminates. AIAA 1975 Aircraft Systems and Technology Meeting; 1975; Los Angeles, California.

121. Hertz J. Investigation into the high-temperature strength degradation of fiber-reinforced resin composite during ambient aging. No: GDCA-DBG73-005, Contract NASA-27435. Huntsville, Alabama: National Aeronautics and Space Administration; 1973.

122. Pérez-Pacheco E, Cauich-Cupul JI, Valadez-González A, Herrera-Franco PJ. Effect of moisture absorption on the mechanical behavior of carbon fiber/epoxy matrix composites. Journal of Materials Science. 2013; 47: 1873-1882.

123. Sinmaçelik T, Armağan Arici A. Influence of various fluids on the interlaminar shear strength (ILSS) and impact behaviour of carbon/PEI composites. Journal of Materials Science. 2006; 41: 3255-3262.

124. Shen C-H, Springer GS. Effects of moisture and temperature on the tensile strength of composite materials. Journal of Composite Materials. 1977; 11(1): 2-16.

125. Hofer Jr KE, Larsen D, Humphreys VE. Development of engineering data on the mechanical and physical properties of advanced composites materials. Technical Report. No: AFML-TR-74-266. Dayton, Ohio: Air Force Materials Laboratory, Air Force Systems Command, Wright-Patterson Air Force Base; 1975.

126. Husman GE. Characterization of wet composite materials. Mechanics of Composites Review; 1976; Bergamo Center, Dayton, Ohio.

127. Kaminski BE. Effects of specimen geometry on the strength of composite materials. In: Whitney JM, editor. Analysis of the Test Methods for High Modulus Fibers and Composites, ASTM STP521; 1973.

128. Kerr JR, Haskins JF, Stein BA. Program definition and preliminary results of a long-term evaluation program of advanced composites for supersonic cruise aircraft applications. In: Christian JL, Witzell WE, Stein BA, editors. Environmental Effects on Advanced Composite Materials, ASTM STP 602; 1976.

129. Hanson MP. Effect of temperature on the tensile and creep characteristics of PRD49 fiber/epoxy composites. In: Norton BR, editor. Composite Materials in Engineering Design; 1972.

130. Shen C-H, Springer GS. Environmental effects on the elastic moduli of composite materials. Journal of Composite Materials. 1977; 11(3): 250-264.

131. Hoa SV, Lin S, Chen JR. Effects of moisture content on the mechanical properties of polyphenylene sulfide composite materials. In: Newaz GM, editor. Advances in Thermoplastic Matrix Composite Materials, ASTM STP 1044; 1989; Philadelphia.

132. Deng H, Reynolds CT, Cabrera NO, Barkoula NM, Alcock B, Peijs T. The water absorption behaviour of all-polypropylene composites and its effect on mechanical properties. Composites Part B: Engineering. 2010; 41(4): 268-275.

133. Viña J, Castrillo MA, Argüelles A, Viña I. A comparison between the static and fatigue properties of glass-fiber and carbon-fiber reinforced polyetherimide composites after prolonged aging. Polymer Composites. 2002; 23(4): 619-623.

134. Sala G. Composite degradation due to fluid absorption. Composites Part B: Engineering. 2000; 31(5): 357-373.

135. Wilkins DJ. Environmental sensitivity tests of graphite-epoxy bolt bearing properties. In: Davis JGJ, editor. Composite Materials: Testing and Design (Fourth Conference), ASTM STP 617; 1977.

136. Cândido GM, Costa ML, Rezende MC, Almeida SFM. Hygrothermal effects on quasi-isotropic carbon epoxy laminates with machined and molded edges. Composites Part B: Engineering. 2008; 39(3): 490-496.

137. Browning CE. The effects of moisture on the properties of high performance structural resins and composites. Technical Report AFML TR-72-94. Dayton, Ohio; 1972.

138. Kim RY, Whitney JM. Effect of environment on the notch strength of laminated composites. Mechanics of Composites Review; 1976; Bergamo Center, Dayton, Ohio.

139. Aoki Y, Yamada K, Ishikawa T. Effect of hygrothermal condition on compression after impact strength of CFRP laminates. Composites Science and Technology. 2008; 68(6): 1376-1383.

140. Bullions TA, Loos AC, McGrath JE. Moisture sorption effects on and properties of a carbon fiber-reinforced phenylethynyl-terminated poly(etherimide). Journal of Composite Materials. 2003; 37(9): 791-809.

141. Alawsi G, Aldajah S, Rahmaan SA. Impact of humidity on the durability of E-glass/polymer composites. Materials & Design. 2009; 30(7): 2506-2512.

142. Buehler FU, Seferis JC. Effect of reinforcement and solvent content on moisture absorption in epoxy composite materials. Composites Part A: Applied Science and Manufacturing. 2000; 31(7): 741-748.

143. Khan LA, Nesbitt A, Day RJ. Hygrothermal degradation of 977-2A carbon/epoxy composite laminates cured in autoclave and Quickstep. Composites Part A: Applied Science and Manufacturing. 2010; 41(8): 942-953.

144. Kalfon E, Harel H, Marom G, Druker E, Green AK, Kressel I. Delamination of laminated composites under the combined effect of nonuniform heating and absorbed moisture. Polymer Composites. 2005; 26(6): 770-777.

145. Tsai YI, Bosze EJ, Barjasteh E, Nutt SR. Influence of hygrothermal environment on thermal and mechanical properties of carbon fiber/fiberglass hybrid composites. Composites Science and Technology. 2009; 69(3): 432-437.

146. Davies P, Pomies F, Carlsson LA. Influence of water and accelerated aging on the shear fracture properties of glass/epoxy composite. Applied Composite Materials. 1996; 3: 71-87.

147. Aktas L, Hamidi Y, Cengiz Altan M. Effect of moisture on the mechanical properties of resin transfer molded composites. Part I: Absorption. Journal of Materials Processing and Manufacturing Science. 2002; 10: 239-254.

148. Ankara A, Weisgerber D, Vilsmeier J. Influence of thermal spiking on properties of carbon fibre reinforced plastic. Materials Science and Technology. 1986; 2(11): 1081-1085.

149. Seneviratne WP, Tomblin JS. Environmental compensation factor influence on composite design and certification. FAA JAMS 2010 Technical Review Meeting; 2010; Seattle, Washington.

150. Hergenrother PM, Jensen BJ, Havens SJ. Thermoplastic composite matrices with improved solvent resistance. The 29th National SAMPE Symposium; 1984.

151. Zenasni R, Bachir AS, Viña I, Arguelles A, Viña J. Effect of hygrothermomechanical aging on the interlaminar fracture behavior of woven fabric fiber/PEI composite materials. Journal of Thermoplastic Composite Materials. 2006; 19(4): 385-398.

152. Huang G, Sun H. Delamination behavior of glass/polyester composites after water absorption. Materials and Design. 2008; 29: 262-264.

153. Davidson BD, Kumar M, Soffa MA. Influence of mode ratio and hygrothermal condition on the delamination toughness of a thermoplastic particulate interlayered carbon/epoxy composite. Composites Part A: Applied Science and Manufacturing. 2009; 40(1): 67-79.

154. Walker L, Hu XZ. Mode I delamination behaviour of short fibre reinforced carbon fibre/epoxy composites following environmental conditioning. Composites Science and Technology. 2003; 63(3): 531-537.

155. Gong XJ, Wong KJ, Tamin MN. Moisture absorption effects on interlaminar fracture toughness of woven glass/epoxy composite laminates. In: Tamin MN, editor. Damage and Fracture of Composite Materials and Structures, Advanced Structured Materials. Springer; 2012. p. 107-129.

156. Benzeggagh ML, Kenane M. Measurement of mixed-mode delamination fracture toughness of unidirectional glass/epoxy composites with mixed-mode bending apparatus. Composites Science and Technology. 1996; 56(4): 439-449.

157. Gong XJ. Rupture interlaminaire en mode mixte I+II de composites stratifiés unidirectionnels et multidirectionnels verre/epoxy. [Ph.D Thesis, In French]. Université de Technologie de Compiègne; 1992.

158. Gong XJ, Benzeggagh ML. Mixed mode interlaminar fracture toughness of unidirectional glass/epoxy composite. In: Martin RH, editor. Composite Materials: Fatigue and Fracture - Fifth Volume, ASTM STP 1230; 1995; Philadelphia.

159. Chua PS, Dai RS, Piggott MR. Mechanical properties of the glass fibre-polyester interphase. Part II: Effect of water on debonding. Journal of Materials Science. 1992; 27(4): 919-924.

160. Beland S, Komorowski JP, Roy C. Hygrothermal influence on the interlaminar fracture energy of graphite/bismaleimide modified epoxy composite (IM6/5245C). In: Matthews FL, Buskell NCR, Hodgkinson JM, Morton J, editors. Sixth International Conference on Composite Materials and Second European Conference on Composite Materials; 1987; London, UK.

161. O'Brien TK. Residual thermal and moisture influences on the analysis of local delaminations. Journal of Composites Technology and Research. 1992; 14(2): 86-94.

162. Russell AJ, Street KN. Moisture and temperature effects on the mixed-mode delamination fracture of unidirectional graphite/epoxy. In: Johnson WS, editor. Delamination and Debonding of Materials, ASTM STP876; 1985.

163. Lucas JP, Odegard BC. Moisture effects on mode I interlaminar fracture toughness of a graphite fiber thermoplastic matrix composite. In: Newaz GM, editor. Advances in Thermoplastic Matrix Composite Materials, ASTM STP 1044; 1989; Philadelphia.

164. Garg A, Ishai O. Hygrothermal influence on delamination behavior of graphite/epoxy laminates. NASA-TM-85935. National Aeronautics and Space Administration; 1984.

165. Asp LE. The effects of moisture and temperature on the interlaminar delamination toughness of a carbon/epoxy composite. Composites Science and Technology. 1998; 58(6): 967-977.

166. Katnam KB, Crocombe AD, Sugiman H, Khoramishad H, Ashcroft IA. Static and fatigue failures of adhesively bonded laminate joints in moist environments. International Journal of Damage Mechanics. 2011; 20(8): 1217-1242.

167. Crocombe AD, Hua YX, Loh WK, Abdel Wahab MM, Ashcroft IA. Predicting the residual strength for environmentally degraded adhesive lap joints. International Journal of Adhesion and Adhesives. 2006; 26(5): 325-336.

168. Loh WK, Crocombe AD, Abdel Wahab MM, Ashcroft IA. Environmental degradation of the interfacial fracture energy in an adhesively bonded joint. Engineering Fracture Mechanics. 2002; 69(18): 2113-2128.

169. Banea MD, da Silva LFM. Adhesively bonded joints in composite materials: An overview. Proceedings of the Institution of Mechanical Engineers, Part L: Journal of Materials Design and Applications. 2009; 223(1): 1-18.

170. Davies P, Evrard G. Accelerated ageing of polyurethanes for marine applications. Polymer Degradation and Stability. 2007; 92(8): 1455-1464.

171. Ameli A, Azari S, Papini M, Spelt JK. Characterization and prediction of fracture properties in hygrothermally degraded adhesive joints: an open-faced approach. Journal of Adhesion Science and Technology. 2012: 1-24.

172. Loh WK, Crocombe AD, Abdel Wahab MM, Ashcroft IA. Modelling interfacial degradation using interfacial rupture elements. The Journal of Adhesion. 2003; 79(12): 1135-1160.

173. Loh WK, Crocombe AD, Abdel Wahab MM, Watts JF, Ashcroft IA. The effect of moisture on the failure locus and fracture energy of an epoxy-steel interface. Journal of Adhesion Science and Technology. 2002; 16(11): 1407-1429.

174. Hua Y, Crocombe AD, Abdel Wahab MM, Ashcroft IA. Modelling environmental degradation in EA9321-bonded joints using a progressive damage failure model. The Journal of Adhesion. 2006; 82(2): 135-160.

175. Bowditch MR, Clark JD, Stannard KJ. The strength and durability of adhesive joints made underwater. In: Allen KW, editor. Adhesion. Londion: Elsevier Applied Science; 1987. p. 1-16.

176. Ameli A, Datla NV, Azari S, Papini M, Spelt JK. Prediction of environmental degradation of closed adhesive joints using data from open-faced specimens. Composite Structures. 2012; 94(2): 779-786.

177. Katnam KB, Sargent JP, Crocombe AD, Khoramishad H, Ashcroft IA. Characterisation of moisture-dependent cohesive zone properties for adhesively bonded joints. Engineering Fracture Mechanics. 2010; 77(16): 3105-3119.

178. Liljedahl CDM, Crocombe AD, Abdel Wahab MM, Ashcroft IA. Modelling the environmental degradation of adhesively bonded aluminium and composite joints using a CZM approach. International Journal of Adhesion and Adhesives. 2007; 27(6): 505-518.

179. Goglio L, Rezaei M, Rossetto M. Moisture degradation of open-faced single lap joints. Journal of Adhesion Science and Technology. 2012: 1-12.

180. Temiz Ş, Özel A, Aydin MD. A study on durability of joints bonded with pressure-sensitive adhesives. Journal of Adhesion Science and Technology. 2004; 18(10): 1187-1198.

181. Bowditch MR, Stannard KJ. Adhesive bonding of GRP. Composites. 1982; 13(3): 298-304.

182. Ashcroft IA, Digby RP, Shaw SJ. A comparison of laboratory-conditioned and naturally-weathered bonded joints. The Journal of Adhesion. 2001; 75(2): 175-201.

183. Broughton WR, Mera RD. Environmental degradation of adhesive joints, accelerated testing. NPL Report CMMT (A) 197. 1999.

184. Abdel Wahab MM, Ashcroft IA, Crocombe AD, Hughes DJ, Shaw SJ. The effect of environment on the fatigue of bonded composite joints. Part 2: fatigue threshold prediction. Composites Part A: Applied Science and Manufacturing. 2001; 32(1): 59-69.

185. Crocombe AD. Durability modelling concepts and tools for the cohesive environmental degradation of bonded structures. International Journal of Adhesion and Adhesives. 1997; 17(3): 229-238.

186. Kinloch AJ. Durability of structural adhesives. Amsterdam: Elsevier Publishers; 1983.

187. Adams RD, Comyn J. Structural adhesive joints in engineering. Heidelberg: Springer; 1997.

188. Kinloch AJ, Little MSG, Watts JF. The role of the interphase in the environmental failure of adhesive joints. Acta Materialia. 2000; 48(18-19): 4543-4553.

189. Ameli A, Papini M, Spelt JK. Fracture R-curve of a toughened epoxy adhesive as a function of irreversible degradation. Materials Science and Engineering: A. 2010; 527(20): 5105-5114.

190. Ameli A, Papini M, Spelt JK. Evolution of crack path and fracture surface with degradation in rubber-toughened epoxy adhesive joints: Application to open-faced specimens. International Journal of Adhesion and Adhesives. 2011; 31(6): 530-540.

191. Gledhill RA, Kinloch AJ, Shaw SJ. A model for predicting joint durability. The Journal of Adhesion. 1980; 11(1): 3-15.

192. Hambly HO. The strength of adhesively bonded joints degraded by moisture. [Ph.D Thesis]. University of Surrey; 1998.

193. Minford JD. Adhesives. In: Kinloch AJ, editor. Durability of Structural Adhesives. London: Applied Science Publishers; 1983. p. 135.

194. Orman S, Kerr S. Effect of hostile environments on adhesive joints. In: Alner DJ, editor. Aspects of Adhesion. London: University of London Press; 1971. p. 64.

195. Brewis DM, Comyn J, Tegg JL. The durability of some epoxide adhesive-bonded joints on exposure to moist warm air. International Journal of Adhesion and Adhesives. 1980; 1(1): 35-39.

196. Brewis DM, Comyn J, Cope BC, Moloney AC. Further studies on the effect of carriers on the performance of aluminium alloy joints bonded with an epoxide polyamide adhesive. Polymer. 1980; 21(12): 1477-1479.

197. Rahimi H. Strengthening of concrete structures with externally bonded fibre reinforced plastics. [Ph.D Thesis]. Oxford Brookes University; 1996.

198. Robson JE, Matthews FL, Kinloch AJ. The bonded repair of fibre composites: Effect com of composite moisture content. Composites Science and Technology. 1994; 52(2): 235-246.

199. He X. A review of finite element analysis of adhesively bonded joints. International Journal of Adhesion and Adhesives. 2011; 31(4): 248-264.

200. Crocombe AD, Ashcroft IA, Abdel Wahab MM. Environmental degradation. In: da Silva L, Öchsner A, editors. Modeling of Adhesively Bonded Joints. Springer Berlin Heidelberg; 2008. p. 225-241.

201. Jumbo FS, Ashcroft IA, Crocombe AD, Wahab MMA. Thermal residual stress analysis of epoxy bi-material laminates and bonded joints. International Journal of Adhesion and Adhesives. 2010; 30(7): 523-538.

202. Yu Y, Ashcroft IA, Swallowe G. An experimental investigation of residual stresses in an epoxy-steel laminate. International Journal of Adhesion and Adhesives. 2006; 26(7): 511-519.

203. Abdel Wahab MM, Ashcroft IA, Crocombe AD, Shaw SJ. Diffusion of moisture in adhesively bonded joints. The Journal of Adhesion. 2001; 77(1): 43-80.

204. de Moura MFSF, Gonçalves JPM, Chousal JAG, Campilho RDSG. Cohesive and continuum mixed-mode damage models applied to the simulation of the mechanical behaviour of bonded joints. International Journal of Adhesion and Adhesives. 2008; 28(8): 419-426.

205. Lee D-B, Ikeda T, Miyazaki N, Choi N-S. Effect of bond thickness on the fracture toughness of adhesive joints. Journal of Engineering Materials and Technology. 2004; 126(1): 14-18.

206. Gonçalves JPM, de Moura MFSF, de Castro PMST. A three-dimensional finite element model for stress analysis of adhesive joints. International Journal of Adhesion and Adhesives. 2002; 22(5): 357-365.

207. Liljedahl CDM, Crocombe AD, Abdel Wahab MM, Ashcroft IA. Damage modelling of adhesively bonded joints. International Journal of Fracture. 2006; 141(1-2): 147-161.

208. Soutis C, Hu FZ. Design and performance of bonded patch repairs of composite structures. Proceedings of the Institution of Mechanical Engineers, Part G: Journal of Aerospace Engineering. 1997; 211(4): 263-271.

209. Hart-Smith LJ. Further developments in the design and analysis of adhesive-bonded structural joints. ASTM Symposium on Joining of Composite Materials; 1980; Minneapolis, Minnesota.

210. Hart-Smith LJ. An engineer's viewpoint on design and analysis of aircraft structural joints. Proceedings of the Institution of Mechanical Engineers, Part G: Journal of Aerospace Engineering. 1995; 209(2): 105-129.

211. Soutis C, Duan DM, Goutas P. Compressive behaviour of CFRP laminates repaired with adhesively bonded external patches. Composite Structures. 1999; 45(4): 289-301.

212. Liu X, Wang G. Progressive failure analysis of bonded composite repairs. Composite Structures. 2007; 81(3): 331-340.

213. Tsai SW, Wu EM. A general theory of strength for anisotropic materials. Journal of Composite Materials. 1971; 5(1): 58-80.

214. Ye L. Role of matrix resin in delamination onset and growth in composite laminates. Composites Science and Technology. 1988; 33(4): 257-277.

215. Campilho RDSG, de Moura MFSF, Ramantani DA, Morais JJL, Domingues JJMS. Tensile behaviour of three-dimensional carbon-epoxy adhesively bonded single- and double-strap repairs. International Journal of Adhesion and Adhesives. 2009; 29(6): 678-686.

216. Campilho RDSG, de Moura MFSF, Ramantani DA, Morais JJL, Domingues JJMS. Buckling strength of adhesively-bonded single and double-strap repairs on carbon-epoxy structures. Composites Science and Technology. 2010; 70(2): 371-379.

217. Gong XJ, Cheng PC, Rousseau J, Aivazzadeh S. Effect of local stresses on fatigue life of patch-repaired composite panels. Proceedings of 16th International Conference on Composite Materials; 2007; Kyoto, Japan.

218. Cheng P, Gong XJ, Aivazzadeh S. Optimisation of patched repair for CFRP laminates. Proceedings of 17th International Conference on Composite Materials; 2009; Edinburgh, UK.

219. Cheng P, Gong X-J, Hearn D, Aivazzadeh S. Tensile behaviour of patch-repaired CFRP laminates. Composite Structures. 2011; 93(2): 582-589.

220. Cheng P, Gong XJ, Aivazzadeh S. Design and optimization of composite laminates repaired by bonding external patches. Proceedings of 18th International Conference on Composite Materials; 2011; Jeju, Korea.

221. Peng LL, Gong XJ, Guillaumat L. Numerical simulation of damage propagation in CFRP laminates repaired by external bonded patches under tensile loading. Proceedings of 18th International Conference on Composite Materials; 2011; Jeju, Korea.

222. Vlattas C, Soutis. C. Composites repair: Compressive behaviour of CFRP plates with reinforced holes. 7th European Conference on Composite Materials 1996; London, UK.

223. Cheng P. Etude et optimisation de la réparation des composites stratifiés par collage des patchs externes. [Ph.D Thesis, In French]. Université de Bourgogne; 2010.

224. Peng LL. Modélisation numérique d'assemblages collés: Application à la réparation de structures en composites. [Ph.D Thesis, In French]. Université de Bourgogne; 2013.

225. ASTM D5229. Standard test method for moisture absorption properties and equilibrium conditioning of polymer matrix composite materials. ASTM International: West Conshohocken, Pennsylvania, United States; 2010.

226. ASTM D3171. Standard test methods for constituent content of composite materials. ASTM International: West Conshohocken, Pennsylvania, United States; 2009.

227. Costa ML, Rezende MC, de Almeida SFM. Effect of Void Content on the Moisture Absorption in Polymeric Composites. Polymer-Plastics Technology and Engineering. 2006; 45(6): 691-698.

228. Thomason JL. The interface region in glass fibre-reinforced epoxy resin composites: 2. Water absorption, voids and the interface. Composites. 1995; 26(7): 477-485.

229. Duda JL, Ni YC, Vrentas JS. Diffusion of ethylbenzene in molten polystyrene. Journal of Applied Polymer Science. 1978; 22(3): 689-699.

230. Shirell CD. Diffusion of water vapour in graphite/epoxy composites. In: Vinson JR, editor. Advanced Composite Materials - Environmental Effects, ASTM STP 658; 1978.

231. Structil resin selector guide. Aero Consultants AG. 2009. Available from: http://www.aero-consultants.ch.

232. Philipson S. Major PAN-based carbon fibre producers product comparison. Sigmatex. 2006. Available from: http://www.fatol.nl/PDF/Carbon_Fibre_Properties_(2006).pdf.

233. Blikstad M, Sjöblom POW, Johannesson TR. Long-term moisture absorption in graphite/epoxy angle-ply laminates. Journal of Composite Materials. 1984; 18(1): 32-46.

234. Loos AC, Springer GS, Sanders BA, Tung RW. Moisture absorption of polyester-E glass composites. Journal of Composite Materials. 1980; 14(2): 142-154.

235. Blackadder DA, Keniry JS. Difficulties associated with the measurement of the diffusion coefficient of solvating liquid or vapor in semicrystalline polymer. II. Sorption-desorption kinetics. Journal of Applied Polymer Science. 1974; 18: 699-708.

236. Kumins CA, Kwei TK. Free volume and other theories. In: Crank J, Park GS, editors. Diffusion in polymers. Academic Press; 1968. p. 107.

237. Blackadder DA, Keniry JS. The morphological consequences of annealing high-density polyethylene in solvents. Journal of Applied Polymer Science. 1972; 16(5): 1261-1280.

238. Halpin JC. An assessment of life assurance methodology for advanced composite structures. AIAA/ASME 18th Structures, Structural Dynamics and Materials Conference; 1977; San Diego.

239. Bagley E, Long FA. Two-stage Sorption and Desorption of Organic Vapors in Cellulose Acetate1,2. Journal of the American Chemical Society. 1955; 77(8): 2172-2178.

240. Vannucci P, Verchery G. A new method for generating fully isotropic laminates. Composite Structures. 2002; 58(1): 75-82.

241. ASTM D3039. Standard test method for tensile properties of polymer matrix composite materials. ASTM International: West Conshohocken, Pennsylvania, United States; 2008.

242. ASTM D3518. Standard test method for in-plane shear response of polymer matrix composite materials by tensile test of a $\pm 45^{o}$ laminate. ASTM International: West Conshohocken, Pennsylvania, United States; 2007.

243. ASTM D5528. Standard test method for mode I interlaminar fracture toughness of unidirectional fiber-reinforced polymer matrix composites. ASTM International: West Conshohocken, Pennsylvania, United States; 2007.

244. Irwin GR, Kies JA. Critical energy rate analysis of fracture strength. Welding Journal Research Supplement. 1954; 33: 193-198.

245. Pereira AB, de Morais AB. Mode I interlaminar fracture of carbon/epoxy multidirectional laminates. Composites Science and Technology. 2004; 64(13–14): 2261-2270.

246. Tao J, Sun CT. Influence of ply orientation on delamination in composite laminates. Journal of Composite Materials. 1998; 32(21): 1933-1947.

247. Mula S, Ray BC, Ray PK. Assesment of interlaminar shear strength of hybrid composites subjected to a fluctuating humid environment. International Symposium of Research Students on Materials Science and Engineering; 2004; Chennai, India.

248. Todo M, Nakamura T, Takahashi K. Effects of moisture absorption on the dynamic interlaminar fracture toughness of carbon/epoxy composites. Journal of Composite Materials. 1998; 34(8): 630-648.

249. Chiou P, Bradley WL. The effect of sea water exposure on the fatigue edge delamination growth of a carbon/epoxy composite. 9th International Conference on Composite Materials; 1993.

250. Selzer R, Friedrich K. Inluence of water up-take on interlaminar fracture properties of carbon fibre-reinforced polymer composites. Journal of Materials Science. 1995; 30(2): 334-338.

251. Selzer R, Friedrich K. Mechanical properties and failure behaviour of carbon fibre-reinforced polymer composites under the influence of moisture. Composites Part A: Applied Science and Manufacturing. 1997; 28(6): 595-604.

252. Schaffer JP, Saxena A, Antolovich SD, Sanders Jr. TH, Warner SB. The science and design of engineering materials. Chicago: Irwin; 1995.

253. Wong KJ, Gong XJ, Aivazzadeh S, Tamin MN. Numerical simulation of mode I delamination behaviour of multidirectional composite laminates with fibre bridging effect. 15th European Conference on Composite Materials; 2012; Venice, Italy.

254. Gutkin R, Laffan ML, Pinho ST, Robinson P, Curtis PT. Modelling the R-curve effect and its specimen-dependence. International Journal of Solids and Structures. 2011; 48(11–12): 1767-1777.

255. Camanho PP, Davila CG, de Moura MFSF. Numerical Simulation of Mixed-Mode Progressive Delamination in Composite Materials. Journal of Composite Materials. 2003; 37(16): 1415-1438.

256. Dugdale DS. Yielding of steel sheets containing slits. Journal of the Mechanics and Physics of Solids. 1960; 8(2): 100-104.

257. Barenblatt GI. The mathematical theory of equilibrium cracks in brittle fracture. In: Dryden HL, Kármán Tv, Kuerti G, Dungen FHvd, Howarth L, editors. Advances in Applied Mechanics. Elsevier; 1962. p. 55-129.

258. Gong XJ, Hurez A, Verchery G. On the determination of delamination toughness by using multidirectional DCB specimens. Polymer Testing. 2010; 29(6): 658-666.

259. Mohamed Rehan MS, Rousseau J, Gong XJ, Guillaumat L, Ali JSM. Effects of fiber orientation of adjacent plies on the mode I crack propagation in a carbon-epoxy laminates. Procedia Engineering. 2011; 10: 3179-3184.

260. Mohamed Rehan MS, Rousseau J, Gong XJ, Fontaine S, Ali JSM. Effects of fiber orientation on mode I crack propagation in a multidirectional carbon-epoxy laminates. 15th European Conference on Composite Materials; 2012; Venice, Italy.

261. Peng LL, Gong XJ, Wong KJ, Guillaumat L. Application of cohesive-zone models to delamination behaviour of composite material. World Journal of Engineering. 2012; 9(2): 109-118.

262. da Silva LFM, da Silva RAM, Chousal JAG, Pinto AMG. Alternative methods to measure the adhesive shear displacement in the thick adherend shear test. Journal of Adhesion Science and Technology. 2008; 22(1): 15-29.

263. Pinto AMG, Campilho RDSG, Mendes IR, Durão LMP, Silva RF, Baptista APM. Effect of plug-filling, testing velocity and temperature on the tensile strength of strap repairs on aluminium structures. Journal of Adhesion Science and Technology. 2012; 26(10-11): 1481-1496.

264. Pires I, Quintino L, Durodola JF, Beevers A. Performance of bi-adhesive bonded aluminium lap joints. International Journal of Adhesion and Adhesives. 2003; 23(3): 215-223.

265. Gaillot C. Comportement statique et dynamique d'assemblages collés de composites stratifiés. [Ph.D Thesis, In French]. Université de Bourgogne; 2007.

266. da Silva LFM, de Magalhães FACRG, Chaves FJP, de Moura MFSF. Mode II fracture toughness of a brittle and a ductile adhesive as a function of the adhesive thickness. The Journal of Adhesion. 2010; 86(9): 891-905.

267. de Moura MFSF, Campilho RDSG, Gonçalves JPM. Pure mode II fracture characterization of composite bonded joints. International Journal of Solids and Structures. 2009; 46(6): 1589-1595.

268. Blackman BRK, Kinloch AJ, Paraschi M. The determination of the mode II adhesive fracture resistance, GIIC, of structural adhesive joints: an effective crack length approach. Engineering Fracture Mechanics. 2005; 72(6): 877-897.

269. Bardis JD, Kedwad KT. Effects of surface preparation on long-term durability of composite adhesive bonds. 13th International Conference on Composite Materials; 2001; Beijing, China.

270. de Moura MFSF, Campilho RDSG, Gonçalves JPM. Crack equivalent concept applied to the fracture characterization of bonded joints under pure mode I loading. Composites Science and Technology. 2008; 68(10-11): 2224-2230.

271. Kinloch AJ, editor. Adhesion and adhesives. London: Chapman and Hall; 1987.

272. Molitor P, Barron V, Young T. Surface treatment of titanium for adhesive bonding to polymer composites: a review. International Journal of Adhesion and Adhesives. 2001; 21(2): 129-136.

273. Baldan A. Review: Adhesively-bonded joints and repairs in metallic alloys, polymers, and composite maerials: Adhesives, adhesion theories and surface treatment. Journal of Materials Science. 2004; 39: 1-49.

274. Jölly I, Wolfahrt M, Wolfberger A, Pinter G, Kern W, Noisternig J. Study of mechanical and physico-chemical surface properties of composites and their impact on bond strengths in repair technologies. 15th European Conference on Composite Materials; 2012; Venice, Italy.

275. Mubashar A, Ashcroft IA, Critchlow GW, Crocombe AD. Strength prediction of adhesive joints after cyclic moisture conditioning using a cohesive zone model. Engineering Fracture Mechanics. 2011; 78(16): 2746-2760.

276. Comrie R, Affrossman S, Pethrick RA. Ageing of adhesive bonds with various surface treatments, Part 2: Acrylic modified amine–cured epoxy resin. The Journal of Adhesion. 2005; 81(12): 1183-1197.

277. Wylde JW, Spelt JK. Measurement of adhesive joint fracture properties as a function of environmental degradation. International Journal of Adhesion and Adhesives. 1998; 18(4): 237-246.

278. Hutchinson AR, Hollaway LC. Environmental durability. In: Hollaway LC, Leeming MB, editors. Strengthening of reinforced concrete structures: using externally-bonded

FRP composites in structural and civil engineering. Cambridge, England: Woodhead Publishing Ltd; 1999. p. 156-182.

279. Anyfantis KN, Tsouvalis NG. Experimental and numerical investigation of Mode II fracture in fibrous reinforced composites. Journal of Reinforced Plastics and Composites. 2011; 30(6): 473-487.

280. Advanced Materials: Araldite 2015 Structural Adhesives Technical Data Sheet. Huntsman Advanced Materials. April 2007. Available from: http://www.intertronics.co.uk/data/ara2015.pdf.

281. Satthumnuwong P. Approche expérimentale et numérique de la rupture des assemblages colles de composites stratifiés. [Ph.D Thesis, In French]. Université de Bourgogne; 2011.

282. Hashin Z, Rotem A. A fatigue failure criterion for fiber reinforced materials. Journal of Composite Materials. 1973; 7(4): 448-464.

283. Hashin Z. Failure criteria for unidirectional fiber composites. Journal of Applied Mechanics. 1980; 47(2): 329-334.

284. Naghipour P, Schneider J, Bartsch M, Hausmann J, Voggenreiter H. Fracture simulation of CFRP laminates in mixed mode bending. Engineering Fracture Mechanics. 2009; 76(18): 2821-2833.

285. Valot E, Verchery G, Akkus N, Vannucci P, Aivazzadeh S. Ultimate strength of quasi-isotropic laminates in tension: theoretical and experimental analysis. 5th International Conference on Durability Analysis of Composite Systems; 2001; Tokyo, Japan.

286. Hessabi ZR, Majidi B, Aghazadeh J. Effects of stacking sequence on fracture mechanisms in quasi-isotropic carbon/epoxy laminates unter tensile loading. Iranian Polymer Journal. 2005; 14(6): 531-538.

287. Liu PF, Chu JK, Liu YL, Zheng JY. A study on the failure mechanisms of carbon fiber/epoxy composite laminates using acoustic emission. Materials & Design. 2012; 37: 228-235.

288. Ceysson O, Salvia M, Vincent L. Damage mechanisms characterisation of carbon fibre/epoxy composite laminates by both electrical resistance measurements and acoustic emission analysis. Scripta Materialia. 1996; 34(8): 1273-1280.

289. Kim S-T, Lee Y-T. Characteristics of damage and fracture process of carbon fiber reinforced plastic under loading-unloading test by using AE method. Materials Science and Engineering: A. 1997; 234–236: 322-326.

Abstract

The work presented in this thesis is first to study the process of water penetration in carbon/epoxy composites, and secondly, to study the effects of the water absorption on the mechanical performance of the composites and their adhesive joints. The integration of these physical phenomena in the numerical modelling is of great importance in predicting the durability of a composite structure undergone hygrothermal ageing. Therefore, this work is not only limited to experimental observations, but also involving numerical simulations. Correlations between the experimental and numerical results obtained allow on one hand to better understand what happens in an adhesive bonded composite system subjected to mechanical loads and the damage initiation until final failure; on the other hand, to validate a robust numerical model for design and optimisation. The originality of this work lies at different levels by proposing:

1. a new two-phase diffusion model to better describe the effects of the laminate thickness on water penetration;
2. a new Residual Property Model (RPM) to predict the degradation of mechanical properties due to water uptake;
3. a new linear-exponential traction separation law to describe the R-curve observed in mode I DCB tests in composite laminates and its integration into numerical models.

Keywords: carbon/epoxy composites, adhesive bonded joints, water uptake behaviour, mechanical performance, numerical simulations, two-phase diffusion model, Residual Property Model, linear-exponential traction separation law.

Résumé

Le travail présenté dans ce mémoire avait pour objectif d'étudier le processus de la pénétration d'eau dans les composites en carbone/époxyde dans un premier temps, et dans un deuxième temps, d'étudier l'effet de la prise en eau par ces matériaux sur les performances mécaniques des composites et leur joints collés. L'intégration de ces phénomènes physiques dans la modélisation numérique est d'une grande importance dans la prédiction de la durabilité d'une structure en composite subissant un vieillissement hygrothermique. Par conséquent, ce travail consiste non seulement en des observations expérimentales, mais aussi en des simulations numériques. Des corrélations entre les résultats obtenus permettent d'une part de mieux comprendre ce qui se passe dans un système composite avec l'assemblage collé soumis à des charges mécaniques, de l'initiation d'endommagement jusqu'à la rupture finale ; d'autre part, de valider un modèle numérique robuste dans le but de la conception et de l'optimisation. Les originalités de ce travail se situent à différents niveaux en proposant :

1. un nouveau modèle de diffusion à deux-phases permettant de mieux décrire l'effet de l'épaisseur des stratifiés sur la pénétration de l'eau;
2. un nouveau modèle RPM « Residual Property Model » afin de prévoir la dégradation des propriétés mécaniques due à la prise en eau ;
3. une nouvelle loi de traction-séparation linéaire-exponentiel pour décrire la courbe-R observée dans les essais DCB en mode I pur sur les composites stratifiés afin de les intégrer plus facilement dans les modèles numériques.

Mots clés: composites carbone/époxyde, joints collés, comportement d'absorption d'eau, performances mécaniques, simulations numériques, modèle de diffusion à deux-phases, modèle RPM, loi de traction-séparation linéaire-exponentiel